BUTREDDY, PRAVALIKA. Ph.D. Design and Synthesis of Coordination Polymer Frameworks for Solid-State Electrolytes. (2023)
Directed by Dr. Hemali Rathnayake. 204 pp.

Current energy storage technologies suffer from low energy density, heaviness, high cost, and materials scarcity. Thus, lightweight, long-lasting, quick charging, eco-friendly, and low-cost battery technology is crucial for the expansion of power electronics and electric vehicle market, which fall short with conventional batteries. Aiming at solving these key shortcomings in current energy storage technologies, this dissertation envisions producing stable, low-cost, and eco-friendly solid-state electrolytes, a critical component in solid-state batteries. The overall objective is to tailor the structure and functionality of materials, which are already in demand for energy storage applications, at the molecular level and explore the lithium-ion conduction in solid state to design next generation lithium-ion conductors, which are superior in function, lightweight, and environmentally benign.

Towards this vision, this dissertation research has explored one of the most abundant materials in demand, coordination polymers (CPs) and its subclass of metal-organic frameworks (MOFs), as potential candidates for solid lithium-ion conductors. Utilizing an abundant agricultural waste product precursor, tannic acid, lithium-tannate coordination complex (*TALi*), a novel bio-based coordination complex, has been synthesized as the very first lithium-based coordination complex for lithium-ion conduction. The structural and compositional analysis revealed the successful formation of microstructures of lithium-tannate coordination network, which is thermally stable up to 250 ºC. The solid-state lithium-ion conduction in *TALi* was deduced by blending different weight ratios of lithium perchlorate with ethylene carbonate as the plasticizer and lithium-ion mediator. Our temperature-dependent ionic conductance results exhibit ionic conductivity in the range of 1×10^{-5} S/cm to ~ 9×10^{-5} S/cm at room temperature

for the optimum salt concentration, establishing the scientific foundation on lithium-ion conduction in lithium-tannate-based coordination complexes. Incorporating Si-O rich silsesquioxane matrix into the lithium-tannate structure, the lithium-ion conduction improved by 10-fold (in the range of 1 x 10^{-4} S/cm), owing to its high porosity and highly crosslinked silsesquioxane network. Augmenting a base-catalyzed sol-gel polymerization method in the presence of an organoalkoxy silane, porous microstructures of lithium-tannate silsesquioxane coordination polymer was prepared, with size range from 60 nm to 170 nm.

Aiming at understanding the isoreticularity of MOFs, the second research project has focused on the lithium-ion conduction in three known isoreticular MOFs with lithium oxide metal nodes using 1,4-benzene dicarboxylic acid (BDC), 2,6-naphthalene dicarboxylic acid (NDC), and 4,4'-biphenyl dicarboxylic acid (BPDC) as organic linkers. A solvothermal approach was used to synthesize highly crystalline microstructures of isoreticular Li-MOFs having monoclinic topology. Compositional, morphology, and thermal analysis confirmed the formation of 3D porous microstructures with framework stability up to 500 ℃. These isoreticular Li-MOF-based SSEs showed promising solid-state ionic conductivities in the range of ~10^{-5} S/cm with activation energies < 0.72 eV. The trend in ionic conductivities of each Li-MOFs at room temperature exhibit no significant effect on the isoreticular expansion, however, the Li^+ conduction mechanism in each Li-MOF strongly depends on the reticular expansion of the framework and the size of the pore aperture. The vibronic absorption spectral analysis of the SSEs reveals the Li^+ conduction mechanism, allowing us to propose an ion hopping and a vehicle type Li^+ conduction mechanisms for these porous solids. Thus, our results could lead to tailor the solid-state Li^+ conduction at the molecular level by manipulating framework functionality and pore dimension.

DESIGN AND SYNTHESIS OF COORDINATION POLYMER FRAMEWORKS FOR SOLID-STATE ELECTROLYTES

by

Pravalika Butreddy

A Dissertation
Submitted to
the Faculty of The Graduate School at
The University of North Carolina at Greensboro
in Partial Fulfillment
of the Requirements for the Degree
Doctor of Philosophy

Greensboro

2023

Approved by

Dr. Hemali Rathnayake
Committee Chair

DEDICATION

This work is dedicated to my parents (Dr. Ravinder Reddy and Padma Butreddy). Thank you for encouraging me to pursue my dreams and motivating me constantly throughout graduate school and life.

APPROVAL PAGE

This dissertation written by Pravalika Butreddy, has been approved by the following committee of the Faculty of The Graduate School at The University of North Carolina at Greensboro.

Committee Chair

Dr. Hemali Rathnayake

Committee Members

Dr. Joseph Starobin

Dr. Tetyana Ignatova

Dr. Kristin Dellinger

May 15, 2023

Date of Acceptance by Committee

May 15, 2023

Date of Final Oral Examination

ACKNOWLEDGEMENTS

I sincerely thank my advisor, Dr. Hemali Rathnayake, for the continuous guidance and encouragement she provided me for the past four years. Her dedication and profound interest in motivating and helping students has been solely responsible for completing my Dissertation work. I want to thank my committee members, Dr. Joseph Starobin, Dr. Tetyana Ignatova, and Dr. Kristin Dellinger, for their input and evaluation of my research work.

I want to acknowledge the financial support for my doctoral studies provided by the Joint School of Nanoscience and Nano engineering (JSNN), a collaboration between the University of North Carolina Greensboro and North Carolina A&T State University. I sincerely thank the staff at JSNN for their training, and equipment troubleshooting, particularly Dr. Kyle Nowlin, Dr. Gayani Pathiraja, Dr. Steven Crawford, and Dr. Olubunmi Ayodele. I would also like to thank my fellow group members and senior colleagues for their valuable support and guidance.

Finally, I would like to express my indebtedness to my family for their constant support and encouragement throughout my research. They have always inspired me to achieve bigger and be a better version of myself. I would also take this opportunity to express my regards to all my friends who always kept me motivated for the research and their endless support, care, and help.

TABLE OF CONTENTS

LIST OF TABLES

LIST OF FIGURES

LIST OF SCHEMES

CHAPTER I: INTRODUCTION

1.1 Overview

Solid-state electrolytes play a significant role in the next generation of lithium-ion batteries as they offer improved safety and high thermal stability. They eliminate the risk of thermal runaway and electrolyte leakage by replacing the organic liquid electrolytes. Their potential usage with high-capacity lithium metal anodes could significantly enhance the current lithium batteries' energy density and cycle life.[1] However, they possess low ionic conductivities at room temperature due to their poor interfacial kinetics and ionic mobility. Although solid inorganic electrolytes based on highly crystalline ceramics show ionic conductivities in the order of 10^{-3} S/cm along with good mechanical and thermal stability, poor interfacial contacts, high operating temperatures, and commercial processability are proven to be the prime concerns.[2,3] Consequently, solid-polymer electrolytes (SPEs) have emerged promising due to their high processability, shape flexibility, and good interfacial contact between the electrolyte and electrodes.[4] These SPEs have polymers with polar groups that dissolve the lithium salts and assist lithium-ion hopping through the coordination points along the polymer host, mainly in the amorphous regions.[5] Lithium-ion mobility largely depends on the lithium ion-polymer chain interactions, such as lithium-ether oxygen coordination bonds in polyethylene oxide-based SPEs. Further, the segmental motion of the polymer hosts and the local relaxation is essential for high ionic conductivity in these SPEs.[5] However, the current SSEs have not reached the ionic conductivities of liquid electrolytes, which are 10^{-2} S/cm. Therefore, the major challenge is designing a solid-state electrolyte with high reliability without compromising ionic conductivity.

Over the past two decades, various filler materials, plasticizers, lithium salts, and ionic liquids were incorporated into the polymer matrix to achieve high ionic conductivities in SPEs.[6–8] Various kinds of polymers such as polyethylene oxide (PEO), polyacrylonitrile (PAN), polyvinyl chloride (PVC), and polyvinylidene fluoride (PVDF), etc., have been widely demonstrated as polymer matrices. But in recent times, researchers have focused on developing 'sustainable/green' LIBs from renewable sources; natural polymers are alternatively substituting synthetic polymers as they are abundantly available in nature, inexpensive, and environmentally friendly.[9–11] As an interesting new approach, natural polymers, such as cellulose, gelatin, and pectin, are increasingly being integrated as polymer matrices for sustainable, safer, lighter, biodegradable, and cost-effective SSEs.[9,10,12–14] Among the natural polymers used for solid-state electrolytes, polyphenols demonstrate fascinating chemical and physical properties. They have large oxygen-rich phenolic hydroxyl groups and aromatic rings, which allow hydrogen bonding and hydrophobic interactions.[15,16] After deprotonation, these aromatic hydroxyl groups possess a high charge density and can act as 'poly-dentate ligands', providing strong metal chelating sites to form metal-polyphenol coordination complexes.[17,18] Although polyphenols demonstrate promising properties for lithium coordination and their oxygen-rich structures show great potential for high ionic conduction, the successful incorporation of polyphenols into SSEs has not been extensively explored.

Coordination polymer frameworks (CPFs) and their subclass, metal-organic frameworks (MOFs), have attracted attention as a potential class of solid-state electrolyte materials due to their high ionic conductivity and good mechanical and chemical stability.[19–22] Particularly, MOF-based SSEs are advantageous due to their adjustable pore size, which provides a pathway for lithium-ion transport, and their surface polarity enables Lewis-acid base interactions to enhance

the overall electrochemical properties. Further, these nanosized frameworks provide better contact with the electrodes. The open metal sites in MOFs restrict the anion movement by binding to them, which is promising for lithium-cation conduction in SSEs. However, in most MOF-based SSEs, the 'carboxylic acids or nitrogen-containing ligands' bind to the metal sites, leaving no excessive areas for lithium cation binding and transport.[23,24] Hence, incorporating bioinspired metal-phenolate coordination polymer frameworks rich with hydroxyl and ether functionalities into SSEs may overcome the current low ionic conduction challenge and provide an innovative approach for enhancing the lithium-ion conduction along these porous, oxygen-rich frameworks.

1.2 Challenges with Lithium-ion batteries (LIBs)

Lithium-ion batteries are widely used for applications in electric vehicles (EVs), portable devices, and grid energy storage due to their high energy densities and cycling performances. However, over the years, they have also caused severe threats, for instance, the Tesla EV battery fire, Samsung Note 7 explosions, the Boeing 787 Dreamliner battery issues, etc. These safety issues are due to the flammable organic liquid electrolyte used in the LIBs caused due to thermal runaways. Thermal runaway occurs when the battery's temperature rises above ~80 ℃ due to overcharging/ external debris/ internal shorting caused by lithium dendrite formation. The increase in temperatures leads to higher exothermic reaction rates causing overheating and oxygen accumulation, resulting in the combustion of highly flammable and volatile organic liquid electrolytes, causing fires and explosions.[25] Therefore, increasing the thermal stability of the LIBs is essential.

The present LIBs largely depend on the 'carbon-lithium metal oxide' intercalation chemistry, and alternative chemistries such as introducing lithium metal anodes and high voltage

cathode materials is a step towards developing high energy density batteries for electric vehicles.[26,27] Although lithium metal has a high specific capacity of 3.86 $Ah.g^{-1}$ (2.06 $Ah.cm^{-3}$) and a low electronegative potential (-3.04 V), these lithium metal batteries increase the possibility of short-circuiting when used with organic liquid electrolytes based on carbonate solvents due to lithium dendrite formation upon charging.[27,28] The growth of these lithium dendrites can be partially suppressed by using additives in these liquid electrolytes.[26,28] Still, the ideal strategy would be completely replacing liquid electrolytes with non-flammable solid-state electrolytes. Moreover, an all-solid-state battery also eliminates the use of separators that reduces the battery manufacturing cost and plays a key role in the development of next generation sustainable electric vehicle technologies. Therefore, to develop an all-solid-state battery, learning how to design a suitable solid electrolyte plays a crucial role.

Figure 1. Roadmap for developing Li-based batteries.[29]

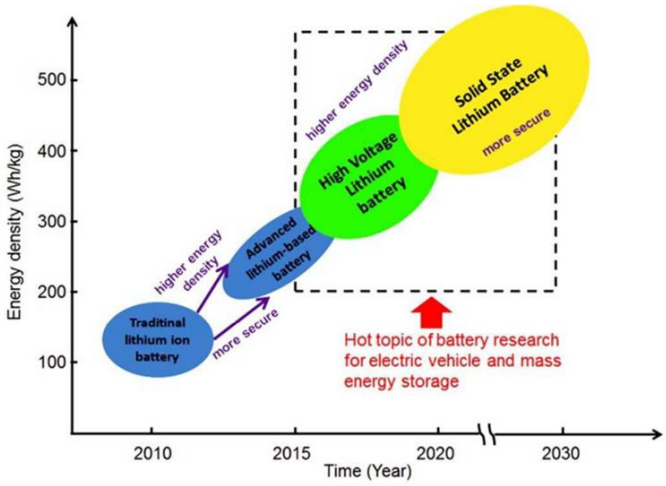

1.3 Current State of the Art in Solid-State Electrolytes in LIBs

Solid-state electrolytes (SSEs) have advantages such as no electrolyte leakage and restraining the moss-like lithium dendrite formation at the anode. They require less packaging, have longer cycle lives, and enable operation at high voltages when compared to liquid

electrolytes. SSEs offer high electrochemical stability to expand the working temperature and potential window. Most SSEs have substantially higher transference numbers than liquid electrolytes, which might help with concentration polarization difficulties. Furthermore, SSEs may reduce self-discharge and lead to increased battery capacity retention.[28,30] However, they have drawbacks, such as complex manufacturing processes, large interfacial impedance, and poor mechanical strength. To design solid-state electrolytes for practical applications, the main properties to be considered are high ionic conductivity ($\sigma_{Li+} > 10^{-4}$ S/cm), adequate mechanical strength (>30 MPa), and a small number of structural flaws to prevent lithium dendrite penetration, low-cost raw materials and simple production methods, and low activation energy for lithium-ion diffusion.[31,32]

Several approaches have been used to develop SSEs, and they are mainly classified into Inorganic solid-state electrolytes (ISEs) and Solid-Polymer electrolytes (SPEs). Inorganic SSEs are mostly inorganic/ceramic-based electrolytes (such as oxide and sulfide-type conductors) whose ionic conduction is through crystal defects. Although ISEs have high ionic conductivities similar to organic liquid electrolytes, they pose issues such as metallic-Li penetration, high cost, processing difficulties, and possess high interfacial impedance with the electrodes.[27,33] Conversely, solid polymer electrolytes (SPEs) are a more popular approach for next-generation solid-state batteries. They are composed of polymer matrices and fillers such as lithium salts, ionic liquids, ceramics, or MOFs.[11,19] SPEs have shape flexibility, are lightweight, have easy processability, high cycle-life, and low flammability; no leakage of the electrolytes, no internal shorting due to lithium dendrites; and good interfacial contact between the electrolyte and electrodes.[4] For their applications in Li-ion batteries, these SPEs should possess a high Li-ion conductivity ($\geq 10^{-5}$ S/cm at 25 °C), safe potential window (≥ 4 V), greater mechanical strength

(≥30 MPa), thermal stability (>150 ℃), and a lithium-oxygen index (>27%).[34] The most widely used polymer matrices are poly(ethylene oxide) (PEO), poly(acrylonitrile) (PAN), poly(ethylene glycol) (PEG), poly(ethylene carbonate) (PEC), poly(vinylidene fluoride) (PVDF), and its copolymers.[35–40]

The commonly used lithium salts in polymer electrolyte systems are $LiBF_4$, $LiClO_4$, $LiPF_6$, $LiAsF_6$, $LiCF_3SO_3$, $LiN(CF_3SO_2)_2$ and arranged in the descending order of their mobility.[7,41] The classic SPEs with dissolved lithium salts in polymer matrices have low ionic conductivities (10^{-5} – 10^{-6} S/cm) and lithium transference numbers ($t_{Li}^+ < 0.5$) due to the simultaneous movement of anions and cations.[7] Different approaches to increase the ionic conductivity, t_{Li}^+, and reduce the activation energy have been used like (1) incorporation of plasticizers such as carbonate solvents (ethylene carbonate (EC), diethyl carbonate (DEC), dimethyl carbonate (DMC), propylene carbonate (PC) or ethyl methyl carbonate (EMC)) and ionic liquids which increase the amorphous nature, and ionic mobility as well as ion-dissociation in the polymer matrix; or (2) using inactive fillers such as micro/nano-ceramic particles (Al_2O_3, SiO_2, and TiO_2, etc.) are used to enhance the ionic conductivity in the SPEs substantially.[29,37,39]

PEO has been the most favorable polymer matrix in terms of being a solid solvent for the dissolution of lithium salts.[42] This is because of ether oxygens' strong electron donor behavior and the flexible segments of ethylene oxide, which readily dissolve the lithium cations. Polysiloxanes have a flexible backbone and two sites for cross-linking on each monomer. As Li^+ coordinates with four oxygen atoms, in PEO-based electrolytes, four repeating units of PEO polymer dissolve one Li^+ ion as each unit has one electron donor atom.[43] Recently, nano-SiO_2 particles were integrated into 3D PEO networks using a rigid-flexible coupling method to produce SiO_2-PEO SPEs in situ. The siloxane polar group promotes the PEO polymer chains to

crosslink and form a 3D network. The incorporation of SiO_2 nanoparticles enhances the PEO polymer chain movements due to the strong Lewis acid-base and hydrogen bond interactions. Further, a decrease in PEO crystallinity was observed due to the interactions between PEO hydroxyl groups with SiO_2 nanoparticles and $LiClO_4$. Therefore, SiO_2-PEO SPEs exhibits good ionic conductivity (~10^{-4} S/cm at 30℃), significantly increased solid-solid interface stability, and a high cycling capacity (~ 90mA h g^{-1} after 100 cycles under 2C at 90℃).[39]

Various polymer hosts, such as poly (vinyl pyrrolidone) (PVP), poly (acrylonitrile) (PAN), poly (vinyl chloride) (PVC), etc., are used to make these 'polymer gels' or 'gel electrolytes.' These gels were made from appropriate amounts of lithium salts, organic solvents, and polymer hosts and further heated to temperatures of 120-150 ℃ until a clear, viscous liquid was formed. The ionic conductivities observed in a few of these gel electrolyte systems lie in the range of 10^{-3}-10^{-4} S/cm.[44] The most widely studied gel or plasticized systems are PEO, PAN, PVdF, or PMMA-based polymer electrolytes. Polymer gel electrolytes undergo the 'syneresis effect' when stored for an extended period. This effect will cause the solvent to ooze onto the electrolyte's surface, which makes the electrolyte gradually turbid. This increases the electrolyte's viscosity, leading to lower ionic mobility and, ultimately, lower ionic conduction.[45] Other minor issues with the gel electrolytes include compositional compatibility, mechanical strength, and interfacial stability, which must be tackled for their commercial applications. Zhang et al. used LLZTO fillers in the polyacrylonitrile-$LiClO_4$ matrix to improve the mechanical strength (10.3 MPa) and ionic conductivity of 2.2 x 10^{-4} S/cm with good stability against Li metal.[36]

PVDF is also a standard binder for electrode materials in Li-ion batteries. However, PVDF-SPEs have low crystallinity and reduced ionic conductivity due to less amorphous paths, and they can be plasticized to improve ionic conduction. Still, the conductivity of these PVDF-

gels is mainly due to the carbonate solvation of cation/anions, leading to lithium-transference numbers less than 0.45. Another approach is to use single-ion conducting polymer structures (SIPE) wherein the anion is bound to the polymer backbone, leaving Li-ion as the only mobile ion, which also prevents lithium dendrite formation. The SIPE based on Li-PVDF membranes after solvent doping in a mixture of EC/PC exhibited a high ionic conductivity of 10^{-4} S/cm at 30 °C, electrochemical stability up to 4.3 V (vs. Li^+/Li), and a lithium transport number of 0.87.[40]

Inorganic fillers such as ceramic fillers, clay, and carbon nanotubes (CNTs), MOFs are dispersed into a polymer matrix, producing organic-inorganic hybrid composite electrolytes. This hybrid solid electrolyte will retain its structure even at high temperatures. This is essentially done to enhance the mechanical properties and ionic conduction and improve the interfacial stability of the polymer electrolytes. [34,46] It has also been reported that the crystallinity of the polymer composite system decreases as the particle size reduces (i.e., when nanoparticles are incorporated); thereby, the ionic conductivity increases.[47,48] The increase in ionic conductivity of these composite electrolytes is also due to the 'percolating interfacial effect' wherein the anions get adsorbed onto the filler surfaces and increase the interfacial conductivity.[49] Therefore, the particle size and the filler surface area play a crucial role in the conductivity of the composite solid-state electrolytes.

Due to their unique properties such as natural abundance, low-cost production, eco-friendly and biodegradable nature, natural polymers such as cellulose, chitosan, Lignin, and gelatin, etc., have been studied as alternatives to synthetic polymers for developing eco-friendly solid-state electrolytes.[11,50] Cellulose and its derivatives were first used as a re-enforcement to improve the mechanical properties of polymer electrolytes. Cellulose has polar functional groups which dissolve lithium salts, and its high T_g brings the required mechanical strength. Recently,

Hadad et al.[43] investigated amorphous cellulose-based gel electrolytes and SPEs with high ionic conductivities of ~ 10^{-2} S/cm and excellent capacity retention of 90% after 100 cycles. Amorphous cellulose derivatives such as oxidized carboxymethyl cellulose (OCMC) and cellulose acetate (CA) have a minimum of 13 electron donor groups in each repeating unit coordinated with 3 Li^+ ions.[43] The amorphous nature and irregularity of the chains with their high oxygen atoms created a Li^+ conduction path in these systems (as shown in **Figure 2**). Recently, Lignin was grafted with PEG and mixed with PVDF-HFP to prepare an SPE with an ionic conductivity of ~10^{-5} S/cm at 25 °C. The ether oxygens in PEG-lignin promoted the interchain Li^+ hopping among lignin polymer chains, and also the abundant aromatic moieties in Lignin enhanced the Li^+ association.[51]

Figure 2. Li^+ ion movement in PVA-OCMC electrolyte.[43]

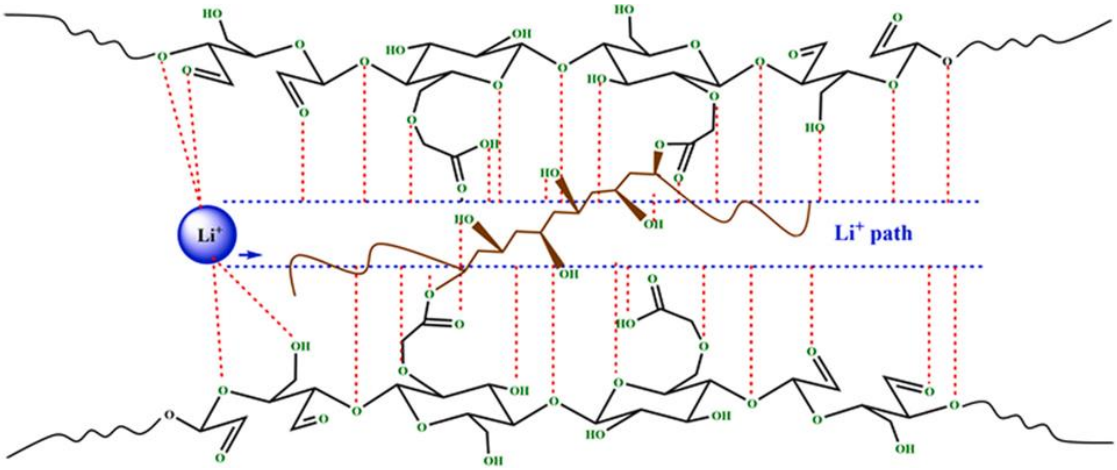

Li et al. used chitosan-silica fillers in a PEO-based SPE, and the chitosan-silica aerogel was prepared via the sol-gel method.[52] The aerogels' organic-inorganic interpenetrating network provides strength to the PEO polymer matrix, and an ionic conductivity of ~10^{-4} S/cm was achieved. The presence of silica was determined using FTIR, EDS, and Raman spectroscopy. The hydroxyl groups in chitosan act as acidic sites and the ether and amine groups form primary

sites making complex interactions in the polymer matrix. Further, fillers increase the amorphous nature; they can reduce the effective ionic conduction paths when used in large proportions; therefore, it is necessary to get an optimal solution.[52] Biopolymer pectin, lithium salt, and plasticizer EC were used to develop a solid electrolyte using a solution casting technique. The amorphous pectin electrolyte films produced an ionic conductivity of ~ 10^{-4} S/cm. The plasticizer EC has a higher dielectric constant and donor number when compared to DMC/PC. EC's effect in the plasticized pectin-based electrolyte was studied using C=O and O=C-O stretching using FTIR spectroscopy.[53]

1.4 Coordination polymer frameworks/ Metal-organic frameworks as SSEs

According to the 2005 IUPAC Red Book of inorganic nomenclature, 'A coordination compound is any compound with a coordination entity. A coordination entity is a neutral molecule, or an ion made of a central atom, generally a metal, to which a surrounding array of atoms or groups of atoms, each known as a ligand, is attached.' Coordination polymers comprise inorganic units and organic ligands as integral constituents extending to one-, two-, and infinite three-dimensional networks via coordinative bonding.[54] Since their appearance in the 1960s, coordination polymers have been crucial to organic-inorganic hybrid materials. Due to their highly tunable molecular building blocks, versatile physical and chemical properties can be achieved; hence, they are essential in various fields.[55] In 1995, Yaghi and co-workers defined a new class of porous coordination polymers known as Metal-organic frameworks (MOFs), which are crystalline coordination networks having organic ligands (or linkers) bound to metal centers (secondary building units (SBUs)) forming 2D or 3D porous structures.[56,57] More than 20,000 different MOFs have been synthesized by changing the SBUs and organic linkers. Their versatile properties, such as high surface area and porosity, are desirable for gas storage and

separation[58,59], sensing[60], catalysis[61], thin films[62], and so on[63]. Most MOFs are obtained by coordinating transition metal ions with organic linkers such as nitrogen or carboxylate units.[64]

Figure 3. Classification of coordination polymers and metal-organic frameworks.[65]

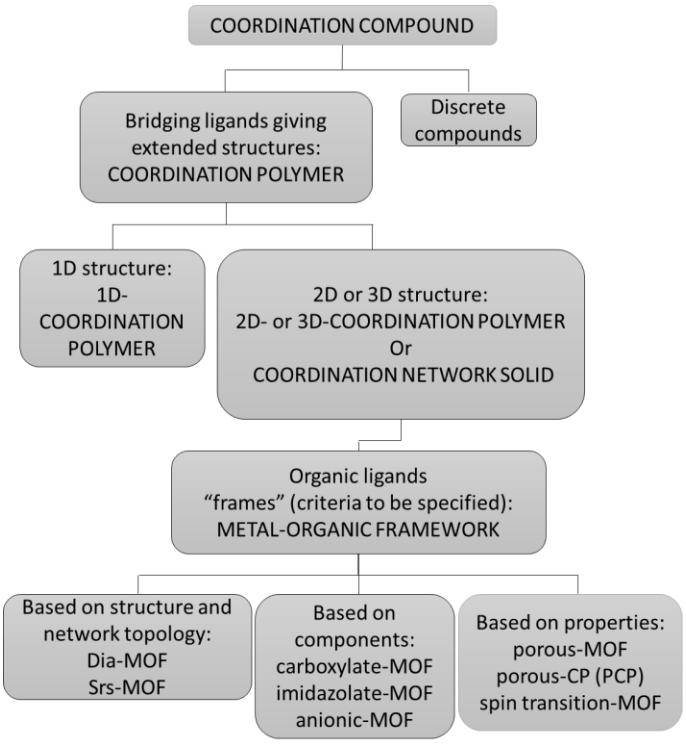

The most common method for synthesizing MOFs right is solvothermal synthesis, which performs at high temperature. Several new methods emerged, such as microwave, ultrasonic, electrochemical, and mechano-chemical synthesis. These methods often employ cheap inorganic salts as metal precursors and use multidentate organic linkers to produce flexible MOFs of high surface area and dynamically respond to external factors such as pressure, temperature, or guest molecules. These frameworks are structurally flexible to modulate the pore size due to weak interactions such as hydrogen bonding, π-π, and van der Waals interactions, apart from the coordination bonds. Hence, their functional diversity, along with low framework density and cheap starting materials, make them suitable for applications in clean energy storage devices

such as fuel cells, hydrogen sorption and generation, solar cells, supercapacitors, and rechargeable Li-ion batteries.[64,66,67]

More recently incorporation of MOFs into solid-state electrolytes (SSEs) has emerged as a desirable research hotspot. The high surface area and surface polarity of MOFs could enhance the Lewis-acid base interactions and the overall electrochemical properties due to more contact with other components.[22] Furthermore, their periodic crystalline structure and tunable porosity, along with ordered channels, facilitate well-defined ionic pathways for cation transfer and aid in forming a uniform interfacial layer along with enhanced cycling stability. Additionally, they suppress the side reactions by trapping the unwanted by-products in the system due to their strong adsorption and surface energy capabilities.[22] Therefore, these versatile properties of MOFs show great potential for designing battery-specific-SSEs. Broadly, in three ways, MOFs have been demonstrated as SSEs, namely, 'MOF-incorporated polymer hybrids' as SSEs, 'ionic liquid (IL) -loaded MOF hybrids' as SSEs and 'neat MOFs' as SSEs.

The 'MOF-incorporated polymer hybrids' are organic/inorganic hybrid electrolytes in SSEs, consisting of polymer matrices, metal salts, plasticizers, and MOF fillers. Incorporating plasticizers and MOF fillers enhances ion dissociation in metal salts and segmental polymer mobility. The increase in mobile ions and migration pathways further enhances the ionic conductivity of these composite SSEs. Therefore, the high-surface areas, along with the rich porosity of MOFs, provide better contact with polymers and metal salts than the traditional filler materials in hybrid SSEs and also provide preferential anion attachment due to Lewis acidity.[22]

Incorporating ILs into MOFs is another powerful approach for advanced properties in SSEs. ILs have gained attention as new green solvents composed of ions with a low melting point (<100 °C) possessing high ionic conductivity and solubility, non-flammability, minimal

volatility, and high thermal stability.[68] MOFs can behave as reservoirs for ILs without the risk of leakage, owing to their strong adsorptive capacity and high porosity and surface area in these frameworks. Further, confinement of ILs in the micro/meso-pores of MOFs promotes ion diffusion and selective ion bonding with polar MOF surfaces, enhancing the transference number and the overall ionic conductivity.[68] There are several approaches to making these IL@MOF composites, the first approach being the 'post-impregnation approach' wherein the synthesized MOFs are socked in IL-containing solutions. The second is the 'capillary action-promoted diffusion,' where the stoichiometric amounts of IL and MOF are physically mixed and annealed. And the third is the 'ship-in-bottle' method which involves introducing IL precursors into MOF pores and assembling them to obtain an IL inside the MOF pores.[69] Strong interactions such as coulombic, π-π, hydrogen-bonding, Vander Waals, and coordination interactions facilitate IL dispersion and capillary adsorption in MOFs. Hence, while designing these IL@MOF composites, carefully considering MOF pore size, size of ILs, and structural and coordination parameters of MOFs is beneficial.[22]

1.4.1 Metal-carboxylate Frameworks in SSEs

Modular chemistry allows the use of discrete molecular building units to build extended networks at near room temperature and impart the desired physical properties to the target frameworks. Understanding the concept of secondary building units (SBUs) is critical to designing robust MOFs with permanent porosity and those with unsaturated open-metal sites. The aggregates of metal ions, i.e., M-O-C clusters, are referred to as SBUs, which can be obtained using multidentate ligands such as carboxylates. They form rigid frameworks because the carboxylates lock the metal ions and form rigid vertices to give extended neutral frameworks with high structural flexibility. To achieve highly porous frameworks, either the longer linkers

that increase the void space, known as *expansion,* or a net of vertices can produce highly rigid, non-interpenetrating networks known as *decoration.*[70] Di-, tri- and tetranuclear 'metal-carboxylate clusters' such as copper and zinc acetate were used as SBUs to generate porous crystalline metal-carboxylate frameworks with polytopic linkers such as 1,4-benzenedicarboxylate (BDC), 1,3,5-benzenetricarboxylate (BTC), 4,4′-azodibenzoate (ADB), and 1,3,5,7-adamantanetetracarboxylate (ATC).[70]

These crystalline porous and rigid metal-carboxylate frameworks have applications in catalysis, gas storage, sensors, and SSEs.[22,70] For instance, MIL-53(Al) (Aluminum 1,4-benzenedicarboxylate)[71] and MOF-5 (Zn_4O(1,4-benzenedicarboxylate)$_3$)[72] were incorporated as filler materials into PEO-based SSEs. In the case of MIL-53(Al), a thin-film electrolyte was made using the lithium bis(trifluoromethanesulfonyl)imide (LITFSI) salt and PEO as the polymer matrix.[71] The interactions between the Lewis acidic surfaces of MIL-53(Al) and $N(SO_2CF_3)_2$ anions improved the LITFSI dissolution, which gave an enhanced ionic conductivity (9.66×10^{-4} S cm^{-1} at 120 ℃) and oxidation potential (5.10 V) for the electrolyte. Further, this composite electrolyte was incorporated to fabricate an all-solid state $LiFePO_4$/Li button cell and gave an initial discharge capacity of 136.4 mA h g^{-1} (at 5 C and 120 ℃). An increase in the thermal and mechanical stability was observed as MIL-53(Al) particles acted as cross-linking centers with PEO.[71] Similarly, when MOF-5 was incorporated into the PEO and LITFSI matrix the interaction between the alkoxide chains of PEO and Lewis acidic sites of MOF-5 accelerated the salt dissolution and PEO chains movement.[72] Further, MOF-5 could trap the trace solvents and impurities which promoted ionic conduction and avoided side-reactions with the Li/CPE interface.[72] Furthermore, Kitagawa and co-workers demonstrated the incorporation of ionic liquids like EMI-TFSA (1-ethyl-3-methylimidazolium bis(trifluoromethylsulfonyl)amide) into

the chemically and thermally stable MOF, ZIF-8 (Zn(2-methylimidazole)$_2$) to demonstrate an IL-loaded MOF system as SSEs.[24,73] Their results suggested a lithium ion-diffusion mechanism wherein the Li-cations diffuse through the ZIF-8 micropores by exchanging the solvating $TFSA^-$ anions, similar to the 'Grotthusss mechanism' in proton conductivity.[24]

1.4.2 Lithium coordination compounds

Lithium was first recognized as a new alkali metal in 1817 by J.A. Arfvedson and lithium compounds were found to be less soluble in water than sodium (Na) and potassium (K).[74] Lithium is the third element (Z = 3) in the periodic table having two isotopes (^{6}Li and ^{7}Li) with an atomic weight of 6.941 (amu) and an electronic configuration of $1s^2\ 2s^1$. It occurs in ferromagnesian minerals by partially replacing magnesium and its most commercially available mineral is spodumene ($LiAlSi_2O_6$). It has a relatively low abundance of about 18 ppm by weight in crustal rocks. It is the smallest element with the highest ionization energy and melting point in the alkali metal group and is the solid having the lowest density at room temperature. At least 20 different coordination geometries of lithium are known with coordination numbers ranging from 1-12.[74]

The modern concepts on coordination compounds are based on Alfred Werner's study on 'spatial arrangement of ligands around metal centers' in 1893. These coordination compounds have two key concepts namely, oxidation state (or ionizable valence) and coordination number (or non-ionizable valence). Coordination compounds can be broadly classified as coordination polymers, discrete coordination compounds and metal-organic frameworks.[75] Coordination polymer is a metal-coordination compound where the ligand (or the linker) bridges between the metal centers (or the connectors) and each metal would bind to more than one ligand that could extend as an infinite array at least in one dimension through either covalent or coordinate

interactions.[76] More interestingly, compartmentalized ligands are capable of producing heterometallic systems by providing coordination pockets to connect different metal centers. These heterometallic compounds have been widely synthesized using Schiff-base ligands derived from salicylaldehyde and diamines.[77] Coordination compounds have great importance due to their applications in gas adsorption, catalysis, sensing, luminescence, energy storage and so on. Due to their structural diversity, molecular design, tunable pore-size and redox-active sites, these coordination compounds can provide higher density of Li-storage sites, operate at high capacities over wide voltage ranges and also can provide fast Li-ion transport.[75] Hence, understanding the design principles and lithium storage mechanisms in these coordination compounds is of great significance and they have been demonstrated as effective anode, cathode and electrolyte materials in LIBs.[75]

Coordination compounds of lithium and lithium-ion complexes are an interesting field due to their biological significance and applications in LIBs. Lithium (I) compounds commonly exhibit a coordination number between 2 to 8 and their binding is mostly electrostatic.[78] Due to the undirected coulombic forces, the radius of Li ion (0.6 Å) is critical to determine the structure of the final complex. Other factors which affect the coordination number of Li-ion are the number of binding sites, ion-ion interactions (anions) and ion-dipole interactions (neutral ligand and solvent). However, beyond a minimal cavity radius (r_m) the coordination sphere interactions are independent of the cation radius (r_{Li+}) and based on the r_m/ r_{Li+} values, the most promising coordination numbers for Li-ion are found to be 4, 5 and 6. Most lithium complexes selectively exhibit '4-fold tetrahedral' or '5-fold square pyramidal' coordination.[78]

Lithium-ion is known as a 'hard acid' and most of its organic/ inorganic complexes are bound to ligands through the lithium-oxygen (Li-O) interactions. The oxygen atoms (hard base)

in most natural/synthetic ionophores act as donors (such as hydroxyl, keto, carbonyl, carboxylate, ester, ethereal, etc) and the interactions of lithium with oxygen donors are stronger than with nitrogen.[78] For instance, lithium forms stable complexes with hard oxygen atoms of carboxylic acids (mono-, di-, hydroxy-) and give different coordination polyhedra for their coordination numbers 4 (tetrahedral), 5 (trigonal bipyramidal, square pyramidal) and 6 (distorted octahedral) respectively. The strong electrostatic interactions (ion-ion) between hard Li-ion and hard oxygen donor-atoms are responsible for these stable coordination complexes, and as the carboxylic groups for coordination increase, the Li-O bond distance also increases. Contrastingly, the lithium crystal complexes with alcohols are uncommon and, they form tetrahedral or square pyramidal coordination with the hydroxyl-oxygen atoms.[78]

1.5 General Goals of Research

The dissertation research investigates two novel coordination polymer frameworks and three derivatives from its subclass, metal organic frameworks (MOFs) for developing novel solid-state electrolyte systems. ***Aim 1*** focuses on understanding lithium-ion conduction in three isoreticular lithium-based MOFs (Li-MOFs) synthesized via a solvothermal method augmenting the isoreticular framework expansion approach. Utilizing tannic acid, a natural polyphenol, ***Aim 2*** focuses introducing a novel lithium-based coordination polymer, lithium-tannate coordination complex (TALi) and its lithium-ion conduction in solid-state. Introducing the silsesquioxane network via a sol-gel synthesis method, ***Aim 3*** targets modifying the structure and functionality of TALi complex to make porous microstructures of TALi-silsesquioxanes.

Rationale: Coordination polymer frameworks and MOFs could be potential candidates as SSEs owing to their high porosity, ordered channels, structural modularity, and capability for high tunability. These unique characteristics offer several advantages to surpass the traditional

liquid electrolytes, resulting in high ionic conductivities, improved safety, and longer lifespan.[30] Past research has evidenced that MOF-based solid-state electrolytes can confine small amounts of liquid electrolyte inside the host matrix of porous frameworks. They are safer than liquid electrolytes at higher operating temperatures, have good electrode contact, stability, and higher ionic conductivities than SSEs, and provide mechanical stiffness to block dendrites.[79–81] The addition of plasticizer increases the free volume by adding additional salts to increase charge carriers, boosting the dielectric constant to improve salt dissociation.[82,83] Ethylene carbonate (EC) was used as the plasticizer because of its high dielectric constant (89.1), which can help dissociate lithium salts easily, a high donor number (16.4), and a high boiling point (248 °C).[53,84] Reducing EC content can help the solid-electrolyte interphase (SEI) formation on the electrode surface for higher stability. Mainly, EC-based electrolyte is efficient at limiting the graphite anode exfoliation compared to PC-based electrolytes, resulting in better battery stability and lifetime. The higher stability of the Li-EC pair than other Li-solvent pairs helps suppress electrolyte decomposition.[85] $LiClO_4$ was used because it's easy to purify, inexpensive, and forms highly conductive solutions with carbonate solvents and highly compatible with graphite electrodes.[86]

Impact on the Scientific Community: It is a step towards producing low-cost, safe, efficient, and eco-friendly solid-state electrolytes. Also, integrating renewable resources and principles of green chemistry in synthesizing lithium-tannate-based CPFs is very appealing to the scientific community.

Aim 1: Design and Synthesis of isoreticular Li-MOFs to investigate lithium-ion conduction for Li-MOF based solid-state electrolytes.

Objective: To understand the effect of isoreticulation on ionic conductivity in Li-MOFs.

Hypothesis: The porosity of the frameworks might increase with the increase in the organic linker length, thereby providing additional lithium-ion conduction pathways which may lead to an increase in the ionic conductivity.

To complete Aim 1, this research targets the following two tasks:

Task 1: Synthesis of Li-MOFs using the three carboxylate linkers (1,4- BDC; 2,6- NDC and 4,4'-BPDC) and characterization.

Task 2: Studying the ionic conduction in the Li-MOFs using electrochemical impedance spectroscopy.

Novelty: Solid-state ionic conduction in these isoreticular Li-MOFs as SSEs has not been explored yet.

Expected Outcomes: Isoreticular Li-MOFs to use as low-density SSEs.

Aim 2: Design and Synthesis of lithium-tannate coordination complex to investigate lithium-ion conduction for TALi based solid-state electrolytes.

Hypothesis: The lithium-tannate coordination complexes with rich oxygen functionality will aid lithium-ion hopping through oxygen-coordination centers in solid-state.

Rationale: Tannic acid has abundant oxygen-rich, phenolic hydroxyl groups which can act as 'polydentate ligands' providing strong metal chelating sites for binding metal ions at higher pH. Catechol and gallol groups allow five-sided ring coordination with different metal ions.[87] Furthermore, the polymers with polar groups –O-, =O, -S-, -N-, -P-, C=N, -NH- (imide), -S- (thiol), and C=O will be able to dissolve the lithium salts.[7] This dissociation in turn determines the number of free lithium ions in the electrolyte matrix, which affects the ionic conductivity. The ion transport is due to the electrostatic interactions between polar groups in these coordination polymers and electron-withdrawing Li-ions which generate the ionic transport pathways.[83]

To complete Aim 2, this research targets the following two tasks:

Task 1: Synthesis and characterization of lithium-tannate (TALi) complex from tannic acid.

Task 2: Studying lithium-ion conduction in the TALi-based electrolytes using electrochemical impedance spectroscopy.

Novelty: Lithium-tannate complexes and its potential as a solid-state electrolyte.

Expected Outcomes: Lithium-tannate complexes to use as bio-based SSEs.

Aim 3: Design and Synthesis of lithium-tannate-silsesquioxane microstructures to investigate the lithium-ion conduction for TALi-SSQ based solid-state electrolytes.

Hypothesis: The lithium-tannate silsesquioxane network with silsesquioxane structure will provide added functionality to aid lithium-ion hopping through Si-O matrix, resulting in high ionic conductivity compared to TALi complexes.

Rationale: Sol-gel synthesis is a versatile bottom-up method that involves conversion of a colloidal solution into a network of discrete particles or polymers. Under a basic environment, condensation is rapid when compared to hydrolysis and formation of silane linkages is increased.[88] In this base-catalyzed sol-gel reaction, first hydrolysis occurs wherein trimethoxy groups convert into trihydroxy groups and then polycondensation occurs with the surface hydroxyl groups of lithiated tannic acid.[89] Also, 3-APT has an amine group which is hydrophobic would facilitate interactions with the free hydroxyl groups of lithiated tannic acid.[90] The silsesquioxane nanocages with the formula ($RSiO_{1.5}$) have reactive functional groups at cage corners which are available for surface bonding.[91] Further, these silica cages can entrap plasticizer within the SSE which can exhibit higher ionic conductivities at room temperatures.[91] The internal inorganic silicon oxygen

core of the silsesquioxanes materials facilitates the lithium-ion conduction and also hinders crystallization of the host polymer.[92]

To complete Aim 3, this research targets the following two tasks:

Task 1: Synthesis and characterization of lithium-tannate silsesquioxane (TALi-SSQ) microstructures.

Task 2: Studying the ionic conduction in the TALi-SSQ-based electrolytes using electrochemical impedance spectroscopy.

Novelty: Synthesis and Characterization of the novel lithium-tannate-silsesquioxane based SSEs, and their solid-state ionic conduction.

Expected Outcomes: TALi-SSQ microstructures to use as silsesquioxane-based SSEs.

1.6 Dissertation Layout

This dissertation consists of seven chapters, and a brief introduction to each of the chapters is described here. Chapter 1 starts with an overview of the current challenges in lithium-ion batteries and the need for solid-state electrolytes. Further, the chapter discusses the state-of-the-art in SSEs, emphasizing the solid polymer electrolytes, both synthetic and natural polymers. Finally, an introduction to CPFs/MOFs-based SSEs and state-of-the-art metal-carboxylate-based SSEs has been discussed. Chapter 2 introduces natural polyphenols in LIBs and reviews plastic crystal-based SSEs, lithium coordination compounds, and the basics of a LIB. Later, Chapter 2 describes the ionic conduction mechanisms in SPEs and MOFs and then describes the working principle in electrochemical impedance spectroscopy (EIS) technique and ionic conductivity measurements in detail. Chapter 3 presents the experimental sections for the preparation of materials (Li-MOFs, TALi, and TALi-SSQ), the characterization techniques, and the sample preparation methods used. Chapter 4 presents the synthesis and characterization of Li-MOFs.

Further, ionic conductivity measurements and ionic conduction in Li-MOF-based SSEs are described using EIS and FTIR spectroscopy. Chapter 5 discusses the synthesis, characterization, and ionic conduction of TALi complexes. Chapter 6 discusses the synthesis, characterization, and ionic conduction of TALi-SSQ microstructures. The dissertation is finally summarized in Chapter 7, which also makes some comments and recommendations for future directions.

CHAPTER II: BACKGROUND

2.1 Natural Polyphenols

Natural polyphenols are mostly the biologically active components of plant-based edibles such as fruits, vegetables, coffee, and cereals.[93] Although these compounds have complex structures consisting mainly of catechol and galloyl groups, phenolic ring acts as their basic monomer. They can be widely classified into condensed and hydrolysable families, and possess attractive biological properties such as antioxidant, anti-bacterial, antiviral, anti-inflammatory, antitumor activity, etc. Hence, they have been widely used in food industry, water treatment, pharmaceutical research, oil-field chemistry, leather industry and so on.[87,93] Moreover, due their biocompatible nature along with intriguing chemical and physical properties such as metal chelation, hydrogen bonding, amphiphilic nature; they are widely being integrated into engineering functional materials in multi-disciplinary fields like diagnostics, drug-delivery, and designing of hydrogels, thin-films, core-shell/hollow particles and metal-phenolic coordination compounds.[87,94–99]

Metal-phenolic networks (MPNs) are 'supramolecular network structures' formed due to the coordination between metal ions and phenolic ligands. They are of great interest because they can act as versatile platforms to engineer 'green', low-cost nanomaterials and biointerfaces.[97] Natural phenolic acids such as gallic acid (GA), ellagic acid (EA) and tannic acid (TA) have been widely studied for their interactions with transition metals, proteins, and DNA to form coordination complexes. These coordination complexes could be tuned to result in formation of advanced materials such as hydrogels[87,100], films[87,101], capsules[99,102] and various nanostructures[87,101]. For instance, fluorescence quenching in DNA was studied using these phenolic acids (TA, GA and EA) and strong interactions of DNA with the phenolic acids were

observed, indicating the intercalation of these phenolic acids into DNA.[97] Furthermore, metallogels synthesized using the Fe^{3+}-catechol complexes showed self-healing properties and high elastic modulus due to the reversible nature of the metal-phenolic coordination. Contrastingly, Fe^{3+}-catechol coordination bonds have strength comparable to covalent bonds and possess pH responsive nature due to the need to deprotonate the hydroxyl groups which is favorable at higher pH.[103,104]

The deprotonated phenol group generates an oxygen center having a high charge density, which is known as a "Hard Acid".[18] Most phenols have a pK_a value range of 9-10 in the presence of cations such as Fe^{3+}, Cu^{2+}, while the protons get displaced at a lower pH range 5-8. Hence, a pH around 7 is most suitable for metal chelation by phenols. Oxidation occurs in catechols producing the products semiquinone and quinone which coordinate with metal cations. For instance, the *peri* positions of phenolic hydroxyl groups in TA act as oxygen anions to react with metal cations and form stable "five-numbered ring complexes".[105] The oxidation state of coordinated metal is often difficult to determine because of the delocalization of orbitals among the metal and at least one phenolic ring. Interestingly, the stoichiometry of TA complexes with Fe^{+2} and Fe^{+3} metal cations were found using the UV-Visible spectroscopy since TA shows intense absorption bands at 274 nm, as TA is a strong 'UV absorbing chromophore'.[105] Intramolecular electron-transfer reactions can also be observed in metal-catechol complexes such as with Fe and Cu, where the value of pH and presence of other ligands could influence the equilibrium.[18] Due to the numerous chelation sites available on TA, it has been extensively studied for coordination with about 18 different metals, that mostly include transition metals, to produce MPN films which are capable of forming hollow capsules.[99] Although, there is significant research on MPNs mostly with the transition metals such as Fe, there is still lack of

research pertaining to coordination of phenolic ligands with alkali metals such as lithium and sodium, which is of great interest in the field of energy storage.

2.1.1 Natural Polyphenols in Lithium-ion Batteries

Due to the increased research in high-performance renewable energy storage devices, sustainable rechargeable batteries and all-solid-state batteries are in huge demand in recent times.[34,106] Traditional inorganic materials mostly based of metal-oxides show slow lithium-ion diffusion kinetics, large volume changes and also produce toxic heavy-metal waste, that leads to fast capacity fading and huge polarizations.[107] Hence, researchers have shifted to organic compounds as the weak intermolecular interactions accommodate diverse metal ions and give superior electrochemical properties, besides being inexpensive and abundant in nature.[108,109] In the light of this, natural polyphenols such as ellagic acid, tannic acid, have been demonstrated as potential separator[110–112] and electrode materials[113,114] in lithium-ion batteries, due to the presence of π-π conjugated aromatic structures, rich carbonyl, carboxyl and phenolic groups.

Ellagic acid is formed by the dimerization of gallic acid resulting in a biaryl structure. Tannic acid is an oligomer of gallic acid having ten galloyl units around a glucose center. The numerous π-π conjugated structures in TA and EA provide "layer-by-layer intermolecular interactions" and enhanced diffusion of lithium cations leading to a superior ionic conductivity. When EA and TA were used as active anode materials against a Li metal counter electrode in a coin cell containing a liquid electrolyte, they gave specific capacities of 364 and 451 mAh g^{-1} at 0.2 A g^{-1} after 250 cycles. These discharge capacities were higher than imine-, azo-, carbonyl-, organosulfur- based active materials and were comparable to that of metal-oxide based anodes. TA and EA-based LIBs showed higher cycling stabilities than the metal-oxide based LIBs.[113] In a similar study performed by Goriparti et al.[114], EA demonstrated high reversible capacities of

450 mAh g^{-1} and 200 mAh g^{-1} at C/10 and C/2.5 discharge rates, respectively. They have demonstrated that the process of lithiation-delithiation in EA is reversible through ex-situ NMR spectroscopy and have also proposed the possible mechanism.[114] Xu et al.[115] demonstrated TA as a potential organic anode material in LIBs due to the presence of abundant oxygen-functionalities. They have found that the dissolution of TA in an electrolyte consisting of LiTFSI salt was considerably lower than in $LiPF_6$ and confirmed the insertion of lithium-ions into the TA framework. Further, TA in high concentrations of LiTFSI gave higher specific capacity and longer cycling life.[115] TA was also used to improve the lithium-ion diffusion in $Li_{1.2}Mn_{0.6}Ni_{0.2}O_2$ (LMNO) cathodes.[116] The catechol groups of TA formed a metal-organic coordination complex (MOC) with the transition metal Ce to produce nanofilms (~10 nm) on the surface of LMNO cathode. This CeO_2-coated LMNO provides a pathway along the MOC for the fast diffusion of lithium ions and hence the discharge capacity increased to 132 mAh g^{-1} at 8C from 86 mAh g^{-1} of the pristine LMNO.[116]

Separators in LIBs play a critical role in cycling stability and overall battery performance. The most used commercial separator materials are microporous polyolefin films with good mechanical strength, chemical and thermal stability. But their hydrophobic surface and low surface energy causes poor wettability as their pores are incompletely filled with liquid electrolytes, leading to higher ionic resistance with the electrodes.[111] In order to increase the hydrophilicity on the surface of the polyolefin separators, such as polyethyleneimine[110] (PEI) and polypropylene[111,112] (PP) were modified using tannic acid and were demonstrated as potential separator materials for lithium-ion batteries. Multiple phenolic units in tannic acid can self-polymerize and form hydrophilic coating on the surface of the polyolefin separators, besides being a cheap and green modification technique when compared to dopamine.[110] TA coated

polypropylene (TA-PP) films showed no change in porosity or thermal stability but showed a decrease in the contact angle of water to 72^0. This showed that TA-PP membranes became more hydrophilic and exhibited better wettability (~125 wt % uptake) with the liquid electrolyte (1M $LiPF_6$ in EC/DMC). This further increased the ionic conductivity of TA-PP separator to 0.46 mS cm^{-1} from 0.23 mS cm^{-1} (PP separator) and also a slight increase in the specific capacity of the cell.[111] Zhang et al.[110] extensively explained the self-assembly process between TA and PEI where hydrogen bonding and oxidation polymerization were the two possible mechanisms. The catechol and pyrogallol units in TA were oxidized in alkali solutions to form quinoid structures generating functional layers by the reaction of amines of PEI through a Schiff base reaction.[110]

Solid-state electrolytes have received great attention in the past few decades as they provide superior safety than the conventional liquid electrolytes. Additionally, they have properties such as no leakage of the electrolyte, 'wide electrochemical stability window', better thermal stability, great mechanical strength, flexibility and processability, which make them suitable for high energy and 'high power density' rechargeable batteries.[34] Poly(ethylene oxide) (PEO)-based polymer electrolytes are extensively studied because the lithium-ion conduction takes place through the ethylene oxide groups.[117] They still have a drawback of low ionic conductivity when compared with the liquid electrolytes, due to the poor polymer chain mobility and high crystallinity of ethylene oxide chains at low temperature.[118] In order to increase the polymer chain mobility and further the ionic conduction, modified TA was used as a plasticizer and a cross-linking agent with polymer electrolytes without disturbing the solid-state of polymers.[119] It was observed that addition of small amounts of plasticizer (2.0 wt %) and cross-linking agent (0.1 wt %) to polymerize poly(ethylene glycol) methyl ether methacrylate (PEGMA), gave a higher ionic conductivity (5.6×10^{-4} S cm^{-1}) at room temperature.[119] Cho et

al.[120] created a quasi-SPE using PEGMA polymer matrix, Methacrylated TA (MTA) as crosslinker, nano-SiO_2 and liquid electrolyte as a plasticizer which resulted in a honeycomb-branched structure. This QSPE film gave an ionic conductivity of ~10^{-3} S/cm at room temperature and a voltage window of 5.1 V.[120] Due to their diverse properties, there is a lot of scope for polyphenols to be used as a main matrix in solid-state electrolytes and there is an immense need for extensive research in this area in order to build green-all solid-state LIBs.

2.2 Plastic Crystal-based Solid-State Electrolytes

There is an increase in demand for shape-conformable solid-state Li-ion batteries due to their diverse applications in flexible displays and electronics. One effort to manufacture such shape-conformable electrolytes is to use plastic crystals. These plastic crystal-based polymer electrolytes are composed of plastic crystals, which have good solvating capacity, and lithium salts.[121] The concept of plastic crystals is not an entirely new one and was explicitly described by Timmermans in his historical review, in 1961. He has described the process of melting to be complex in the liquid crystals as it depends entirely on the "thermal movements of molecules".[122] If the molecules are able to move freely in all directions, they form 'isotropic liquids', whereas long molecules having double bonds form 'anisotropic liquids' due to their restricted motion. On the contrary, in plastic crystals, the freedom to rotate in a crystal already exists due to its globular shape but the coherence of the crystal is broken at its melting point.[122]

These plastic crystals are quasi-spherical or gluobular or disk-shaped molecules having rotational disorder while preserving their translational order.[121] Due to their structural disorder plastic crystals show greater diffusivity and plasticity when compared to rigid crystals. Plastic crystals based on the ionic species show ionic conductivity. Inorganic salts like Li_2SO_4 and Na_3PO_4, molecular species like succinonitrile (SN) and sebaconitrile, and organic ionic plastic

crystals (OIPCs) exhibit plastic crystal behavior thus far. Plastic crystals have more plasticity and diffusivity when compared to conventional rigid crystals. Therefore, solid-electrolytes based on lithium salts dissolved in plastic-crystals exhibit remarkably high conductivities.[123–125]

In 1999, Macfarlane et al. demonstrated fast-ionic conductivity in a plastic crystal-based electrolyte wherein salts containing the 'imide' cations or anions were doped in the P_{1x} matrix.[126] From the ionic conductivity measurements, it was observed that doping about 1% cationic Li into the P_{11} and P_{12} matrix had enhanced the conductivity by 20-fold. The thermograms of the doped materials showed rotational disorder and presence of vacancies in the lattice.[126] Similarly, many other ion-conducting plastic crystal systems were investigated and reported good ionic conductivity values. One such report on pyrazolium imides demonstrated conductivity values of about 6.2×10^{-3} S/cm at 60 ^{0}C in the plastic crystal phase. By doping small amounts of lithium bis-trifluoromethanesulfonimide (LiTFSI), a tenfold increase in the ionic conductivity was observed at room temperature.[127]

Alarco et al. investigated that a polar, non-ionic plastic-crystal form of succinonitrile can be used as a conductive matrix for the applications in solid-state batteries. Due to its high polarity, it is able to dissolve many salts and the ionic conductivity originates entirely from the doped ionic salts in this non-ionic matrix. The plastic phase of succinonitrile extends from -35 ^{0}C to 62 ^{0}C (melting point). It has a higher ability to separate charges than the other liquid solvents due to the various conformations possible (from syn to anti), which also results in a dielectric constant of 55 at 25 ^{0}C. It also has a lesser tendency to solvate cations owing to its lower donor number (15) as compared to PEO (22).[128] Since the plasticity of succinonitrile is comparable to that of polymer electrolytes, it would be able to accommodate the volume changes which occur due to the mechanical stress induced by the intercalation/de-intercalation process. Various salts

were doped with succinonitrile to produce transparent films and a maximum ionic conductivity of 3 x 10^{-3} S/cm was achieved.[128]

The lithium doped succinonitrile based plastic-crystal electrolytes (PCEs) which show the *trans-guache* isomerism (i.e., the rotation of molecules about the C-C bonds of succinonitrile) exhibit a greater ionic conductivity in the order of 10^{-3} S/cm. The *trans*-isomer is an impurity phase which lowers the activation energy for ionic conduction by increasing the lattice defects in succinonitrile.[121] A comprehensive study was done by Das et al. on the ionic conduction mechanisms in the succinonitrile-lithium perchlorate PCEs. It was reported that both configurational isomerism and ion-solvation mechanisms were responsible for the ion-transport in the SN-$LiClO_4$ electrolyte. X-Ray diffraction and cryo-crystallography for single crystals were used for the structural investigations in these PCEs. It was found that with increase in temperature and salt-concentration the configurational dynamics increased due to a higher degree of disorder. On the contrary, higher salt-concentration results in ion association which negatively affects the ion conduction. Therefore, an optimal salt concentration is desirable.[129]

Ha et al. demonstrated the fabrication of semi-interpenetrating PCEs from LiTFSI doped succinonitrile and imparted mechanical bendability along with electrochemical stability.[121] Following this, Zhou et al. imparted cyanoethyl polyvinyl alcohol (PVA-CN) into succinonitrile (PVA-CN/SN) based PCE. This PVA-CN based electrolyte was prepared by the sequential addition of the two lithium salts (LiTFSI and $LiPF_6$) in PVA-CN/SN at a weight ratio of 5:1.[130] A high mechanical stress of 15.4 MPa was obtained when PVA-CN/SN electrolyte was dispersed in the pores of PAN-based electrolyte. The ionic conductance obtained at room temperature was 0.3 S and a high lithium-ion transference number of 0.57 was achieved, along with good flexibility.[130]

2.3 Basics of an LIB

Although many battery technologies have been tested on a laboratory scale, only a few of them could be commercialized after going through several safety cycles. Since rechargeable (secondary) batteries are mostly preferred over disposable (primary) batteries, therefore the companies were keen on commercializing them. The first ever successful lithium-ion battery (LIB) was based on the prototype of Yoshino et al.[131] and was commercialized by SONY in 1991. This LIB has carbon as its anode and discharged $LiCoO_2$ as its cathode. Though many electrode materials, electrolytes and separators have been explored, the present-day battery is not very different from the cell SONY first commercialized.

In a rechargeable LIB, the electrodes are connected to an external electrical supply. During the charging process, electrons are released at the cathode and move to the anode externally, while internally lithium ions move from cathode to anode through the electrolyte. The opposite occurs during discharge as shown in **Figure 4**. In this manner the electrical energy is converted to the electrochemical potential of the cell. Since the Li^+ ions move between the cathode and anode, this mechanism is called the 'shuttle chair' mechanism.[132] Ionic resistivity arises from anything that hampers the motion of Li-ions in the battery, which could be from the electrolyte, the interface between the electrolyte and the electrodes, or from the resistance inside the electrode materials.[133] The external electric field and the concentration gradient are the two driving forces that allow the Li-ions to pass through the electrolytic media. Mobility is the ease with which Li-ions pass through electrolyte when an electric field is applied, whereas diffusivity is the ease with which Li-ions pass through under a concentration gradient. Mobility and diffusivity are the two fundamental properties that affect the ionic conductivity in a LIB.[133]

Figure 4. Illustration of a lithium-ion cell's fundamental components and basic operating principle.[134]

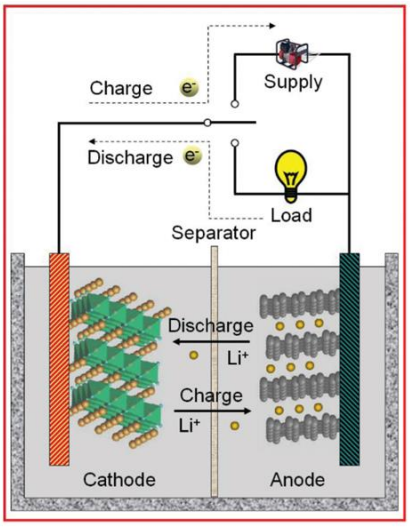

The theoretical cell voltage is given by,

$$\Delta E = -\frac{\Delta G}{nF}, \qquad \text{Eq. 2.1}$$

where ΔG is the total Gibbs free energy determined by the electrode materials, n is the number of electrons transferred, and F is the Faraday's constant. Other parameters which determine the performance of LIBs are specific energy/gravimetric energy density, cyclability/cycle life, safety abuse tolerance, charge/discharging rate, and coulombic efficiency.[132,135] Coulombic efficiency is given by,

$$\eta = \frac{Q_{dis}}{Q_{ch}}, \qquad \text{Eq. 2.2}$$

where Q is the total charge per unit weight. Specific capacity (Ah/kg) is the total amount of charge stored reversibly per unit mass. Specific energy (Wh/kg) is the energy stored per unit mass and given by the product of specific capacity and operating cell voltage (V). Ionic conductivity is given by,

$$\sigma = enZ\mu, \qquad \text{Eq. 2.3}$$

where Ze is the ionic charge, n is the carrier concentration, μ depends on the mobility of the ion[136]. The mobility of the ions depends on the activation energy for the ionic conduction. Whereas the ionic conductivity for a solid electrolyte pellet from the impedance measurements can be calculated using,

$$\sigma = \frac{L}{A.R_b}, \qquad \text{Eq. 2.4}$$

where L is the thickness of the pellet, A is the cross-sectional area of the pellet and R_b is the bulk resistance.[137] Ion transport (or transference) number, t_i, is the fraction of total current passed through an electrolyte due to a particular anion, with $\sum t^i = 1$. For a single salt containing monovalent ions, the t_i is given by,

$$t_i = \frac{\mu_{\pm}}{\mu_{-}+\mu_{+}}, \qquad \text{Eq. 2.5}$$

where $\mu_{\pm}$ are the mobilities of cation and anion respectively. These transport numbers can be determined by using methods such as Hittorf, radiotracers or moving boundaries.[138]

Li-ion conductivity and the Li-ion transference number (t_{Li+}) are the two main parameters that are looked up for practical applications in solid-state Li-ion batteries. A high Li-ion transference number, ideally near 1, is a highly desired attribute for electrolytes because a low transference number suggests significant anion mobility, which could result in concentration polarization during battery operation. $t_{Li+} < 1$ will lead to concentration gradients at the electrodes and cause limiting currents. Hence, the limiting currents in the battery and the cell cyclability depend on t_{Li+}, whereas the maximum power attainable depends on the ionic conductivity. Li-ion transport number and its diffusion coefficient are generally calculated using the Tubandt method, concentration cell method, and various NMR techniques.[41] The ionic conductivity of polymer electrolytes with respect to temperature follows the Vogel-Tammann-Fulcher (VTF) or the Arrhenius mechanism.

2.3.1 Ionic Conduction Mechanism in solid polymer electrolytes (SPEs)

Ion conductivity is an indispensable feature of electrolytes since it measures the ionic mobility and availability for the ongoing electrochemical reactions, which significantly influence the cell's power output. A low viscosity and high dielectric permittivity to dissolve the salt are required for a solvent to meet the ion transport and interfacial stability requirements with the electrodes. Most often, solvents with either high dielectric permittivity or low viscosity are chosen since there is no single solvent available satisfying both properties. In most lithium-ion battery (LIB) applications, ethylene carbonate (EC) is a key ingredient along with other carbonate or carboxylic ester solvents like dimethyl carbonate (DMC), diethyl carbonate (DEC), mixed with lithium salts that reach ionic conductivities of 5-10 mS/cm at ambient temperatures.[139]

It is crucial to understand the Li^+ ion-solvent interaction to understand the ionic conduction mechanism in electrolyte systems. Li^+ ion being the second smallest cation has strong interactions with the nucleophilic sites on solvent molecules when compared to other metal cations. In conventional liquid electrolytes, Li^+ ion binds with the carbonyl oxygen of carbonate molecules whose lone-pair electrons effectively neutralize the coulombic attraction of the small Li^+ cation.[140] FTIR spectroscopy reveals that the strong perturbation of the carbonyl stretching at ~1800 cm vibration was observed due to the dissolution of lithium salts.[141] In addition, the C^{13} NMR studies show downfield shifts of carbonyl and the ^{17}O NMR study shows that the carbonyl O is deshielded which indicates that Li^+ directly coordinates with the carbonyl oxygen instead of ethereal oxygen in carbonate ester solvents.[142,143]

Solid polymer electrolytes (SPEs) are a class of materials that include a polymer matrix with a low lattice energy salt that is dissolved in an organic solvent having a high dielectric

constant and low viscosity. Mostly the polymers with polar groups –O-, =O, -S-, -N-, -P-, C=N, -NH- (imide), -S- (thiol), and C=O will be able to dissolve the lithium salts.[7] Low lattice energy of the salt and a high dielectric constant of the host polymer facilitate the dissociation of these salts.[144] This dissociation in turn determines the number of free lithium ions in the polymer matrix, which affects the ionic conductivity. At normal temperatures, polymer electrolytes are known to have both amorphous and crystalline fractions. Ion transfer is known to take place mostly in amorphous regions.[145,146] There are three major Li-ion transport mechanisms in solid-polymer electrolytes namely, segment motion, ion hopping (Grotthuss mechanism), and the vehicle mechanism (mass diffusion). Segment motion is the most common mechanism in polymer electrolytes than ion-hopping or vehicle mechanism.

In segment motion, ionic transport is largely dependent on the segmental motion of the polymer chains (liquid-like conduction), mostly in the amorphous regions above the glass transition temperature (T_g).[146] As depicted in **Figure 5(a**), ion transport is due to the electrostatic interactions between polymer sidechains and electron-withdrawing groups, and as the polymer chain segments move, they create free-volume sites generating ionic transport pathways.[83] The cation component in the dopant salt is initially protected by the electron donor panel in the polymer, which then aids ion separation and causes ionic conductivity. The rapid segmental mobility of the polymer matrix and the intense Lewis-type acid-base interaction between the cation and donor atom causes ionic conduction.[139] Ionic conductivity depends on the amorphous phase in polymers as the segmental motion of polymer chains occurs in amorphous regions only. Hence, polymers with low T_g are desirable for high flexibility and fast ion movement. Temperature dependence of ionic conductivity largely dependent on segmental relaxation in

polymers follows the Vogel-Tammann-Fulcher (VTF) model given by the non-linear equation[83,145],

$$\sigma = AT^{-1/2} \exp\left[-\frac{B}{k_B\,(T-T_0)}\right], \qquad \text{Eq. 2.6}$$

where T_0 ($T_0 = T_g$ - 50 K) is also known as the 'Vogel temperature' corresponding to zero configurational entropy, A is the pre-exponential factor related to the number of charge ions, k_B is the Boltzmann constant, and B is the pseudo-activation energy associated with the polymer segmental motion.[83,145] The VFT theory (**Figure 5(c)**) was developed for purely polymeric systems and, it is in accordance with the free volume theory which correlates the dynamics of polymers with the amount of free space available for macromolecular movement.[82] According to this theory, below *Tg*, the conventional SPE has almost no ionic conduction. Therefore, the ionic conductivity in an SPE can be increased by the addition of plasticizers or residual solvents as it increases the free volume, by adding additional salts to increase charge carriers, boosting the dielectric constant to improve salt dissociation; and by increasing segmental mobility (reducing *Tg*).[82,83]

Figure 5. (a) Li-ion transport assisted by segmental motion (liquid-like) in the polymer matrix, (b) Ion-hopping mechanism (solid-like) through the free-volume sites.[83] **(Abbreviation: TFSI, bis(trifluoromethanesulfonyl)imide.), and (c) Arrhenius (solid line) and VTF-behaviors (dotted line) in SPEs.**[82,83]

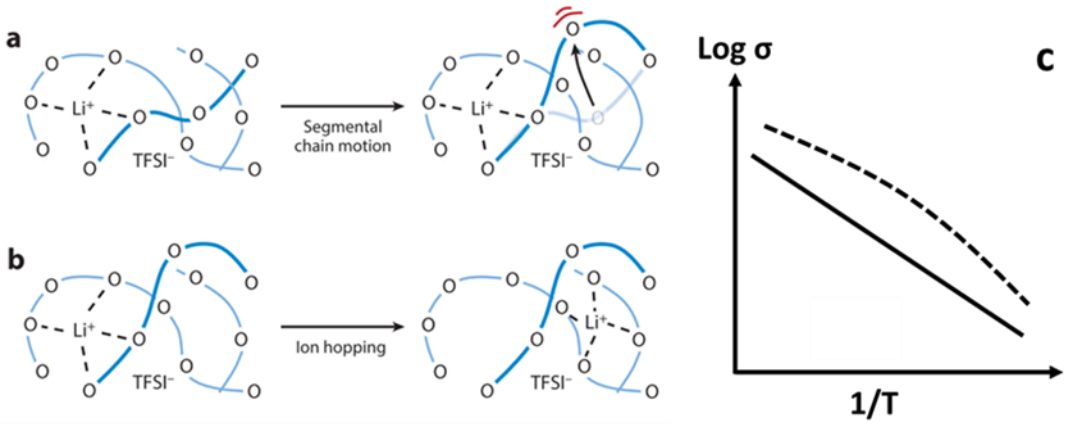

The ion-hopping mechanism (solid-like) is mostly observed in solid-inorganic electrolytes or ionic crystals wherein the ion-hopping is assisted by the point defects (vacant sites) in the lattice without any lattice rearrangement.[145,146] In comparison to inorganic electrolytes, cation-polymer interactions are typically strong, and the mean free path of ion hopping is comparatively large in solid-polymeric systems. Therefore, to enable high ionic conductivity via the ion hopping mechanism, these two problems must be solved in SPEs.[146] In conventional SPEs, the Arrhenius relationship represents that the ions migrate due to simple ionic hopping between the free-volume sites within the polymer matrix independent of the segmental polymer motion, as shown in **Figure 5(b)**.[145,146] According to Arrhenius's theory (**Figure 5(c)**), the relationship between temperature and ionic conductivity is as follows:

$$\sigma = \sigma_0 \exp\left(-\frac{E_a}{k_B T}\right), \qquad \text{Eq. 2.7}$$

where E_a, σ_0 and k_B are the activation energy, pre-exponential factor and Boltzmann constant, respectively. Unlike polyethers, polyalcohols and polynitriles are less associated with

the VFT behavior because their ionic conduction is less coupled with the polymer matrix.[82] For instance, the Arrhenius mechanism in SPEs were reported in PVP:$KClO_4$, PVP:IL, and chitosan-OA:LiOAc electrolytes.[147–149] Ion hopping in polymers may also be accompanied by polymer chain segmental motion, relaxation, or breathing. Some reports suggest that Li^+ ions can move along the polymer chains and then hop from one chain to another because of the cooperative polymer segment and ionic motions.[146]

In the vehicle mechanism, ions are transported by the free diffusion of charge carriers which is typically observed in liquids. For instance, proton transfer through the pores of the Nafion membrane is via the vehicle mechanism. Li^+ ion transport in polymers via the vehicle mechanism has not been extensively studied.[146]

2.3.2 Ionic Conduction Mechanism in Metal-Organic Frameworks (MOFs)

Although the ionic conductivity of polymer electrolytes has improved to a practical degree due to the addition of organic solvents, the polymer dissolves to generate a gel that no longer prevents dendritic penetration.[150] Hence, MOFs having a highly porous crystalline structure and ordered host-guest chemistry have been studied in recent times as solid-state electrolytes (SSEs) as they have a great potential to improve upon polymer electrolytes.[30] These frameworks can hold an organic electrolyte without gelling because of their three-dimensional pore system, and crystalline structure made of strong bonds. A high density of immobilized anions can be created by tweaking the molecular building blocks in MOFs, which leaves the Li-ion as the only mobile species. MOF electrolytes can be classified into two major categories: (1) all solid-state electrolytes (SSEs) consisting of lithium salts with MOFs and (2) ‘pseudo/quasi-SSEs’ with the addition of organic solvents, liquid electrolytes, or ionic liquids.[146,151]

The mechanism of lithium-ion transport with lithium salts grafted in MOFs continues to lack understanding. While the porous structure permits the occurrence of the Grotthuss (ion hopping) or vehicle mechanism, the periodic organic crystalline structure can impede ligand transport.[146,152,153] In order to demonstrate how MOFs immobilize anions in the porous framework, two widely accepted mechanisms have been developed. Anions coordinating with open metal sites in charge-neutral skeletons, or the anions being restricted by the inherent nanoporous MOF structure acting as a cage/host to facilitate Li-ion transport.[154,155] The cations can travel relatively freely along the pores because the metallic center of MOF materials can trap the anions of Li salt. For instance, the encapsulation of $TFSI^-$ anions in ZIF-67 MOF revealed the strong interactions among the $TFSI^-$ anions and MOF metallic center.[155]

The nanostructured and microporous structure of MOFs can be used as a scaffold for encapsulating liquid electrolytes and enhancing the ionic conductivities in these 'quasi-solid' systems. These 'quasi-solid state' electrolytes have ionic conductivities very close to liquid phase and possess the stability of a solid matrix as well. This hybrid system acts as a reservoir of liquid electrolytes due to MOF's wide porosity and high absorption capacity.[79,146,156] The process for Li^+ transfer is more intricate in 'quasi-solid-state' MOF-based electrolytes. The Li-ions first diffuse through the channel-like pores, after which the liquid electrolyte is nano-confined by the MOF's micro-porosity and easily retained due to capillary effects in the rigid matrix. The metallic center also serves as the anion coordination unit, enabling Li^+ ions to freely move between sites.[79] These hybrid conductors possess high Li-ion transference numbers, high ionic conductivities, better mechanical, and thermal stability when compared to traditional pristine MOFs.[146]

Mg-MOF-74 was demonstrated as a quasi-solid electrolyte (QSSE) by soaking in two different liquid electrolyte solutions, $LiClO_4$ (2M)-PC and $LiClO_4$ (1M) in EC-DMC to introduce conductive liquid guests into the MOF frameworks.[156] The effect of electrolyte nanoconfinement on the Li-ion dynamics was studied using the electrochemical and full solid-state NMR tests. The room temperature Li^+ ion conductivity of $LiClO_4$-PC@MOF-74 (1.4×10^{-4} S/cm) was one order higher than the $LiClO_4$-EC/DMC@MOF-74 (4.6×10^{-5} S/cm) quasi-solid electrolyte. Also, the $LiClO_4$-PC@MOF-74 electrolyte pellet shows a higher transference number (0.7) and lower activation energy (0.2 eV) due to the lower solution viscosity compared to $LiClO_4$-EC/DMC, promoting faster ionic transport. NMR experiments on the two QSSEs confirmed the presence of adsorbed Li^+ ions in the porous ionic channels of Mg-MOF-74 (in-pore adsorbate) and the non-adsorbed Li^+ cations in the interparticle void spaces (ex-pore adsorbate). Further, the ^7Li NMR relaxometry suggests two possible Li^+ diffusion mechanisms, the slower 1D diffusion through the MOF channels and faster Li^+ diffusion through the crystallites.[156]

A molecular dynamics simulation of the solvent PC infused-MOF-688(Mn) was modeled to investigate the influence of the metal center on Li^+ ionic conduction. The Li^+ ion conduction mechanism in this MOF-based QSSE was primarily solvent-assisted hopping between the metallic clusters.[151] Another class of QSSEs is 'ionogels' constructed using ionic liquids in MOF frameworks. Chen et al.[155] reported a simple ionogel using LiTFSI-based ionic liquid and the ZIF-67 MOF particles. The ionic liquid maintains dynamic mobility after being enclosed in MOF 3D channels because the metal atoms of the MOF interact strongly with $TFSI^-$ anions and increase Li^+ mobility. The successful confinement of the ionic liquid was confirmed using the FTIR and Raman spectroscopy.[155]

The ionic conduction mechanism in MOFs is complex, and the proton conduction studies have contributed significantly to our understanding of ionic conductivity in MOFs. **Figure 6(a**) shows the vehicle mechanism wherein the larger protic carriers aid translational proton motion, and the proton conductivity is determined by the rate at which the carrier molecules diffuse. In the Grotthuss mechanism (**Figure 6(b)**), the protons hop from one site to another aided by the water molecules or conducting media. The Grotthuss process involves breaking and forming hydrogen bonds; hence, the activation energy required is lower than 0.4eV because the dissociation energy of one hydrogen bond is only 0.11 eV. However, the vehicle process needs a carrier molecule to diffuse over long distances with little proton exchange between the vehicles and has much greater activation energy (0.5-0.9 eV).[153,157]

Conceptually, ion-conducting MOFs are like ion-conducting polymers, wherein the polymer is swollen due to solvent and exists in a gel-like state. But MOF-based SSEs retain the properties of a true solid despite being activated by soaking in a liquid electrolyte in most cases. These soaked MOF-SSEs/QSSEs are dry powders containing solvent in the pores which enables processing them into thin-films. This liquid electrolyte in MOF pores facilitates the ionic conduction and hence, both the Grotthuss and vehicular solution-based transport mechanisms that are utilized to explain ion diffusion in the single-ion and cooperative solid-state materials must also be considered in MOFs.[153,157]

Figure 6. (a) Vehicle and (b) Grotthuss-type mechanisms of proton conduction within the frameworks.[153]

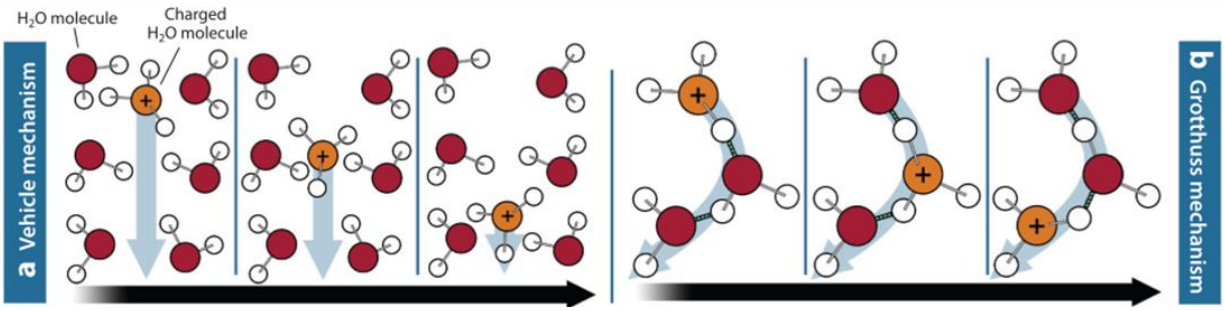

2.3.3 Ionic Conductivity Measurements

Electrochemical impedance spectroscopy (EIS) is a non-destructive technique used to study the electrical characteristics of solid electrolyte materials and their interfaces (i.e., electrode/electrolyte interfaces). In this technique, the electrochemical system's impedance is determined by recording the current response to an applied voltage (1-10 mV) at various frequencies (mHz to MHz). Another name for this technique is AC impedance spectroscopy or complex impedance spectroscopy (CIS) or dielectric spectroscopy which is a common technique for determining the SSEs' dielectric relaxation and ion conduction mechanism. This is a standard technique to determine the ionic conductivity and activation energy in SSE's.

A dielectric material's resistance cannot be calculated using a direct current (DC) method because of the polarization of charges at the electrode-electrolyte interface. However, an alternating current (AC) applied to the sample measures the impedance of the sample and thereby, the polarization effect can be avoided.[145,158] In a potentiostatic EIS (PEIS), a small sinusoidal voltage (E(t)) is applied to an SSE sandwiched between two ion-blocking electrodes resulting in a linear current density (j(t)) and the impedance, Z(t) is given by,

$$Z(t) = \frac{E(t)}{j(t)} \qquad \text{Eq. 2.8}$$

Impedance is influenced by the electrolyte, morphology, and content of the electrode materials, as well as the nature of the electrode-solution contact.[159] The charge transfer at surface of electrodes occurs in the faradaic heterogeneous reactions, and in these types of reactions, the change in impedance is due to the adsorption of responding species, ion diffusion, and charge transfer by redox species. [159] The electrochemical impedance spectrum is commonly represented in two forms, namely, the Nyquist plot (the imaginary part ($-Z_{im}$) versus the real part (Z_{re}) of impedance) or the Bode plot (the norm of phase angle and impedance versus frequency). The impedance of the electrolyte as measured at a specific frequency is represented by each data point on the Nyquist plot (also called as Argand diagram or complex plane plot), and it is divided into high frequency and low frequency regions. The low frequency zone is plotted away from the origin of x- and y-axes, whereas the high frequency region is plotted in the direction of the origin (**Figure 7(b)**).[159,160] The Nyquist plot is mostly used for SSE's, represented by the following equations:

$$Z_{re} = \frac{R_b}{1+(\omega RC)^2} \qquad \text{Eq. 2.9}$$

and

$$Z_{im} = \frac{\omega {R_b}^2 C}{1+(\omega R_b C)^2} + \frac{2}{\omega C_e} \qquad \text{Eq. 2.10}$$

where C_e is the electrical double-layer (EDL) capacitance, R_b is the bulk resistance of the solid electrolyte, and C is the bulk geometrical capacitance. The shape of these equations suggests that the Nyquist plot is made up of a vertical spike and a perfect semicircle with the center on the real impedance axis. The spike denotes an ideal capacitor and is represented by the second term of Eq. 2.10. The EDL (or electrode polarization) is created due to the accumulation of charged ions at the respective opposite charged electrodes (**Figure 7(a)**), which hinders the impedance measurements of most electrolytic systems.[160,161] The parameters C_e , R_b and C are given by,

$$C_e = \frac{\varepsilon_r \varepsilon_0 A}{\lambda}$$ Eq. 2.11

$$C = \frac{\varepsilon_r \varepsilon_0 A}{t}$$ Eq. 2.12

$$R_b = \frac{t}{\sigma A}$$ Eq. 2.13

where ε_r is the electrolyte's dielectric constant, ε_0 is the dielectric permittivity of vacuum (8.85 x 10^{-14} F cm^{-1}), λ is the thickness of EDL, A is the electrolyte/electrode contact area, σ is the ionic conductivity of the solid electrolyte, and t is thickness of the electrolyte.

Figure 7. (a) Schematic of an SSE between the two blocking electrodes, and (b) Nyquist plot for an SSE with a perfect semicircle.[160]

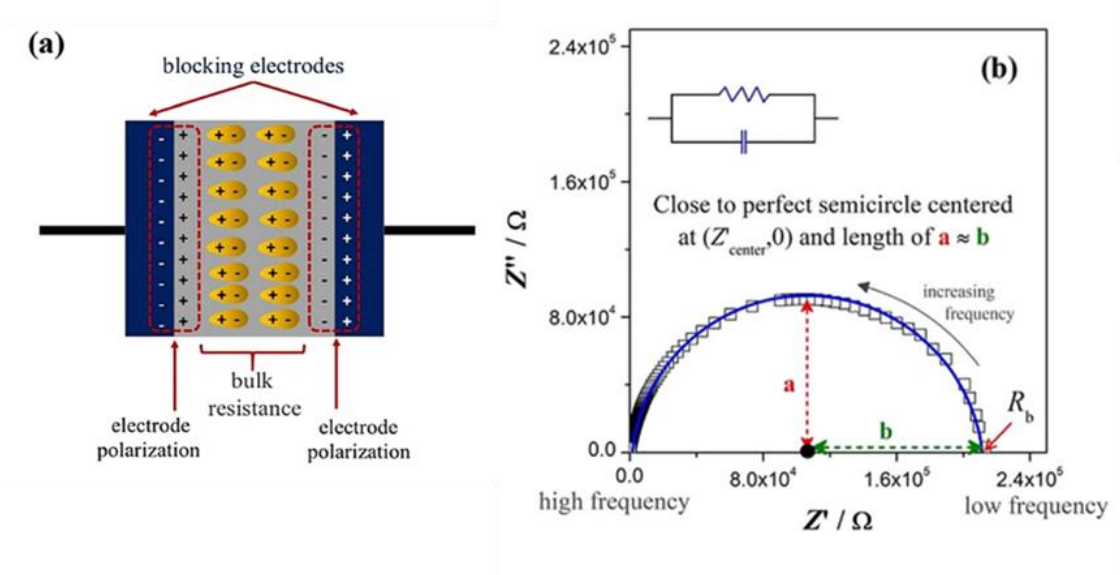

A perfect semicircle in the Nyquist plot is not frequently seen experimentally, and processes with identical time constants will overlap, necessitating careful modeling and spectrum fitting. Hence, it is a common practice to use the 'equivalent circuit modeling,' which involves fitting complex non-linear least squares (CNLS) to the experimental data using specialized software, such as ZView (Scribner Associates) or EC-Lab (Biologic). Since no EIS spectrum solution is unique, adding additional parts tends to make the equivalent circuit model (ECM) fit

better, thus typical scientific modeling practices, such as selecting the simplest solution possible, should be followed, and the number of elements in the model should be kept as few as possible.[159,162]

Standard electrical components like resistors (R), capacitors (C), constant phase elements (CPE or Q), Warburg (Z_w), and inductors (L) constitute most of the circuit components used in ECM. A resistor can represent the SSE's bulk ionic and grain boundary resistance as well as the resistance due to charge transfer between the SSE and the electrodes. A capacitor can be utilized to illustrate charge accumulation and depletion at the interface between the SSE and the electrode as well as across the phase boundaries. The constant phase element is used for non-ideal capacitances (or leaky capacitors) that may be due to surface roughness, porosity, chemical inhomogeneity, and the non-homogeneous nature of the EDL surface. Warburg impedance can describe resistances caused by mass transfer or diffusion, which are most noticeable at low frequencies. Inductors represent impedance contributions at low and high frequencies caused by degradation processes and electrical connections, respectively.[159,161–163]

Nyquist plots generated from impedance measurements can consist of a depressed semicircle, a tilted spike, or a depressed semicircle along with a tilted spike. The Nyquist plot having a depressed semicircle can be represented by an equivalent circuit consisting of a constant phase element (CPE or Q) and a resistor linked in parallel. The plot that resembles a spike can be represented by a resistor connected in series with a CPE. A parallel combination of a resistor and capacitor (or CPE) that are linked in series with another capacitor (or CPE) (**Figure 8(a)**) can be used to produce the Nyquist plot (**Figure 8(b)**), which consists of a depressed semicircle with a slanted spike. The tilted spike symbolizes the electrical double layer, while the depressed semicircle depicts the bulk material.[161,163] **Figure 8(c)** shows another common fit, the Randles

equivalent circuit, where R_b is the bulk electrolyte resistance, C_{dl} is the double layer capacitance, R_{ct} is charge transfer or polarization resistance, and Z_w is Warburg impedance.[159,164] After fitting the experimental EIS data with the equivalent circuits, the bulk resistance (R_b) value is used to calculate the ionic conductivity of the SSE using equation 2.13.

Figure 8. (a) Equivalent circuit model for the Nyquist plot of an SSE[160], (b) Nyquist plot for an SSE with a depressed semicircle and a tilted spike[160], and (c) Randles equivalent circuit model and the corresponding Nyquist plot.[164]

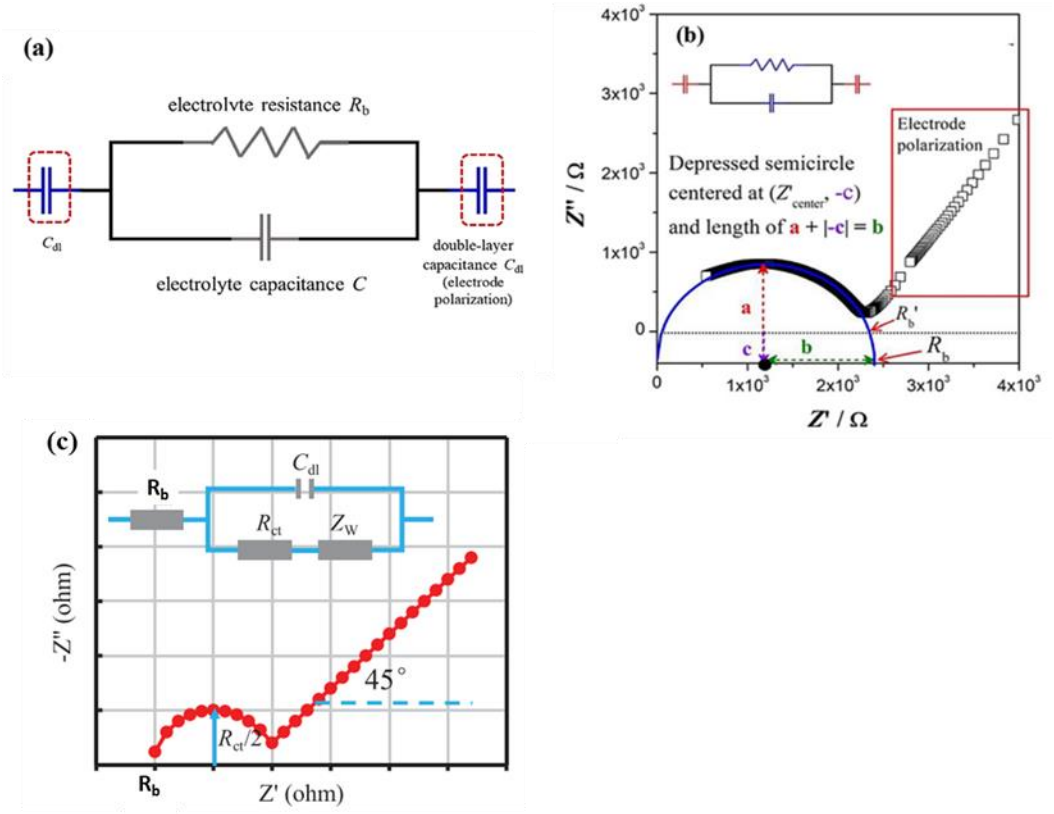

CHAPTER III: EXPERIMENTAL SECTION

3.1 Materials

All the chemicals were used as received.

Tannic Acid ($C_{76}H_{52}O_{46}$; Molar mass = 1701.19 g/mol), (3-aminopropyl)trimethoxysilane (3-APT: $C_6H_{17}NO_3Si$; Molar mass = 179.29 g/mol), lithium perchlorate ($LiClO_4$; Molar mass = 106.39 g/mol), ethylene carbonate (EC: $C_3H_4O_3$; Molar mass = 888.06 g/mol), and anhydrous ethanol (200 proof) were obtained from Sigma-Aldrich. Lithium hydroxide monohydrate ($LiOH.H_2O$; Molar Mass = 41.96 g/mol) was obtained from Alfa Aesar. Lithium nitrate ($LiNO_3$) was purchased from Honeywell. Terephthalic acid (Benzene-1,4- Dicarboxylic acid – 98%), 2,6-Naphthalenedicarboxylic acid (2,6-NDC, 95%), Biphenyl-4,4'-dicarboxylic acid (4,4'-BPDC, 97%), and *N*,*N*-Dimethylformamide (DMF: anhydrous, 99.8%) were obtained from Sigma-Aldrich.

3.2 Characterization

This section describes all the characterization techniques used in the dissertation work.

The UV-visible spectral traces were collected in ethanol using a UV-visible spectrometer, (Varian Cary 6000i) and used a 10mm x 4mm quartz cell. The functional groups from the molecular fingerprint were obtained using Fourier transform infrared spectroscopy (FTIR-Varian 670-IR spectrometer). The chemical composition and oxidation states of the materials were obtained from X-ray photon spectroscopy (XPS-Escalab Xi+-Thermo Scientific). Morphology analysis was performed using the field emission scanning electron microscope (Zeiss Auriga FIB/FESEM) and transmission electron microscope (TEM Carl Zeiss Libra 120 and JEOL 2100 HR-TEM equipped with STEM/EDS). A 7 nm gold-palladium coating was used to coat the SEM samples on the Leica ACE200 Sample Coater. The thermal stability was investigated on 10-15

mg of sample and placed into sample pan of the thermogravimetric analyser (TA instruments Q500). The samples were heated up to 800°C/1000°C at the increment of 5°C/min under the nitrogen gas flow. Dynamic Light Scattering (DLS Malvern Nano ZS) and zeta potential measurements were performed on the suspensions of the samples re-dispersed in absolute ethanol after sonication of the samples for about 20 minutes. The powder XRD analysis was conducted using Cu K_α radiation (40 kV, 40 mA, λ=1.540 Å) with an exposure time of 90 s at a working distance of 55 mm on the X-ray diffractometer (XRD, Agilent technologies Gemini). The simulated powder diffraction pattern was generated by loading the .cif files into the VESTA software (for λ=1.540 Å), obtained from the crystallography databases (i.e., Crystallography Open Database (COD), and Cambridge Crystallographic Data Center (CCDC)) for each of the Li-MOFs. The simulated XRD pattern obtained from the VESTA software was matched with the experimental XRD data in Origin.

The Micrometrics analyzer accelerated surface area and porosimetry (ASAP #2060) system by Micromeritics Instrument Corp was used to obtain the Brunauer-Emmett-Teller (BET) surface area, Barrett-Joyner-Halenda (BJH) adsorption/desorption isotherms, BJH adsorption and desorption cumulative pore volumes and cumulative pore area distributions using t-plots. The pore width and pore volume distributions were obtained using non-local density functional theory (NLDFT) and Horvath-Kawazoe Cumulative Pore Volume Plots. Approximately, 150-200mg sample was loaded into the BET sample tube and the sample was degassed at 90 °C for one hour, followed by additional 12 hours at 250 °C (for Li-MOFs samples) and 180 °C (for TALi and TALi-SSQ samples) to remove any moisture and atmospheric gases occupied in the accessible pores. The full N_2-adsorption/desorption isotherms were measured at 77 K. A low-

pressure incremental dose amount of 3.0 cm^3/g STP was used for Li-MOF samples and 0.01 cm^3/g STP was used for TALi-SSQ samples with equilibration intervals 40, 30, and 20 seconds.

Ionic conductivity measurements were collected using electrochemical impedance spectroscopy (EIS) with a VMP3 Bio-Logic multichannel potentiostat. The diameter and thickness of the pellets were measured with vernier calipers. The pellet samples were sandwiched between two gold-coated copper disk (25 mm diameter) electrodes, which were linked to an alternating current of 10 mV amplitude with a frequency range from 10^6 to 10 Hz. The ionic conductivity (σ, S/cm) was determined based on $\sigma = L/ (R_b \times A)$ using the bulk resistance (R_b, Ohm) from the Nyquist plot, thickness of the pellet (L, cm), and surface area of the pellet (A, cm^2). EC-Lab software was used to fit EIS data using the Zfit function and determine the R_b of the samples. Ionic conductivity was measured at various temperatures between 25-65 ˚C, repeated three times at each temperature in the air using a hot plate. The pellets were sandwiched in between the two gold-coated copper disk electrodes and subsequently placed on the hot plate connected to the EIS system using the two probes. The temperature of the pellet was increased by incrementally increasing the temperature of hot plate and monitored it using a temperature gun. After reaching the desired temperature on the pellet (~upper electrode surface), ionic conductivity was measured three times at each temperature using the EIS system. Further, the activation energies were computed from the slope of ln σ versus 1000/T graphs (refer **Appendix B and C**) for each of the samples using the Arrhenius equation, $\sigma\,(T) = Ae^{-\frac{E_a}{RT}}$, with a linear fitting coefficient of approximately 0.99, where A is the pre-exponential factor, R is the gas constant (8.3145 $J\,K^{-1}\,mol^{-1}$) and E_a is the activation energy. The activation energy was calculated from the slope of ln σ versus 1000/T graph, where E_a = -(Slope * R *1000) J/mol. For the Cyclic voltammetry (CV) measurements, the TALi@LEC and TALi-Si@LEC electrolyte

pellets were sandwiched between the two stainless steel spacers in a CR2032 coin cell and placed it in a coin-cell holder connecting it to the two probes of the potentiostat. Cyclic voltammetry was conducted for 4 cycles using stainless steel as counter, reference and working electrodes at a scan rate ranging from 5-100 mV/s in the -1 to 1 V range.

3.3 Experimental Procedures

3.3.1 Synthesis of Li-BDC MOF

To a vial (20.0 mL), $LiNO_3$ (0.69 g, 0.010 mol) and 1,4-BDC (0.83 g, 0.005 mol) were added and dissolved in anhydrous DMF (10 mL). The vial was sonicated for 20 minutes until the precursors were dissolved, resulting in an opaque solution. The reaction vial was charged with a small magnetic stir bar and heated at 110 ℃ for three days. The colorless crystals were collected after multiple washing with anhydrous DMF, followed by anhydrous ethanol, using gravity filtration. The precipitate collected after washing was dried at room temperature to yield colourless crystals (418 mg, 28%). FTIR stretching (cm^{-1}): 1570 (sharp peak, metal ion-coordinated carbonyls), 1500 (aromatic C=C stretching), 1392 (sharp peak, Li-O-C=O), 1095 (multiple peaks, C-O), 826 (sharp peak, Li-O), 753 (aromatic C=C bending); XPS elemental compositional analysis (weight%) for the formula $Li_2C_8H_4O_4$: Experimental - C (55.98), Li (7.87), and O (36.15); Theoretical - C (53.98), Li (7.80), O (35.95) and H (2.27).

3.3.2 Synthesis of Li-NDC MOF

To a vial (20.0 mL), $LiNO_3$ (0.69 g, 0.010 mol) and 2,6-NDC (1.08 g, 0.005 mol) were added and dissolved in anhydrous DMF (10 mL). The vial was sonicated for 20 minutes until the precursors were dissolved, resulting in a white solution. The precursor solution was heated to 110 ℃ for three days after being charged with a small magnetic stirrer bar. Yellow precipitates settled at the bottom of the vial, which was collected after multiple washing with anhydrous

DMF, followed by anhydrous ethanol, using gravity filtration. The yellow precipitate was dried at room temperature to yield a yellow powder (663 mg, 37%). FTIR stretching (cm^{-1}): 1602-1565 (metal ion-coordinated carbonyls), 1497 (aromatic C=C stretching), 1396 (sharp peak, Li-O-C=O), 1196-1144 (multiple peaks, C-O), 802 (sharp peak, Li-O), 778 (aromatic C=C bending); XPS elemental compositional analysis (weight%) for the formula $Li_2C_{12}H_6O_4$: Experimental - C (64.03), Li (6.05), and O (29.92); Theoretical - C (63.20), Li (6.09), O (28.06) and H (2.65).

3.3.3 Synthesis of Li-BPDC MOF

To a vial (20.0 mL), $LiNO_3$ (0.69 g, 0.010 mol) and 4,4'-BPDC (1.21 g, 0.005 mol) were added and dissolved in anhydrous DMF (10 mL). The vial was sonicated for 20 minutes until the precursors were dissolved, resulting in a white solution. The reaction vial was charged with a small magnetic stir bar and heated at 110 ℃ for three days. A lemon-yellowish precipitate settled at the bottom of the vial, which was collected after multiple washing with anhydrous DMF, followed by anhydrous ethanol and centrifugation at 10,000 rpm for 15 min. The white precipitate collected after washing was dried at room temperature to yield a white powder (510 mg, 27%). FTIR stretching (cm^{-1}): 1585 (sharp peak, metal ion-coordinated carbonyls), 1538 (aromatic C=C stretching), 1397 (sharp peak, Li-O-C=O), 1270-1003 (multiple peaks, C-O stretching), 840 (sharp peak, Li-O), 772 (aromatic C=C bending); XPS elemental compositional analysis (weight%) for the formula $Li_2C_{14}H_8O_4$: Experimental - C (68.48), Li (4.89), and O (26.63); Theoretical - C (66.18), Li (5.46), O (25.19) and H (3.17).

3.3.4 Preparation of LEC@Li-MOF solid-state electrolytes

Li-MOF powder (300 mg) were heated to 250 ℃ under vacuum overnight and soaked in the presence of 5wt% $LiClO_4$ in 2 g EC at 80 ℃. These LEC@Li-MOF powders were collected

using filtration on a Whatman filter at 80 ℃ and dried under ambient conditions. The dry powder (400-600 mg) prepared in this manner was pressed into pellets with a diameter of 1.5 cm at 44 MPa force on a hydraulic press. Prior to the electrochemical testing, the pellets' surfaces were cleaned with a Kim wipe. The temperature-dependent ionic conductivity measurements were conducted on the Li-MOF@LEC solid pellets at the temperature ranged between 25-55 ℃ on a hot plate after sandwiching the pellet with two gold-coated copper disk electrodes. Area of the pellet $A = \pi d^2/4$, where d = 1.5 cm. XPS Elemental compositional analysis for the LEC@Li-BDC: Experimental - C (48.28), Li (8.51), Cl (0.54) and O (42.67). XPS Elemental compositional analysis for the LEC@Li-NDC: Experimental - C (51.38), Li (6.25), Cl (1.87) and O (40.51). XPS Elemental compositional analysis for the LEC@Li-BPDC: Experimental - C (42.56), Li (6.32), Cl (2.44) and O (48.68)

3.3.5 Synthesis of Lithium-tannate coordination complex (TALi)

Tannic acid (TA- 2g, 1.176 mmol) and Lithium hydroxide (LiOH- 986.7 mg, 23.52 mmol) were dissolved in absolute ethanol in two separate conical flasks, respectively, and were sonicated to yield clear solutions. Tannic acid solution was a clear yellow color solution, and the lithium hydroxide solution is an opaque suspension. The dropwise addition of the lithium hydroxide (100 mL) solution into the tannic acid solution (100 mL) showed a color change of the suspension from brownish to dark violet to a dark green suspension, under vigorous stirring (**Figure 10**). The resulting dark greenish suspension was allowed to stir for 24 hours, under ambient conditions. The precipitate was collected after washing with ethanol using centrifugation at 8000 rpm for 10 min. The precipitate collected in this manner was dried at room temperature to yield a brown powder (**Figure 9 (b)**) (2.124 g, 71.13%). FTIR stretching (cm^{-1}): 3371 (broad O-H), 1582-1502 (aromatic C=C stretching), 1391-1333 (multiple peaks, Li-O), 1205-1052

(multiple peaks, C-O), 865-834 (aromatic sp^2 C-H bending), 760 (aromatic C=C bending); XPS elemental compositional analysis (weight%) for the formula $Li_{18}C_{76}H_{34}O_{46}.8H_2O$: Experimental - C (47.3), Li (6.71), and O (45.99); Theoretical - C (46.76), Li (6.4), O (44.76) and H (2.58).

Figure 9. (a) Experimental setup for making TALi, (b) Image of TALi powder, and (c) Image of TALi@LEC powder.

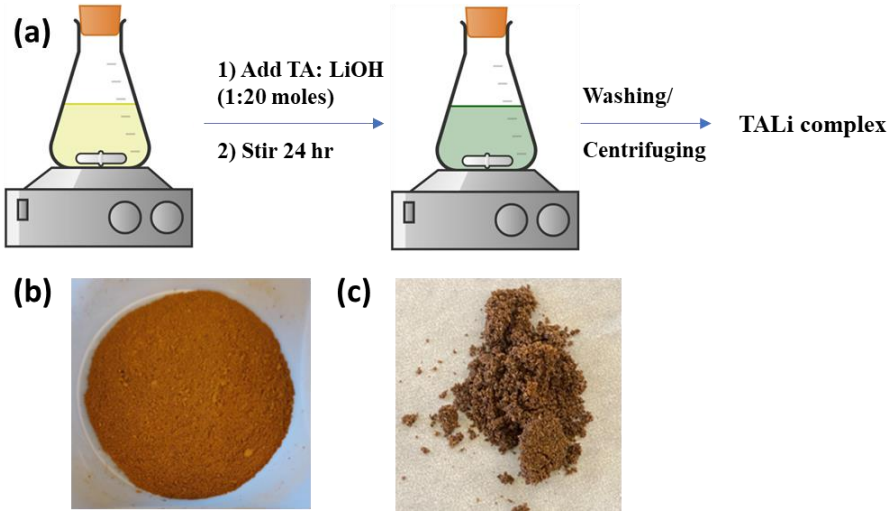

Figure 10. Color changes during the formation of TALi-complex.

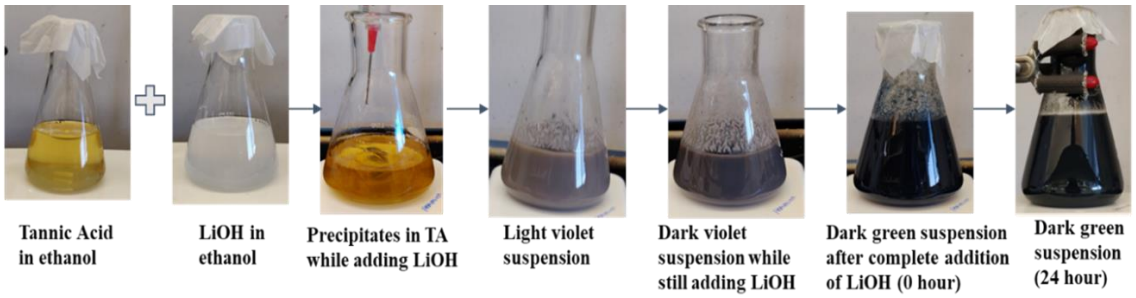

3.3.6 Preparation of TALi@LEC solid-state electrolytes

TALi powder (300 mg) was soaked in the presence of 5wt% $LiClO_4$ in 2 g EC at 80 ℃, followed by collected using filtration on a Whatman filter at 80 ℃ and dried it under ambient conditions. In a similar manner, varying $LiClO_4$ %weight (2-20 wt%), TALi@LEC pellets were prepared. Further, the TALi@LEC powder (**Figure 9 (c)**) was collected using a motor-pestle and

pressed into pellets with a diameter of 1.9 cm at 44 MPa on a hydraulic press. The temperature-dependent ionic conductivity measurements were conducted on TALi@LEC (5wt%) solid pellet between 25-45 ℃ using a hot plate. Area of the pellet $A = \pi d^2/4$, where d = 1.9 cm.

3.3.7 Synthesis of Lithium-Tannate Silsesquioxane (TALi-SSQ) microstructures

Tannic acid (TA- 1.0 g, 0.58 mmol in 5 mL anhydrous ethanol) and lithium hydroxide (LiOH- 247.1 mg, 5.8 mmol in 15 mL anhydrous ethanol) were dissolved in absolute ethanol in two separate conical flasks, respectively. Tannic acid solution was a clear yellow color solution, and the lithium hydroxide solution is an opaque suspension. A drop-wise addition of the lithium hydroxide (15 mL) solution at a continuous rate of 1 mL/min into the tannic acid solution (5 mL) showed a color change of the solution from brown suspension to dark violet suspension, under vigorous stirring. The reaction mixture was allowed to stir for another 5 minutes and then 3-aminopropyltrimethoxy silane (3-APT, 2.0 mL) was added at once, followed by addition of 1 mL 28% ammonium hydroxide (28%NH_4OH) dropwise at a continuous rate of 0.5 mL/min. The resulting dark greenish suspension was allowed to stir for 24 hours, under ambient conditions to yield dark brown, thick suspension. A chocolate brown precipitate was collected after centrifugation at 10000 rpm for 20 min and repeated washing with anhydrous ethanol (~ 15 mL). This precipitate was dried at room temperature to yield a chocolate brown fine powder (2.184 g, 66.16%) (**Figure 11 (b)**). FTIR stretching (cm^{-1}): 3348 (broad O-H), 2948 (alkane sp^3 C-H stretching), 1582-1498 (aromatic C=C), 1371 (Li-O), 1204 (C-O), 1096 (Si-O-C), 862 (aromatic sp^2 C-H bending), 762 (C=C bending); XPS elemental compositional analysis (weight%): Experimental - C (39.84), Li (2.07), Si (14.4), N (7.14) and O (36.55).

Using the same synthesis procedure, a series of TALi-SSQ microstructures were prepared by changing the 3-APT from 2 mL to 1.0, 0.5, and 0.25 mL. In the second series, by changing

the base concentration, TALi-SSQ were also synthesized. **Table 1** summarizes the TALi-SSQ samples with respect to the 3-APT and base concentrations.

Table 1. Experimental volumes of 3-APT and 28%NH_4OH were used to prepare TALi-SSQ microstructures and their respective yields.

Sample Name	3-APT (mL)/NH_4OH (mL)	Yield (%)
TALi-Si-B1	2/1	66.2
TALi-Si-B2	2/0.5	83.3
TALi-Si-B3	2/0.25	58.9
TALi-Si-B4	1/1	77.8
TALi-Si-B5	0.5/1	89.7
TALi-Si-B6	0.25/1	78.9

Figure 11. (a) Experimental setup for making TALi-SSQ microstructures, (b) Image of TALi-Si-B1 powder, and Image of TALi-Si-B1@LEC powder.

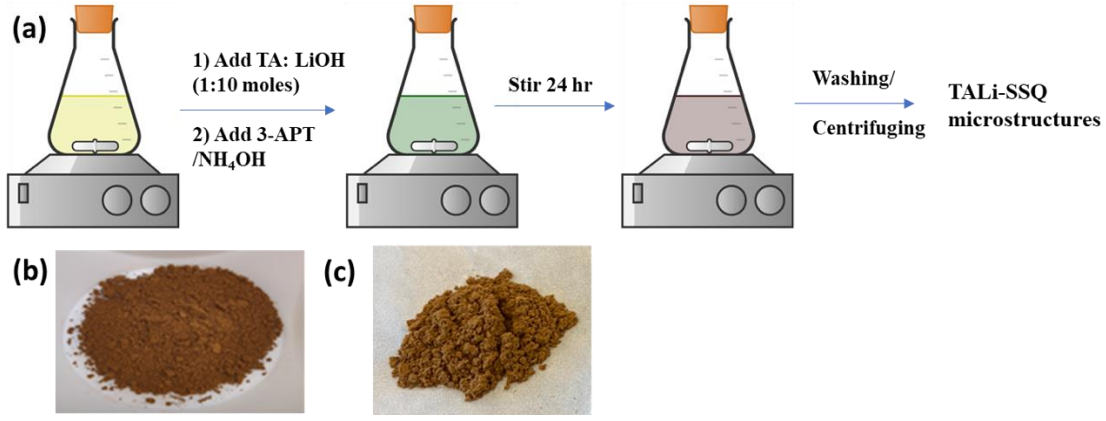

3.3.8 Preparation of TALi-Si@LEC solid-state electrolytes

TALi-SSQ microstructures (300 mg) were soaked in the presence of 5wt% $LiClO_4$ in 2 g EC at 80 ℃, collected using filtration on a Whatman filter at 80 ℃ and dried it under ambient conditions. The TALi-Si@LEC powders (**Figure 11 (c)**) were collected using a motor-pestle and pressed into pellets with a diameter of 1.9 cm at 44 MPa on a hydraulic press. Prior to the

electrochemical testing, the pellets' surfaces were cleaned with a kim-wipe. The temperature-dependent ionic conductivity measurements were conducted on the TALi-Si@LEC solid pellets by varying the temperature between 25-65 ℃, using a hot plate after sandwiching the pellet between the two gold-coated copper disc electrodes. Area of the pellet $A = \pi d^2/4$, where d = 1.9 cm.

CHAPTER IV: DESIGN AND SYNTHESIS OF ISORETICULAR LI-MOFS TO INVESTIGATE LI-ION CONDUCTION FOR LI-MOF-BASED SOLID-STATE ELECTROLYTES

4.1 Introduction

Metal organic frameworks are a major class of porous materials composed of secondary building units and metal ions. MOFs as powerful adsorbents and have versatile applications mainly gas storage, but recently they emerged as platforms for developing solid-state Li-ion conductors. Their high surface areas, tunable pore sizes, low electronic conductivities and ordered channels provide ideal platforms for designing solid-state electrolytes with high ionic conductivities and transference numbers.[22] They can provide well aligned one-dimensional channels for transport pathways with Li cations. Mostly, MOF-based solid-state electrolytes were successfully demonstrated by incorporating free Li^+ ions into MOF architectures by modifying their SBUs or forming anion binding sites.[22] Li-metal ions in the MOF framework would induce effective ionic transport through the MOF channels. For example, Nath et al. synthesized Li-MOFs using the carboxylate linkers AOIA and TMCA. Additionally, doping lithium salts into the activated Li-MOF channels enhanced the Li-ion hopping through these porous bio-inspired ionic channels to achieve a room temperature ionic conductivity in the order of 10^{-5} S/cm.[165] However, isoreticular Li-MOFs as solid–state electrolytes have not been fully explored.

The direct incorporation of lithium salts into porous MOFs shows low Li-ion transference numbers (<0.5), relatively low ionic conductivity and high interfacial resistance.[166] Hence, Li-cation solvating plasticizers such as ethylene carbonate (EC) and propylene carbonate (PC) were

incorporated into the microporous MOFs which improved the dissociation of lithium salts leading to better ionic mobility. These hybrid conductors have high ionic conductivity, lithium-ion transference numbers, and mechanical and thermal stability.[79] For instance, Park et al. synthesized single-ion solid electrolytes using Cu-azolate MOF and PC-filled pores loaded with the lithium salts (LiCl, LiBr, $LiBF_4$) having ionic conductivities in ~ 4 $x10^{-4}$ – 10^{-5} S/cm with activation energies in the range of 0.16-0.32 eV. A solvothermal method was used to make these Cu-azolate MOFs having multiple anion binding sites (open-metal sites), leaving free cations in the pores.[167] Similarly, Mg-based MOF was used as a solid lithium-ion electrolyte material after soaking it in a $LiBF_4$-EC-DEC solution which gave an ionic conductivity of ~10^{-4} S/cm and an activation energy of 0.15 eV.[168] The intraparticle processes dominate the ionic conduction in the conduction channels of these polycrystalline particles more than the boundary ones.[168] HKUST-1 is another common MOF for designing MOF-based SSEs[80,169,170] loaded with ionic liquids or liquid electrolytes. Shen et al. developed HKUST-1 MOF with biomimetic ionic channels having 3D pores of ~1nm, which were used as a scaffold for incorporating $LiClO_4$-PC electrolyte. The open metal sites in these MOFs anchor the ClO_4^- anions enabling faster Li-ion transport with low activation energy (0.21 eV) and superionic conduction (>1mS/cm).[169] A single ion conductor developed using UiO-66 MOF by incorporation of the plasticizers EC-PC gave ionic conductivities in the ~10^{-4} S/cm, wherein the anions were covalently linked to the MOF structure and the Li-ions diffused freely through the MOF channels.[171]

The majority of the MOFs use first row transition metals for framework construction due to their preferential coordination with aromatic polycarboxylate ligands. Incorporating light weight metals such as lithium into framework construction is less explored. But developing porous lithium-based MOFs could result in increased gravimetric storage capacity due to strong

electrostatic interactions of uncoordinated lithium centers and the adsorbed molecules.[172] This property could be beneficial in developing Li-MOF based solid-state electrolytes. Therefore, in this study, isoreticular Li-MOFs using the carboxylate linkers (1,4-BDC; 2,6-NDC and 4,4'-BPDC) were synthesized. The parameters like temperature, amount of solvent, precursor concentrations were optimized to obtain highly crystalline, porous Li-MOFs. Their chemical composition, crystallinity, thermal stability, and morphology were investigated. The lithium-ion conduction in Li-MOFs in solid-state was studied using electrochemical impedance spectroscopy, XPS and FTIR spectroscopy.

4.2 Background

The combination of coordination chemistry and solid state/zeolite chemistry led to the development of Metal-Organic Frameworks (MOFs), also called porous coordination polymers.[173] MOFs are self-assembled nanostructures that belong to the class of porous crystalline organic-inorganic materials, wherein organic ligands link the inorganic metal ions to form crystalline structures.[174] In MOFs, coordination bonds connect metal nodes to the organic linkers, resulting in porous 3D hierarchical structures.[175] Depending on their pore size and shape, MOFs have applications in gas storage, separation, catalysis, energy storage, etc.[174]

IRMOF-1 (i.e., MOF-5) was the first MOF synthesized by the Yaghi group. They have developed a series of porous materials by reticulation of metal ions and the carboxylate linkers named isoreticular MOFs (IRMOFs).[176] An isoreticular series of MOFs shares the same net topology by differing only in nature and size of organic linkers.[175,177] The concept of isoreticular MOFs was introduced with MOF-5 in 2002 and extended to mixed-linker compounds to play around with the pore size and their functionality.[173] For instance, MOF-5 has octahedral Zn-O-C clusters and benzene links which can be functionalized with organic groups to increase its pore

size, resulting in isoreticular series of MOF-5, IRMOFs.[178] Many applications linked to the distinctive properties of various IRMOFs-n (n = 1, 3, 6, 8) linkers have been investigated.

It is challenging to synthesize crystalline solid-state materials by systematically adjusting the chemical composition, functionality, and molecular dimensions without affecting the underlying topology. To synthesize the targeted extended structures with same precision, the starting building blocks should have similar attributes of the desired structures and the synthesis should be tunable to use derivatives of those building blocks to produce structures with the same skeleton but different functionalities.[179] The most common and first method used for IRMOF-1 introduced by the Yaghi group was the solvothermal method in a closed container which gave high yield. The conventional solvothermal method requires longer time for crystallization and yields a porous network. Other techniques such as sonochemical, microwave, hydrothermal, micro-fluidic strategy, and room-temperature synthesis, etc, have also been adopted for MOF synthesis over the years.

MOFs have high surface areas and pore volumes that are helpful for capturing and storing the adsorbate. They are physically, chemically, and thermally stable adsorbents to be used even in challenging environments. Their excellent tunability through modification allows for the improvement of their adsorption performance. IRMOFs have a great potential to be used as adsorbents because the pore-size can be expanded keeping the topology same. This design criteria helps adsorption of different size molecules.[176] The defects in MOFs can be well-engineered to benefit adsorption by controlling the temperature, water content, and modulating acids in the reaction. For instance, in UiO-66 MOF defects were tuned to generate active sites generating open frameworks for adsorption.[171,180] Open-metal sites can be created if the solvent molecules coordinate with the unsaturated metal centers during the MOF synthesis. Further, the

solvent molecules can be removed from the unsaturated metal sites to create open metal sites using the 'activation' technique.

Solvent (guest) molecules inadvertently get entrapped in the pores of the framework during the synthesis of MOFs, and excess linkers may also be trapped in a few cases. Activation is a process to eliminate solvent molecules to reach the high surface areas and permanent porosity promised by many framework structures.[181,182] Conventional activation involves removing the solvent molecules by using heat and vacuum treatment, and this strategy is mainly used to activate zeolites.[183] The activation temperature should be significantly above the solvent's vacuum boiling point and far below the framework's decomposition temperature.[181] In case of framework collapse with conventional heating, solvent exchange with a lower boiling point solvents such as ethanol or acetone can be performed prior to heating under vacuum. Other techniques such as super critical CO activation, freeze-drying or chemical treatments can be used to activate MOFs.

4.3 Results and Discussion

4.3.1 Synthesis and Characterization of Li-MOFs

The initially reported isoreticular (IRMOFs) of Li-BDC[184], Li-NDC[185] (ULMOF-1), and Li-BPDC[186] (ULMOF-2) were synthesized using the solvothermal synthesis from the precursor salts such as lithium perchlorate/lithium nitrate ($LiNO_3$), and the organic linkers (1,4-BDC, 2,6-NDC, and 4,4'-BPDC) in either mixture of N,N-dimethyl formamide (DMF)/ethylene glycol or DMF/ammonium fluoride. Typically, in solvothermal synthesis, the temperature is below 220 °C, and the crystallization time varies from several hours to days.[187] Higher yields are possible using solvothermal synthesis, and the product has superior crystallinity. The solvent can be heated above its boiling point because of the increased pressure, which improves the solubility of

the reacting salts and speeds up the reactions. Additionally, regular big crystals with a large interior surface area result from gradual crystallization from a solution. One benefit of this process is the ability to completely control the synthesis settings over an extended period, which enables the reproducible creation of procedures.[188]

Scheme 1. Schematic representation of the synthesis route to Isoreticular Li-MOFs

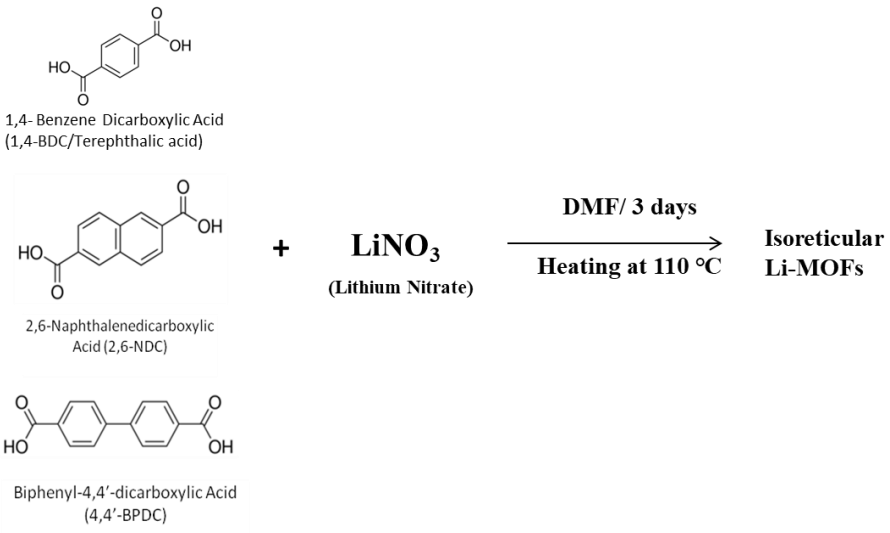

The chemistry to create isoreticular Li-MOFs is depicted in **Scheme 1**. Herein, we used a slightly modified solvothermal synthesis with the metal-ion precursor $LiNO_3$ in the presence of DMF for developing the highly crystalline microstructures of the three isoreticular Li-MOFs. In the typical procedure, microstructures of Li-BDC, Li-NDC, and Li-BPDC were prepared from precursor solutions of $LiNO_3$ and the respective organic ligands with initial sonication at room temperature followed by controlled heating at 110 ℃ for 3 days in the presence of DMF to yield the respective nanocrystals of Li-MOFs. The structural and morphological characterizations were performed using FTIR, UV-Visible spectroscopy, TEM, and SEM. The structural, compositional analysis and thermal stability were elucidated by X-ray photoelectron spectroscopy (XPS), elemental composition analysis, and thermogravimetric analysis. The porosity distribution was obtained

from the N_2 absorption-desorption analysis. The crystal structures and unit cell parameters were assessed by comparing the experimental powder XRD patterns with the simulated powder XRDs obtained from their original crystal structures (CCDC 664607, COD ID 4509412, and COD ID 4509710), reported previously.

The UV-Visible spectrum of 1,4-BDC obtained in anhydrous ethanol (**Figure 12(a)**) shows absorption maximum at 239 nm, with a weak shoulder peak at 294 nm which could be assigned to the π- π^* transition from the aromatic ring and n - π^* transition from the carbonyl group in the carboxylic acid moiety.[189] The absorption peak at 239 nm is red shifted ~ 8 nm (λ_{max} = 247.5 nm) in Li-BDC MOF, attributed to lithium-ion coordination to aromatic carboxylic acid, resulting in electronic structure delocalization in benzene ring. The shoulder peak at 290 nm in 1,4-BDC is also red-shifted in Li-BDC MOF, further confirming the lithium-ion coordination to carboxylic acid group. **Figure 12(b)** exhibits the comparison UV-Vis spectral traces for Li-NDC MOF along with 2,6-NDC dicarboxylic acid linker. The absorption peaks at 204, 242, 270, 283, and 293 nm are characteristics to vibronic transitions of naphthalene moiety and are slightly red shifted in Li-NDC MOF with no absorption peak at 204 nm. The UV-vis absorption spectrum of Li-BPDC along with the respective linker absorption show two absorption maxima at 204 nm and 281 nm, respectively, and are characteristics to biphenyl rings (**Figure 12(c)**). Although there are no noticeable peak shifts in Li-BPDC compared to the organic linker along, there is a drastic decrease in the absorption intensity in the absorption spectrum of Li-BPDC compared to the absorption intensity of BPDC linker.

Figure 12. UV-Visible spectra of (a) Li-BDC MOF, (b) Li-NDC MOF, and (c) Li-BPDC MOF.

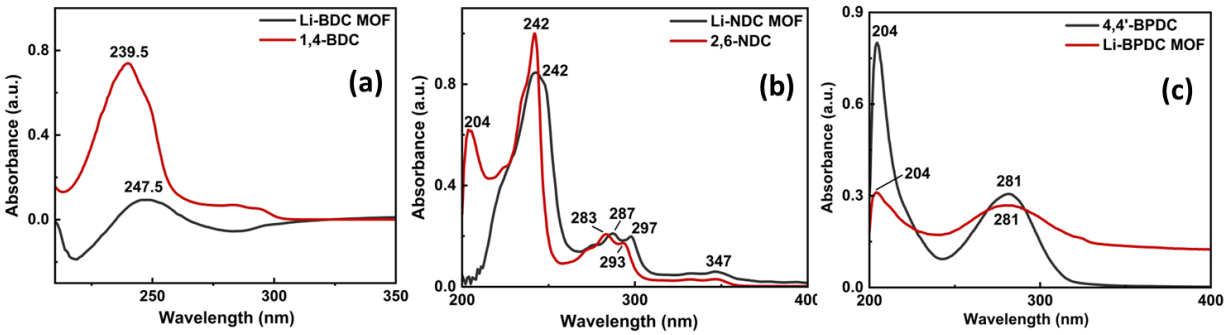

As depicted in **Figure 13(a),** the strong band at 1672 cm^{-1} corresponds to carbonyl (C=O) stretching in carboxylic acid group of terephthalic acid (1,4-BDC). It appears at a lower frequency due to the strong hydrogen bonding interactions between the acid's carbonyl group and hydroxyl groups of dimers.[190] The stretching at 1421 cm^{-1} and 1672 cm^{-1} are assigned respectively to the symmetric and anti-symmetric modes of the carboxylic acid groups.[191] The absorption peaks at 1508 cm^{-1} and 1421 cm^{-1} correspond to the aromatic C=C stretching and O-H bending of terephthalic acid. The C=O stretching peak at 1672 cm^{-1} in the 1,4-BDC linker shifted to 1570 cm^{-1} in Li-BDC MOF. Further, the C-O stretching peak was observed 1095 cm^{-1} in Li-BDC. The strong Li-O bending peaks were observed at 1392 cm^{-1} and 826 cm^{-1} which corresponds to the lithium-coordinated carboxylate groups in Li-BDC MOF.[184] The absorption peak at 753 cm^{-1} corresponds to the C=C bending of the benzene ring in Li-BDC MOF.

The FTIR spectra of Li-NDC MOF (**Figure 13(b)**) shows the carbonyl (-C=O) peak shift from 1674 cm^{-1} in 2,6-NDC to 1602-1565 cm^{-1} in Li-NDC indicating the lithium coordination.[192] The strong O-Li bending peaks at 1396 cm^{-1} and 802 cm^{-1} indicate the lithium coordinated carboxylic acid groups in Li-NDC MOF. The FTIR spectra of Li-BPDC MOF (**Figure 13(c)**) show the peak shifts in C=O stretching from 1670 cm^{-1} to 1585 cm^{-1} indicates the coordination of

carboxylate groups (COO^-) to the Li^+ metal center.[193,194] Also, the O-H bending peak shift from 1426 to 1397 cm^{-1} and the Li-O peak at 840 cm^{-1} in Li-BPDC MOF confirms the Li-ion coordination with the carboxylic acid groups of 4,4'-BPDC.

Figure 13. FTIR spectra of (a) Li-BDC MOF, (b) Li-NDC MOF, and (c) Li-BPDC MOF

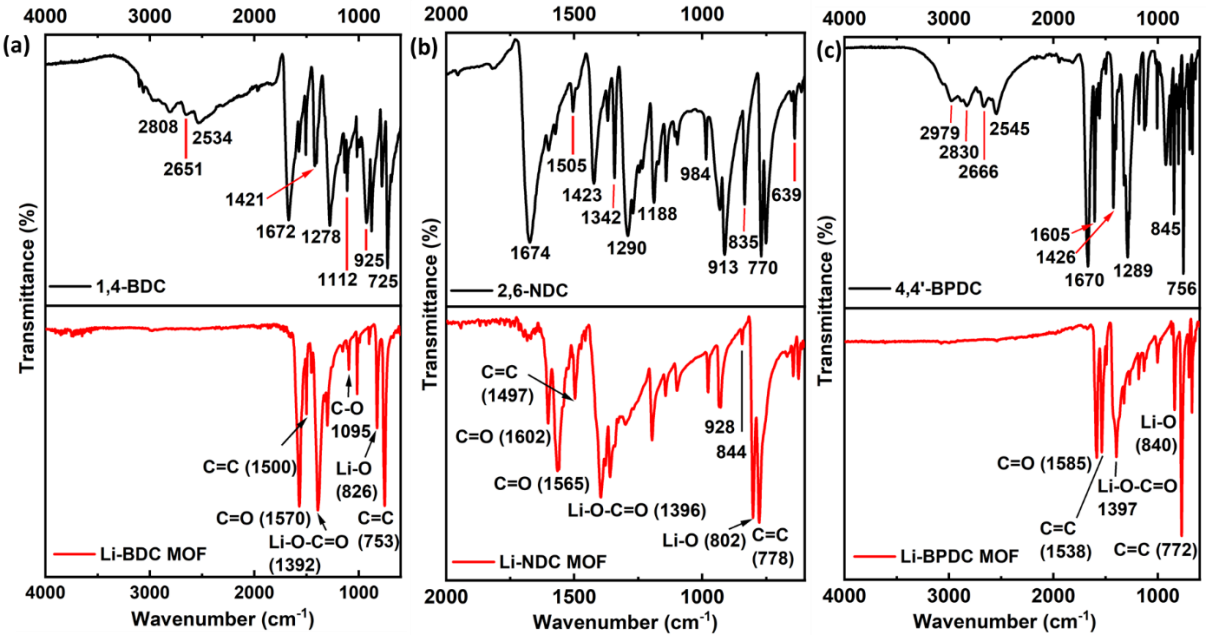

The chemical composition study was conducted by XPS elemental survey and supported the empirical formula of Li-BDC to be $Li_2C_8H_4O_4$. The chemical composition is consistent with the theoretical elemental composition. Similarly, the theoretical empirical formula for Li-NDC MOF ($Li_2C_{12}H_6O_4$) agrees with the elemental composition survey analysis performed by XPS and both Li-BDC and Li-NDC MOFs indicate the presence of the elements C, O, and Li. the XPS survey analysis of Li-BPDC MOF confirms the presence of elements C, O, Li with absence of solvent molecules (i.e., DMF) in the frameworks (**Figure 14(a) and (e)**). The binding energy spectra for C 1s, O 1s, and Li 1s for Li-BDC and Li-NDC MOFs are shown in **Figure 14 (b)-(d) and (f)-(h).** The binding energy spectrum of C 1s for Li-BDC and Li-NDC MOFs show peaks at 284.8 eV and 288.5 eV, which is assigned to the sp^2 bonded carbon of the C phenyl and C

carboxyl groups of the organic linkers (1,4-BDC), respectively.[194] The O 1s scan of Li-BDC and Li-NDC MOFs shows two peaks at 531.5-532 eV and ~533 eV, which correspond to the sp^2 C=O and C-O bonds of the carboxylate groups.[195]

Figure 14. (a) XPS survey spectrum of Li-BDC and binding energy spectra of Li-BDC MOF for (b) C1s, (c) O 1s, and (d) Li 1s; and (e) XPS survey spectrum of Li-NDC and binding energy spectra of Li-NDC MOF for (f) C1s, (g) O 1s, and (h) Li 1s

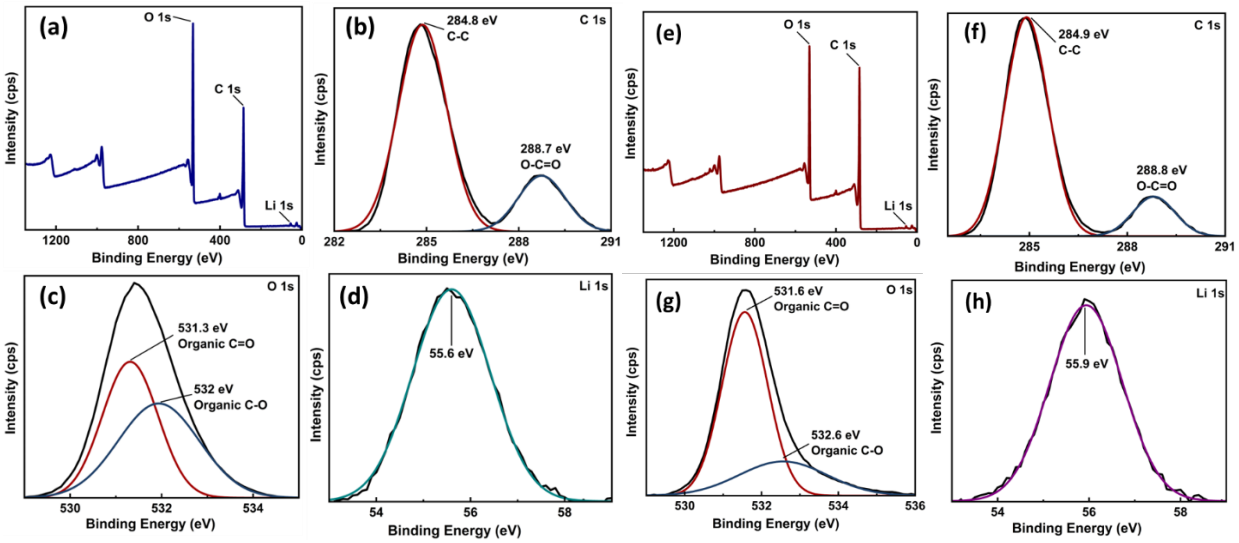

From **Figure 15(a),** the XPS survey analysis of Li-BPDC MOF confirms the presence of elements C, O, Li with absence of solvent molecules (i.e., DMF) in the frameworks, and the respective binding energy spectra are also shown in **Figure 15(b)-(d).** The C 1s and O1s scans show peaks corresponding to the binding energies for carboxylate groups in the organic linker 4,4'-BPDC. The empirical formula calculated from the peak table obtained to match the expected empirical formula, $Li_2C_{14}H_8O_4$ (Li_2(4,4'-BPDC)), and the theoretical weight percentage values of elements are in close agreement with the values obtained from XPS analysis. The full width at half maximum (FWHM) of 4.12 eV, 4.04 eV, and 3.95 eV for O 1s in Li-BDC, Li-NDC and Li-BPDC MOFs further supports the oxygen chemical bonding state of O^{-2} corresponding to

the carboxylate form.[194,196,197] In all the three Li-MOFs, Li 1s gave an FWHM of 3.69 eV, 3.68 eV and 3.67 eV for the Li-BDC, Li-NDC and Li-BPDC MOFs supporting the oxidation state of +1 (Li^+) along with its binding energy peak at ~55.7 eV.[198]

Figure 15. (a) XPS survey spectrum and binding energy spectra of Li-BPDC MOF for (b) C1s, (c) O 1s, and (d) Li 1s.

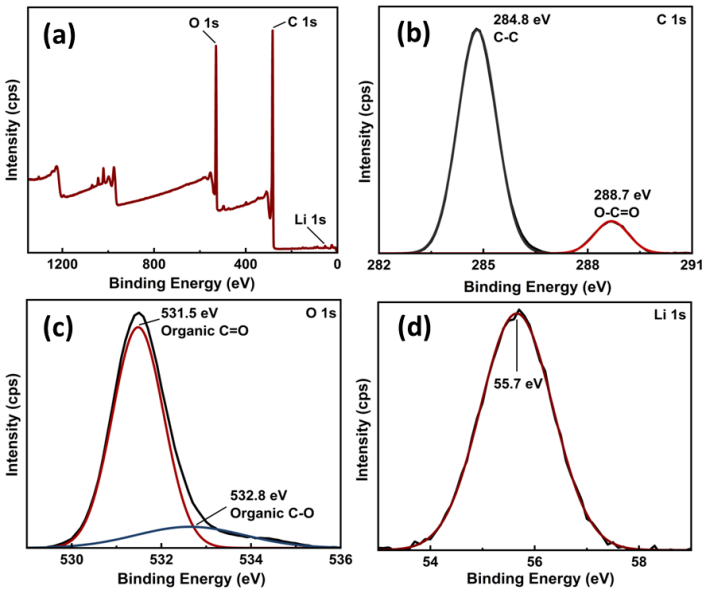

Thermal stability of Li-MOF samples was studied after vacuum dried the samples to 250 ℃ overnight. The thermogravimetric analysis of the 1,4-BDC linker exhibits stability upto 276 ℃ and completely decomposes at 382 ℃ due to the sublimation of 1,4-BDC.[199] The first degradation of the Li-BDC framework (**Figure 16(a)**) occurs at 551 ℃ with a weight loss of 46%, demonstrating that the framework is stable up to that temperature. Thereafter, the framework starts to collapse and completely decomposes to char at 709 ℃. Although most BDC-coordination polymers[200] lose organic components in the temperature range of 220-400 ℃, the Li-BDC framework shows a significant high thermal stability, perhaps due to the lack of solvent molecules incorporated into the structure.[201] The total weight loss of 74% occurs in the 551-1000 ˚C range due to the degradation of the framework and the loss of organic components, and the

final char of 26% corresponds to Li_2O.[202] A similar trend was observed with the Li-NDC MOF, in which the framework is stable up to 554 ˚C and decomposes by 713 ˚C, resulting in a char weight of 18%.[203] The peak degradation values obtained for Li-BDC and Li-NDC MOFs are closer to the originally reported values.[185,202] The major weight loss for Li-BPDC MOF begins at 496 ˚C with a weight loss of 71%, demonstrating the framework stability up to that temperature, and the char obtained is 19%.[204] An overall weight loss of 78% occurs in the 520-1000 ˚C range due to the degradation of framework and the loss of organic component.[202] The initial weight loss of 1-2% in the range of 380-500 ℃ could be due to the surface absorbed moisture. The thermal stability of these Li-MOFs was higher when compared to the Li-AOIA and Li-TMCA MOFs, whose major degradation occurs in the 250-400 ℃ region due to the bound solvent molecules in the framework structures.[165]

Figure 16. TGA and derivative thermograph of (a) Li-BDC, (b) Li-NDC, and (c) Li-BPDC MOFs.

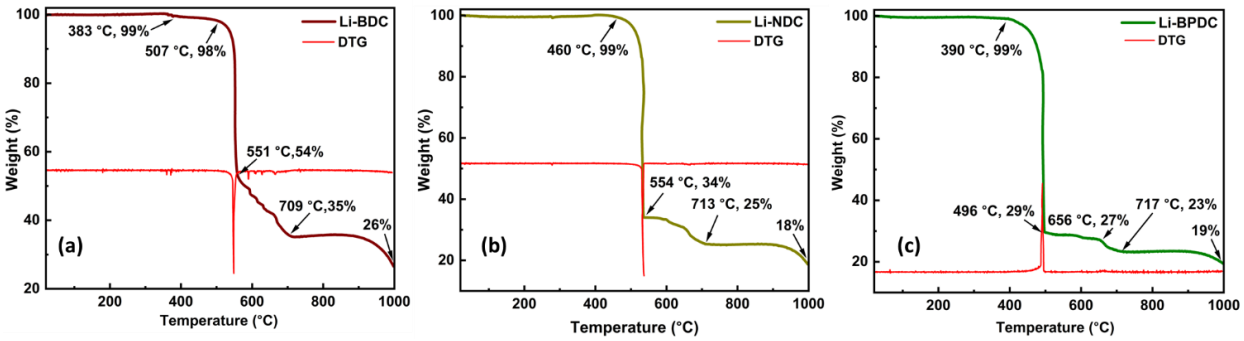

4.3.2 Morphology and Crystallinity studies

The experimental powder XRD patterns were collected and compared with the simulated powder XRD patterns from original crystal structures reported for Li-BDC, ULMOF-1, and ULMOF-2 (CCDC 664607, COD ID 4509412, and COD ID 4509710). The simulated XRD patterns generated from the crystal structures of Li-BDC[184], Li-NDC[185], and Li-BPDC[186] MOFs

perfectly overlap with the experimental diffraction patterns (**Figure 17(a-c)**) and confirm that their crystal structures agree with the reported crystal structures (**Figure 17(d-f)**). The crystal structure of Li-BDC MOF is a 3D network built using bridge-quadridentate fashion (four lone pairs bound to the central metal ion) formed by lithium ions and carboxylate groups from 1,4-BDC, as shown in **Figure 17(d).** Four oxygen atoms from four bridging 1,4-BDC ligands coordinate the central lithium ion, giving it a distorted tetrahedral coordination geometry since the O-Li-O bond angles are between 103.33 - 123.10° and Li^+ ions frequently have a coordination number of 4.[78,184,205,206] Three of the four 1,4-BDC ligands that are coupled to a single Li^+ ion is parallel to each of the three planes, except for one 1,4-BDC ligand being in a distorted position in a different plane. A branch-shaped motif is formed by two 1,4-BDC ligands overlapping one another. Li-BDC MOF crystallizes with a monoclinic topology that belongs to the space group *P2(1)/c* with the lattice parameters a = 8.365 Å, b = 5.129 Å, c = 8.516 Å, and β = 92.916.[184]

The aromatic bridging unit and alternating layers of LiO make up the structure of Li-NDC MOF, and the lithium atom with the carboxylate oxygen coordinate in the distorted tetrahedral geometry. Each lithium atom is connected to four separate naphthalene rings (**Figure 17(e)**) by the four carboxylate moieties, and the lithium's bond valence sum is predicted to be +1. A 2D layer of Li-O-Li is formed due to the tetrahedral coordination with the two carboxylate groups connecting the two LiO layers.[185] The 2D LiO (*abab* type) layers form an antifluorite-type motif consisting of edge-shared tetrahedra with tetrahedral vacancies.[185] The close contact between the naphthalene rings allows possible $\pi - \pi^*$ interactions among the adjacent rings.[185] Li-NDC MOF also crystallizes with a monoclinic topology belonging to the space group *P2(1)/c* having the lattice parameters a = 10.302 Å, b = 5.345 Å, c = 8.662 Å, and β = 98.659.[185]

A 3D framework of Li-BPDC MOF comprises alternating LiO layers joined by aromatic biphenyl bridging units isoreticular to both the Li-BDC and Li-NDC MOFs, wherein the lithium atom is in a distorted tetrahedral geometry. The 2D LiO layers consist of edge-sharing lithium tetrahedra dimers which are corner-shared forming a layered structure.[204] Li-BPDC MOF also crystallizes with a monoclinic topology belonging to the space group *P2(1)/c* having the lattice parameters a = 12.753 Å, b = 5.138 Å, c = 8.420 Å, and β = 97.218.[204] A similar distorted tetrahedral geometry was observed in other lithium-based MOFs (Li-AOIA and Li-TMCA with the linkers being 5,5'-((anthracene-9,10-diylbis(methylene))bis(oxy))diisophthalic acid (H_4AOIA), and 5,5'-(((2,3,5,6-tetramethyl-1,4-phenylene)bis(methylene))bis(oxy))diisophthalic acid (H_4TMCA)) synthesized via the solvothermal approach using DMF and belongs to the space group C2/c, wherein the lithium-ion coordinates three dicarboxylate units and one solvent molecule.[165] The average crystallite size was calculated for the Li-BDC, Li-NDC, and Li-BPDC MOFs were calculated to be 10.94 (±3.06) nm, 11.98 (±3.57) nm, and 15.25 (±4.59) nm, respectively. Debye-Scherrer equation (4.1) was used to calculate the crystal size.

$$D = \frac{K\lambda}{\beta cos\theta}, \qquad \text{Eq. 4.1}$$

Where K is the shape factor (0.94 for spherical crystals with cubic symmetry), D is the crystallite size, λ is the wavelength of X-ray (λ =0.154 nm), β is the full-width at half maximum (FWHM) calculated using the origin software, and θ is the diffraction angle.[207]

Figure 17. The powder XRD spectrum of microstructures and simulated powder XRD spectra of original (a) Li-BDC MOF, (b) Li-NDC MOF, (c) Li-BPDC MOF, respectively, and the crystal structure generated from the crystallography data of (d) Li-BDC MOF[184], (e) Li-NDC MOF[185], (f) Li-BPDC MOF[186] respectively.

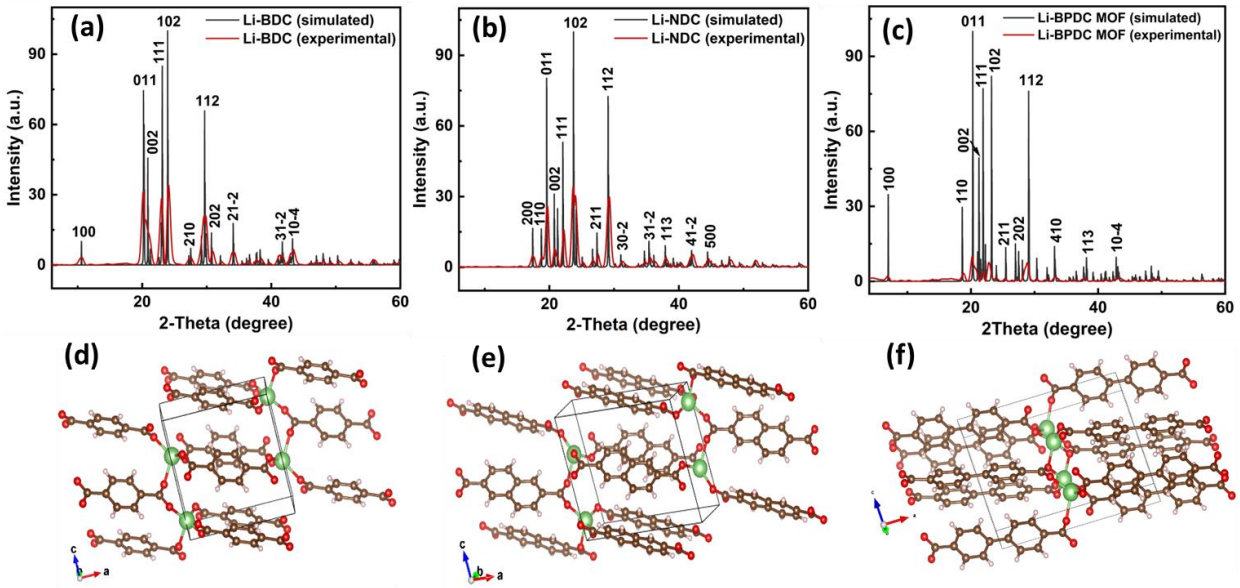

The morphology studies on Li-MOFs were performed using scanning and transmission electron microscopy. The SEM images in Figure 19 show truncated rods and irregularly shaped microstructures of the isoreticular Li-MOFs. Li-BDC microstructures (**Figure 18(a,b)**) have average widths and lengths of 8-35 μm and 18-67 μm, Li-NDC microstructures (**Figure 18(c,d)**) have average widths and lengths of 13-20 μm and 26-74 μm, and Li-BPDC microstructures (**Figure 18(e,f)) have** average widths and lengths of 3-16 μm and 5-23 μm, respectively.

Figure 18. SEM images of (a, b) Li-BDC, (c, d) Li-NDC, and (e, f) Li-BPDC MOFs.

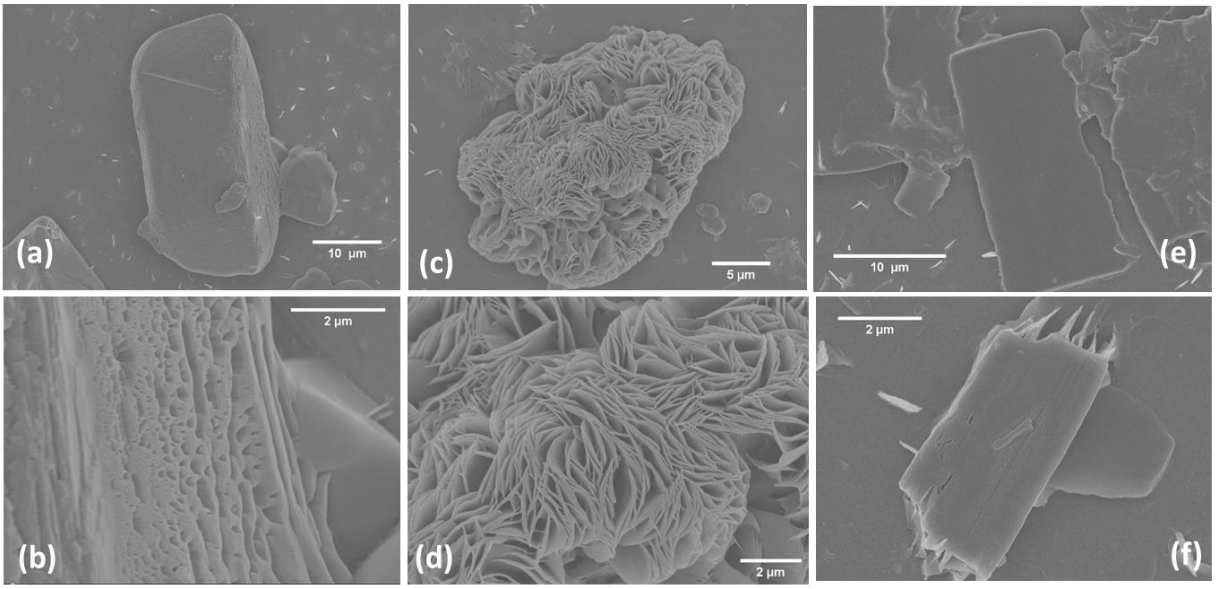

As shown in **Figure 19 (a,c,e)**, HRTEM images of the microstructures show that they are composed of a hierarchy of self-assembled nanocrystal layers with randomly ordered voids between the nanocrystals. The interplanar spacing measured from the TEM images of the respective Li-MOFs is shown in **Figure 19 (b,d,f)**. The lattice spacings are calculated from the images using ImageJ software, and the lattice distances are approximately 0.44 nm & 0.39 nm in Li-BDC, 0.29 nm in Li-NDC, and 0.33 nm in Li-BPDC, respectively. From **Figure 19(b),** the lattice spacing of 0.44 nm resembles the distance between the two Li atoms along the plane [001] and 0.39 nm resembles the spacing between the two neighboring oxygen atoms bonded to the Li in the distorted tetrahedron in Li-BDC MOF. From **Figure 19(d)**, the lattice spacing of 0.29 nm corresponds to the distance between the two O-atoms in the tetrahedron node in Li-NDC MOF.[185] From **Figure 19(f)**, the lattice spacing of 0.33 nm corresponds to distance between the O-atoms of the distorted tetrahedron in Li-BPDC MOF.[204]

Figure 19. TEM images and lattice spacings of (a, b) Li-BDC, (c, d) Li-NDC, and (e, f) Li-BPDC MOFs, respectively.

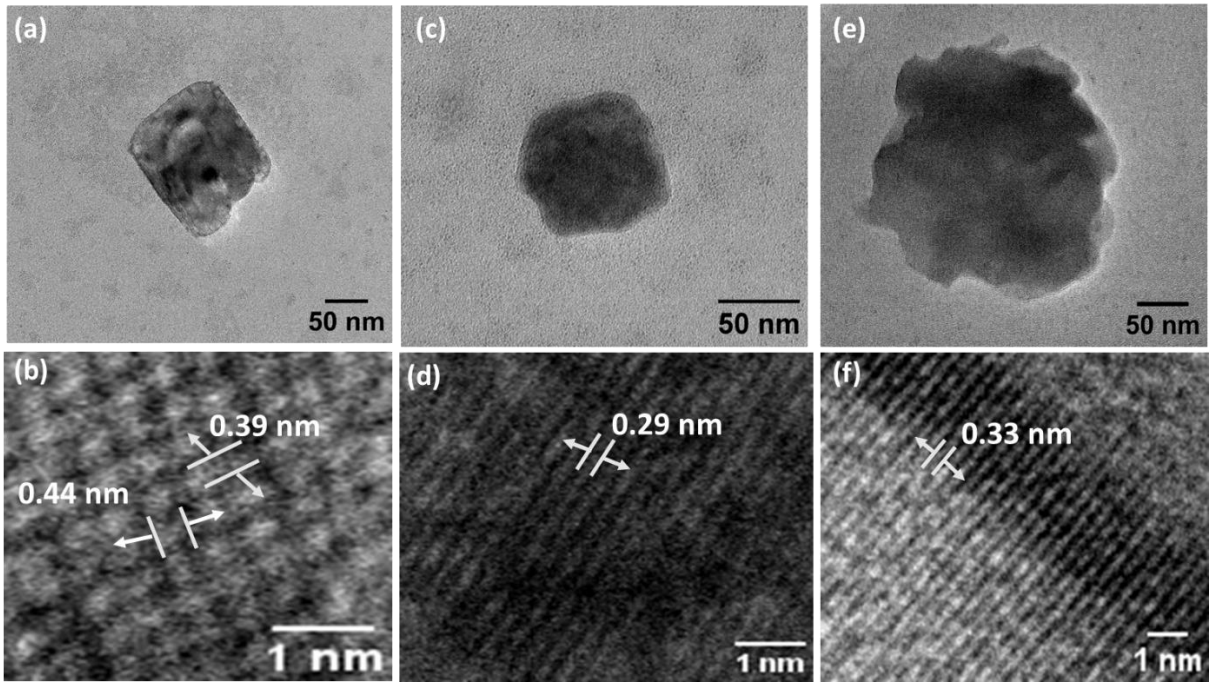

4.3.3 BET measurements

To understand the Li-ion conduction in these porous Li-MOFs, studying the adsorption-desorption behavior of Li-MOFs is essential. The surface area of Li-MOF microstructures and surface porosity distribution were evaluated using the N_2 Brunauer–Emmett–Teller (BET) (**Figure 20(d**)) and Barret–Joyner–Halenda (BJH) analyses (**Figure 20(e**)) as summarized in **Table 2**. The full N_2 adsorption-desorption isotherms obtained after the Chi-square goodness of fit test exhibits Type I(b) reversible isotherms for all the three Li-MOFs. Type I(b) isotherm is for solids containing both wider micropores (<2nm) and narrow mesopores.[208] Due to lack of hysteresis in the isotherms, the pores are cylindrical allowing reversible adsorption-desorption without any pore blocking phenomenon.[209] The BET surface areas obtained for all the three Li-MOFs are high with Li-NDC MOF having the largest BET surface area of 894.76 m^2/g. However, BET method can give overestimated surface areas for materials with micropores

below 20Å due to micropore filling rather than mono/multi-layer coverage.[208,210] Hence, BET theory can be applied to microporous materials if an appropriate pressure range is used.[208] The N_2 molecules first populate the corners followed by a monolayer formation till the pores get filled completely. This process occurs in the pressure range ($0.05<P/P_0<0.3$) where the BET surface area is commonly calculated.[208] Herein, the single-point BET ($P/P_0 = 0.3$) surface areas of Li-BDC, Li-NDC and Li-BPDC MOFs are 410.49 m^2/g, 446.10 m^2/g, and 382.63 m^2/g, respectively. The BET surface area and BJH pore volume of Li-NDC was found to be largest when compared to the Li-BDC and Li-BPDC MOFs due to the packing arrangement of ligands.

Table 2. N_2 BET surface area and BJH pore distribution analyses of Li-MOFs.

Li-MOFs	BET surface area (m^2/g)	BJH desorption cumulative pore volume (cm^3/g)	BJH desorption cumulative pore area (m^2/g)	BJH adsorption average pore widths (Å)
Li-BDC	834.84	0.650	569.35	45.97
Li-NDC	894.76	0.708	614.46	45.27
Li-BPDC	741.54	0.618	526.62	47.26

The classic BJH method uses the Kelvin model for pore filling and is widely used for porosity characterization. The average BJH adsorption pore widths for the three Li-MOFs were in the mesopore range 4.5 nm to 4.7 nm. BJH method mostly gives accurate results for the mesoporous and microporous materials. It does not account for interactions between the pore surface and sorptive fluid in finer pore sizes (<8nm). For microporous materials (pore size less than 2nm), the Horvath-Kawazoe method can be applied. However, NLDFT (Non-local Density Functional theory) model allows obtaining a continuous pore-size distribution across

microporous (<2nm) through mesoporous (2-50nm) to macroporous (>50nm) regions. Using the Horvath-Kawazoe method, the pore size distributions in the microporous regions were obtained for the three Li-MOFs. The average micropore widths were found to be 18.71 Å, 18.65 Å, 18.59 Å for Li-BDC, Li-NDC, and Li-BPDC, respectively. From **Figure 20(a-b),** the NLDFT model gave accurate pore distributions for three Li-MOFs microstructures have bimodal pore distributions containing both the micropore (10 to 20 Å) and mesoporous (20 to 200 Å) regions. Due to this bimodal pore distribution, high N_2 BET surface areas and BJH pore volumes were observed in these isoreticular Li-MOFs similar to the microporous IRMOF-6 and MOF-5 frameworks.[179,211]

Figure 20. Porosity distribution plots obtained from NLDFT analysis for Li-MOFs: (a) a line graph of dV/dw pore volume distribution, (b) a bar graph of dV/dw pore volume distribution, (c) the 3D plot of pore volume distribution in the micropore size region, (d) N_2 BET Isotherms, and (e) BJH adsorption and desorption pore volume distribution plots for Li-MOFs.

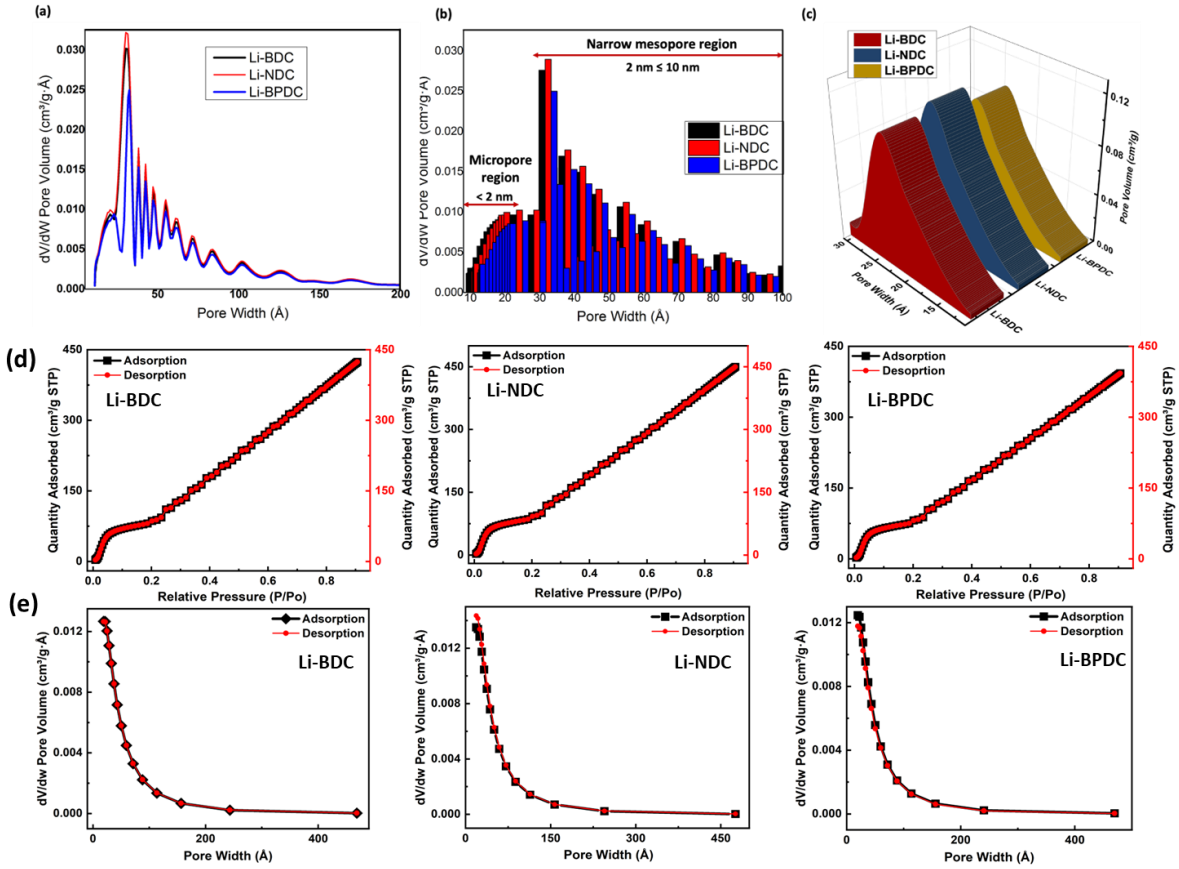

4.3.4 Ionic conductivity studies

Prior to conducting the ionic conductivity analysis, Li-MOFs were pre-heated at 250 ˚C under vacuum overnight, to remove any surface adsorbed moisture and residual solvents (DMF) molecules. Then Li-MOFs powder samples were subsequently soaked in the LEC ($LiClO_4$-ethylene carbonate) electrolyte solution to incorporate Li^+, ClO_4^-, and EC as guest molecules into these porous isoreticular Li-MOF frameworks. These LEC@Li-MOF powders prepared in this

manner were pressed into dense pellets and analysed on the EIS to evaluate their ionic conductivities. As a control, EIS analysis was performed on the Li-MOF pellets prior to soaking in LEC electrolyte solution and open-circuit graphs (**Figure A47**) were obtained indicating no ionic conductivity.

The total ionic conductivity (σ) obtained at 25 °C is reported in **Table 3**, following normalization for pellet thickness (1.2-2mm). The ionic conductivities of the pellets were in the range of 10^{-5} S/cm, with respect to the linker length of Li-MOFs, and the highest ionic conductivity of 6.66 x 10^{-5} S/cm was obtained for the Li-BPDC frameworks. The main factors which influence the ionic conductivity are binding strength, coordination, and dynamics of Li^+ ions apart from the aromatic linker flips, guest molecules' reorientation and local motions.[212] Herein, the slight increase in ionic conductivity with framework expansion could be due to the difference in LEC guest molecules loaded into the pores of the frameworks. EC having a static diameter is 5.74Å[213], facilitates the solvation of lithium salt thereby enabling the mobile Li^+ ions to hop along the porous channels. Due to the different pore volume distributions observed in Li-MOFs, the Li^+, ClO_4^-, and EC guest molecules' loading in the pores can vary which led to variation in ionic conductivities. The pore volumes of Li-BDC and Li-NDC were higher than Li-BPDC thereby allowing higher concentration of LEC guest molecules in the frameworks which can hinder the Li-ion mobility and cause lower ionic conductivities. Therefore, the Li-ion conduction mechanism could be a pore-filling mechanism via hopping through the EC molecules. The ionic conductivities were a order of magnitude lower than the lithium-based MOF electrolytes (Li-AOIA@NO_3 and Li-TMCA@BF_4)[165] and MOF-based solid-state electrolytes such as LPC@HKUST-1[154], $LiClO_4$- EC-DMC@MgMOF74[214], Mg_2(dobdc)[168] and Cu-azolate[23] MOFs.

Temperature-dependent ionic conductivity studies were performed on the LEC@Li-MOFs pellets in the temperature range of 25-55 °C below the glass-transition temperature (T_g) of the solid-pellets. **Figure 21** shows the ln σ versus reciprocal temperature (1000/T) plots for all three Li-MOFs. These experimentally obtained temperature dependent ionic conductivities were fitted using the Arrhenius expression and corresponding activation energies were calculated from the corresponding slopes of the fitted curve. Arrhenius theory describes the conductivity of a thermally initiated ion-transport mechanism in an amorphous phase below T_g and activation energy is the energy required to initiate this process.[215] Above T_g, the temperature-dependent ionic conductivity in the amorphous polymer electrolytes is mostly non-Arrhenius and the equations such as Vogel-Tamman-Fulcher (VTF) are used to fit these non-Arrhenius curves.[215,216] The loss of trapped EC was observed during the temperature-dependent ionic conductivity measurements as the LEC@Li-MOF electrolyte pellets turn semi-solid in nature with increase in temperature beyond 55 °C. The experimental data indicates that the ionic conductivity with increasing temperature obeys the Arrhenius relationship with highest correlation coefficient (R^2) in LEC@Li-BPDC (R^2 =0.99), when compared to LEC@Li-BDC (R^2 =0.98) and LEC@Li-NDC (R^2 =0.97) which imply poor fits and the non-linearity of the data. The non-linear Arrhenius behavior indicates that the local environment surrounding the mobile Li^+ ions is dynamic (non-rigid). This implies that the activation energy involves the energy required for the rearrangement of local structure as well as the energy barrier for the lithium-ion hopping between the coordination sites in the electrolytes.[215] The activation energy values range from 0.635-0.719 eV, with the lowest activation energy corresponding to the Li-BPDC frameworks. Activation energy measures the energy required to initiate a chemical reaction which determines the rate of a chemical reaction, and generally, a higher activation energy

indicates a slower reaction. The activation energy required for the ions to move through the porous frameworks affects the ionic conductivity, and a lower activation energy gives a higher ionic conductivity.[217] Lower activation energies indicate the presence of broader Li-conduction pathways allowing more effective lithium-ion solvation, and perhaps reduction in confinement and tortuosity effects.[169,218] Herein, lower activation energy in LEC@Li-BPDC indicate the presence of faster lithium mobility through the Li-BPDC frameworks when compared to the Li-NDC and Li-BDC MOFs. The smaller porous channels in Li-BPDC could reduce the diffusion distance for Li^+ ions when compared to larger porous channels in Li-BDC and Li-NDC, thereby require less energy to diffuse via the pores. However, the activation energies of these LEC@Li-MOFs were higher than the MOF-based SSEs (Li-AOIA@BF_4[219], Mg_2dobdc[23] and Cu-azolate[220] based SSEs). Hence, in order to further understand the lithium-ion conduction mechanism, and the variation in ionic conductivities of these three isoreticular Li-MOFs, the pellets were characterized by FT-IR, XPS and TGA and are discussed in the follow up section.

Table 3. Ionic conductivity and activation energy values of Li-MOF microstructures.

Sample Name	**Ionic Conductivity at 25 ˚C (S/cm)**	**Activation Energy (eV)**
Li-BDC-EC-5wt% $LiClO_4$	1.72 x 10^{-5}	0.718±0.106
Li-NDC-EC-5wt% $LiClO_4$	3.66 x 10^{-5}	0.719±0.121
Li-BPDC-EC-5wt% $LiClO_4$	6.66 x 10^{-5}	0.635±0.083

Figure 21. Arrhenius plot and activation energy of (a)&(d) LEC@Li-BDC, (b)&(e) LEC@Li-NDC, and (c)&(f) LEC@Li-BPDC electrolytes (inset- images of the pellets).

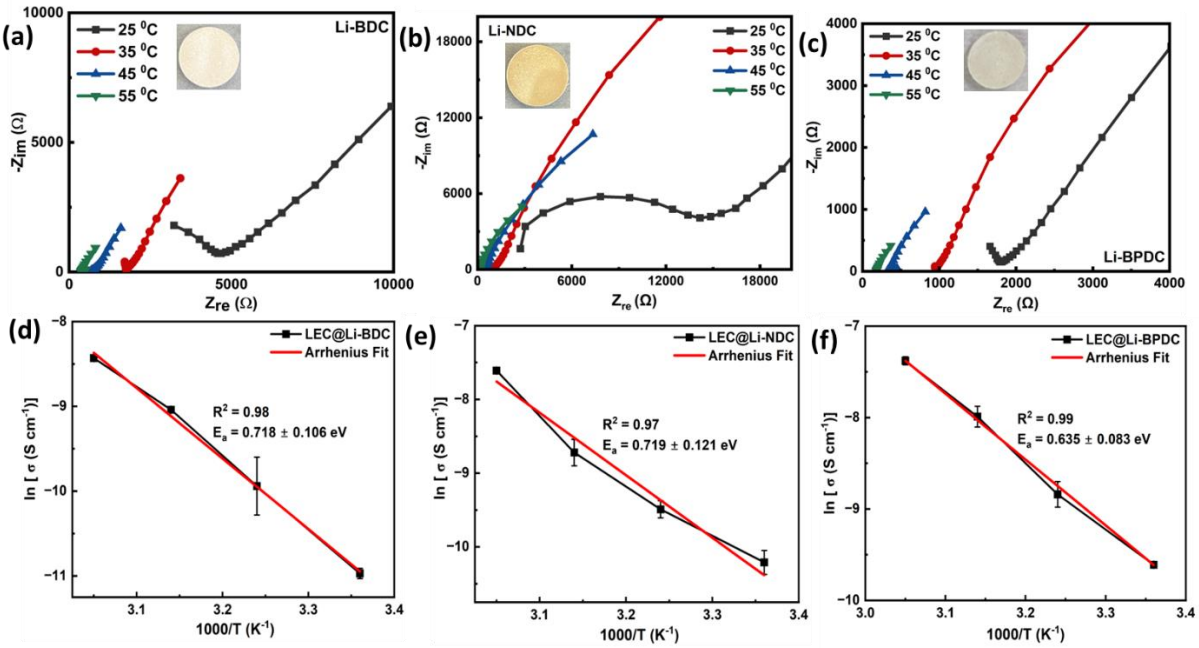

4.3.5 FTIR Spectroscopy Measurements on LEC@Li-MOF electrolytes

In order to understand the hypothesized pore filling Li-ion conduction mechanism in the Li-MOF@LEC electrolytes, FTIR spectroscopy was performed on LEC@Li-MOF (prior to ionic conductivity measurements), Li-MOF@EC, Li-MOFs, and EC samples, respectively. The major peaks for EC at 1789 cm^{-1}, 1768 cm^{-1}, 1554 cm^{-1}, 1146 cm^{-1}, and 1058 cm^{-1} are assigned to C=O stretching (carbonate ester), CH_2 bending vibrations and C-O stretching vibrations, respectively (**Figure 22(a)**).[221,222] Originally, the C=O stretching mode of EC occurs at 1771 cm^{-1}.[223] But the splitting of bands into 1768 cm^{-1} and 1789 cm^{-1} is due to the Fermi resonance of the C=O stretching mode with an overtone of ring breathing at 891 cm^{-1} and the short-range ordering of molecular orientation caused by the dipole-dipole interaction of two EC molecules.[222,223] EC's ring breathing mode occurs at 891 cm^{-1} and EC's ring bending mode occurs at 715 cm^{-1}.[224] Interactions with other molecules profoundly influence the C=O stretching vibrations in EC.[222]

In **Figure 22(a)**, LEC@Li-BDC spectra shows a reduction in the Li-BDC's C=O peak at 1570 cm^{-1} along with peak broadening in the region 1585-1593 cm^{-1} which is due to the interactions of EC's C=O group with the Li^+ nodes in the Li-BDC framework. The CH_2 bending peak of EC appears at 1554 cm^{-1} exhibits reduced absorption in LEC@Li-BDC, featuring a weak shoulder, which is associated to the binding of the carbonyl oxygen with Li^+ in the framework's metal oxide nodes. An additional peak at 1540 cm^{-1} suggests the interactions of EC's carbonyl oxygens with the solvated Li^+ ions of the $LiClO_4$ salt. Further, the shifts in EC's carbonyl bands to 1795 cm^{-1} and 1771 cm^{-1} along with the reduced absorption intensities is due to the EC's carbonyl interactions with the solvated Li^+ ions. Some of the Li ions may also interact with the oxygen atoms in the EC ring along with the interactions through the EC's C=O groups.[224] **Figure 22(b)** shows the peak shifts in C-O-C stretching of EC at 1146 cm^{-1} and 1058 cm^{-1} to 1156 cm^{-1} and 1067 cm^{-1}. These peaks shifts confirm the interactions of EC's ether oxygens with the mobile Li^+ ions from the $LiClO_4$ salt due to solvation. These interactions between the plasticizer, EC, and lithium salt leads to reduction in the coulombic interaction between the cation and anion of salt, thus dissociating the lithium salt to produce more mobile Li-ions.[222] From the **Figure 22(c),** the additional peaks at 841 cm^{-1} along with slight reduction of Li-O peak at 826 cm^{-1} corresponds to the interactions of solvated Li^+ ions from $LiClO_4$ salt with the oxygen atoms in the metal-oxide nodes of the frameworks. The reduction in intensity of the benzene ring bending peak at 753 cm^{-1} along with the slight shoulder peak at 764 cm^{-1} further confirm the interactions of solvated Li^+ ions with the oxygen atoms in the metal-oxide nodes of the frameworks.The ring breathing mode of EC at 891 cm^{-1} showed shoulder peak at 867 cm^{-1}, and the ring bending mode of EC at 715 cm^{-1} shifted to 710 cm^{-1} along with a weak shoulder peak at 704 cm^{-1} which confirms the Li-ion solvation due to EC's carbonyl and ether oxygen groups.[224] From **Figure**

22(d), the peak at 623 cm^{-1} belongs to one of the vibrational mode of perchlorate (ClO_4^-) anion having a tetrahedral structure. The additional shoulder peaks at 636 – 646 cm^{-1} indicate that the symmetry of ClO_4^- anion has been disturbed by EC molecules.[224] Further, previous studies suggest that two EC molecules bind to the free Li^+ leading to stable complexes of $Li^+(EC)_2ClO_4^-$.[225] Therefore, from the FTIR spectra of LEC@Li-BDC, it is evident that the EC interacts with the $LiClO_4$ salt resulting in dissociation of the salt into Li^+ and ClO_4^- ions. These free Li^+ ions hop along the porous channels while interacting with the EC's carbonyl/ether oxygens, Li-O framework oxygens as well as the carbonyl oxygens of the linker. These strong interactions of the Li^+ ions with the framework oxygens can lead to higher activation energy required for Li-ion conduction through the pores.

Figure 22. The normalized FTIR spectra of LEC@Li-BDC, Li-BDC, and EC in the region (a) 1900-1500 cm^{-1}, (b) 1200-1000 cm^{-1}, (c) 925-725 cm^{-1}, and (d) 725-600 cm^{-1}.

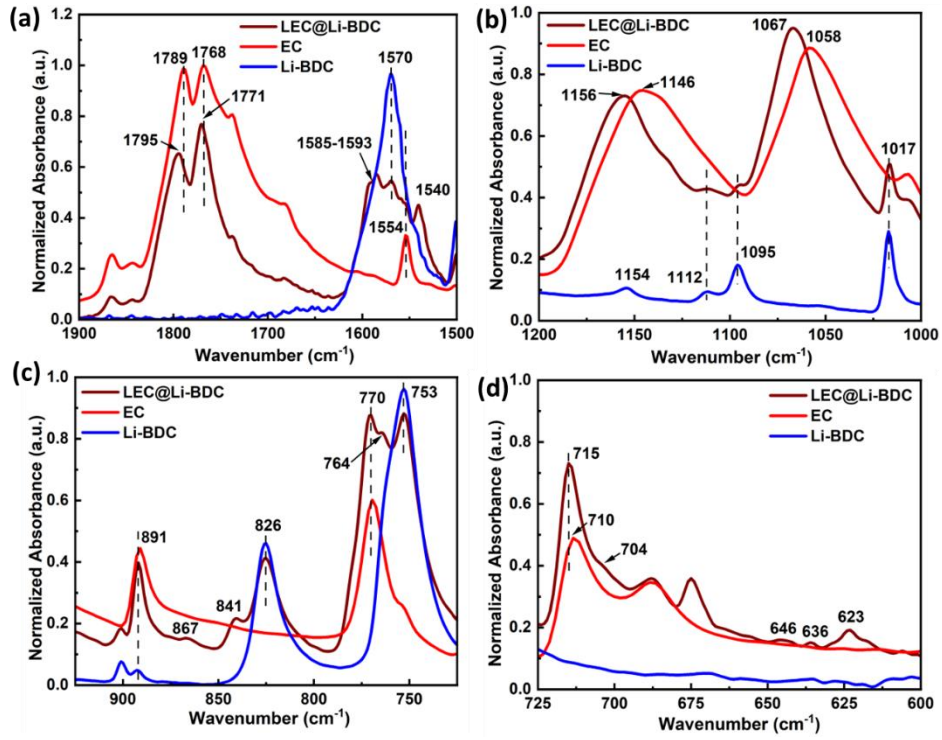

In **Figure 23(a)**, LEC@Li-NDC spectra shows a reduced absorption in the C=O peak at 1565 cm^{-1} along with a shoulder peak at 1574 cm^{-1} which is due to the interactions of EC's C=O group with the Li^+ nodes in the Li-NDC framework. Also, there were no noticeable shifts in EC's carbonyl bands at 1789 and 1768 cm^{-1} but the reduced absorption intensities indicate lower probability of EC's carbonyl interactions with the solvated Li^+ ions of the $LiClO_4$ salt. **Figure 23(b)** shows peak shift in the C-O- Li^+ stretching peak of Li-NDC from 1396 to 1391 cm^{-1} in LEC@Li-NDC along with the disapperance of C-O stretching peaks at 1379 cm^{-1} and 1341 cm^{-1} indicate the free Li^+ ion interactions with the oxygen atoms in the metal-oxide nodes of the frameworks. **Figure 23(c)** shows no noticeable peak shifts in EC's C-O-C stretching at 1146 cm^{-1} and 1058 cm^{-1} but observed a slight reduction in peak intensities indicating lower probability of EC's ether oxygens interactions with the solvated Li^+ ions. Further, **Figure 23(d)** shows the peak shift from 778 cm^{-1} to 770 cm^{-1} in the naphthalene ring bending peak which confirms the interactions of EC's carbonyl oxygen with the Li^+ metal nodes in the Li-NDC framework. The FTIR spectra of LEC@Li-NDC show no noticeable interactions between the EC molecules and the mobile Li^+ ions of the salt, while the mobile Li^+ ions bind to the oxygens of metal-oxide nodes of the frameworks. This suggests the lithium hopping over the framework edges as opposed to hopping through the porous channels via EC molecules. This is due to the largest pore volume observed in the Li-NDC MOF which does not favor the binding of free Li^+ ions and EC guest molecules.

Figure 23. The normalized FTIR spectra of LEC@Li-NDC, Li-NDC, and EC in the region (a) 1900-1500 cm^{-1}, (b) 1450-1300 cm^{-1}, (c) 1200-1000 cm^{-1}, and (d) 825-600 cm^{-1}

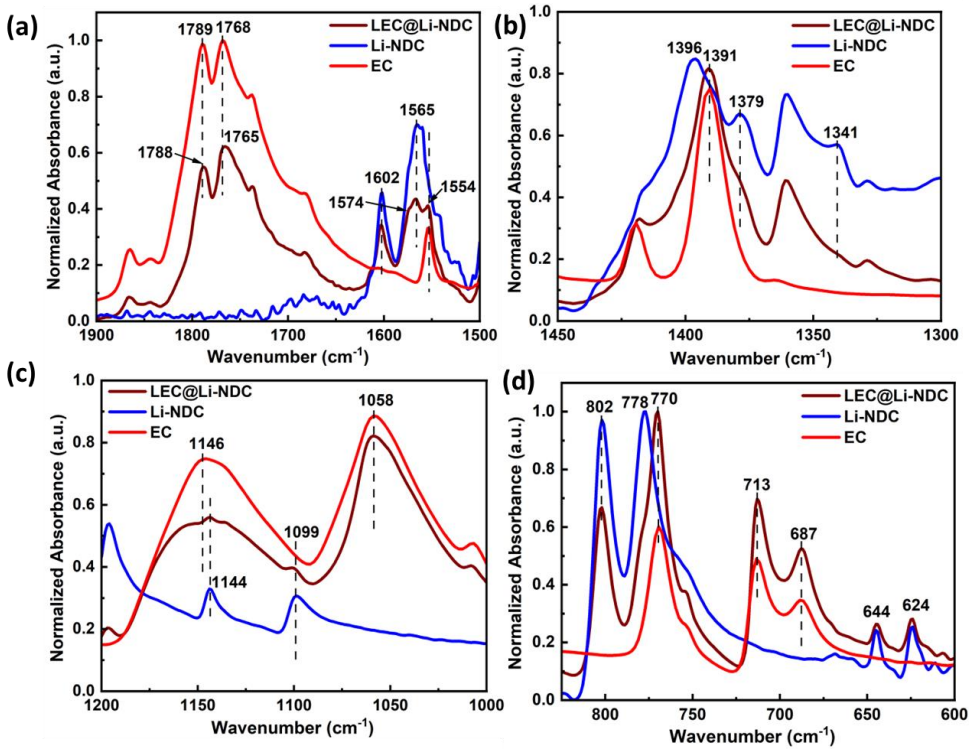

In **Figure 24(a**), the slight C=O peak shifts from 1789 and 1768 cm^{-1} in pure EC to 1797 and 1770 cm^{-1} in LEC@Li-BPDC possibly indicates the EC molecules solvated to Li-ions, i.e., the interactions of oxygen atoms of EC's carbonyl (C=O) with Li^+ ions of the lithium perchlorate salt.[222] There were no noticeable peak shifts in the Li-BPDC MOF's carbonyl at 1585 cm^{-1} indicating no major interactions of EC with the Li-BPDC frameworks. **Figure 24(b)** shows a slight shift in O-C- Li^+ peak from 1397 cm^{-1} in Li-BPDC to 1392 cm^{-1} indicating the EC interactions with the metal nodes of the Li-BPDC frameworks. The reduced absorption intensities of peaks at 1485, 1471 and 1554 cm^{-1} corresponds to the CH_2 scissoring and CH_2 bending of EC could be due to the EC's carbonyl group and ether oxygen bind to Li^+ metal nodes in the framework.[226,227] From **Figure 24(c**), the C-O peak shifts at 1158 cm^{-1} and 1067 cm^{-1} in LEC@Li-BPDC indicate further interaction between the ether oxygens of EC and Li^+

ions from $LiClO_4$ salt due to solvation, i.e., between the ether oxygens (C-O-C) with Li^+ ions of the salt.[222] In **Figure 24(d),** no changes were observed in Li-O stretching mode of Li-BPDC at 840 cm^{-1} and, also no shifts in the aromatic ring bending mode at 772 cm^{-1} indicating minimal interactions of mobile Li^+ ions with the framework metal oxide nodes. Further, the appearance of shoulder peak at 903 cm^{-1} to the EC's ring breathing mode at 891 cm^{-1} confirms the Li-ion solvation due to EC. Further, the shift in EC's ring bending stretch at 710 cm^{-1} to 715 cm^{-1} confirms the interactions of EC's ether oxygens with the free Li^+ ions of the salt. Additionally, the peak at 623 cm^{-1} belonging to one of the vibrational mode of ClO_4^- anion along with an additional shoulder peak at 636 cm^{-1} confirms the interactions of ClO_4^- anion with EC molecules.[224] Hence, the FTIR spectra of LEC@Li-BPDC confirms the EC's interations with $LiClO_4$ salt result in dissociation of the salt into Li^+ and ClO_4^- ions. These free Li^+ ions hop along the porous channels while interacting with the EC's carbonyl/ether oxygens. There is no presence of interactions of the free Li^+ ions with the framework functional sites. Therefore, the mobile Li^+ ions only move along the EC guest molecules through the porous channels in Li-BPDC which resulted in lower activation energy required for Li-ion conduction.

Figure 24. The normalized FTIR spectra of LEC@Li-BPDC, Li-BPDC, and EC in the region (a) 1900-1500 cm^{-1}, (b) 1500-1350 cm^{-1}, (c) 1200-1000 cm^{-1}, and (d) 925-600 cm^{-1}

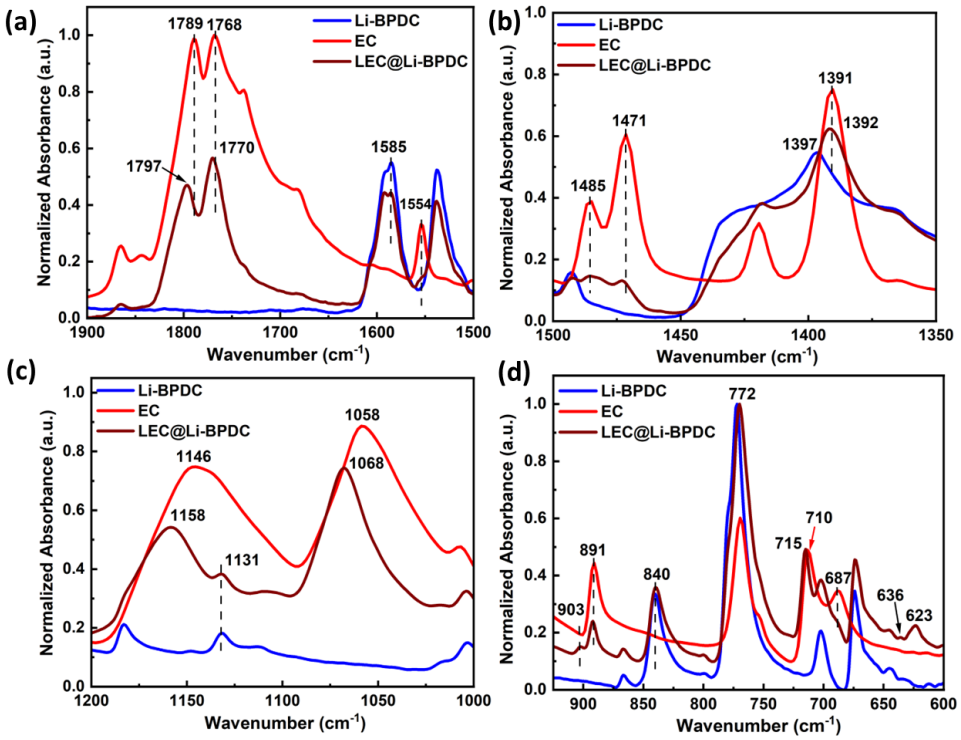

4.3.6 XPS and TGA measurements on LEC@Li-MOF electrolytes

XPS analysis was performed on the Li-MOFs and LEC@Li-MOF samples (prior to the EIS measurements) as shown in **Figures 25-27**. From the XPS survey spectra for each of the LEC@Li-MOF samples, a Cl 2p peak was observed which corresponds to the lithium perchlorate salt along with the O 1s, C1s, and Li 1s peaks of the Li-MOFs. From **Figure 25(b)**, the C 1s scan shows an additional C-O-C peak at 286.1 eV corresponding to the ether bonds in ethylene carbonate in LEC@Li-BDC.[228] Also, the peak at 290.8 eV belongs to the CO_3^{2-}ion from the carbonyl groups of EC.[229–231] Further, in the O 1s scan **Figure 25(d)**, there is an increased strength in the C=O peak with a slight peak shift of 0.4 eV and the C-O peak has a 1.4 eV peak shift corresponding to the carbonyl and ether oxygens from EC, respectively. Further, the Li 1s scan **Figure 25(c)**, shows an additional peak at 57.9 eV corresponds to the lithium from the

lithium perchlorate salt.[232,233] The Li 1s peak at 55.99 eV corresponds to the lithium oxides i.e., lithium coordinated to the BDC ligand.[232,234] **Figure 25(e)** shows the Cl 2p spectra for the Li-BDC soaked in LEC solution which exhibits $LiClO_4$ signals with $2p_{3/2}$ and $2p_{1/2}$ doublets at 208.9 eV and 210.2 eV.[233,235] The slight shoulder peak at 200.6 eV corresponds to the presence of some LiCl as a minor byproduct.[229,233] From previous studies, it was observed that the lithium metal reacts with $LiClO_4$ to generate LiCl and Li_2O.[229] A similar trend was observed in both the LEC@Li-NDC and LEC@Li-BPDC electrolytes. From **Figures 26(b) and 27(b)** additional C-O-C and C carbonyl peaks corresponding to the ether and carbonyl species of ethylene carbonate. **Figures 25(b), 26(b) and 27(b)** show the C1s scans in Li-MOF hosts, the C-C peaks and O-C=O peaks at ~284.8 eV and ~288.7 eV which indicate no noticeable peak shifts due to incorporation of the LEC electrolyte. **Figures 26(d) and 27(d)** show a similar increase in strength of C-O peak in the O 1s scans along with the additional $LiClO_4$ peaks in Li 1s spectra and the presence of doublets in Cl 2p spectra. Therefore, the XPS data confirms the presence of EC as well as the lithium perchlorate in the LEC@Li-MOF electrolytes.

Figure 25. (a) Comparison of XPS survey spectrum and binding energy spectra of Li-BDC MOF with LEC@Li-BDC for: (b) C 1s, (c) Li 1s, (d) O 1s; and (e) Cl 2p in LEC@Li-BDC MOF.

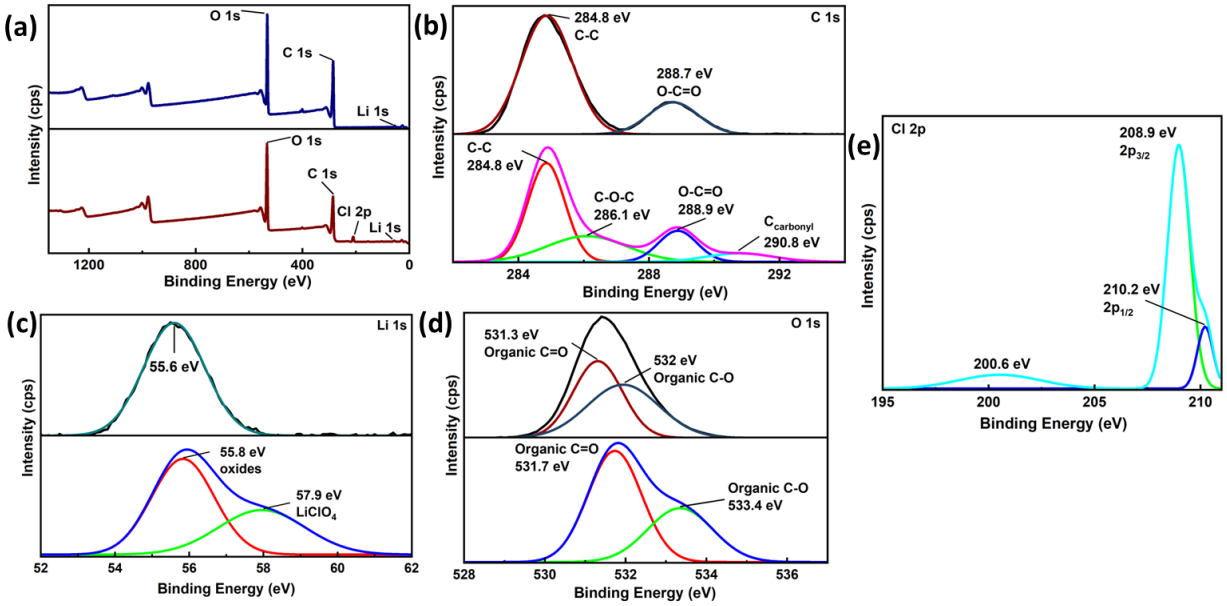

Figure 26. (a) Comparison of XPS survey spectrum and binding energy spectra of Li-NDC MOF with LEC@Li-NDC for: (b) C 1s, (c) Li 1s, (d) O 1s; and (e) Cl 2p in LEC@Li-NDC MOF.

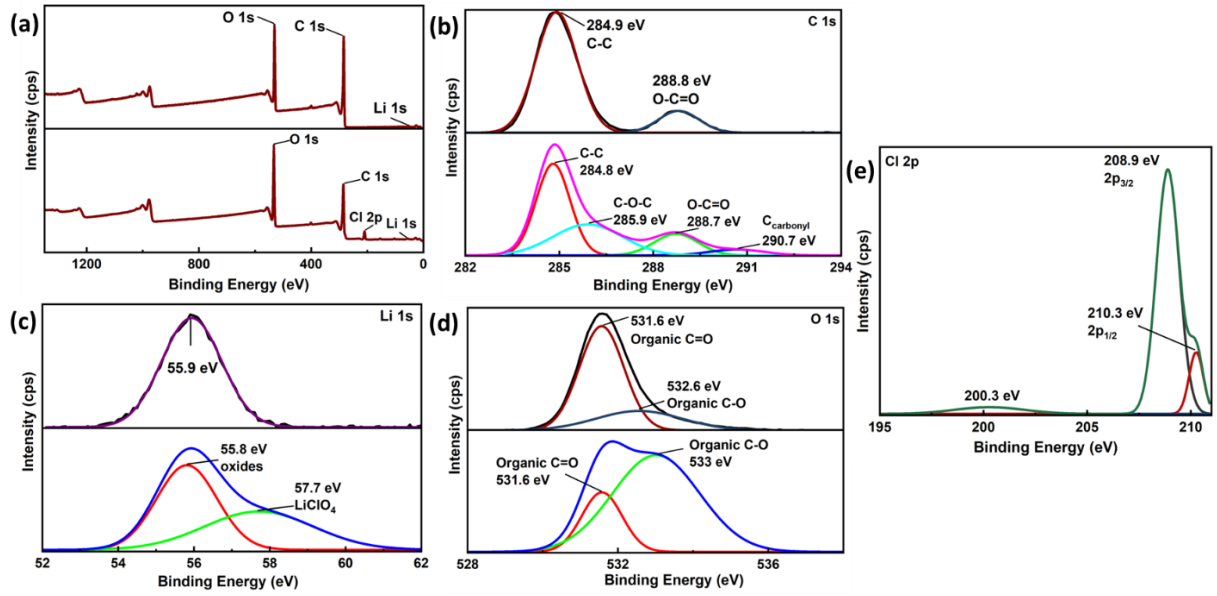

Figure 27. (a) Comparison of XPS survey spectrum and binding energy spectra of Li-BPDC MOF with LEC@Li-BPDC for: (b) C1s, (c) Li 1s, (d) O 1s; and (e) Cl 2p in LEC@Li-BPDC MOF.

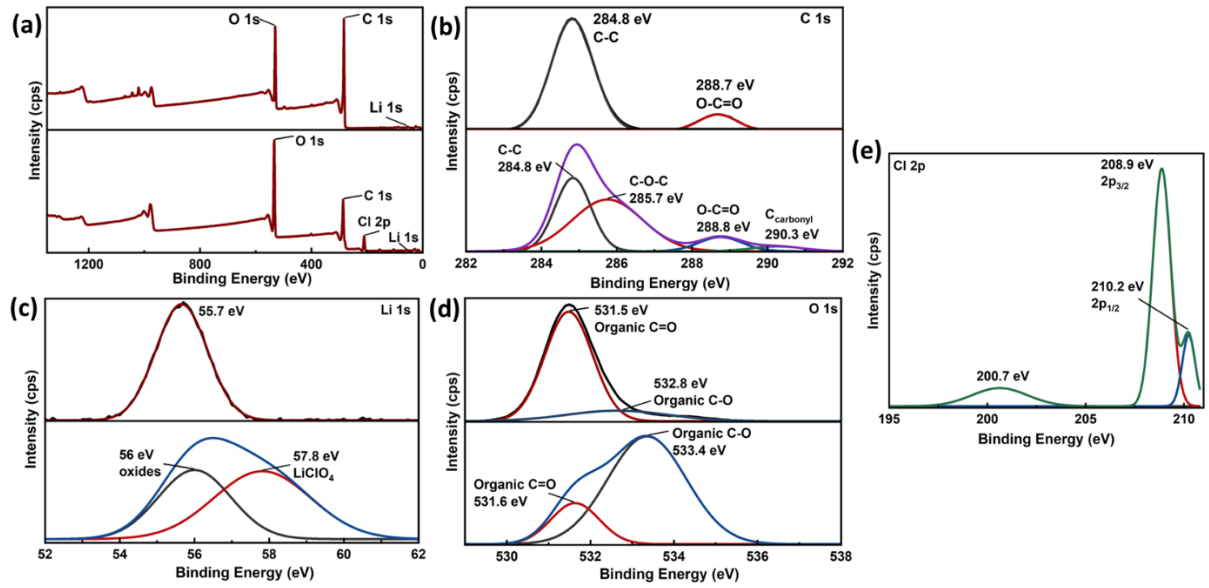

The thermal stability of LEC@Li-MOF electrolytes were studied using the TGA analysis as shown in **Figure 28**. Pure EC starts to degrade around 90 ℃ and completely decomposes before 150 ℃.[236] Addition of lithium perchlorate salt could reduce the decomposition temperature and lower the thermal stability of LEC.[237] Hence, in LEC@Li-BDC (**Figure 28(a)**), the initial weight loss of 11% occurs at 106 ℃ which corresponds to the encapsulated LEC electrolyte in the Li-BDC frameworks. A total weight loss of 62% was observed at 535 ℃ corresponding to the framework degradation which occurs at a slightly lower temperature than Li-BDC (551 ℃). Further, a weight loss of 9% occurs in the region 535 – 701 ℃ and a char of 20% which is similar to the Li-BDC frameworks. The initial degradation of LEC in the Li-MOF hosts starts in the 45-50 ℃ range and hence, the LEC@Li-MOF electrolytes are stable upto 50 ℃ without the loss of LEC in the frameworks. In the LEC@Li-NDC sample (**Figure 28(b)**), an initial weight loss of 19% occurs at 112 ℃ which corresponds to the encapsulated LEC

electrolyte in the Li-NDC frameworks, followed by framework degradation at 510 ℃ and a char of 15% was obtained. Similarly, in the LEC@Li-BPDC sample (**Figure 28(c)**), an initial weight loss of 52% at 129 ℃ was observed indicating a higher amount of LEC in the Li-BPDC frameworks, followed by framework degradation at 496 ℃ and a char of 5% was obtained. There was an increase in weight% of encapsulated LEC in the frameworks as the linker length increased from Li-BDC to Li-BPDC MOFs which could be a reason for increased ionic conductivity observed with linker length. TGA analysis shows that the LEC@Li-MOF electrolytes were stable upto 500 ℃ indicating no major structural changes due to the incorporation of the LEC electrolyte solution into the Li-MOFs.

Figure 28. TGA thermographs of (a) LEC@Li-BDC, (b) LEC@Li-NDC, and (c) LEC@Li-BPDC electrolytes.

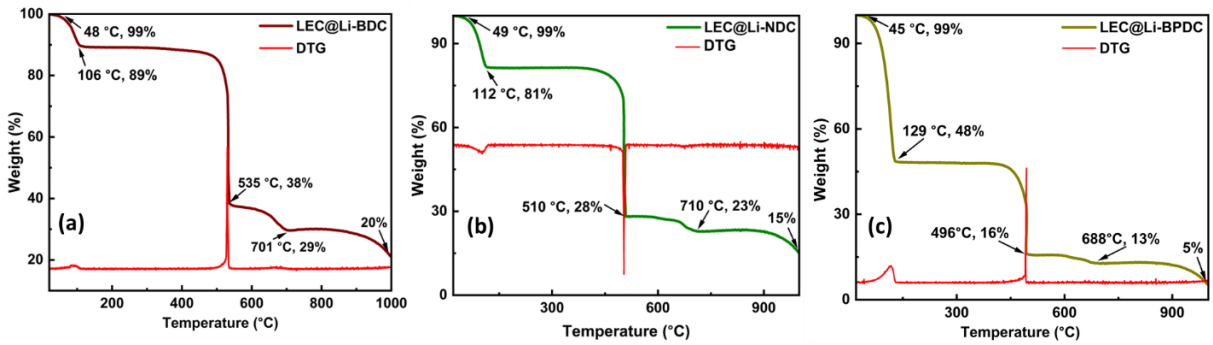

4.3.7 Discussion

In the prior research in MOF-based SSEs, Li-ion conduction involves complex interactions of the cations and anions in the porous frameworks. During the motion along the porous channels, the free carboxylic acid groups could exchange their acidic protons with lithium, or EC can partially solvate the lithium ions on the carboxylic acid groups, causing 'linker hopping'.[238] Another feasible mechanism is the lithium ion hopping from one bound EC molecule to another.[151,239] Recently, MIL53(Al)@LiCoD frameworks adopted an open-pore

conformation mechanism wherein the inserted Li-ions exhibited both free and bound states forming mutually communicating chains through the MOF nanochannels enabling both long-range charge transfer and thereby, macroscopic conductivity.[240] The ion transport in MIL53(Al)@LiCoD frameworks was a solid-like mechanism wherein the ion jumps over an energy barrier which is driven by electrostatic and elastic forces.[240,241] The free Li^+ ions were in the open-pore channels whereas the bound Li^+ were coordinated to structural defects and narrow pore channels. Further, the additional grain boundary resistance of these MIL53(Al)@LiCoD frameworks lead to high activation energies (0.92-0.98 eV).[240]

Due to absence of solvent molecules (i.e., lack of open-metal sites) in the Li-MOF frameworks confirmed from XRD, TGA and XPS analysis of Li-MOFs, the Li-MOF-based SSEs may follow a pore-filling Li-ion conduction mechanism in contrast to the MOF-based SSEs with anionic channels[242]. TGA and XPS analysis of LEC@Li-MOFs indicate that no structural modifications occur due to incorporation of LEC guests in Li-MOFs. A lower activation energy was observed for the highest ionic conductivity sample (LEC@Li-BPDC) indicating that the Li-ions easily move through the LEC@Li-BPDC electrolyte as lower energy is required for conduction through this solid electrolyte. From the TGA data of LEC@Li-MOF electrolytes, the increase in ionic conductivity could possibly be due to the increased loading of LEC electrolyte guest molecules in the pores due to the isoreticular framework expansion.[239] The FTIR analysis supports the Li-ion solvation due to EC molecules and, the possibility of Li-ion hopping via the encapsulated EC molecules and the framework functional sites in the porous Li-MOF channels. The pore filling Li-ion conduction mechanism is different for each of LEC@Li-MOF electrolytes due to the variation in pore volume and the different interactions of lithium salt with plasticizer and framework sites.

The FTIR data supports the Li-ion conduction in the LEC@Li-BDC (**Scheme 2(a)**), electrolyte by formation of two Li^+ bound states with framework metal oxide nodes and pore filled ECs, which create two bridging complexes Li_2O-Li^+-EC, and EC-Li^+-EC, respectively. The Li_2O-Li^+-EC bridging complex facilitates the Li hopping between unit cells in the crystal lattice while the EC-Li^+-EC bridging complex allows the Li-hopping via EC molecules in the porous channels. Since the Li-ions move as single ion bound state with no movement of counter anions, LEC@Li-BDC electrolyte could be an ideal candidate for a single-ion solid-state conductor. The high activation energy and low ionic conductivity observed is due to the over binding of Li^+ ions to the Li-BDC frameworks.

The largest pore volume observed in Li-NDC and the FTIR spectra of LEC@Li-NDC (**Scheme 2(b)**), supports the presence of Li^+ binding interactions with frameworks functional sites which suggests the Li^+ conduction along the framework and pore edges. Therefore, the Li^+ ions form Li^+ bound states with the framework's metal oxide nodes and carboxylate groups by forming two different bound state complexes [Li_2O-Li^+-OLi_2] and [COO-Li^+-OOC]. The weakly bound EC with the framework nodes minimizes the over-binding of Li-ions with the framework coordination sites and this could be a reason for slightly higher ionic conductivity observed in the LEC@Li-NDC electrolyte.

In LEC@Li-BPDC electrolyte (**Scheme 2(c)**), from the FTIR spectra, it is observed that the Li^+ ions favor binding to the plasticizer EC, over the framework functional sites which suggests a vehicular Li^+ ion conduction. In this vehicle process, EC acts as a carrier molecule for Li^+ ion diffusion through the porous channels. Further, from the vibronic stretching of LEC@Li-BPDC electrolyte, Li-ion conduction involves both ion-hopping and the solid-phase vehicle mechanism due to the minimal binding of Li-ions to the frameworks and favorable EC binding to

the framework segments. This decoupling of Li^+ ions from the hosts' framework segments favors both the ion hopping and vehicle mechanisms.[243,244] Thus, Li-ion conduction in LEC@Li-BPDC is via long-range continuous Li-ion hopping through the porous channels by the bridging EC molecules bound to frameworks' metal-nodes and pore filled Li^+ & ClO_4^- ions creating continuous chain of (Li_2O-EC-Li^+-EC-) and (-EC-Li^+-EC-ClO_4^-) bridging complexes. The Li^+ bound states create free volume for the free state Li^+ ions to hop along the porous channels which lowered the activation energy required for the ion transport in LEC@Li-BPDC electrolyte.

Scheme 2. Schematic representations of the proposed Li^+ ion conduction mechanisms in: (a) LEC@Li-BDC, (b) LEC@Li-NDC, and (c) LEC@Li-BPDC.

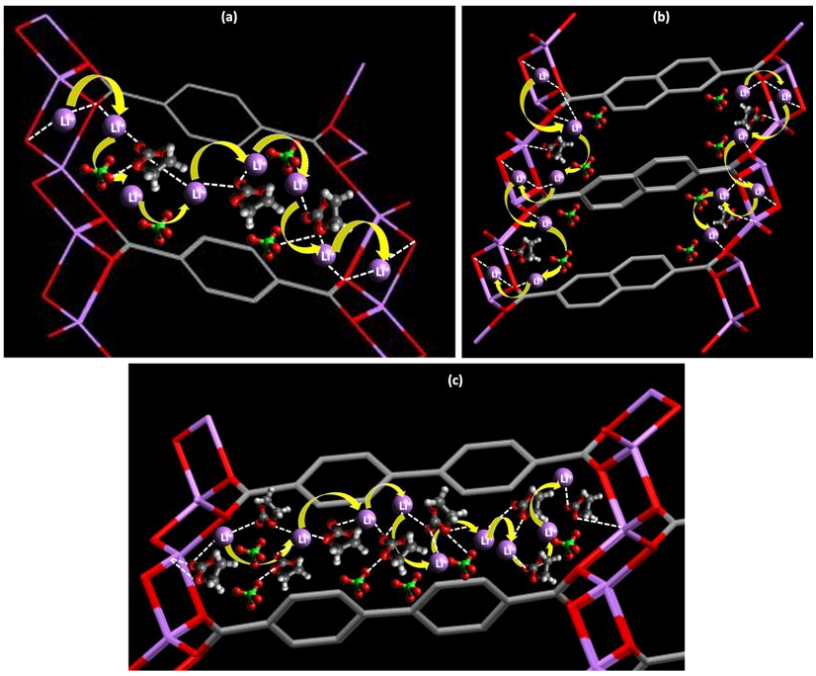

4.4 Conclusion

In summary, this study demonstrated the successful synthesis of isoreticular Li-MOFs with three carboxylate linkers (1,4-BDC; 2,6-NDC and 4,4'- BPDC) using the solvothermal synthesis. The synthesis method is a simple technique with reasonable control over the design of MOFs with the variation of linkers, easily reproducible and scalable to achieve higher yields.

XRD and HRTEM analysis shows that the resulting isoreticular Li-MOFs were self-assembled nanocrystals to form highly crystalline, porous microstructures with a similar monoclinic topology belonging to the space group *P2(1)/c*. The compositional and morphology analysis performed on these MOFs confirm the 3D porous microstructures match their respective unit formulae. The TGA profiles of the three Li-MOFs show that these microstructures possess excellent thermal stability until 500 °C. A bimodal pore distribution was observed in Li-MOFs which do not necessarily follow the framework expansion with respect to linker length but rather results in an optimal pore volume (in the order of Li-NDC<Li-BDC<Li-BPDC). The ionic conductivities of these isoreticular LEC@Li-MOF electrolytes were 1.7-6.7 x 10^{-5} S/cm at room temperature (in the order of Li-BDC<Li-NDC<Li-BPDC) with activation energies between 0.635-0.719 eV. Interestingly, the LEC@Li-BPDC electrolyte showed a lower activation energy (0.63 eV) and a high ionic conductivity (6.66 x 10^{-5} S/cm) than the Li-BDC and Li-NDC MOFs. The FTIR, XPS and TGA analysis on the LEC@Li-MOFs show the presence of encapsulated LEC electrolyte.

The ionic conductivities were comparable to the current state-of the art solid-polymer and MOF-based SSEs, but the rather high activation energies observed were due to the presence of free and bound states of Li^+ ions in the Li-ion transport process. Although, according to our initial hypothesis the isoreticular expansion did not affect the ionic conductivities at room temperature significantly but the reticular expansion and pore size of Li-MOFs affect the Li^+-ion conduction mechanisms. Further, we found that the Li-MOF based SSEs followed a 'pore-filling driven Li ion conduction' involving both free and bound states of Li^+ ions which move either via ion-hopping or both ion-hopping and vehicular mechanism, foregoing on the isoreticularity of each of the Li-MOFs. The pore-filled EC molecules allow the solvation of lithium salts and act

as Li^+ ion carriers along these porous Li-MOF channels. Herein, we have demonstrated the design and synthesis of isoreticular Li-MOFs as hosts for developing Li^+ diffusion pathways in these SSEs. The choice of organic ligands and the frameworks' porosity significantly impact the ionic conductivity. Thus, these Li-MOF-based SSEs show the importance of reticular design of MOFs to understand the ionic conduction and enable the development of next-generation solid-state Li-ion conductors.

CHAPTER V: DESIGN AND SYNTHESIS OF LITHIUM-TANNATE COORDINATION COMPLEX TO INVESTIGATE LITHIUM-ION CONDUCTION FOR TALI-BASED SOLID-STATE ELECTROLYTES

5.1 Introduction

The substitution of the most often used materials as solid-state electrolyte with more ecologically friendly ones is becoming increasingly important to solve circular economy concerns and the growing concern about environmental issues with battery e-waste, even though they may not always be as functionally successful. Therefore, in recent times researchers have focused on developing 'sustainable/green' LIBs from renewable sources. Natural polymers are alternatively substituting synthetic polymers as they are inexpensive, abundant in nature, and environmentally friendly.[9–11] Natural polymers such as cellulose, pectin, gelatin, and tannic acid have been demonstrated as electrodes, binders, separators, and electrolytic materials for the next generation LIBs.[10,13,110,245,246]

The natural polymers were integrated into synthetic polymer matrices like PEO, PVP, and PEG to enhance the ionic conductivities. For instance, a solid polymer electrolyte (SPE) of cellulose ether and PEO (TPEOCELL) along with the lithium salt $LiCF_3SO_3$.[247] The glass transition temperature (T_g) increased with the increase in the salt concentration which indicates a reduction in the polymer chain mobility. This can possibly be due to the crosslinking of ether oxygen and the cations in the salt. The ionic conductivities of TPEOCELL complexes were measured to be in the range of 10^{-7} S/cm^{-1} at room temperature and ~10^{-4} S/ cm^{-1} at 373 K. When temperatures were increased, higher salt concentrations showed maximum ionic conductivities, and this is due to increase in contribution of charge carriers towards conductivity at higher

temperatures. Interestingly, Arrhenius behavior of ion conductivity with temperature was observed which indicates that segmental motion is less prominent in the ion conduction.[247] Similarly, a composite gel-electrolyte was developed from polyvinylpyrrolidone (PVP) synthesized on lignin matrix. The PVP-lignin membrane was further dissolved in a liquid electrolyte solution to obtain better electrochemical properties. Addition of PVP to the lignin matrix increased its mechanical strength by 670% and the thermal decomposition temperature increased to 301 ℃. Due to the liquid electrolyte uptake of PVP-lignin, a high ionic conductivity of 2.52 x 10^{-3} S/cm and a capacity retention of 95.3% after 100 cycles was achieved.[248] Further, a quasi-solid polymer electrolyte was developed by entrapping polyethylene glycol (PEG) inside the networked cellulose (NC) wherein PEG remained as a liquid in the random and highly porous NC structure.[249] The hydrogen bonding interactions between the hydroxyl groups of NC chains and PEG might have caused the encapsulation of PEG in NC. Ionic conductivity in the order of 10^{-4} S/cm at room temperature was obtained at 12.8wt% NC and it was observed that conductivity reduced with increase in NC content in the PEG/$LiClO_4$ matrix.[249]

To improve the ionic conductivities in bio-polymer electrolytes, plasticizers and ionic liquids were used. For instance, lignin as an environmentally friendly gel electrolyte was fabricated using a liquid electrolyte (EC/DMC/EMC) and distilled water. The tensile strength of the lignin-based electrolyte (1.16 MPa) was higher than the pure lignin (0.85 MPa) and it also exhibited good thermal stability below 100 ℃. A high lithium-ion transference number of 0.85 was achieved due to the increase in number of lithium ions in the gel polymer electrolyte. The strong hydrogen bonding from the phenolic groups in lignin promoted the dissociation of anions of the lithium salt thereby increasing the number of charge carriers.[250] Similarly, a chitosan-based gel electrolyte was fabricated which consisted of ionic liquid as a plasticizer and lithium chloride salt to enhance the

ionic conductivity. Both adipic acid and acetic acid were used to disperse the chitosan. A maximum ionic conductivity of 4.6 x 10^{-3} S/cm was obtained from the film having adipic acid. It was observed that the ionic conductivity reduced with increase in LiCl concentration beyond an optimum value. This was due to the increase in viscosity of the gel as the salt concentration increases which results in clusters and ion-pair formation.[251]

As an alternative approach, succinonitrile (SN) was used as a plasticizer along with the lithium salt, $LiClO_4$, to improve the ionic conductivity of iota-carrageenan biopolymer electrolyte. SN improved the ionic conductivity of iota-carrageenan to 3.3 x 10^{-3} S/cm at room temperature and the inclusion of 0.5% $LiClO_4$ gave a high ionic conductivity of 3.57 x 10^{-4} S/cm.[252] Similarly, glycerol was used as a plasticizer in gelatin-based solid polymer electrolytes and the ionic conductivity changes with respect to different acetic acid quantities were observed. The room temperature ionic conductivity for 26.3wt% acetic acid was in the order 10^{-5} S/cm but when the temperature increased to 80 °C, the ionic conductivity increased to 3.6 x 10^{-4} S/cm. This was attributed to the thermal movement of polymeric chains and the greater dissociation of salts at high temperature. The increase in conductivity with acetic acid content is due to an increase in mobile charge carriers.[253]

Tannic acid (TA) is a natural polymer and a plant polyphenol containing abundant oxygen moieties such as quinone, polyphenol, and ketone groups. The five pyrogallol units and their catechol groups provide TA with multiple interaction sites accessible for hydrogen bonding and metal-ion coordination.[254,255] Tannic acid possesses excellent metal-binding abilities, and aqueous tannic acid solutions quickly precipitate with metal ions through complex formation.[256] Owing to these unique characteristics, TA has been significantly used as a surface coating and an adhesive, providing radical-scavenging, antimicrobial and antifouling properties to the

surfaces.[257–260] Recently, our group has introduced a novel aqueous-based synthesis method to make iron-tannate (Fe(III)-TA) coordination polymer frameworks and demonstrate its amphoteric properties to use as sorbents for heavy metals remediation and removing both cations and anions from water resources.[261] These Fe(III)-TA CPFs possessed robust structural frameworks as they are built from a polytopic ligand (tannic acid) and metal nodes, along with a porous hierarchical coordination geometry similar to MOFs.[261]

Additional functionalities can be easily imparted by modifying the phenolic groups of TA, and hence TA-based materials, being renewable and naturally abundant, have the prospects of being incorporated into the all-solid-state LIBs.[110,262] For instance, the hydrophilicity of the commercial polypropylene (PP) membrane was enhanced using TA coating on it. The contact angle of water on the TA-PP separator membrane reduced to ~72^0 from 120^0 (on the PP separator). Hence, the liquid electrolyte could thoroughly wet the surface of the TA-PP membrane, which in turn caused an increase in ionic conductivity and the electrochemical performance of the TA-PP separator.[111] Similarly, when TA coated PP separator was used in the Li-O_2 batteries, it was observed that the discharged product decomposed more efficiently due to the scavenged superoxide radicals and also improved the cycling stability.[112] Further, PP separators modified with a thin TA-polyethyleneimine (PEI) coating improved the wettability and lithium-ion migration. It was shown that the TA/PEI layer promotes the ion pair dissociation and allows lithium ions to migrate through the separator. An ionic conductivity of 0.95 mS/cm and lithium-ion transference number of 0.44 was achieved.[110] TA was further explored as a plasticizer and cross-linking agent in a solid polymer electrolyte. The addition of methacrylated TA to PEGMA (poly(ethylene glycol) methyl ether methacrylate) matrix gave a tensile strength of 2.1073 MPa and an ionic conductivity of 1.6 x 10^{-5} S/cm whereas, the addition of polyethylene

glycol grafted TA to PEGMA enhanced the ionic conductivity (5.6×10^{-5} S/cm) due to an increase in chain mobility.[119] Furthermore, the lithium-ion storage capacity of TA was studied by varying the two salt concentrations (LiTFSI and $LiPF_6$), and precipitation of TA was observed with $LiPF_6$. Also, it was illustrated that TA as an anode material in a half-cell system gave a reversible capacity of 306.83 $mAhg^{-1}$ with a coulombic efficiency of 93.4%.[115] Due to its peculiar properties and easy availability, TA has much scope to be further explored as a solid-state ionic conductor and incorporated into the LIBs.

This study involves the development of bio-based solid-state electrolytes from a novel lithium-tannate (TALi) coordination complex. These TALi complexes were synthesized using a simple room-temperature synthesis by coordination between tannic acid and lithium-ions resulting in the microstructures of a bio-based lithium-tannate coordination complex. The parameters like precursor concentrations, amount of solvent and reaction times were optimized microstructures of TALi complex. Their chemical composition, thermal stability, and morphology were investigated. The lithium-ion conduction through these TALi-based SSEs was studied using the electrochemical impedance spectroscopy and the microstructure's functional group interactions with the lithium salt and the plasticizer were studied from the FTIR spectroscopy measurements.

5.2 Results and Discussion of TALi complex

5.2.1 Synthesis and Characterization of TALi

This project introduces an environmentally friendly room temperature synthesis to make a supramolecular coordination complex by lithiating a natural polyphenol, tannic acid. These supramolecular coordination complexes are commonly obtained by mixing metal and ligand precursors which spontaneously form metal-ligand bonds to produce a single thermodynamically

preferred product. The metal centers in these finite coordination complexes undergo self-assembly with ligands containing multiple binding sites.[263] The preparation method augments the principles of green chemistry, avoiding the use of toxic chemicals and high temperatures. **Scheme 3** depicts the chemistry of synthesis. The synthesis involved dropwise addition of lithium hydroxide solution into tannic acid solution at a rate of 1mL/min under continuous stirring, which yielded a dark-violet precipitate which gradually turned to dark green upon complete addition of lithium hydroxide solution. The gradual color change from initial light-yellow precursor solution to dark violet and eventually dark green suspension indicates the rapid complex formation.

Scheme 3. Synthesis scheme for the preparation of TALi complex.

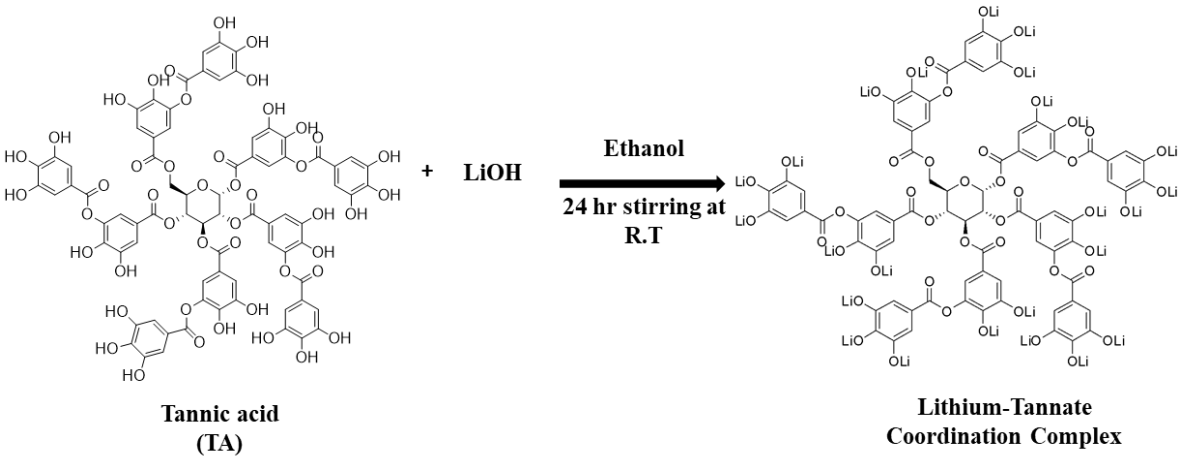

UV-visible analysis was performed on the TALi suspension just after the complete addition of TALi, after one hour and on the purified nanoparticles after 24 hours of redispersal in ethanol (**Figure 29a**). The UV-visible spectra of TA exhibits two characteristic peaks at 219 nm and 277 nm attributed to the π-π^* in aromatic ring and n- π^* transitions, respectively (**Figure 29(a)**).[105,264] The red-peak shifts to 239 nm and 326 nm in TALi are indicative of the potential coordination bonding between the hydroxyl groups of tannic acid and lithium ion.[18,261]

The chemical functionality analyzed by FT-IR (**Figure 29(b)**) exhibits tannic acid's hydroxyl groups' stretching around 3600-3000 cm^{-1} with a strong, wide band centered around 3362 cm^{-1}. In addition, the strong absorption peaks at 1705 cm^{-1} correspond to the carbonyl (C=O) stretching of ester groups in the glucose unit, respectively. The peaks at 1610 cm^{-1} and 1533 cm^{-1} in tannic acid corresponds to the aromatic C=C stretching. The strong peaks at 1310 cm^{-1} and 1191 cm^{-1} belongs to the O-H bending and C-O stretching of phenolic groups in tannic acid (**Figure 29(b,c)**). The peak at 1444 cm^{-1} corresponds to the C-C deformation vibrations in the phenolic groups. The peaks at 871 cm^{-1} and 754 cm^{-1} correspond to the aromatic C-H bending and C=C distortion vibrations in benzene rings, respectively.[265] In TALi, the stretching at 3371 cm^{-1} corresponds to the residual hydroxyl groups in tannic acid. On the other hand, lithium complexation to tannic acid led to drastic peak shift in ester carbonyl stretching from 1705 cm^{-1} in tannic acid to a shoulder peak at 1689 cm^{-1} in TALi-complex. This shift indicates the strong coordination nature of lithium-ion with the carbonyls in pyrogallol units.[261] Further, the aromatic C=C stretching peaks shifted from 1610 cm^{-1}, and 1533 cm^{-1} in tannic acid to 1582 cm^{-1}, and 1502 cm^{-1} in TALi-complex (**Figure 29(b,c)**). The O-H bending peak at 1310 cm^{-1} in tannic acid has become a broad band split into two peaks at 1372 cm^{-1} and 1333 cm^{-1} which indicates the lithium-ion coordination with the hydroxyl groups of tannic acid.[115] A phenolic C-O peak shift was observed from 1191 cm^{-1} to 1205 cm^{-1} along with the reduction in its intensity. The C-O stretching of ester groups in tannic acid shifted from 1083 cm^{-1} and 1023 cm^{-1} to 1093 cm^{-1} and 1052 cm^{-1} suggesting lithium interactions with the ester carbonyls. These peak shifts suggest that both hydroxyl and ester groups in tannic acid could be involved in coordination with lithium-ions.[266,267] Herein, the lithium ion being a Lewis acid could be forming a stable coordination complex with the oxygen donor atoms (hard base) of the carbonyl group as well as

the hydroxyl atoms.[78] However, the coordination geometry is uncertain at this point. From an electrostatic standpoint, tetrahedral coordination is most stable and common among divalent non-transition metal ion complexes.[266] According to HSAB theory, hard acids with LUMO orbitals of high energy prefer to coordinate with hard bases with HOMO orbitals of lower energy. In general, hard acids/electrophiles have a small size with high positive charge and hard bases/nucleophiles have small size with high electronegativity like in carboxylate moieties.[268]

Figure 29. (a) UV-visible absorption spectra taken at different time intervals, (b) and (c) FTIR spectra of TALi complex and tannic acid (TA).

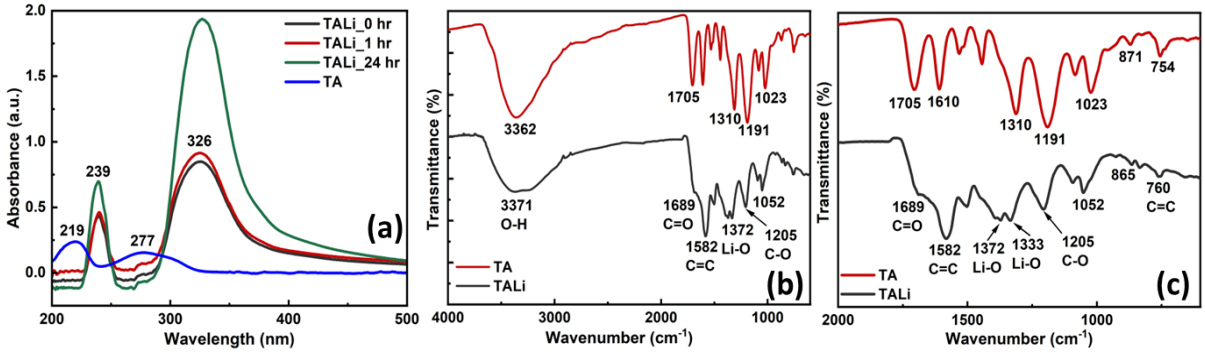

The XPS elemental survey supports the presence of the elements C, O and Li with the empirical formula of $Li_{18}C_{76}H_{34}O_{46}.8H_2O$. The binding energy spectra for each element are shown in **Figure 31(b–d),** supporting their oxidation states.The C 1s scan shows peaks at 284.95 eV, 286.35, and 288.62 eV, which is assigned to the sp^2 bonded carbon of the C phenyl and ester groups of the tannic acid.[195] In the O 1s scan depicted two characteristic peaks at 531.48 eV and 533 eV which correspond to the C=O and C-O bonds of the ester carbonyl[194] and phenol groups in tannic acid. A full-width half maximum (FWHM) value of 4.49 eV for O 1s supports the oxygen chemical bonding state of O^{-2} which corresponds to the phenolate form.[261] Further, Li 1s gave an FWHM of 3.64 eV for TALi supporting the oxidation state of +1 (Li^+) along with its binding energy peak at ~55.5 eV.[198]

The thermal stability of TALi complex was obtained by performing TGA (**Figure 30(e)**) which shows small weight loss in the 25-150 ˚C, corresponding to absorbed water. According to studies, the five outer-layer gallic acid units in tannic acid decompose via decarboxylation between 230 and 400 °C.[269] From **Figure 30(e)**, significant weight loss occurs in the region 200-400 ˚C, which indiactive of the breaking down the complex (27.12 wt%) with a pronounced peak at 246 ˚C confirming the initial degradation temperature of tannic acid.[270] The second pronounced peak from DTG curve is at a higher temperature in TALi (390 ˚C) when compared to tannic acid (306 ˚C).[265] The presence of doublet peaks in DTG may be due to simultaneous decomposition of different gallic acid units from different branches.[269] From **Figure 30(e)**, the second major weight loss corresponding to the degradation of tannic acid occurs after 400 ˚C with a peak at 661 ˚C. Finally, after 700 °C the residual 28 wt% includes lithium oxide and char. The TALi coordination complex although showed similar degradation curve until 300 ˚C they show better thermal stability in the region 300-800 ˚C, when compared to tannic acid.[265]

Figure 30(f) shows pH-dependent surface properties of TALi colloidal solution in anhydrous ethanol. The TALi colloidal solution is very stable in the basic pH range and the magnitude of zeta potential increases with increasing pH, exhibiting a high zeta potential value of -63.1 mV at pH 9. These particles have negative zeta potentials at most pH levels which indicate that the particles have negatively charged surfaces, except a positive zeta-potential of 1.4 mV was observed at pH 1.33. The pH above 7 (basic pH) promotes the deprotonation of hydroxyl groups which contribute to negative charged surfaces. The surface charge stabilization at pH above 7 maybe due to the electrostatic repulsions between the negatively charged particle surfaces which promotes the colloidal stability. The isoelectric point of the TALi colloidal solution is at a pH of 1.8, where the zeta-potential value is zero and the colloidal solution is very

unstable promoting aggregation. Also, the TALi colloidal solution exhibits a positively charged particle surface at pH below 1.8.

Figure 30. (a) The XPS survey spectrum, and the binding energy spectra of: (b) C 1s and (c) O 1s (d) Li 1s of TALi, (e) thermogravimetric analysis, and (f) zeta potential versus pH of TALi colloids in ethanol.

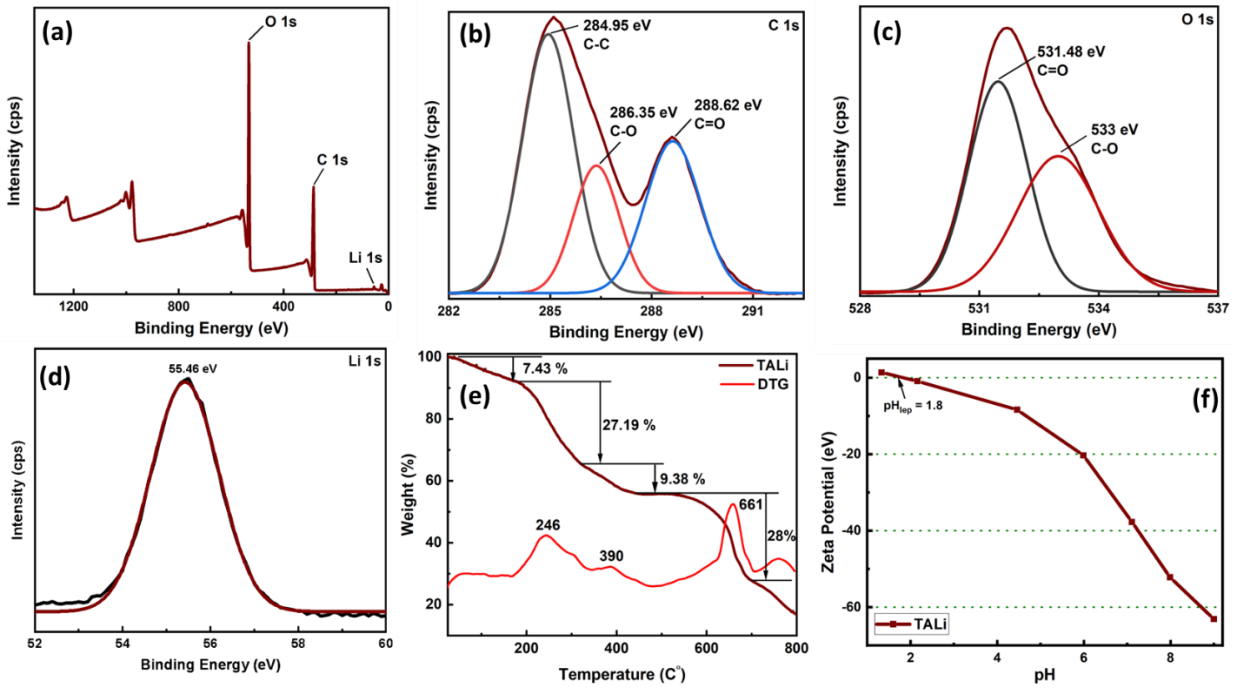

Morphologies of TALi microstructures were studied using the SEM and TEM images depicted in **Figure 31**. The SEM images (**Figure 31(a,b)**) of the particles show irregular spherical nanoparticles with aggregated clusters. They have a variety of size distribution ranging from 40-100 nm with a mean particle diameter of 63 nm (**Figure 31(c)**) with void spaces (30-70 nm) between the aggregated clusters. The TEM images (**Figure 31(d-f)**) of these aggregated clusters show irregular large cavities (> 100 nm). The pore-size distribution and pore volume obtained from the N_2 adsorption-desorption isotherms (**Figure 31(g-i)**) using the Brunauer−Emmett−Teller Surface analysis. A Type IV(a) isotherm was obtained, which is typical for mesoporous (2-50 nm) materials.[208] The average BJH adsorption pore width and BJH

desorption pore volume were 15 nm and 0.016 cm^3/g with a very low BET surface area of 4.76 m^2/g. Capillary condensation is accompanied by hysteresis in Type IV(a) isotherms. These H3 hysteresis loops could be due to the presence of non-rigid aggregates and macroporous pore networks, which are not completely filled with pore condensate.[271] The low BET surface area and low pore volume indicate few or no available mesopore volumes in the TALi complexes.

Figure 31. (a) & (b) SEM images, (c) size distribution curves for the aggregated particles, (d-f) TEM images, (g) N_2 BET Isotherms, (h) BJH Adsorption dV/dw pore volume distribution plot, and (i) NLDFT Cumulative pore volume distribution plot for TALi.

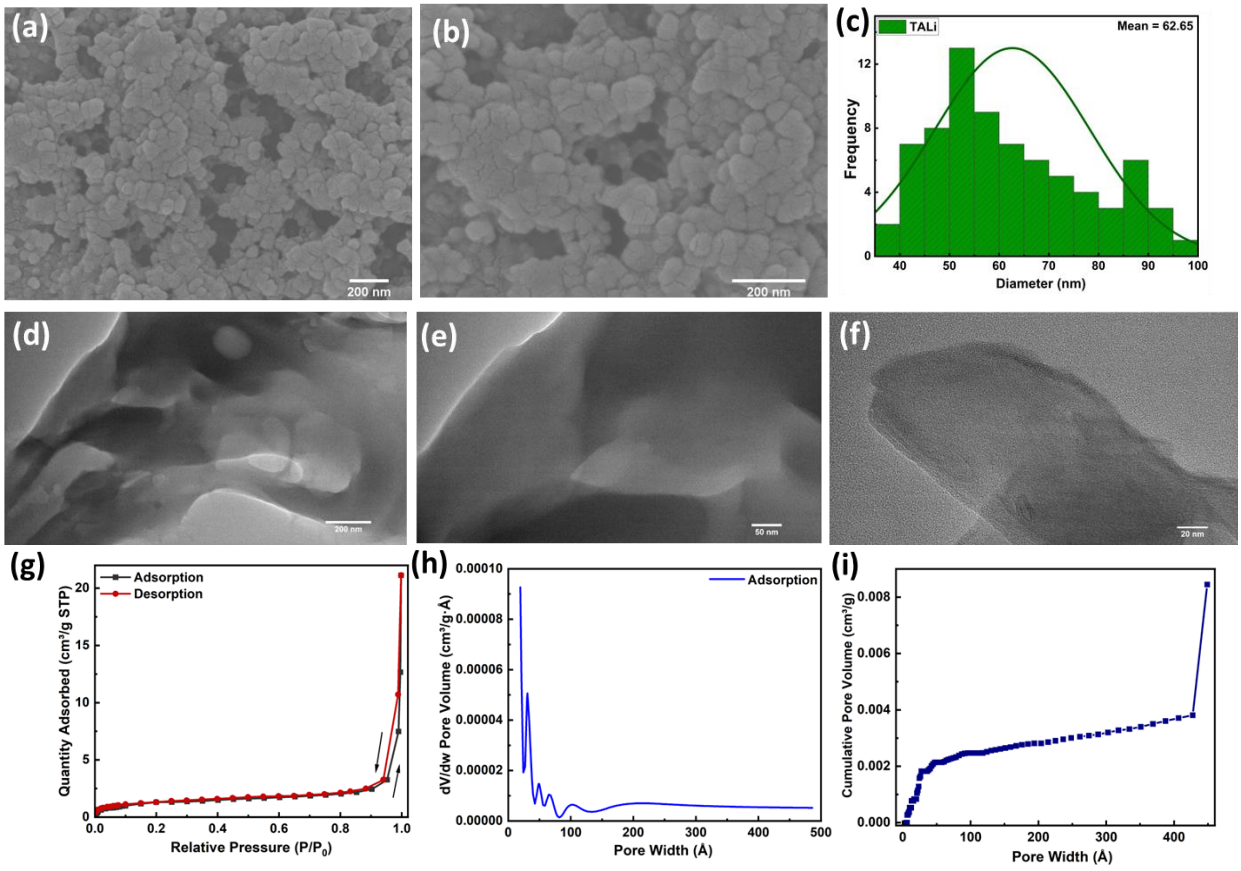

5.2.2 Ionic Conductivity studies

To evaluate the ionic conductivity, TALi@LEC powders were pressed into dense pellets, having varying lithium perchlorate weight percentages. These pellets were analyzed on the EIS

as shown in **Figure 32(a)** and the overall ionic conductivity (σ) of these pellets obtained at 25 °C is illustrated in **Table 4**, after normalizing with the thickness of each pellet (0.74 – 1 mm). The ionic conductivity was calculated using the bulk resistance (R_b) value taken at the intercept of the semicircle in the higher frequency area on the real impedance axis, from the Nyquist plots.[272] The Nyquist plots for all the TALi@LEC pellets consist of a semicircle in the high-frequency area and an inclined line towards the lower frequencies. The semicircle in the high frequency region appears due to a combination of bulk resistance and bulk capacitance (R/C) in solid electrolytes, and the inclined line represents the electrical double layer at the electrolyte/electrode interface. As seen in **Figure 32(a)**, with increasing lithium salt concentrations, the complex plot first shift to the left i.e., towards lower bulk resistances, and then they shift to the right with the optimum composition of lithium perchlorate of 10wt%. In addition, the radius of semicircle, and hence the charge-transfer resistance decreases with increasing salt concentrations upto 10wt%. The ionic conductivities of the pellets were in the range of 10^{-5} S/cm with the highest ionic conductivity of 8.77 x 10^{-5} S/cm for TALi@LEC with 10wt% $LiClO_4$. The increase in ionic conductivity with addition of $LiClO_4$ is due to the increased mobile ions provided by the salt upto 10wt% (**Figure 32(b)**). The decrease in ionic conductivity could be due to the less solvation with the plasticizer, leading to stay as the salt lowering the ion-pair dissociation.[273] Initially, a control sample was investigated having TALi and the plasticizer, ethylene carbonate (EC) only (TALi-EC) which displayed open-circuit behavior indicating no ionic conductivity from the Nyquist plots. The plasticizer EC was used to increase the salt dissociation and facilitating the intramolecular interactions with the complex, thereby providing a Li^+ ion conduction pathway.[274]

Figure 32(c) shows the ln $\sigma_{(T)}$ versus reciprocal temperature plot for the TALi@LEC pellet and the experimental data obeys the Arrhenius theory wherein the ionic conductivity increases linearly with temperature. The loss of EC was observed during the temperature-dependent ionic conductivity measurements as the TALi@LEC pellet turns semi-solid in nature with increase in temperature beyond 55 °C. The activation energy calculated from the Arrhenius fit for the TALi@LEC electrolyte is 0.855±0.146 eV for the salt concentration of 5wt%. Activation energy indicates the energy required to move ions through complex and, the activation energies higher than 0.15 eV are observed typically in lithium-salt systems with organic solvents.[275] Herein, an activation energy of 0.855±0.146 eV indicates strong interactions between the TALi complex and the ions within the TALi@LEC electrolyte. The ionic conductivity values in the TALi@LEC electrolyte are comparable to bio-based solid polymer electrolytes such as cellulose[276,277], chitosan[278,279], agar[280] based electrolytes but the activation energy obtained for TALi@LEC was higher. Cyclic voltammetry (CV) was performed on the TALi@LEC pellet applying the potential range of −1 to +1 at different scan rates as shown in **Figure 32(d)**. In a CV experiment, a potential waveform is supplied to the electrode, and the resulting current is measured. The resulting current is related to the capacitance of the electrode-electrolyte interface, and the faradaic and non-faradaic processes which occur at the electrode surface. The capacitance behavior of CV is explained using the electrical double-layer theory, which describes the behavior of charged particles at electrode-electrolyte interface. When the potential is applied to the electrode, charged particles in the electrolyte are attracted to the opposite electrode surface, forming a layer of charge known as the electrical double layer (EDL). This layer of charge acts as a capacitor storing charge and affects the current measured during the CV experiment. EDL capacitance behavior is observed at the solid-electrolyte/electrode

interface, and this can affect the performance of solid-state batteries especially their charge-discharge rates. The CV curves in **Figure 32(d)** show that as scan rate increased the shape of the curve changed from a slightly rectangular shape to leaf like shape which is due to some internal resistance during the measurement.[281] The curves did not depict any noticeable peaks that explained that the system did not undergo any oxidation/reduction reaction. It can also be observed that the charge-discharge of both EDL capacitors occurs reversibly at the electrode/solid-electrolyte interface.

Figure 32. (a) Nyquist plots for TALi@LEC pellet containing 2wt% - 20wt% $LiClO_4$, (b) composition dependence of ln σ versus $LiClO_4$ concentration, (c) Arrhenius plot of TALi@LEC electrolyte (included an image of the pellet) and its activation energy for lithium-ion conduction, (d) CV plot of TALi@LEC pellet at various scan rates from 5-100 mV/s.

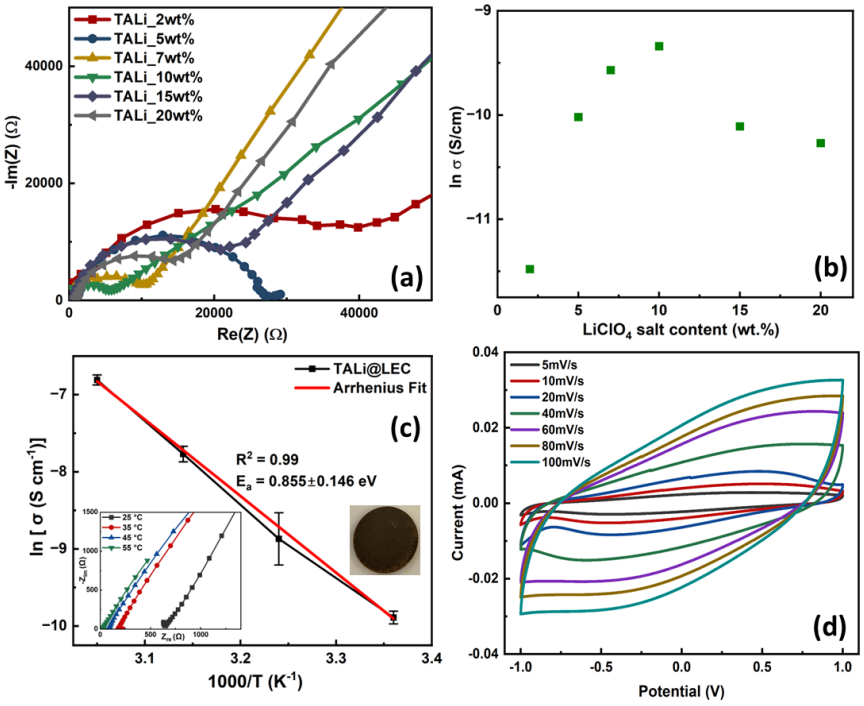

Table 4. Ionic conductivities of TALi@LEC with different formulations of LEC.

Sample Name	Ionic Conductivity at 25 °C (S/cm)	ln σ
TALi_EC_2wt% $LiClO_4$	1.03 x 10^{-5}	-11.48
TALi_EC_5wt%$LiClO_4$ (TALi@LEC)	4.45 x 10^{-5}	-10.02
TALi _EC_7wt% $LiClO_4$	6.99 x 10^{-5}	-9.57
TALi _EC_10wt% $LiClO_4$	8.77 x 10^{-5}	-9.34
TALi _EC_15wt% $LiClO_4$	4.08 x 10^{-5}	-10.11
TALi _EC_20wt% $LiClO_4$	3.44 x 10^{-5}	-10.27

5.2.3 FTIR Spectroscopy Measurements

In order to understand the mechanism of Li-ion conduction in the TALi@LEC electrolytes, FTIR spectroscopy, which can reveal the interactions between functional groups, was performed on TALi@LEC, TALi and EC samples, respectively. The major peaks for EC at 1789 cm^{-1}, 1768 cm^{-1}, 1554 cm^{-1}, 1146 cm^{-1}, and 1058 cm^{-1} are assigned to C=O stretching (carbonate ester), CH_2 bending vibrations and C-O stretching vibrations, respectively.[221,222] EC's ring breathing mode occurs at 891 cm^{-1} and EC's ring bending mode occurs at 715 cm^{-1}.[224] Interactions with other molecules profoundly influence the C=O stretching vibrations.[222]

In **Figure 33(a)**, C=O stretching peaks at 1789 cm^{-1} and 1768 cm^{-1} in EC shifted to higher wavenumbers at 1797 cm^{-1} and 1771 cm^{-1}. This indicates the interactions of EC's carbonyl groups with the Li^+ ions due to solvation. Some of the Li ions may also interact with the oxygen atoms in the EC ring along with the interactions through the EC's C=O groups.[224] Further, a reduced absorption intensity at 1689 cm^{-1} of C=O stretching along with a peak shift to 1680 cm^{-1} in TALi@LEC indicate the interactions of EC's carbonyl groups with the Li^+ ions of the TALi complex. Additionally, the reduction in aromatic C=C stretching at 1582 cm^{-1} in TALi

and the CH_2 bending vibrations in EC at 1554 cm^{-1} further confirm the interactions of lithium ions coordinated to the ester groups in tannic acid with the EC's carbonyl oxygens. **Figure 33(b)** shows reduction in intensities of C-O-Li^+ absorption peaks along with slight peak shifts to 1365 and 1326 cm^{-1}, which also corresponds to the strong binding interactions of EC's carbonyl groups with the Li^+ in the TALi complex. From **Figure 33(c)**, the EC's C-O peak shifts at 1146 cm^{-1} and 1058 cm^{-1} to 1158 cm^{-1} and 1068 cm^{-1} in TALi@LEC correspond to the interactions between the ether oxygens of EC and Li^+ ions from $LiClO_4$ salt due to solvation.[222] In **Figure 33(d)**, there was a reduced absorption peak of EC's ring breathing mode at 891 cm^{-1} and the shift in EC's ring bending mode at 710 to 715 cm^{-1} along with the intensity reduction of the secondary band at 687 cm^{-1} confirm the free Li^+-binding to EC's ether oxygens. The aromatic C=C bending mode in TALi complex at 760 cm^{-1} reduced to a shoulder peak with a slight shift to 752 cm^{-1} in TALi@LEC, corresponding to the interactions of the free Li^+ of $LiClO_4$ salt with the residual phenolic oxygens and ester carbonyl groups of TALi complex. Further, the reduced absorption of the aromatic C-H bending modes of TALi at 865 and 834 cm^{-1} are also indicative of mobile Li^+ ions interacting with the oxygens of the TALi complex. The FTIR spectra of TALi@LEC show strong binding between the EC carbonyl groups and the lithium ions in the TALi complex. Additionally, strong interactions between the EC molecules and the $LiClO_4$ salt result in dissociation of the salt into Li^+ and ClO_4^- ions. These mobile Li^+ ions binds to both EC and the TALi complex. The presence of EC increases the Li-ion solvation facilitating the movement of lithium ions along ether oxygens in EC in the TALi@LEC electrolytes. Hence, the FTIR peak shifts indicate that the most probable mechanism (**Scheme 4**) for Li^+ ions transport in the TALi@LEC electrolytes is via the Li interacting with the EC's ether oxygens. While EC acting as a vehicle to carry Li^+ ions, the strong interaction of Li^+ ions with TALi's oxygen functional

sites could hinder the movement of Li^+ ions, thereby contributing to the lower ionic conductivities in ~10^{-5} S/cm and a high activation energy (~ 0.855 eV) observed for TALi@LEC electrolyte. However, for a definitive confirmation on the Li+ transfer mechanism, in-depth investigation is needed.

Figure 33. The FTIR spectra of TALi@LEC, TALi@EC, TALi, and EC in the region (a) 1900-1500 cm^{-1}, (b) 1450-1200 cm^{-1}, (c) 1200-1000 cm^{-1}, and (d) 925-650 cm^{-1}.

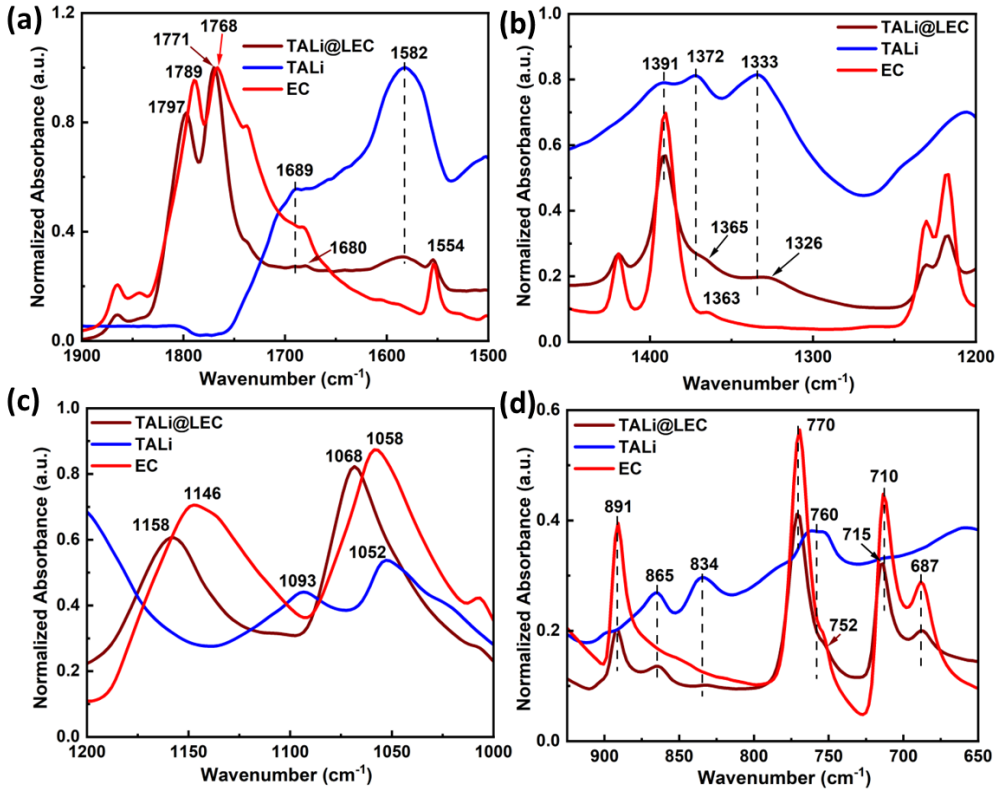

5.3 Conclusion

In summary, this study demonstrated the successful synthesis of bio-based TALi-complex. An environmentally friendly cost-effective synthesis method was used to make these porous lithium-tannate coordination complex (TALi), which showed reproducibility and scalability to achieve higher yields, using an aqueous synthesis method. The UV-visible and FTIR spectroscopy analysis confirm the formation of a stable coordination complex of lithium-

ions with the polytopic ligand, tannic acid, through its phenolic hydroxyl groups and the carbonyl groups. The compositional and morphological analysis confirm the formation of the lithium-tannate coordination network having an empirical formula, [$Li_{18}C_{76}H_{34}O_{46}.8H_2O$]. TALi complex possesses better thermal stability than TA and these particles are very stable in the basic pH range. The ionic conductivities of the TALi@LEC electrolytes were in the range of 10^{-5} S/cm with activation energy of 0.855±0.146 eV (5wt% $LiClO_4$) with a high ionic conductivity of ~ 9 x 10^{-5} S/cm for the increase in salt concentration to 10 wt% $LiClO_4$. Further the FTIR spectroscopy analysis on the TALi@LEC electrolyte shows that the probable Li^+ transfer is via the ether oxygens of EC bound to the TALi. Nonetheless, this work may offer a guide to prepare novel phenolate based lithium-tannate complexes to use as a bio-based solid-state electrolyte material for applications in lithium-ion batteries.

CHAPTER VI: DESIGN AND SYNTHESIS OF LITHIUM-TANNATE-SILSESQUIOXANE MICROSTRUCTURES TO INVESTIGATE LITHIUM-ION CONDUCTION FOR TALI-SSQ-BASED SOLID-STATE ELECTROLYTES

6.1 Introduction

There has been a significant interest over the recent years in designing new polymer electrolytes based on organic-inorganic hybrid nanocomposites because these systems provide improved conductivity compared to the purely organic macromolecules doped with inorganic salts that are typically used as solid electrolytes in batteries.[282] Hybrids can be created by: (1) interpenetrating organic polyelectrolytes and inorganic silica doped with suitable lithium salts[283], or (2) copolymerization of organo-alkoxysilane precursor, which can be turned to lithium conductors after neutralization with LiOH.[284] These organic-inorganic hybrid materials are also lightweight and lead to high energy densities.

A sol-gel approach is the most common path to make organic-inorganic hybrid nanomaterials in which organic-inorganic copolymers serve as hosts for lithium ions due to the presence of ion-dissolving units.[285] Owing to their intriguing properties like strong thermal and electrochemical stability and ease of processing, silica-based inorganic-organic hybrids have also drawn much attention as polymer matrices for solid-polymer electrolytes.[285,286] Several studies have described the applications of chemically modified siloxanes, namely ormolytes[287], polysiloxanes[288], polyoctahedral silsesquioxanes[91], and polysilsesquioxanes[284,288–290] as solid-state electrolytes for lithium-ion batteries. Silsesquioxanes having the chemical formula $[RSiO_{1.5}]_n$ are fascinating nanostructured hybrid materials as they exhibit great thermal stability,

high dimensional stability, and high ionic conductivities when incorporated as solid-electrolyte matrices.[91,289,291]

Silicon-based organic-inorganic hybrid materials have three main sub-categories namely, organo-silica, organically modified silica or ormosils, and silsesquioxanes (SSQs). Organo-silica has the empirical formula R_n-SiO_2, ormosils have the empirical formula of $(R\text{-}Si_2O_3\text{-}SiO_2)_n$, and the SSQs have the empirical formula of $(RSiO_{1.5})_n$, where R stands for organic linkers like methyl, ethyl, phenyl, etc. The silsesquioxanes are characterized by silicon to oxygen ratio of 1:1.5, where 'sil' refers to silicon, 'sesqui' means 'one and a half', and 'oxane' refers to oxygen.[292] Further, the SSQs can be sub-divided into polyhedral oligomeric silsesquioxanes (POSS), polysilesquioxanes (PSQs), and bridged polysilsesquioxanes (BPSQs). POSS or cubic T_8 silsesquioxanes have crystalline, cage-like silica-core structures and organic functional groups. These POSS units introduced to ionic liquids and inorganic salts hinder the crystallization of host polymer and have applications as SSEs.[92] The PSQs are produced via sol-gel synthesis of organotrialkoxy silanes and have been demonstrated to be used as hybrid polymer electrolytes in LIBs.[289] BPSQs have organic fragments attached to more than two trialkoxy silyl groups and they have better thermal properties than PSQs owing to the tightly packed SSQ core structures.[292]

Stöber sol-gel is the foundation for synthesizing silicon-based organic-inorganic hybrids involving either acid/base catalyzed hydrolysis of orthosilicates followed by the condensation to produce silica sols in an alcoholic solution.[293] A typical synthesis involves hydrolysis and condensation of tetraethoxy silane to create a Si-O-Si network. These silica sols can be collected prior to gel formation as silica particles. Further, post functionalization of the silica-sol with organoalkoxy chlorosilane produces surface-functionalized silica nanoparticles. Further, the

synthesis of ormosils involves base-catalyzed hydrolysis and co-condensation of organoalkoxysilane and TEOS. This approach does not give control over size range of particles and the organic ligand content is less than 20%.[292] The organic ligand content can be increased to >90% using the modified stober method, which involving the 'direct hydrolysis and condensation' of organoalkoxysilane monomer in aqueous solvents. PSQs or BPSQs can be synthesized using the modified stöber sol-gel method where the monomers are dissolved, and polymerization is initiated in the presence of a weak base typically in ethanolic solution.[292] This base-catalyzed sol-gel approach is a versatile method to design three dimensional SSQ hybrid nanomaterials.

Hybrid organic-inorganic polymeric networks can be obtained by metallo-organic precursors (such as silica or titanium) and natural polymers such as polysaccharides, derivatives of vegetable oils and cellulose materials.[282] These natural polymers contain hydroxy groups that could interact with the in-situ produced metal-oxo polymers.[282] Similarly, tannic acid's hydroxyl groups provide suitable sites for metal coordination as demonstrated in Chapter 5 to make the lithium-tannate coordination complex. Previous reports have demonstrated the tannic acid-silica hybrid nanoparticles for heavy metal adsorption[294] and catalytic activity[295]. Recently, our group has demonstrated nanoporous tannic acid-nanoparticles to create dielectric nanomaterials, wherein a silsesquioxane core was introduced via a sol-gel polymerization method.[296]

In this study, a silsesquioxane network was introduced into the lithiated tannic acid complex to produce microstructures of TALi-SSQ using a sol-gel approach wherein residual hydroxy functional groups of tannic acid were functionalized with 3-aminopropyl trimethoxy silane. The introduction of the silica network is advantageous for: (1) introducing the porosity[294–296] into the lithiated tannic acid , (2) the incorporation of the silsesquioxane matrix enhances the

amorphous nature (3) the silsesquioxane nanocages ($RSiO_{1.5}$) have reactive functional groups at cage corners which are available for surface bonding[92], and (4) silica cages can entrap plasticizers[91] and also increase the thermal stability of the final material as silsesquioxanes possess higher glass transition temperature. Hence, this study involves the development of solid-state electrolytes from the novel lithium-tannate silsesquioxane (TALi-SSQ) microstructures, hoping to achieve higher ionic conductivity compared to TALi complexes, at room temperatures. The parameters like silane precursor concentrations, amount of the base, and reaction times were optimized to obtain the porous TALi-SSQ microstructures. Their chemical composition, thermal stability, and morphology were investigated. The lithium-ion conduction of TALi-SSQ-based solid-state electrolytes was studied using electrochemical impedance spectroscopy. The lithium-ion interactions with the microstructures and the plasticizer were deduced using FTIR spectroscopy analysis.

6.2 Results and Discussion of TALi-SSQ microstructures

6.2.1 Synthesis and Characterization of TALi-SSQ microstructures

In this work, lithiation followed by base-catalyzed sol-gel process[297,298] was used to synthesize the lithium-tannate silsesquioxane (TALi-SSQ) microstructures. In a typical synthesis process, first tannic acid was randomly lithiated using lithium hydroxide to make TALi complex, which was further reacted with 3-aminopropyl trimethoxy silane in the presence of ammonium hydroxide as a base. [105]**Scheme 5** depicts the chemistry of producing TALi-SSQ microstructures. These TALi-SSQ microstructures have a silsesquioxane core structure of lithiated-tannic acid upon the sol-gel polymerization.[297,298] The effect of the base concentration and the amount of 3-APT on the formation of microstructures was also studied. The morphology, thermal stability, and particle's chemical compositions of TALi-SSQ microstructures prepared in this manner were

evaluated. The pellets of solid-state electrolytes from TALi-SSQ microstructures were fabricated by mixing with the lithium salt and EC and evaluate the electrochemical properties of these biodegradable silica-based organic-inorganic hybrid nanomaterials and compared with the properties of biodegradable natural polymers such as cellulose, lignin, pectin, and gelatin.[12,13,299,300]

Scheme 4. Synthesis schematic of lithium-tannate silsesquioxane (TALi-SSQ) microstructures.

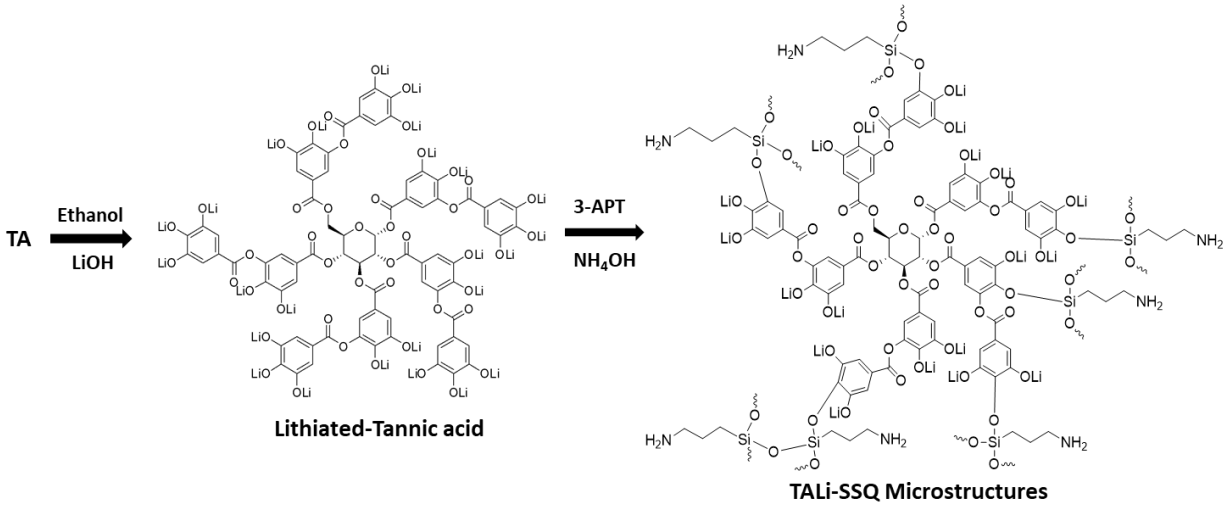

TALi-SSQ microstructures were collected after washing multiple times with anhydrous ethanol to remove the unreacted precursors and dried under air. The powder was re-dispersed in ethanol. UV-visible spectral traces for the microstructures prepared at different base concentrations are depicted in **Figure 34(c)**. Tannic acid exhibits a strong UV absorption with two characteristic absorption bands at 219 nm and 277 nm, attributed to the π-π^* and n- π^* transitions respectively (**Figure 34(c)**).[105,264] For the TALi-SSQ microstructures prepared with a base volume of 0.25mL NH_4OH, a red-shift was observed from 219 nm to 240 nm along with a less pronounced peak at 277 nm when compared to tannic acid. An additional absorption peak at 330 nm is an indicative of the lithiation as well as the functionalization of pyrogallol hydroxyl

groups with the silane precursor.[297] Similar absorption bands at 240 nm and 355 nm were observed in TALi-SSQ microstructures prepared at the base amount of 0.5 mL and the peak at 277 nm seems to have disappeared. For the microstructures prepared at the base amount of 1mL, a more pronounced peak at 226 nm was observed when compared to tannic acid's peak at 219 nm along with a small shoulder peak at 277 nm and an additional peak at 330nm.

The FTIR analysis was performed on the dried powder of TALi-SSQ microstructures prepared at three different base concentrations and silane precursor (3-APT) concentrations and are depicted in **Figures 34(a) and 34(b)**. The strong, broad peak at ~3350 cm^{-1} in all the TALi-SSQ microstructures correspond to the residual hydroxyl groups in the tannic acid. The peak at ~2940 cm^{-1} corresponds to C-H stretching of alkyl groups of the silane precursor.[294] The characteristic bands for Si-O-C (1096-1085 cm^{-1}) confirm that the silsesquioxane cores were successfully incorporated into the tannic acid structure. Further from **Figure 34(b)**, a gradual increase in peak intensity at 1085 cm^{-1} with increase in silane precursor possibly indicates the more incorporation of silane units. The huge reduction in peak intensity and peak shift from 1705 cm^{-1} to 1689 cm^{-1} assigned to C=O stretching is due to the insertion of lithium ions in the tannic acid framework.[115,194] The strong peaks observed at 1582 cm^{-1} and 1498 cm^{-1} along in all the TALi-SSQ microstructures correspond to the aromatic C=C stretching similar to TALi complex. The O-H bending and phenolic C-O stretching peaks in tannic acid at 1309 cm^{-1} shifted to 1341-1371 cm^{-1} in the TALi-SSQ microstructures indicating the lithium-ions coordinated to the hydroxyl groups of tannic acid. Further from **Figure 34(b)**, a reduction in peak intensity at 1341-1371 cm^{-1} and 1200 cm^{-1} with increase in silane precursor possibly indicates the lower incorporation of lithium ions at the phenolic hydroxyl groups of tannic acid. From **Figure 34(a)**,

there was no noticeable variation in the peaks with change in the base contents in the TALi-SSQ microstructures.

Figure 34. (a)-(b) FTIR spectra of TALi-SSQ microstructures prepared at different 3-APT content, and NH_4OH content respectively, and (c) UV-Visible spectra of TALi-SSQ microstructures with variation in NH_4OH content.

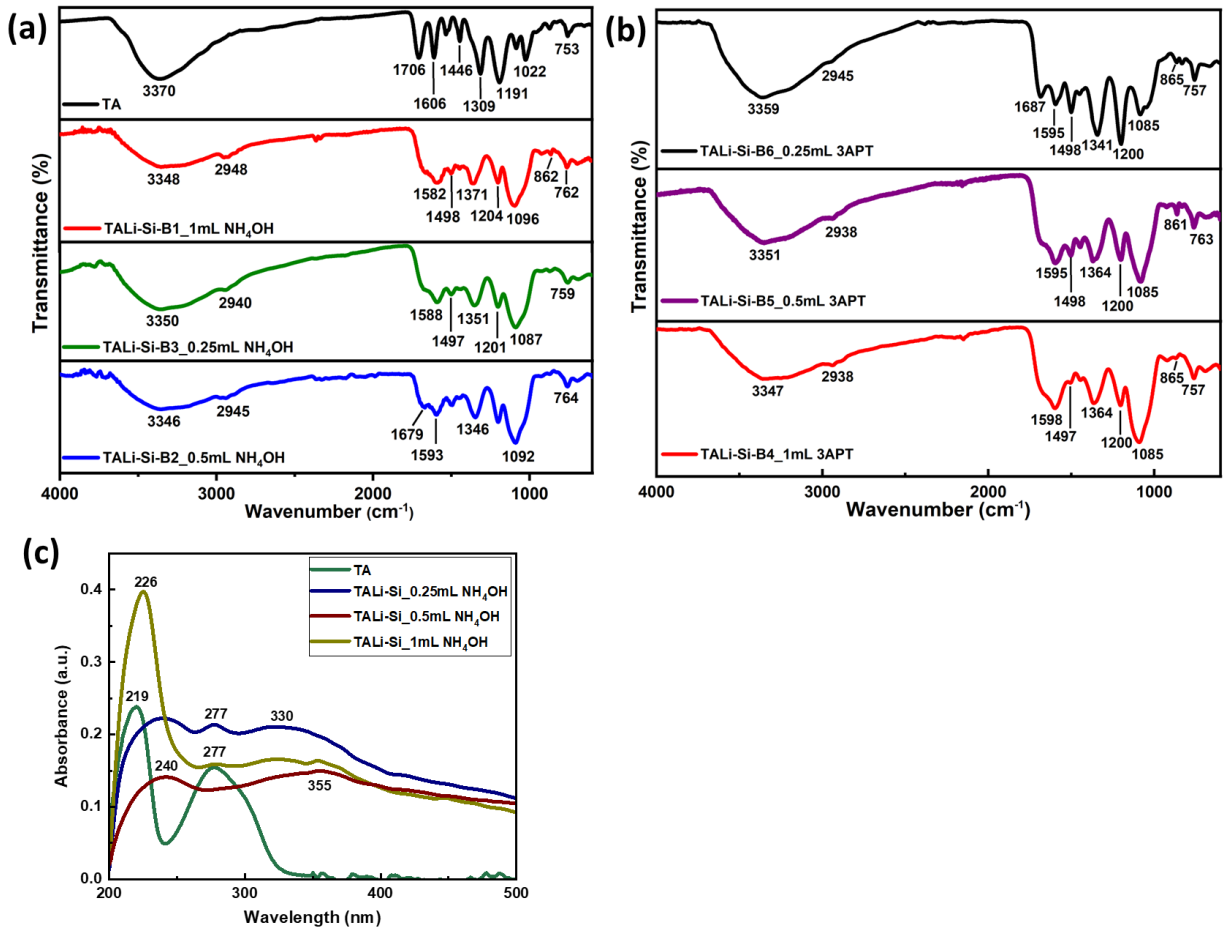

The influence of the amounts of the base and the silane precursor on the morphology and size distribution of TALi-SSQ microstructures was visualized using SEM and are depicted in **Figure 35**. While keeping the 3-APT volume (2mL) constant, at all three different base amounts (1 mL, 0.5 mL, and 0.25 mL), there were no significant changes in particle morphologies and particles sizes were ranged between 50-300 nm with the average size between 110-170 nm

(**Figures 35(g-i)**)**.** However, the microstructures with the lowest base concentration showed the presence of some hollow particles as marked in **Figure 35(c).** Similarly, with respect to three different volumes of 3-APT precursor, at the base volume of 1mL, there were no significant changes in morphologies, but the particle size range reduced to between 50-120 nm with the average size between 59-68 nm (**Figures 35(j)-(l)**)**.** The mean particle size of the TALi-Si-B1 to TALi-Si-B3 microstructures increased almost twice as much when compared to TALi-Si-B4 to TALi-Si-B6 microstructures, i.e., the particle size increases with incorporation of more silsesquioxane cores into the TALi network. The TEM images of these microstructures (**Figure 36**) show presence of large void spaces between the aggregated nanoparticles and the darker regions in these microstructures indicate the presence of dense silsesquioxane cores.[301]

Figure 35. (a)-(f) are SEM images of as-synthesized TALi-SSQ microstructures with varying compositions of 3-APT and NH_4OH, (g)-(l) are size distribution curves for the aggregated particles corresponding to SEM images (a)-(f), respectively.

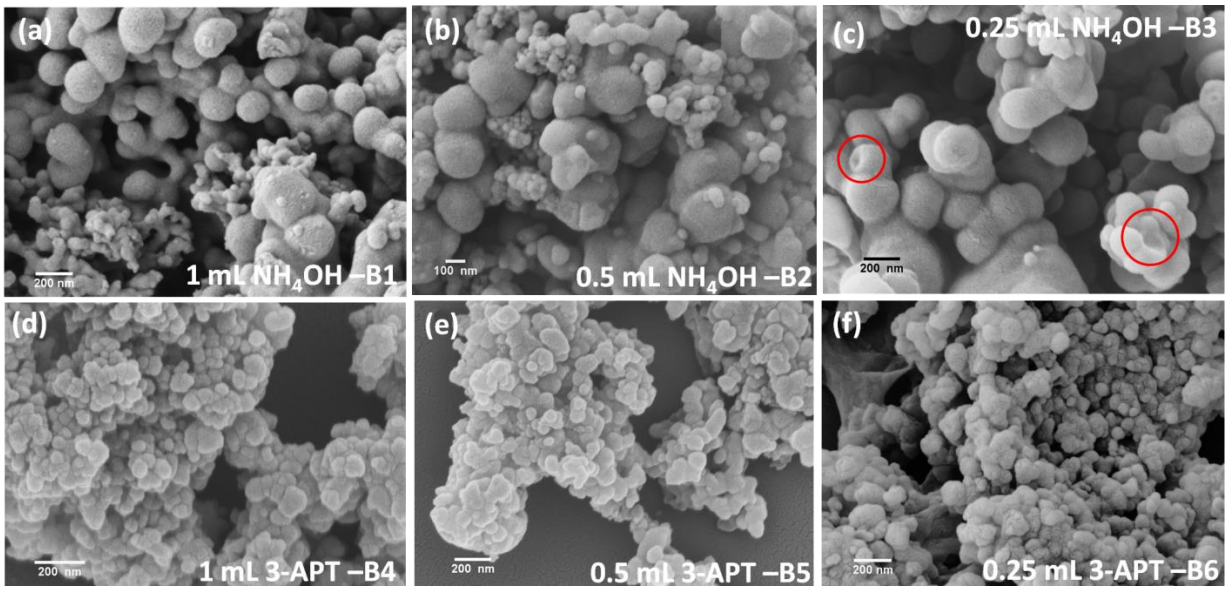

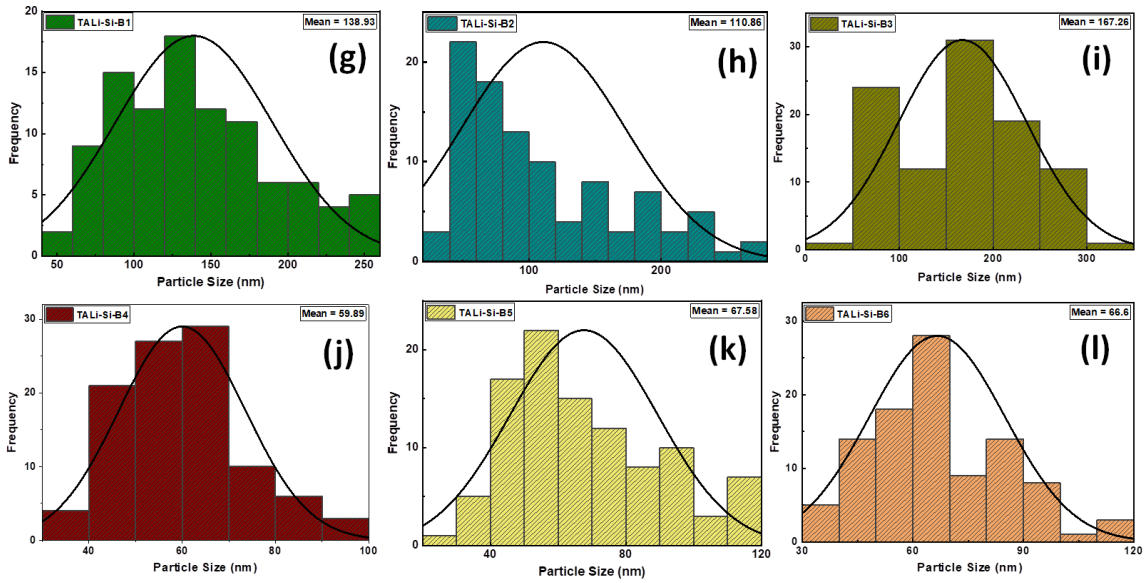

Figure 36. (a-d) TEM images of TALi-Si-B1 microstructures.

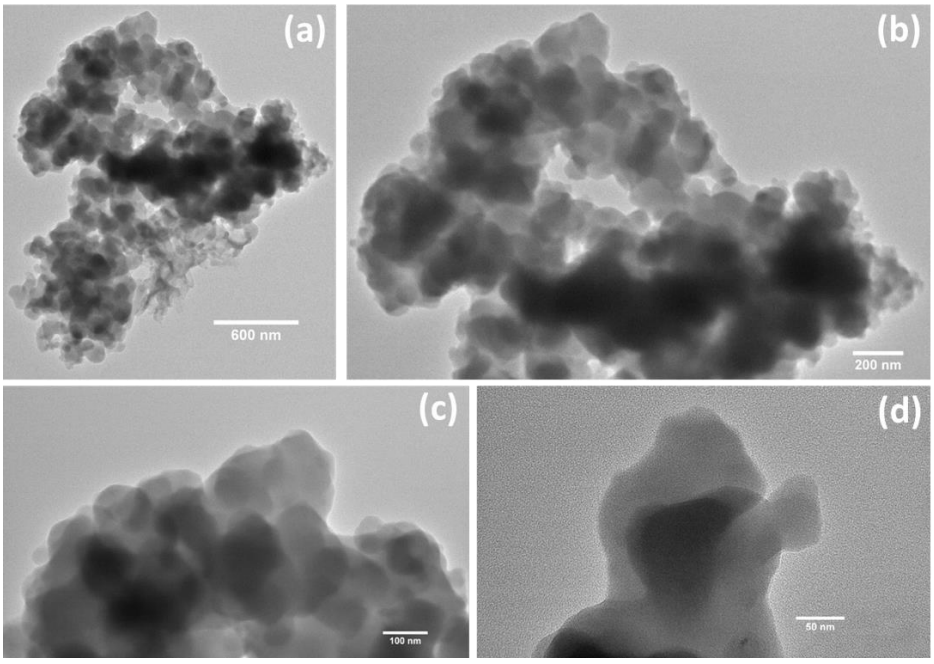

Dynamic light-scattering (DLS studies) and zeta potential studies were performed on these microstructures in anhydrous ethanol solution, which gave a polydispersity index (PDI) in the range of 0.4-0.7, indicating that the particle size distribution is broad and exhibits high aggregation in these systems when re-dispersed in anhydrous ethanol solutions. A lower poly dispersity index (PDI) of 0.06 and hydrodynamic diameter of 561 nm were observed for TALi-

SSQ microstructures prepared with 0.25mL 3-APT amount, which indicates the presence of smaller aggregates when compared with the other TALi-SSQ microstructures. The hydrodynamic diameters of the TALi-SSQ microstructures prepared at varying base and silane precursors were in the range of 560-1126 nm as mentioned in **Table 5**. The zeta-potential studies were performed on as-synthesized TALi-SSQ microstructures after re-dispersing them in anhydrous ethanol. The zeta potential values were mostly below -30 mV showing that the suspensions of these microstructures are unstable, and their low zeta-potentials are indicative of aggregation as there is less force to prevent these particles from coming together. A higher zeta potential of -41 mV was observed in TALi-SSQ microstructures prepared from 0.25mL base concentration (TALi-Si-B3) which is a more stable suspension when compared with the other TALi-SSQ microstructures.

Table 5. DLS size measurements and zeta potential values of TALi-SSQ microstructures.

Sample Name	3-APT (mL)/ NH_4OH (mL)	PDI	Hydrodynamic diameter (nm)	Zeta potential (mV)
TALi-Si-B1	2/1	0.6	1068	-26
TALi-Si-B2	2/0.5	0.6	814	-27
TALi-Si-B3	2/0.25	0.7	867	-41
TALi-Si-B4	1/1	0.4	855	-21
TALi-Si-B5	0.5/1	0.6	1126	-28
TALi-Si-B6	0.25/1	0.06	561	-29

To use these microstructures as biodegradable solid-state electrolytes, understanding the thermal stability is crucial and hence, thermogravimetric analysis (TGA) was performed. The TALi-SSQ microstructures prepared with 2mL 3-APT possessed similar thermal degradation profiles. Their maximum weight loss was observed in the temperature range of 250-350 °C which corresponds to the decomposition of tannic acid, as observed in TALi-complex (**Figure**

37(a)). This implies that variation in the base concentration does not affect the thermal stability in these TALi-Si-B1 to TALi-Si-B3 microstructures. Contrarily, rapid weight loss at around 300 ℃ corresponding the decarboxylation of tannic acid was observed, when the 3-APT concentration was reduced which indicates a slightly lower thermal stability in these TALi-Si-B4 to TALi-Si-B6 microstructures (**Figure 37(b)**). Also, the microstructures in **Figure 37(b)** have the first weight loss starting slightly earlier than the ones in **Figure 37(a).** Further**,** a second degradation occurred in the region 300 – 450 ℃ in the TALi-Si-B6 microstructures prepared with lowest 3-APT amount. This second degradation profile is similar to the TALi which corresponds to the simultaneous decomposition of different gallic acid units from different branches.

When compared to TALi's thermal degradation peak at ~250 ℃,[113,195] the TALi-SSQ microstructures exhibit better thermal stability as their maximum degradation peak shifted to 312 ℃ (**Figure 37(c)**) which is due to the silane units introduced into the tannic acid core structure.[297] The DTG curve for TALi-Si-B3 in **Figure 37(c)** shows a 4% weight loss at 57 ℃ due to the surface absorbed moisture, a second degradation peak at 532 ℃ corresponding to the weight loss due to the residual alkoxide groups, and a high char yield of about 30%.[294] The char yield (**Figure 37(a)**) in the TALi-SSQ microstructures (B1-B3) prepared with a higher amount of silane precursor (2mL 3-APT) and same base concentration was around 30% implying that all the three microstructures have similar degradation with change in the base concentrations. While the char yield reduced with a reduction in the silane precursor with the lowest being for 0.25mL 3-APT at about 15% at 600 ℃ (**Figure 37(b)**). This implies that the microstructures with lower silica content degrade faster and at a lower temperature due to lower incorporation of silsesquioxane networks into the TALi structure.

Figure 37. (a)-(b) TGA thermographs of TALi-SSQ microstructures with variation in base and silane precursor contents, (c) TGA and derivative thermograph of TALi-Si-B3 microstructures.

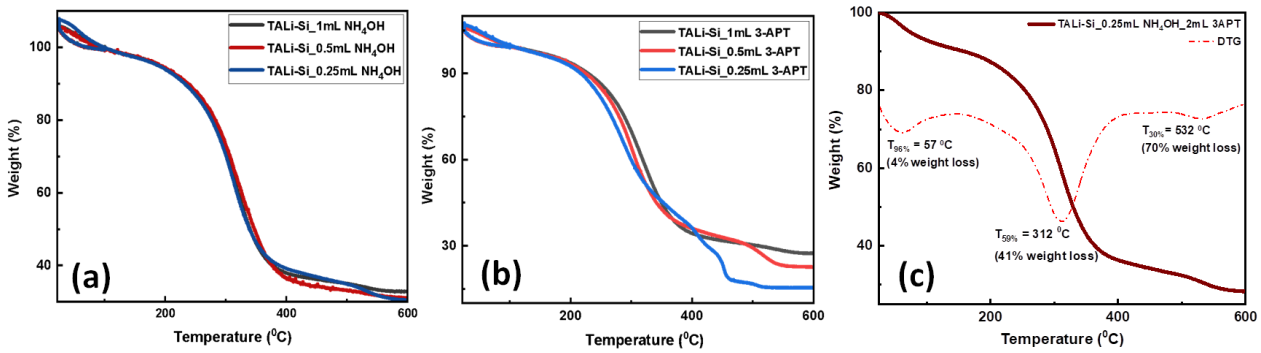

The integration of silane units and lithiation without altering the tannic acid glucose core structure is confirmed by the chemical composition analysis and the XPS survey spectrum of TALi-Si-B1 microstructures as illustrated in **Figure 38(a)**. The elemental binding energy spectra for C 1s, O 1s, Si 2p, N 1s, and Li 1s are shown in **Figure 38(b-f)**. **Figure 38(b)** shows three characteristic binding energy peaks for C 1s at 284.96 eV, 286.22 eV, and 288.14 eV which are assigned to the sp^2 bonded carbon of the C phenyl and C ester groups of tannic acid.[113,297] O 1s spectrum (**Figure 38(c)**) shows peaks at 531.94 eV, and 533.81 eV from the ester carbonyl and phenol groups in the tannic acid core.[195] The additional peak at 532.73 eV corresponds to the Si-O bond from the silane units attached to the tannic acid.[297] The N 1s scan (**Figure 38(e)**) gave peaks at 401.43 eV and 399.96 eV corresponding to the amine NH and N-C bonding from the silane precursor.[302] The Si 2p binding energy spectrum exhibits three peaks at 102.5 eV, 103.14 eV, and 101.86 eV corresponding to the Si-C (organic), Si-O, and amine groups of the alkoxysilane units attached to the tannic acid.[297] Similar binding energy spectra were exhibited by the TALi-SSQ microstructures prepared with varying 3-APT and base volumes and are included in the **Appendix A**. **Table 6** shows the binding energy and FWHM values of the

individual elements for all the TALi-SSQ microstuctures. A full-width half maximum (FWHM) value of ~ 4.2-4.7 eV for O 1s supports the oxygen chemical bonding state of O^{-2}.[261] Further, Li 1s gave an FWHM of ~3-4 eV for TALi supporting the oxidation state of +1 (Li^{+}) along with its binding energy peak at ~55.5 eV.[198] Further, Si 2p gave an FWHM values ~4 eV corresponding to the silica oxidation state of +4. From **Table 7**, approximately, 2-4 wt% (4-8 at%) Li and 4-14 wt% (2-7 at%) Si were incorporated into the TALi-SSQ microstructures. With variation in the base concentration, the silane units' incorporation was almost the same while the lithium content changed with a maximum of ~7 at% for TALi-Si-B2 microstructures. Contrarily, the silica percentage reduced with a reduction in 3-APT concentration, and lithiation was higher with a maximum of 8.4 at% (**Table 7)**.

Figure 38. (a) XPS survey spectrum and binding energy spectra of TALi-Si-B1 microstructures for: (b) C1s, (c) O 1s, (d) Si 2p, (e) N 1s, and (f) Li 1s.

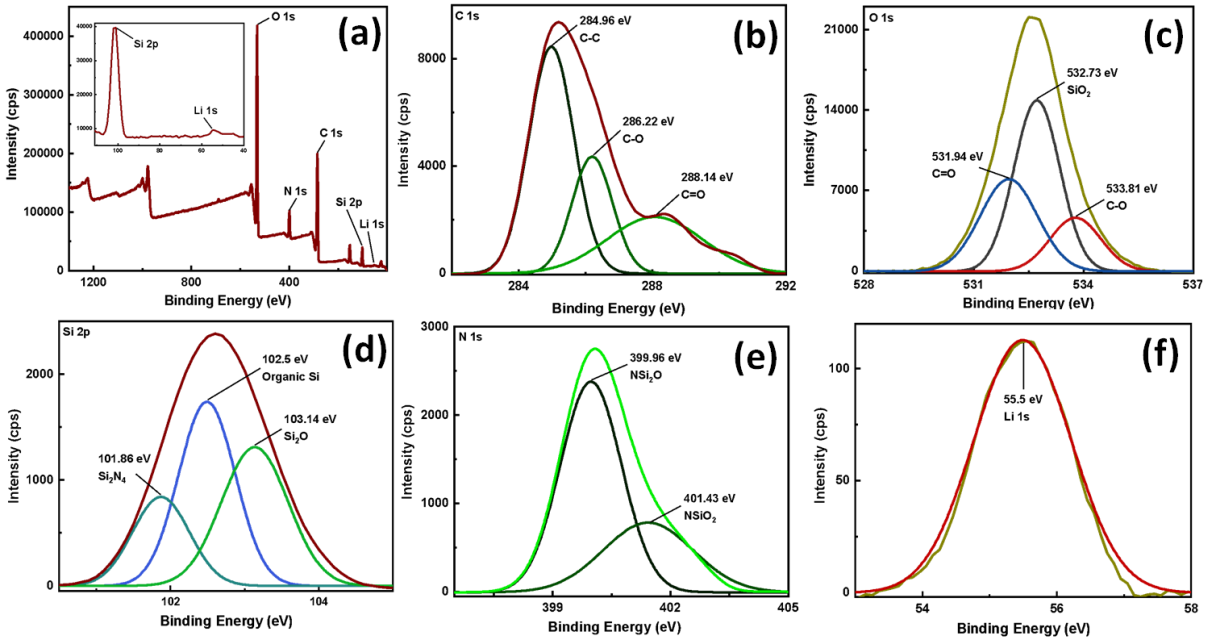

Table 6. Binding energies of TALi-SSQ microstructures.

Sample Name [3-APT (mL)/ NH_4OH (mL)]	Binding Energies (eV) [FWHM values]				
	Li	**Si**	**N**	**C**	**O**
TALi-Si-B1 [2/1]	55.5 [3.72]	101.86, 102.5 & 103.14[4.15]	399.96 & 401.43[4.57]	284.96, 286.22 & 288.14[4.88]	532.73, 531.94 & 533.81[4.41]
TALi-Si-B2 [2/0.5]	55.43 [3.61]	101.95, 102.61 & 103.29[3.87]	399.92 & 401.81[4.45]	284.84, 286.05 & 288.18[4.77]	532.47, 531.47 & 533.36[4.27]
TALi-Si-B3 [2/0.25]	55.49 [2.92]	101.88, 102.59 & 103.4 [3.79]	399.82 & 401.43[4.34]	284.91, 286.17 & 288.19[4.58]	532.68, 531.55 & 533.42[4.23]
TALi-Si-B4 [1/1]	55.37 [2.54]	101.87, 102.61 & 103.54[4.08]	399.89 & 401.63[4.52]	284.88, 286.21 & 288.42[4.71]	532.54, 531.71 & 533.41[4.39]
TALi-Si-B5 [0.5/1]	55.52 [3.54]	101.84, 102.57 & 103.45[3.89]	399.86 & 401.42[4.21]	284.86, 286.19 & 288.41[5]	532.44, 531.83 & 533.45[4.24]
TALi-Si-B6 [0.25/1]	55.42 [4.57]	101.85, 102.67 & 103.33[4.23]	399.85 & 401.5[4.51]	284.92, 286.31 & 288.88[5.54]	532.41, 531.35 & 533.78[4.75]

Table 7. XPS survey analysis and elemental composition of TALi-SSQ microstructures.

Sample Name	Atomic (%)					Weight (%)				
[3-APT (mL)/ NH_4OH (mL)]	**Li**	**Si**	**N**	**C**	**O**	**Li**	**Si**	**N**	**C**	**O**
TALi-Si-B1 [2/1]	4.31	7.41	47.92	7.36	33.00	2.07	14.4	39.84	7.14	36.55
TALi-Si-B2 [2/0.5]	6.56	7.35	46.58	6.67	32.83	3.19	14.43	39.12	6.53	36.73
TALi-Si-B3 [2/0.25]	4.68	7.68	48.57	6.99	32.09	2.25	14.95	40.44	6.78	35.58
TALi-Si-B4 [1/1]	3.03	7.13	51.91	7.45	30.48	1.47	13.94	43.39	7.26	33.94
TALi-Si-B5 [0.5/1]	8.35	4.08	47.67	5.94	33.95	4.23	8.35	41.75	6.07	39.61
TALi-Si-B6 [0.25/1]	8.29	2.00	48.96	4.71	36.04	4.28	4.17	43.75	4.91	42.89

6.2.2 BET Measurements

The pore-size distribution and pore volume obtained from the N_2 adsorption-desorption isotherms (**Figure 39(a-c**) using the Brunauer−Emmett−Teller Surface analysis. As shown in **Table 8**, BET surface areas and pore volumes obtained for TALi-SSQ microstructures were 10-fold higher compared to the BET surface area and the pore volume of TALi complexes. The BET surface areas obtained in these TALi-SSQ microstructures were comparable to some clays having mesopores with nanometer-sized slit shaped pores.[303] Type IV(a) isotherm with very narrow hysteresis was obtained for all the TALi-SSQ microstructures (shown in **Appendix D**) which is typical for mesoporous (2-50 nm) adsorbents.[208] This occurs if the pore width exceeds a certain critical width depending on the adsorption system and temperature.[271] Interpretation of physisorption hysteresis is essential for the characterization of pore structure.[304] The isotherm resembles a Type H3 hysteresis loop, which has pseudo-type II isotherm characteristics due to the delayed capillary condensation and the metastability of the adsorbed multilayer.[304] The N_2

isotherm gave a Type H3 hysteresis loop indicating the presence of non-rigid aggregates giving rise to slit-shaped pores.[271,305] The BJH computational method proposed by Barrett, Joyner and Halenda is commonly used for mesopore-size distribution.[306] The BJH average adsorption pore widths were in the range of 16-39 nm and BJH desorption pore volume ranged from 0.077-0.17 cm^3/g.

Figure 39. (a) N_2 BET Isotherms, (b) BJH Adsorption dV/dw pore volume distribution plot, and (c) NLDFT Cumulative pore volume distribution plot for TALi-Si-B1 microstructures.

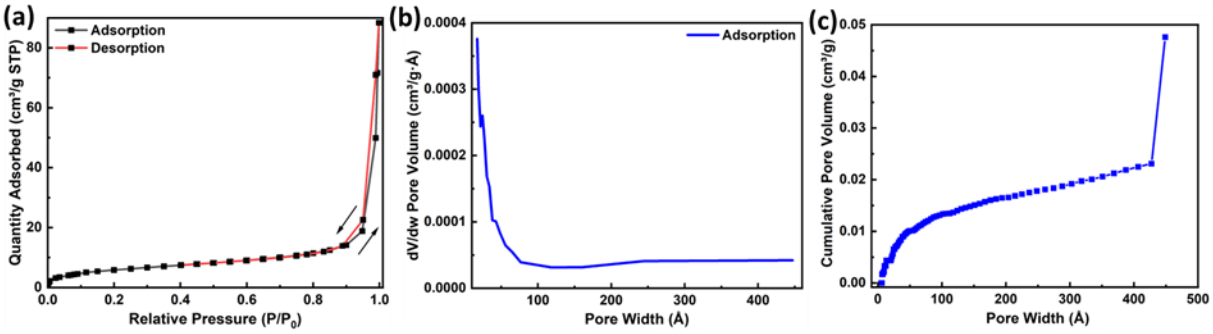

Table 8. N_2 BET surface area and BJH pore distribution analyses of TALi-SSQ microstructures.

	BET surface area (m^2/g)	BJH desorption cumulative pore volume (cm^3/g)	BJH adsorption average pore widths (Å)
TALi-Si-B1	21.36	0.106	239.105
TALi-Si-B2	13.78	0.077	199.86
TALi-Si-B3	25.39	0.174	159.87
TALi-Si-B4	22.002	0.153	283.57
TALi-Si-B5	18.03	0.122	390.9
TALi-Si-B6	18.695	0.142	235.402

6.2.3 Ionic Conductivity studies

To evaluate the ionic conductivity, TALi-Si@LEC powders were pressed into dense pellets having no apparent breaks or splits. TALi-Si@LEC pellets were analyzed using EIS in **Figure 40(a)** and the overall ionic conductivity (σ) of these various pellets obtained at 25 ℃ is illustrated in **Table 9**, normalized by the thickness of each pellet (1.37 – 2.74 mm). The ionic conductivity was calculated using the bulk resistance (R_b) value taken at the intercept of the semicricle in the higher frequency area on the real impedance axis, from the Nyquist plots. The semicircle in the high frequency region indicates the bulk response of the solid electrolyte, and the inclined line represents the double layer charges at the solid electrolyte/electrode interfaces. The salt concentration was 5wt% for all the TALi-Si@LEC electrolyte pellets measured using the EIS system. As observed in **Figure 40(a)**, with increasing silica content (from 2 to 7at%) in these microstructures the complex impedance plot first shifted to the left i.e., towards lower bulk resistances indicating increasing ionic conductivities. Further, the radius of semicircle reduced with increasing silica content indicating decrease in the charge-transfer resistance. The TALi-SSQ microstructures with a high silica content of ~7at% show absence of semicircle implying a very low charge-transfer resistance at the electrolyte/electrode interfaces, and thereby exhibit higher ionic conductivities in 10^{-4} S/cm range. The ionic conductivities of these pellets ranged in between 10^{-4} - 10^{-5} S/cm with the highest ionic conductivity of 5.16 x 10^{-4} S/cm for TALi-Si-B2 microstructures have these optimum values for Si (~ 7at%) and Li (~ 6at%) content. Interestingly, these TALi-Si@LEC electrolytes having a higher silica content (~7at%) show higher ionic conductivities (~10^{-4} S/cm) when compared to the TALi@LEC electrolyte (~10^{-5} S/cm), i.e., the ionic conduction improved with the incorporation of silsesquioxanes networks into the TALi which supports our initial hypothesis. The ionic conductivity of these TALi-

Si@LEC electrolytes at room temperature exceeds most polymer electrolyte systems (e.g., PEO-$LiPF_6$,[307] PEO-$LiClO_4$[308] and PAN-EC-$LiClO_4$[309,310]), and other natural polymer-based electrolytes (e.g., pectin-$LiClO_4$,[12] and lignin[300]).

Temperature-dependent ionic conductivity studies were performed on the TALi-Si@LEC pellets in the temperature range of 25-55 ℃ below the glass-transition temperature (T_g) of the solid-pellets. The loss of trapped EC was observed during the temperature-dependent ionic conductivity measurements as the LEC@Li-MOF electrolyte pellets turn semi-solid in nature with increase in temperature beyond 55 ℃. **Figure 41(a-f)** shows the log σ versus reciprocal temperature (1000/T) plot for the TALi-Si@LEC electrolytes and the experimental data indicates that the ionic conductivity enhanced linearly with increasing temperature. The experimental data was fitted using the Arrhenius equation and the slope of the linear fit was used to calculate the activation energy (E_a) values (**Table 9**). The experimental data indicates that the ionic conductivity with increasing temperature obeys the Arrhenius relationship with slightly lower correlation coefficient (R^2) in TALi-Si-B4@LEC (R^2 =0.96) and TALi-Si-B5@LEC (R^2 =0.97) which imply poor fits and slightly non-Arrhenius behavior of the data. The activation energy values (E_a) values lie in the range of 0.16-0.65 eV which are comparable to the solid electrolytes (e.g., PAN-hybrid films[309], PMMA-$LiBF_4$ films[311] and biopolymers such as pectin[312], lignin[300]). The lowest E_a was observed in the TALi-Si-B2 sample having the highest ionic conductivity and lowest pore volume, making it easy for Li^+-ion hopping due to the shorter diffusion distance in smaller pores and hence, more favorable for Li^+-ion conduction. A higher activation energy was observed in the TALi-Si-B3, TALi-Si-B4 and TALi-Si-B6 microstructures having considerably higher pore volumes in the range 0.14-0.17 cm^3/g, which increases the diffusion distance in larger pores, thereby increasing the energy barrier for Li-ion hopping. The highest activation

energy (0.65 eV) was observed for the TALi-Si-B6 microstructures having lowest silica content (Si~2at%) indicating strong interactions between the TALi-Si-B6 microstructures and the ions within the TALi-Si-B6@LEC electrolyte.

The ionic conductivity values in TALi-Si@LEC electrolytes with high silica content (Si~7at%) and a lithium content (Li~3-6 at%) in the TALi-SSQ microstructures were higher ~10^{-4} S/cm and have low activation energies (<0.3 eV). Hence, these TALi-Si-B1@LEC and TALi-Si-B2@LEC electrolytes can be classified as superionic conductors.[313] Cyclic voltammetry (CV) was on the TALi-Si-B2@LEC pellet the potential range of −1 to +1 at different scan rates as shown in **Figure 40(b)**. The CV curves in **Figure 40(b)** exhibit a leaf like shape as scan rate increased which could be due to the internal resistance due to faradaic reactions. Only an ideal supercapacitor possesses a perfect rectangular shape. The curves did not depict any noticeable peaks that explained that the system underwent any oxidation/reduction reaction. It can also be observed that the charge-discharge of both EDL capacitors occurs almost reversibly at the electrode/solid-electrolyte interface.

Figure 40. (a) Nyquist plots of TALi-Si@LEC electrolytes at ambient temperature and (b) CV plot of TALi-Si-B2@LEC pellet at various scan rates from 5-100 mV/s.

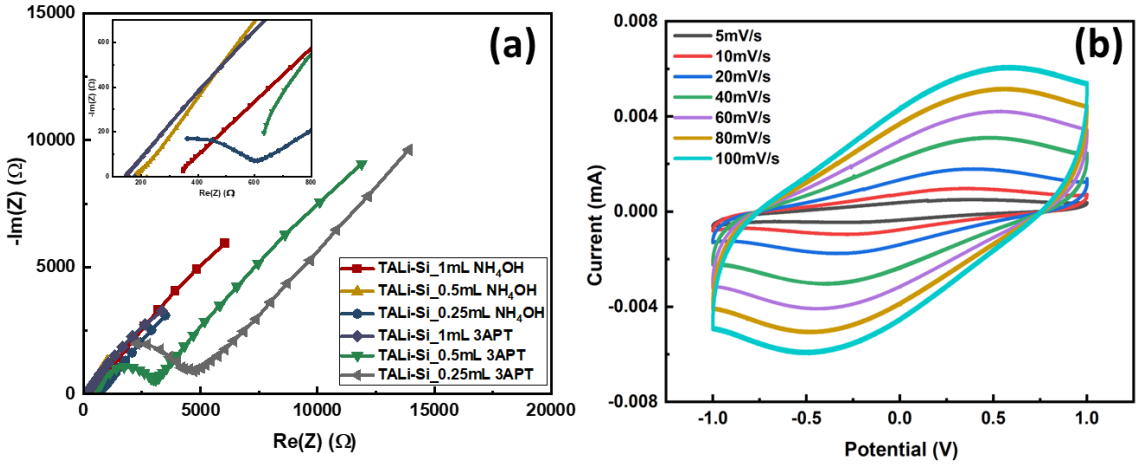

Figure 41. (a)-(f) Arrhenius plots of TALi-Si@LEC electrolyte and their activation energies for lithium-ion conduction, and (g)-(l) Nyquist plots of TALi-Si@LEC electrolytes.

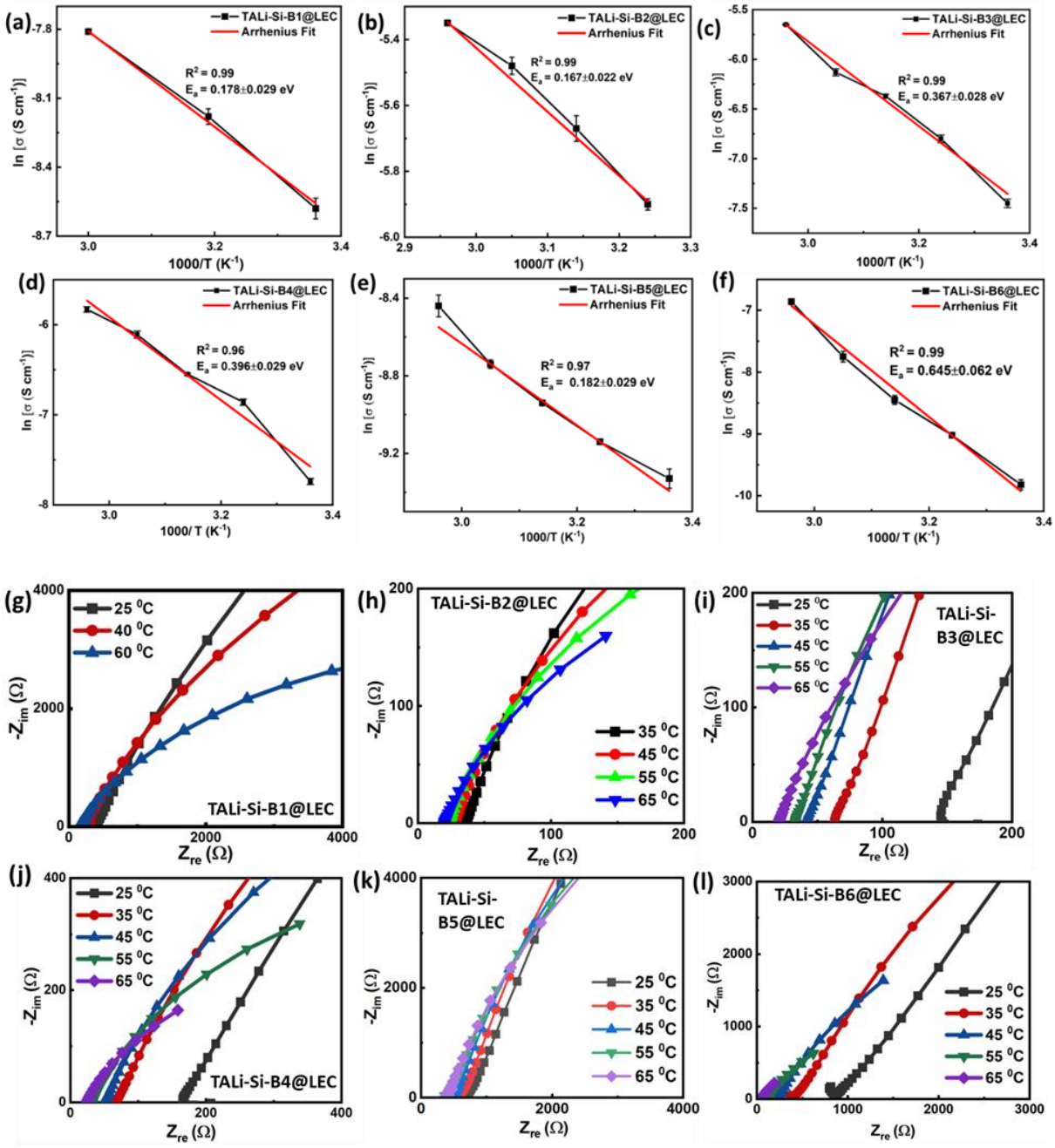

Table 9. Ionic conductivity and activation energy values of TALi-SSQ microstructures

Sample Name	3-APT (mL)/ NH_4OH (mL)	Ionic Conductivity at 25 ℃ (S/cm)	Activation Energy (eV)	BJH desorption cumulative pore volume (cm^3/g)
TALi-Si-B1	2/1	$(1.87\pm0.085) \times 10^{-4}$	0.178±0.029	0.106
TALi-Si-B2	2/0.5	$(8.85\pm0.961) \times 10^{-4}$	0.167±0.022	0.077
TALi-Si-B3	2/0.25	$(5.78\pm0.217) \times 10^{-4}$	0.367±0.028	0.174
TALi-Si-B4	1/1	$(4.35\pm0.151) \times 10^{-4}$	0.396±0.029	0.153
TALi-Si-B5	0.5/1	$(8.85\pm0.437) \times 10^{-5}$	0.182±0.029	0.122
TALi-Si-B6	0.25/1	$(5.43\pm0.492) \times 10^{-5}$	0.645±0.062	0.142

6.2.4 TGA measurements on TALi-Si-B1@LEC electrolyte

The thermal stability of TALi-Si-B1@LEC electrolyte was studied using the TGA analysis as shown in **Figure 42**. Pure EC starts to degrade around 90 ℃ and completely decomposes before 150 ℃.[236] Addition of lithium perchlorate salt could reduce the decomposition temperature and lower the thermal stability of LEC.[237] Hence, in TALi-Si-B1@LEC (**Figure 42**), the major weight loss of 63% with peak degradation at 124 ℃ (from DTG) corresponds to the encapsulated LEC electrolyte in the TALi-Si-B1 microstructures. There is an initial weight loss of ~6% with peak degradation from DTG at 36 ℃ which corresponds to surface absorbed moisture, as observed in TALi-Si-B3 microstructures. Further the degradation profile from 141 ℃ to 600 ℃ is similar to the TALi-Si-B1 microstructures in **Figure 37(a)** with a 7% char yield. From the DTG, the weight loss was observed at 318 ℃ corresponds to the decomposition of tannic acid via decarboxylation, as observed in TALi-Si-B1 microstructures (**Figure 37(a)).**

Figure 42. TGA thermograph of TALi-Si-B1@LEC electrolyte.

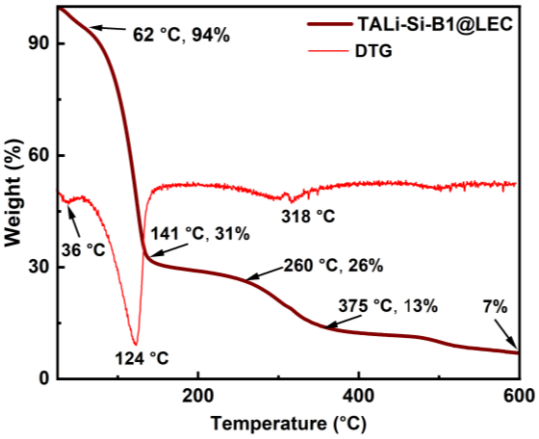

6.2.5 FTIR Spectroscopy Measurements

FTIR spectroscopy was performed on TALi-Si-B1@LEC, TALi-Si-B1 and EC samples to further understand the mechanism of Li-ion conduction in the TALi-Si@LEC electrolytes. In **Figure 42(a)**, C=O stretching peaks at 1789 cm^{-1} and 1768 cm^{-1} in EC shifted to higher wavenumbers at 1794 cm^{-1} and 1770 cm^{-1} which corresponds to the interactions of EC's carbonyl groups with the mobile Li^+ ions due to solvation. Additionally, the reduction in aromatic C=C stretching in TALi-SSQ at 1582 cm^{-1} and the CH_2 bending vibrations in EC at 1554 cm^{-1} indicate the interactions of Li^+ nodes of TALi-SSQ microstructures and EC carbonyl oxygens. **Figure 42(b)** shows reduction in intensities of C-O-Li^+ absorption peaks along with slight peak shifts to 1366 cm^{-1} indicating the strong binding interactions of EC's carbonyl groups with the O-Li^+ sites of TALi-Si microstructures. From **Figure 43(c)**, the EC's C-O peak shifts at 1146 cm^{-1} and 1058 cm^{-1} to 1152 cm^{-1} and 1061 cm^{-1} in TALi-Si-B1@LEC correspond to the interactions between the ether oxygens of EC and Li^+ ions from $LiClO_4$ salt due to solvation.[222] In **Figure 43(d)**, there was a reduced absorption peak of EC's ring breathing mode at 891 cm^{-1} and the shift in EC's ring bending mode at 710 to 715 cm^{-1} along with the intensity reduction of the secondary band at 687 cm^{-1} confirm the free Li^+ binding to EC's ether oxygens. The aromatic

C=C bending mode in TALi-SSQ microstructures at 762 cm^{-1} disapperared to a slight shoulder peak at 753 cm^{-1} in TALi-Si-B1@LEC corresponding to the interactions of the mobile Li^+ of the salt with the residual phenolic oxygens and ester carbonyl groups of TALi-SSQ microstructures. Further, the reduced absorption of the aromatic C-H bending modes of TALi-SSQ at 862 and 832 cm^{-1} are also indicative of mobile Li^+ ions interacting with the oxygens of the TALi-SSQ microstructures. Additionally, the peak at 623 cm^{-1} belonging to one of the vibrational mode of ClO_4^- anion along with a weak shoulder peak at 644 cm^{-1} confirms the interactions of ClO_4^- anion with EC molecules.[224] Hence, the FTIR spectra of TALi-Si-B1@LEC confirms the EC's interations with $LiClO_4$ salt result in dissociation of the salt into Li^+ and ClO_4^- ions. Further, the FTIR spectra also shows strong binding interactions between the EC carbonyl groups and the O-Li^+ groups in the TALi-SSQ microstructures. These mobile Li^+ ions of the salt hop along the porous channels of the TALi-SSQ microstructures while interacting with the EC's ether oxygens and oxygen functional sites of the TALi-SSQ microstructures. The incorporation of silsesquioxane networks into the TALi network could result in restriction of accessible oxygen functional sites for the interactions with the mobile Li^+ of the lithium perchlorate salt when compared to TALi complex. Thereby, favoring the mobile Li^+ ions binding to the plasticizer EC's ether oxygen groups over the frameworks oxygen functional sites and promoting the Li^+ hopping via the EC's ether oxygens (as coordination sites) along the porous channels of TALi-SSQ microstructures. Further, the EC molecules in the pores can provide a continuous Li^+ hopping pathway facilitating Li-ion diffusion through the porous channels. This could be a reason for observing lower activation energies and higher ionic conductivities in TALi-SSQ microstructures when compared to the TALi complexes.

Figure 43. The FTIR spectra of TALi-Si-B1@LEC, TALi-Si-B1@EC, TALi-Si-B1, and EC in the region (a) 1900-1500 cm^{-1}, (b) 1500-1300 cm^{-1}, (b) 1200-1000 cm^{-1}, and (d) 900-600.

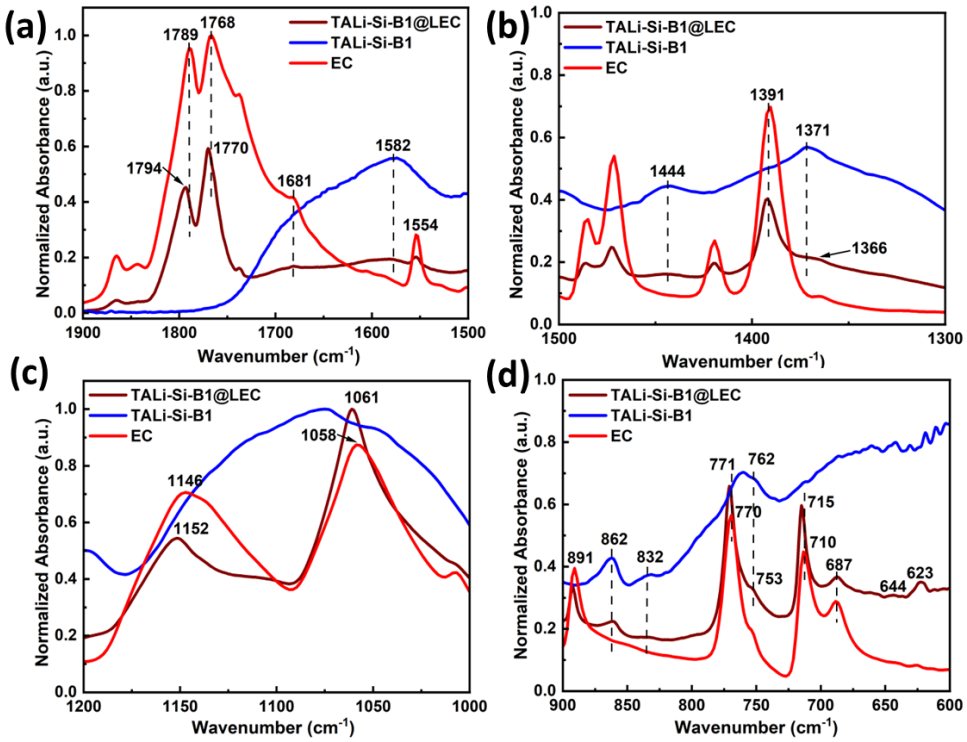

6.3 Conclusion

In summary, this study demonstrated the successful synthesis of TALi-SSQ microstructures with various base and silane precursor concentrations. An effective base-catalyzed sol-gel polymerization method was used to synthesize the TALi-SSQ hybrid microstructures by introducing a silsesquioxane framework into the TALi which serves as a robust backbone while isolating organic segments by connecting them in a well-defined structure. The pyrogallol units in the lithium-tannate complex were modified to create sol-gel reactive sites with a trialkoxysilane precursor. The UV-visible, FTIR, and XPS spectroscopy analysis indicate the presence of lithium coordination as well as the incorporation of silsesquioxane units into the tannic acid structure. Varying the molar ratios of base and silane precursors resulted in nanoparticles with mean particle sizes in the range of 60-170 nm on SEM.

These TALi-SSQ particles possess better thermal stability than TALi and especially, the TALi-Si-B3 particles give more stable suspensions in anhydrous ethanol. The ionic conductivities of the TALi-Si@LEC electrolytes were in the range of 10^{-4} -10^{-5} S/cm with activation energies in the 0.16-0.65 eV range. The TALi-Si@LEC electrolytes with high silica content (~7at%) showed the characteristics of superionic conductors possessing high ionic conductivities~10^{-4} S/cm and low activation energies. The TGA and FTIR analysis of the TALi-Si-B1@LEC electrolyte shows the incorporation of ethylene carbonate into the TALi-SSQ microstructures and a possibility of lithium-ion conduction via the encapsulated EC in the porous TALi-silsesquioxanes. Thus, novel phenolate based lithium-tannate silsesquioxane microstructures were demonstrated as solid-state electrolytes possessing properties of superionic conductors for potential applications in lithium-ion batteries.

CHAPTER VII: CONCLUSION AND FUTURE SCOPE

7.1 Conclusions

This dissertation's goal was to develop novel solid-state electrolyte systems from the carboxylate-based metal-organic frameworks and bio-based coordination polymers by tailoring their structure and functionality. This work offers the following contributions.

- Demonstrated a modified solvothermal method to synthesize an isoreticular series of three highly crystalline, porous lithium-based carboxylate frameworks (Li-MOFs) and developed novel solid-state electrolytes using these Li-MOF hosts.
- Demonstrated an environmentally friendly room-temperature approach to synthesize the porous lithium-tannate coordination complex and developed bio-based solid-state electrolytes.
- Demonstrated a green sol-gel approach to synthesize porous lithium-tannate silsesquioxane microstructures to develop silsesquioxane based solid-state electrolytes.

There is vast literature on fabrication of solid-state electrolytes with diverse types of synthetic polymer matrices using various fillers, plasticizers, and lithium salts to develop solid-state electrolytes with ionic conductivities in the order of liquid electrolytes ($\sim 10^{-2}$ S cm^{-1}). However, utilizing sustainable natural polymers as the main matrix is a less common approach but an expanding area of research to develop novel bio-based solid-state electrolytes which are more environmentally friendly and recyclable. Consequently, this work demonstrates the use of an oxygen-rich polyphenol, tannic acid, as the main matrix for the development of novel bio-based solid-state electrolytes, which is very rarely explored. Due to the strong metal chelating properties of tannic acid, they can form lithium coordinated-phenolate coordination complexes,

which have great potential to produce high ionic conductivities. Further, the silsesquioxane units were incorporated into the TALi to increase the porosity, thermal and chemical stability. The addition of this silica functionality into TALi enhanced the ionic conductivity of the TALi-SSQ microstructures. Additionally, studying the composition, structure, and solid-state ionic conduction in Li-based MOFs with isoreticular expansion gave better insights for understanding the Li-ion conduction in lithium-tannate-based solid-state electrolytes.

Aim 1 of the dissertation research work was synthesizing isoreticular series of highly crystalline Li-MOFs using a solvothermal approach. This solvothermal approach allowed reasonable control with variation in linkers, provided reproducibility, and scalable to achieve higher yields. The detailed compositional analysis, morphology and crystallinity confirms the formation of three isoreticular Li-MOFs. The isoreticular Li-MOFs had irregular shapes and truncated rods with size range in 8-70 μm. These MOFs were highly thermally stable upto 500-550°C owing to the rigidity offered by the frameworks. The structure and crystallinity of the isoreticular Li-MOFs were confirmed after performing a detailed analysis using the XRD and HRTEM. BET measurements showed a bimodal pore distribution for all the three Li-MOFs with pore volumes in the range of 0.61-0.71 cm^3/g and BET surface areas in the range of 741-894 m^2/g. The plasticizer ethylene carbonate and lithium salt, lithium perchlorate was used to develop the LEC@Li-MOF electrolytes. The ionic conductivities of these electrolytes were in the range of 1.7 - 6.6 x 10^{-5} S/cm and activation energy values were in the range of 0.63 – 0.72 eV. Interestingly, the highest ionic conductivity and lowest activation energy was obtained for the LEC@Li-BPDC electrolyte with the longest linker possessing the lowest pore volume. According to our initial hypothesis, the isoreticular expansion did not affect the ionic conductivities at room temperature significantly but the reticular expansion and pore size of Li-

MOFs affect the Li^+-ion conduction mechanisms. The FTIR spectra of Li-MOF based SSEs suggested a 'pore-filling driven Li ion conduction' wherein the free/bound states of Li^+-ion diffuse either via ion-hopping or both ion-hopping and vehicular mechanism. Thus, this work contributes significantly to the basic understanding of ionic conduction in Li-MOF-based SSEs, paving the path for developing all-solid-state batteries.

Aim 2 targeted the development of bio-based SSEs using the lithium-tannate coordination complex, which were synthesized using a cost-effective, eco-friendly method at room temperature. This approach uses the principles of green chemistry avoiding toxic chemicals and involves rapid complex formation to produce the TALi complexes. The UV-visible, FTIR, and XPS spectroscopy analysis confirmed the random coordination of lithium ions onto tannic acid's hydroxyl groups. XPS analysis also revealed that a 1:20 molar ratio of TA to LiOH resulted in approximately 18 lithium bound to each tannic acid's hydroxyl groups. TALi complex showed better thermal stability when compared to tannic acid, and its colloidal solution is highly stable in the basic pH range. The high dielectric constant of plasticizer EC favors the dissociation of the lithium perchlorate salt favoring the ionic hopping and boosting ionic conductivity. The ionic conductivity measurements on the TALi@LEC electrolytes gave ionic conductivities in the $1.03 – 8.77 \times 10^{-5}$ S/cm range. Also, the ionic conductivity in the TALi@LEC electrolytes increased with an increase in salt concentration until the optimum salt concentration of 10wt% $LiClO_4$. The temperature-dependent ionic conductivity data resulted in an Arrhenius fit with an activation energy of 0.85 eV for the TALi@LEC electrolyte (5wt% $LiClO_4$). Further, the FTIR spectroscopy investigation of the TALi@LEC electrolyte confirms the interactions of EC carbonyls with the TALi and the ether oxygens with Li^+ ions of the $LiClO_4$. Thus, the most probable ionic conduction mechanism is Li^+ ion hopping via the ether

oxygens of EC. This work demonstrated the use of the lithium phenolate coordination complex as a solid-state electrolyte and shows potential for developing bio-based solid-state electrolytes.

Aim 3 focused on investigating the ionic conduction properties of the lithium-tannate silsesquioxane microstructures. These silsesquioxane networks were introduced into the lithium-tannate structure using a base-catalyzed sol-gel process. The UV-Visible and FTIR spectroscopy analysis confirmed the lithiation and the incorporation of silane units into these microstructures. There was an increase in the silica content up to ~7% with an increase in the silane precursor amount from 0.25 to 2 mL and maximum lithium incorporation of ~8%. The variation in base and silane precursor concentrations resulted in nanoparticles with mean particle sizes of 60-170 nm. The TEM images showed the presence of large void spaces between the aggregates of these particles. The EIS measurements on the TALi-Si@LEC electrolytes gave ionic conductivities in the 10^{-4}-10^{-5} S/cm. Interestingly, the samples with higher silica content (~7at%) showed higher ionic conductivities in ~10^{-4} S/cm and lower activation energies than TALi@LEC electrolyte. It can be inferred that the silsesquioxane cores incorporation into TALi structure enhanced the ionic conduction depicting the properties of super-ionic conductors. Further, the temperature-dependent ionic conductivity plots of the electrolytes showed Arrhenius behavior resulting in activation energies in the range of 0.16-0.65 eV. The presence of LEC electrolyte in the microstructures was confirmed from FTIR and TGA analysis on the TALi-Si-B1@LEC electrolyte. The ionic conduction in these TALi-Si@LEC electrolytes could be Li^+ ion hopping via encapsulated EC in these porous microstructures. Thus, the incorporation of silsesquioxane networks into the lithiated tannic acid structure resulted in higher ionic conductivities than the TALi complexes and further, the TALi-SSQ based SSEs showed properties of superionic conductors which are promising for incorporation into the all-solid-state batteries.

7.2 Recommendations for Future Research

This dissertation has provided a basic understanding of designing solid-state electrolytes using coordination polymer systems. These CPF-based SSEs have great potential for all-solid-state batteries, which is crucial for developing safer, longer-lasting electric vehicles. Herein, this section provides some potential future directions that can be pursued for potential applications in solid-state batteries.

REFERENCES

(1) Duan, H.; Yin, Y. X.; Zeng, X. X.; Li, J. Y.; Shi, J. L.; Shi, Y.; Wen, R.; Guo, Y. G.; Wan, L. J. In-Situ Plasticized Polymer Electrolyte with Double-Network for Flexible Solid-State Lithium-Metal Batteries. *Energy Storage Mater.* **2018**, *10* (August 2017), 85–91. https://doi.org/10.1016/j.ensm.2017.06.017.

(2) Knauth, P. Inorganic Solid Li Ion Conductors: An Overview. *Solid State Ionics* **2009**, *180* (14–16), 911–916. https://doi.org/10.1016/j.ssi.2009.03.022.

(3) Zhang, H.; Armand, M. History of Solid Polymer Electrolyte-Based Solid-State Lithium Metal Batteries: A Personal Account. *Isr. J. Chem.* **2020**, 1–8. https://doi.org/10.1002/ijch.202000066.

(4) Meyer, W. H. Polymer Electrolytes for Lithium-Ion Batteries. *Adv. Mater.* **1998**, *10* (6), 439–448.

(5) Wakihara, M. Recent Developments in Lithium Ion Batteries. *Mater. Sci. Eng. R Reports* **2001**, *33* (4), 109–134. https://doi.org/10.1016/S0927-796X(01)00030-4.

(6) Yang, G.; Song, Y.; Wang, Q.; Zhang, L.; Deng, L. Review of Ionic Liquids Containing, Polymer/Inorganic Hybrid Electrolytes for Lithium Metal Batteries. *Mater. Des.* **2020**, *190*, 108563. https://doi.org/10.1016/j.matdes.2020.108563.

(7) Long, L.; Wang, S.; Xiao, M.; Meng, Y. Polymer Electrolytes for Lithium Polymer Batteries. *J. Mater. Chem. A* **2016**, *4* (26), 10038–10039. https://doi.org/10.1039/c6ta02621d.

(8) Manuel Stephan, A.; Nahm, K. S. Review on Composite Polymer Electrolytes for Lithium Batteries. *Polymer (Guildf).* **2006**, *47* (16), 5952–5964. https://doi.org/10.1016/j.polymer.2006.05.069.

(9) Varshney, P. K.; Gupta, S. Natural Polymer-Based Electrolytes for Electrochemical Devices: A Review. *Ionics (Kiel).* **2011**, *17* (6), 479–483. https://doi.org/10.1007/s11581-011-0563-1.

(10) Fu, X.; Zhong, W. H. Biomaterials for High-Energy Lithium-Based Batteries: Strategies, Challenges, and Perspectives. *Adv. Energy Mater.* **2019**, *9* (40), 1–41. https://doi.org/10.1002/aenm.201901774.

(11) Barbosa, J. C.; Gonçalves, R.; Costa, C. M.; Lanceros-Méndez, S. Toward Sustainable Solid Polymer Electrolytes for Lithium-Ion Batteries. *ACS Omega* **2022**, *7* (17), 14457–14464. https://doi.org/10.1021/acsomega.2c01926.

(12) Perumal, P.; Selvasekarapandian, S.; Abhilash, K. P.; Sivaraj, P.; Hemalatha, R.; Selvin, P. C. Impact of Lithium Chlorate Salts on Structural and Electrical Properties of Natural Polymer Electrolytes for All Solid State Lithium Polymer Batteries. *Vacuum* **2019**, *159* (July 2018), 277–281. https://doi.org/10.1016/j.vacuum.2018.10.043.

(13) Basu, T.; Goswami, M. M.; Middya, T. R.; Tarafdar, S. Morphology and Ion-Conductivity of Gelatin-LiClO4 Films: Factional Diffusion Analysis. *J. Phys. Chem. B* **2012**, *116* (36), 11362–11369. https://doi.org/10.1021/jp306205h.

(14) Xia, T.; Wang, Y.; Wang, B.; Yang, Z.; Pan, G.; Zhang, L.; Zhang, J. Natural Compounds Gallic Acid Derivatives for Long-Life Li/Na Organic Batteries. *ChemElectroChem* **2019**, *6* (18), 4765–4772. https://doi.org/10.1002/celc.201901064.

(15) Zhou, H.; Sun, X.; Zhang, L.; Zhang, P.; Li, J.; Liu, Y.-N. Fabrication of Biopolymeric Complex Coacervation Core Micelles for Efficient Tea Polyphenol Delivery via a Green Process. *Langmuir* **2012**, *28* (41), 14553–14561. https://doi.org/10.1021/la303062j.

(16) Erel-Unal, I.; Sukhishvili, S. A. Hydrogen-Bonded Hybrid Multilayers: Film Architecture Controls Release of Macromolecules. *Macromolecules* **2008**, *41* (22), 8737–8744. https://doi.org/10.1021/ma8013564.

(17) Xu, L. Q.; Neoh, K. G.; Kang, E. T. Natural Polyphenols as Versatile Platforms for Material Engineering and Surface Functionalization. *Prog. Polym. Sci.* **2018**, *87*, 165–196. https://doi.org/10.1016/j.progpolymsci.2018.08.005.

(18) Hider, R. C.; Liu, Z. D.; Khodr, H. H. Metal Chelation of Polyphenols; 2001; Vol. 6879, pp 190–203. https://doi.org/10.1016/S0076-6879(01)35243-6.

(19) Yao, P.; Yu, H.; Ding, Z.; Liu, Y.; Lu, J.; Lavorgna, M.; Wu, J.; Liu, X. Review on Polymer-Based Composite Electrolytes for Lithium Batteries. *Front. Chem.* **2019**, *7* (August), 1–17. https://doi.org/10.3389/fchem.2019.00522.

(20) Quartarone, E.; Mustarelli, P. Review—Emerging Trends in the Design of Electrolytes for Lithium and Post-Lithium Batteries. *J. Electrochem. Soc.* **2020**, *167* (5), 050508. https://doi.org/10.1149/1945-7111/ab63c4.

(21) Miner, E. M.; Dincă, M. Metal- and Covalent-Organic Frameworks as Solid-State Electrolytes for Metal-Ion Batteries. *Philos. Trans. R. Soc. A Math. Phys. Eng. Sci.* **2019**, *377* (2149), 20180225. https://doi.org/10.1098/rsta.2018.0225.

(22) Zhao, R.; Wu, Y.; Liang, Z.; Gao, L.; Xia, W.; Zhao, Y.; Zou, R. Metal-Organic Frameworks for Solid-State Electrolytes. *Energy Environ. Sci.* **2020**. https://doi.org/10.1039/d0ee00153h.

(23) Park, S. S.; Tulchinsky, Y.; Dincă, M. Single-Ion Li + , Na + , and Mg 2+ Solid Electrolytes Supported by a Mesoporous Anionic Cu–Azolate Metal–Organic Framework. *J. Am. Chem. Soc.* **2017**, *139* (38), 13260–13263. https://doi.org/10.1021/jacs.7b06197.

(24) Fujie, K.; Ikeda, R.; Otsubo, K.; Yamada, T.; Kitagawa, H. Lithium Ion Diffusion in a Metal-Organic Framework Mediated by an Ionic Liquid. *Chem. Mater.* **2015**, *27* (21), 7355–7361. https://doi.org/10.1021/acs.chemmater.5b02986.

(25) Liu, K.; Liu, Y.; Lin, D.; Pei, A.; Cui, Y. Materials for Lithium-Ion Battery Safety. *Sci. Adv.* **2018**, *4* (6). https://doi.org/10.1126/sciadv.aas9820.

(26) Varzi, A.; Raccichini, R.; Passerini, S.; Scrosati, B. Challenges and Prospects of the Role of Solid Electrolytes in the Revitalization of Lithium Metal Batteries. *J. Mater. Chem. A* **2016**, *4* (44), 17251–17259. https://doi.org/10.1039/c6ta07384k.

(27) Zhao, W.; Yi, J.; He, P.; Zhou, H. *Solid-State Electrolytes for Lithium-Ion Batteries: Fundamentals, Challenges and Perspectives*; Springer Singapore, 2019; Vol. 2. https://doi.org/10.1007/s41918-019-00048-0.

(28) Zhang, Q.; Liu, K.; Ding, F.; Liu, X. Recent Advances in Solid Polymer Electrolytes for Lithium Batteries. *Nano Res.* **2017**, *10* (12), 4139–4174. https://doi.org/10.1007/s12274-017-1763-4.

(29) Chen, S.; Wen, K.; Fan, J.; Bando, Y.; Golberg, D. Progress and Future Prospects of High-Voltage and High-Safety Electrolytes in Advanced Lithium Batteries: From Liquid to Solid Electrolytes. *J. Mater. Chem. A* **2018**, *6* (25), 11631–11663. https://doi.org/10.1039/c8ta03358g.

(30) Zhao, R.; Wu, Y.; Liang, Z.; Gao, L.; Xia, W.; Zhao, Y.; Zou, R. Metal–Organic Frameworks for Solid-State Electrolytes. *Energy Environ. Sci.* **2020**, *13* (8), 2386–2403. https://doi.org/10.1039/D0EE00153H.

(31) Manthiram, A.; Yu, X.; Wang, S. Lithium Battery Chemistries Enabled by Solid-State Electrolytes. *Nat. Rev. Mater.* **2017**, *2* (4), 1–16. https://doi.org/10.1038/natrevmats.2016.103.

(32) Famprikis, T.; Canepa, P.; Dawson, J. A.; Islam, M. S.; Masquelier, C. Fundamentals of Inorganic Solid-State Electrolytes for Batteries. *Nat. Mater.* **2019**, *18* (12), 1278–1291. https://doi.org/10.1038/s41563-019-0431-3.

(33) Famprikis, T.; Canepa, P.; Dawson, J. A.; Islam, M. S.; Masquelier, C. Fundamentals of Inorganic Solid-State Electrolytes for Batteries. *Nat. Mater.* **2019**, *18* (12), 1278–1291. https://doi.org/10.1038/s41563-019-0431-3.

(34) Yue, L.; Ma, J.; Zhang, J.; Zhao, J.; Dong, S.; Liu, Z.; Cui, G.; Chen, L. All Solid-State Polymer Electrolytes for High-Performance Lithium Ion Batteries. *Energy Storage Mater.* **2016**, *5*, 139–164. https://doi.org/10.1016/j.ensm.2016.07.003.

(35) Kimura, K.; Tominaga, Y. Understanding Electrochemical Stability and Lithium Ion-Dominant Transport in Concentrated Poly(Ethylene Carbonate) Electrolyte. *ChemElectroChem* **2018**, *5* (24), 4008–4014. https://doi.org/10.1002/celc.201801105.

(36) Zhang, X.; Xu, B.-Q.; Lin, Y.-H.; Shen, Y.; Li, L.; Nan, C.-W. Effects of Li6.75La3Zr1.75Ta0.25O12 on Chemical and Electrochemical Properties of Polyacrylonitrile-Based Solid Electrolytes. *Solid State Ionics* **2018**, *327* (September), 32–38. https://doi.org/10.1016/j.ssi.2018.10.023.

(37) Guzmán-González, G.; Ávila-Paredes, H. J.; Rivera, E.; González, I. Electrochemical Characterization of Single Lithium-Ion Conducting Polymer Electrolytes Based on Sp 3 Boron and Poly(Ethylene Glycol) Bridges. *ACS Appl. Mater. Interfaces* **2018**, *10* (36), 30247–30256. https://doi.org/10.1021/acsami.8b02519.

(38) Senthil Kumar, P.; Sakunthala, A.; Reddy, M. V.; Prabu, M. Structural, Morphological, Electrical and Electrochemical Study on Plasticized PVdF-HFP/PEMA Blended Polymer Electrolyte for Lithium Polymer Battery Application. *Solid State Ionics* **2018**, *319* (May 2017), 256–265. https://doi.org/10.1016/j.ssi.2018.02.022.

(39) Xu, Z.; Yang, T.; Chu, X.; Su, H.; Wang, Z.; Chen, N.; Gu, B.; Zhang, H.; Deng, W.; Zhang, H.; Yang, W. Strong Lewis Acid-Base and Weak Hydrogen Bond Synergistically Enhancing Ionic Conductivity of Poly(Ethylene Oxide)@SiO2 Electrolytes for a High Rate Capability Li-Metal Battery. *ACS Appl. Mater. Interfaces* **2020**, *12* (9), 10341–10349. https://doi.org/10.1021/acsami.9b20128.

(40) Nguyen, T. K. L.; Lopez, G.; Iojoiu, C.; Bouchet, R.; Ameduri, B. Novel Single-Ion Conducting Electrolytes Based on Vinylidene Fluoride Copolymer for Lithium Metal Batteries. *J. Power Sources* **2021**, *498* (April), 229920. https://doi.org/10.1016/j.jpowsour.2021.229920.

(41) Dias, F. B.; Plomp, L.; Veldhuis, J. B. J. Trends in Polymer Electrolytes for Secondary Lithium Batteries. *J. Power Sources* **2000**, *88* (2), 169–191. https://doi.org/10.1016/S0378-7753(99)00529-7.

(42) Zhao, S.; Wu, Q.; Ma, W.; Yang, L. Polyethylene Oxide-Based Composites as Solid-State Polymer Electrolytes for Lithium Metal Batteries: A Mini Review. *Front. Chem.* **2020**, *8* (August), 1–7. https://doi.org/10.3389/fchem.2020.00640.

(43) Hadad, S.; Hamrahjoo, M.; Dehghani, E.; Salami-Kalajahi, M.; Eliseeva, S. N.; Moghaddam, A. R.; Roghani-Mamaqani, H. Cellulose-Based Solid and Gel Polymer Electrolytes with Super High Ionic Conductivity and Charge Capacity for High Performance Lithium Ion Batteries. *Sustain. Mater. Technol.* **2022**, *33* (August), e00503. https://doi.org/10.1016/j.susmat.2022.e00503.

(44) Liang, S.; Yan, W.; Wu, X.; Zhang, Y.; Zhu, Y.; Wang, H.; Wu, Y. Gel Polymer Electrolytes for Lithium Ion Batteries: Fabrication, Characterization and Performance. *Solid State Ionics* **2018**, *318* (August 2017), 2–18. https://doi.org/10.1016/j.ssi.2017.12.023.

(45) Appetecchi, G. B.; Croce, F.; Scrosati, B. Kinetics and Stability of the Lithium Electrode in Poly(Methylmethacrylate)-Based Gel Electrolytes. *Electrochim. Acta* **1995**, *40* (8), 991–997. https://doi.org/10.1016/0013-4686(94)00345-2.

(46) Krawiec, W.; Scanlon, L. G.; Fellner, J. P.; Vaia, R. A.; Vasudevan, S.; Giannelis, E. P. Polymer Nanocomposites: A New Strategy for Synthesizing Solid Electrolytes for Rechargeable Lithium Batteries. *J. Power Sources* **1995**, *54* (2), 310–315. https://doi.org/10.1016/0378-7753(94)02090-P.

(47) Jayathilaka, P. A. R. D.; Dissanayake, M. A. K. L.; Albinsson, I.; Mellander, B. E. Effect of Nano-Porous Al2O3 on Thermal, Dielectric and Transport Properties of the (PEO)9LiTFSI Polymer Electrolyte System. *Electrochim. Acta* **2002**, *47* (20), 3257–3268. https://doi.org/10.1016/S0013-4686(02)00243-8.

(48) Manuel Stephan, A. Nanocomposite Polymer Electrolytes for Lithium Batteries. *Recent Adv. Polym. Nanocomposites* **2009**, *394* (July), 455–482. https://doi.org/10.1557/proc-496-511.

(49) Croce, F.; Persi, L. L.; Scrosati, B.; Serraino-Fiory, F.; Plichta, E.; Hendrickson, M. A. Role of the Ceramic Fillers in Enhancing the Transport Properties of Composite Polymer Electrolytes. *Electrochim. Acta* **2001**, *46* (16), 2457–2461. https://doi.org/10.1016/S0013-4686(01)00458-3.

(50) Rayung, M.; Aung, M. M.; Azhar, S. C.; Abdullah, L. C.; Su'ait, M. S.; Ahmad, A.; Jamil, S. N. A. M. Bio-Based Polymer Electrolytes for Electrochemical Devices: Insight into the Ionic Conductivity Performance. *Materials (Basel).* **2020**, *13* (4), 838. https://doi.org/10.3390/ma13040838.

(51) Li, Q.; Cao, D.; Naik, M. T.; Pu, Y.; Sun, X.; Luan, P.; Ragauskas, A. J.; Ji, T.; Zhao, Y.; Chen, F.; Zheng, Y.; Zhu, H. Molecular Engineering of Biorefining Lignin Waste for Solid-State Electrolyte. *ACS Sustain. Chem. Eng.* **2022**, *10* (27), 8704–8714. https://doi.org/10.1021/acssuschemeng.2c00783.

(52) Li, C.; Huang, Y.; Chen, C.; Feng, X.; Zhang, Z.; Liu, P. A High-Performance Solid Electrolyte Assisted with Hybrid Biomaterials for Lithium Metal Batteries. *J. Colloid Interface Sci.* **2022**, *608*, 313–321. https://doi.org/10.1016/j.jcis.2021.09.113.

(53) Rajendran, S.; Saratha, R. An Evaluation of Solid-State Electrolyte Based on Pectin and Lithium Bis (Trifluoromethanesulphonyl)Imide for Lithium-Ion Batteries. *Mater. Today Proc.* **2020**, *47*, 819–824. https://doi.org/10.1016/j.matpr.2020.12.557.

(54) Zhao, Y.; Li, K.; Li, J. Solvothermal Synthesis of Multifunctional Coordination Polymers. *Zeitschrift fur Naturforsch. - Sect. B J. Chem. Sci.* **2010**, *65* (8), 976–998. https://doi.org/10.1515/znb-2010-0804.

(55) Kitagawa, S.; Kitaura, R.; Noro, S. Functional Porous Coordination Polymers. *Angew. Chemie Int. Ed.* **2004**, *43* (18), 2334–2375. https://doi.org/10.1002/anie.200300610.

(56) Maji, T. K.; Kitagawa, S. Chemistry of Porous Coordination Polymers. *Pure Appl. Chem.* **2007**, *79* (12), 2155–2177. https://doi.org/10.1351/pac200779122155.

(57) Yaghi, O. M.; Li, G. Mutually Interpenetrating Sheets and Channels in the Extended Structure of [Cu(4,4′-bpy)Cl]. *Angew. Chemie Int. Ed. English* **1995**, *34* (2), 207–209. https://doi.org/10.1002/anie.199502071.

(58) Yu, J.; Xie, L. H.; Li, J. R.; Ma, Y.; Seminario, J. M.; Balbuena, P. B. CO2 Capture and Separations Using MOFs: Computational and Experimental Studies. *Chem. Rev.* **2017**, *117* (14), 9674–9754. https://doi.org/10.1021/acs.chemrev.6b00626.

(59) Valenzano, L.; Civalleri, B.; Chavan, S.; Palomino, G. T.; Areán, C. O.; Bordiga, S. Computational and Experimental Studies on the Adsorption of CO, N 2 , and CO 2 on Mg-MOF-74. *J. Phys. Chem. C* **2010**, *114* (25), 11185–11191. https://doi.org/10.1021/jp102574f.

(60) Kreno, L. E.; Leong, K.; Farha, O. K.; Allendorf, M.; Van Duyne, R. P.; Hupp, J. T. Metal–Organic Framework Materials as Chemical Sensors. *Chem. Rev.* **2012**, *112* (2), 1105–1125. https://doi.org/10.1021/cr200324t.

(61) Lee, J.; Farha, O. K.; Roberts, J.; Scheidt, K. A.; Nguyen, S. T.; Hupp, J. T. Metal–Organic Framework Materials as Catalysts. *Chem. Soc. Rev.* **2009**, *38* (5), 1450. https://doi.org/10.1039/b807080f.

(62) Shekhah, O.; Liu, J.; Fischer, R. A.; Wöll, C. MOF Thin Films: Existing and Future Applications. *Chem. Soc. Rev.* **2011**, *40* (2), 1081. https://doi.org/10.1039/c0cs00147c.

(63) Horike, S.; Umeyama, D.; Kitagawa, S. Ion Conductivity and Transport by Porous Coordination Polymers and Metal–Organic Frameworks. *Acc. Chem. Res.* **2013**, *46* (11), 2376–2384. https://doi.org/10.1021/ar300291s.

(64) Morozan, A.; Jaouen, F. Metal Organic Frameworks for Electrochemical Applications. *Energy Environ. Sci.* **2012**, *5* (11), 9269. https://doi.org/10.1039/c2ee22989g.

(65) Batten, S. R.; Champness, N. R.; Chen, X. M.; Garcia-Martinez, J.; Kitagawa, S.; Öhrström, L.; O'Keeffe, M.; Suh, M. P.; Reedijk, J. Coordination Polymers, Metal-Organic Frameworks and the Need for Terminology Guidelines. *CrystEngComm* **2012**, *14* (9), 3001–3004. https://doi.org/10.1039/c2ce06488j.

(66) Li, S. L.; Xu, Q. Metal-Organic Frameworks as Platforms for Clean Energy. *Energy Environ. Sci.* **2013**, *6* (6), 1656–1683. https://doi.org/10.1039/c3ee40507a.

(67) Wang, L.; Han, Y.; Feng, X.; Zhou, J.; Qi, P.; Wang, B. Metal–Organic Frameworks for Energy Storage: Batteries and Supercapacitors. *Coord. Chem. Rev.* **2016**, *307*, 361–381. https://doi.org/10.1016/j.ccr.2015.09.002.

(68) Kinik, F. P.; Uzun, A.; Keskin, S. Ionic Liquid/Metal-Organic Framework Composites: From Synthesis to Applications. *ChemSusChem* **2017**, *10* (14), 2842–2863. https://doi.org/10.1002/cssc.201700716.

(69) Fujie, K.; Kitagawa, H. Ionic Liquid Transported into Metal–Organic Frameworks. *Coord. Chem. Rev.* **2016**, *307*, 382–390. https://doi.org/10.1016/j.ccr.2015.09.003.

(70) Eddaoudi, M.; Moler, D. B.; Li, H.; Chen, B.; Reineke, T. M.; O'Keeffe, M.; Yaghi, O. M. Modular Chemistry: Secondary Building Units as a Basis for the Design of Highly Porous and Robust Metal−Organic Carboxylate Frameworks. *Acc. Chem. Res.* **2001**, *34* (4), 319–330. https://doi.org/10.1021/ar000034b.

(71) Zhu, K.; Liu, Y.; Liu, J. A Fast Charging/Discharging All-Solid-State Lithium Ion Battery Based on PEO-MIL-53(Al)-LiTFSI Thin Film Electrolyte. *RSC Adv.* **2014**, *4* (80), 42278–42284. https://doi.org/10.1039/C4RA06208F.

(72) Yuan, C.; Li, J.; Han, P.; Lai, Y.; Zhang, Z.; Liu, J. Enhanced Electrochemical Performance of Poly(Ethylene Oxide) Based Composite Polymer Electrolyte by Incorporation of Nano-Sized Metal-Organic Framework. *J. Power Sources* **2013**, *240*, 653–658. https://doi.org/10.1016/j.jpowsour.2013.05.030.

(73) Fujie, K.; Yamada, T.; Ikeda, R.; Kitagawa, H. Introduction of an Ionic Liquid into the Micropores of a Metal-Organic Framework and Its Anomalous Phase Behavior. *Angew. Chemie - Int. Ed.* **2014**, *53* (42), 11302–11305. https://doi.org/10.1002/anie.201406011.

(74) Greenwood, N. .; Earnshaw, A. Chemistry of the Elements. In *Springer Handbooks*; 2018; pp 68–102. https://doi.org/10.1007/978-3-319-69743-7_4.

(75) Liu, J.; Xie, D.; Shi, W.; Cheng, P. Coordination Compounds in Lithium Storage and Lithium-Ion Transport. *Chem. Soc. Rev.* **2020**, *49* (6), 1624–1642. https://doi.org/10.1039/C9CS00881K.

(76) Biradha, K.; Ramanan, A.; Vittal, J. J. Coordination Polymers Versus Metal-Organic Frameworks. *Cryst. Growth Des.* **2009**, *9* (7), 8–9.

(77) Tong, M. L.; Chen, X. M. *Synthesis of Coordination Compounds and Coordination Polymers*; Elsevier B.V., 2017. https://doi.org/10.1016/B978-0-444-63591-4.00008-2.

(78) Olsher, U.; Izatt, R. M.; Bradshaw, J. S.; Dalley, N. K. Coordination Chemistry of Lithium Ion: A Crystal and Molecular Structure Review. *Chem. Rev.* **1991**, *91* (2), 137–164. https://doi.org/10.1021/cr00002a003.

(79) Quartarone, E.; Mustarelli, P. Review—Emerging Trends in the Design of Electrolytes for Lithium and Post-Lithium Batteries. *J. Electrochem. Soc.* **2020**, *167* (5), 050508. https://doi.org/10.1149/1945-7111/ab63c4.

(80) Chang, Z.; Yang, H.; Zhu, X.; He, P.; Zhou, H. A Stable Quasi-Solid Electrolyte Improves the Safe Operation of Highly Efficient Lithium-Metal Pouch Cells in Harsh Environments. *Nat. Commun.* **2022**, *13* (1), 1510. https://doi.org/10.1038/s41467-022-29118-6.

(81) Yang, S.; Zhang, Z.; Lin, J.; Zhang, L.; Wang, L.; Chen, S.; Zhang, C.; Liu, X. Recent Progress in Quasi/All-Solid-State Electrolytes for Lithium–Sulfur Batteries. *Front. Energy Res.* **2022**, *10* (July), 1–13. https://doi.org/10.3389/fenrg.2022.945003.

(82) Mindemark, J.; Lacey, M. J.; Bowden, T.; Brandell, D. Beyond PEO—Alternative Host Materials for Li + -Conducting Solid Polymer Electrolytes. *Prog. Polym. Sci.* **2018**, *81*, 114–143. https://doi.org/10.1016/j.progpolymsci.2017.12.004.

(83) Thomas, E. M.; Nguyen, P. H.; Jones, S. D.; Chabinyc, M. L.; Segalman, R. A. Electronic, Ionic, and Mixed Conduction in Polymeric Systems. *Annu. Rev. Mater. Res.* **2021**, *51* (1), 1–20. https://doi.org/10.1146/annurev-matsci-080619-110405.

(84) Ramesh, S.; Ling, O. P. Effect of Ethylene Carbonate on the Ionic Conduction in Poly(Vinylidenefluoride-Hexafluoropropylene) Based Solid Polymer Electrolytes. *Polym. Chem.* **2010**, *1* (5), 702–707. https://doi.org/10.1039/b9py00244h.

(85) Li, Q.; Cao, Z.; Wahyudi, W.; Liu, G.; Park, G. T.; Cavallo, L.; Anthopoulos, T. D.; Wang, L.; Sun, Y. K.; Alshareef, H. N.; Ming, J. Unraveling the New Role of an Ethylene Carbonate Solvation Shell in Rechargeable Metal Ion Batteries. *ACS Energy Lett.* **2021**, *6* (1), 69–78. https://doi.org/10.1021/acsenergylett.0c02140.

(86) Marom, R.; Haik, O.; Aurbach, D.; Halalay, I. C. Revisiting LiClO[Sub 4] as an Electrolyte for Rechargeable Lithium-Ion Batteries. *J. Electrochem. Soc.* **2010**, *157* (8), A972. https://doi.org/10.1149/1.3447750.

(87) Guo, J.; Suma, T.; Richardson, J. J.; Ejima, H. Modular Assembly of Biomaterials Using Polyphenols as Building Blocks. *ACS Biomater. Sci. Eng.* **2019**, *5* (11), 5578–5596. https://doi.org/10.1021/acsbiomaterials.8b01507.

(88) JAL, P. Chemical Modification of Silica Surface by Immobilization of Functional Groups for Extractive Concentration of Metal Ions. *Talanta* **2004**, *62* (5), 1005–1028. https://doi.org/10.1016/j.talanta.2003.10.028.

(89) Liu, Y.; Li, Y.; Li, X.; He, T. Kinetics of (3-Aminopropyl)Triethoxylsilane (APTES) Silanization of Superparamagnetic Iron Oxide Nanoparticles. **2013**. https://doi.org/10.1021/la403269u.

(90) Pang, A. L.; Ismail, H. Tensile Properties, Water Uptake, and Thermal Properties of Polypropylene/Waste Pulverized Tire/Kenaf (PP/WPT/KNF) Composites. *BioResources* **2013**, *8* (1), 806–817.

(91) Lee, J. Y.; Lee, Y. M.; Bhattacharya, B.; Nho, Y.-C.; Park, J.-K. Solid Polymer Electrolytes Based on Crosslinkable Polyoctahedral Silsesquioxanes (POSS) for Room Temperature Lithium Polymer Batteries. *J. Solid State Electrochem.* **2010**, *14* (8), 1445–1449. https://doi.org/10.1007/s10008-009-0968-1.

(92) Shang, D.; Fu, J.; Lu, Q.; Chen, L.; Yin, J.; Dong, X.; Xu, Y.; Jia, R.; Yuan, S.; Chen, Y.; Deng, W. A Novel Polyhedral Oligomeric Silsesquioxane Based Ionic Liquids (POSS-ILs) Polymer Electrolytes for Lithium Ion Batteries. *Solid State Ionics* **2018**, *319* (January), 247–255. https://doi.org/10.1016/j.ssi.2018.01.050.

(93) Abbas, M.; Saeed, F.; Anjum, F. M.; Afzaal, M.; Tufail, T.; Bashir, M. S.; Ishtiaq, A.; Hussain, S.; Suleria, H. A. R. Natural Polyphenols: An Overview. *Int. J. Food Prop.* **2017**, *20* (8), 1689–1699. https://doi.org/10.1080/10942912.2016.1220393.

(94) Wang, X.; Li, X.; Liang, X.; Liang, J.; Zhang, C.; Yang, J.; Wang, C.; Kong, D.; Sun, H. ROS-Responsive Capsules Engineered from Green Tea Polyphenol-Metal Networks for Anticancer Drug Delivery. *J. Mater. Chem. B* **2018**, *6* (7), 1000–1010. https://doi.org/10.1039/c7tb02688a.

(95) Ping, Y.; Guo, J.; Ejima, H.; Chen, X.; Richardson, J. J.; Sun, H.; Caruso, F. PH-Responsive Capsules Engineered from Metal-Phenolic Networks for Anticancer Drug Delivery. *Small* **2015**, *11* (17), 2032–2036. https://doi.org/10.1002/smll.201403343.

(96) Park, C.; Yang, B. J.; Jeong, K. B.; Kim, C. Bin; Lee, S.; Ku, B. C. Signal-Induced Release of Guests from a Photolatent Metal–Phenolic Supramolecular Cage and Its Hybrid Assemblies. *Angew. Chemie - Int. Ed.* **2017**, *56* (20), 5485–5489. https://doi.org/10.1002/anie.201701152.

(97) Labieniec, M.; Gabryelak, T. Interactions of Tannic Acid and Its Derivatives (Ellagic and Gallic Acid) with Calf Thymus DNA and Bovine Serum Albumin Using Spectroscopic Method. *J. Photochem. Photobiol. B Biol.* **2006**, *82* (1), 72–78. https://doi.org/10.1016/j.jphotobiol.2005.09.005.

(98) Ejima, H.; Richardson, J. J.; Liang, K.; Best, J. P.; Van Koeverden, M. P.; Such, G. K.; Cui, J.; Caruso, F. One-Step Assembly of Coordination Complexes for Versatile Film and Particle Engineering. *Science.* **2013**, *341* (6142), 154–157. https://doi.org/10.1126/science.1237265.

(99) Guo, J.; Ping, Y.; Ejima, H.; Alt, K.; Meissner, M.; Richardson, J. J.; Yan, Y.; Peter, K.; von Elverfeldt, D.; Hagemeyer, C. E.; Caruso, F. Engineering Multifunctional Capsules through the Assembly of Metal-Phenolic Networks. *Angew. Chemie* **2014**, *126* (22), 5652–5657. https://doi.org/10.1002/ange.201311136.

(100) He, L.; Fullenkamp, D. E.; Rivera, J. G.; Messersmith, P. B. PH Responsive Self-Healing Hydrogels Formed by Boronate-Catechol Complexation. *Chem. Commun.* **2011**, *47* (26), 7497–7499. https://doi.org/10.1039/c1cc11928a.

(101) Ejima, H.; Richardson, J. J.; Caruso, F. Metal-Phenolic Networks as a Versatile Platform to Engineer Nanomaterials and Biointerfaces. *Nano Today* **2017**, *12*, 136–148. https://doi.org/10.1016/j.nantod.2016.12.012.

(102) Ejima, H.; Richardson, J. J.; Caruso, F. Phenolic Film Engineering for Template-Mediated Microcapsule Preparation. *Polym. J.* **2014**, *46* (8), 452–459. https://doi.org/10.1038/pj.2014.32.

(103) Li, Q.; Barrett, D. G.; Messersmith, P. B.; Holten-Andersen, N. Controlling Hydrogel Mechanics via Bio-Inspired Polymer-Nanoparticle Bond Dynamics. *ACS Nano* **2016**, *10* (1), 1317–1324. https://doi.org/10.1021/acsnano.5b06692.

(104) Holten-Andersen, N.; Harrington, M. J.; Birkedal, H.; Lee, B. P.; Messersmith, P. B.; Lee, K. Y. C.; Waite, J. H. PH-Induced Metal-Ligand Cross-Links Inspired by Mussel Yield Self-Healing Polymer Networks with near-Covalent Elastic Moduli. *Proc. Natl. Acad. Sci. U. S. A.* **2011**, *108* (7), 2651–2655. https://doi.org/10.1073/pnas.1015862108.

(105) Fu, Z.; Chen, R. Study of Complexes of Tannic Acid with Fe(III) and Fe(II). *J. Anal. Methods Chem.* **2019**, *2019*. https://doi.org/10.1155/2019/3894571.

(106) Shanmukaraj, D.; Ranque, P.; Ben Youcef, H.; Rojo, T.; Poizot, P.; Grugeon, S.; Laruelle, S.; Guyomard, D. Towards Efficient Energy Storage Materials: Lithium Intercalation/Organic Electrodes to Polymer Electrolytes—A Road Map (Tribute to Michel Armand). *J. Electrochem. Soc.* **2020**, *167* (7), 070530. https://doi.org/10.1149/1945-7111/ab787a.

(107) Xia, T.; Wang, Y.; Wang, B.; Yang, Z.; Pan, G.; Zhang, L.; Zhang, J. Two-Dimensional Materials as Anodes for Sodium-Ion Batteries. *ChemElectroChem* **2019**, *6* (18), 4765–4772. https://doi.org/10.1016/j.mtadv.2020.100054.

(108) Schon, T. B.; McAllister, B. T.; Li, P.-F.; Seferos, D. S. The Rise of Organic Electrode Materials for Energy Storage. *Chem. Soc. Rev.* **2016**, *45* (22), 6345–6404. https://doi.org/10.1039/C6CS00173D.

(109) Wu, Z.; Xie, J.; Xu, Z. J.; Zhang, S.; Zhang, Q. Recent Progress in Metal–Organic Polymers as Promising Electrodes for Lithium/Sodium Rechargeable Batteries. *J. Mater. Chem. A* **2019**, *7* (9), 4259–4290. https://doi.org/10.1039/C8TA11994E.

(110) Zhang, Y.; Yuan, J.-J.; Song, Y.-Z.; Yin, X.; Sun, C.-C.; Zhu, L.-P.; Zhu, B.-K. Tannic Acid/Polyethyleneimine-Decorated Polypropylene Separators for Li-Ion Batteries and the Role of the Interfaces between Separator and Electrolyte. *Electrochim. Acta* **2018**, *275*, 25–31. https://doi.org/10.1016/j.electacta.2018.03.099.

(111) Pan, L.; Wang, H.; Wu, C.; Liao, C.; Li, L. Tannic-Acid-Coated Polypropylene Membrane as a Separator for Lithium-Ion Batteries. *ACS Appl. Mater. Interfaces* **2015**, *7* (29), 16003–16010. https://doi.org/10.1021/acsami.5b04245.

(112) Wu, C.; Li, T.; Liao, C.; Li, L.; Yang, J. Tea Polyphenol-Inspired Tannic Acid-Treated Polypropylene Membrane as a Stable Separator for Lithium–Oxygen Batteries. *J. Mater. Chem. A* **2017**, *5* (25), 12782–12786. https://doi.org/10.1039/C7TA03456C.

(113) Xia, T.; Wang, Y.; Wang, B.; Yang, Z.; Pan, G.; Zhang, L.; Zhang, J. Natural Compounds Gallic Acid Derivatives for Long-Life Li/Na Organic Batteries-Supplementary. *ChemElectroChem* **2019**, *6* (18), 4765–4772. https://doi.org/10.1002/celc.201901064.

(114) Goriparti, S.; Harish, M. N. K.; Sampath, S. Ellagic Acid – a Novel Organic Electrode Material for High Capacity Lithium Ion Batteries. *Chem. Commun.* **2013**, *49* (65), 7234. https://doi.org/10.1039/c3cc43194k.

(115) Xu, Z.; Ye, H.; Li, H.; Xu, Y.; Wang, C.; Yin, J.; Zhu, H. Enhanced Lithium Ion Storage Performance of Tannic Acid in LiTFSI Electrolyte. *ACS Omega* **2017**, *2* (4), 1273–1278. https://doi.org/10.1021/acsomega.6b00504.

(116) Wu, J.; Han, C.; Wu, H.; Liu, H.; Zhang, Y.; Lu, C. Nanocoating of Ce-Tannic Acid Metal-Organic Coordination Complex: Surface Modification of Layered Li1.2Mn0.6Ni0.2O2 by CeO2 Coating for Lithium-Ion Batteries. *Ionics (Kiel).* **2019**, *25* (7), 3031–3040. https://doi.org/10.1007/s11581-018-2823-9.

(117) Fenton, D. E.; Parker, J. M.; Wright, P. V. Complexes of Alkali Metal Ions with Poly(Ethylene Oxide). *Polymer (Guildf).* **1973**, *14* (11), 589. https://doi.org/10.1016/0032-3861(73)90146-8.

(118) Xue, Z.; He, D.; Xie, X. Poly(Ethylene Oxide)-Based Electrolytes for Lithium-Ion Batteries. *J. Mater. Chem. A* **2015**, *3* (38), 19218–19253. https://doi.org/10.1039/c5ta03471j.

(119) Shim, J.; Bae, K. Y.; Kim, H. J.; Lee, J. H.; Kim, D.-G.; Yoon, W. Y.; Lee, J.-C. Solid Polymer Electrolytes Based on Functionalized Tannic Acids from Natural Resources for All-Solid-State Lithium-Ion Batteries. *ChemSusChem* **2015**, *8* (24), 4133–4138. https://doi.org/10.1002/cssc.201501110.

(120) Cho, S. M.; Shim, J.; Cho, S. H.; Kim, J.; Son, B. D.; Lee, J. C.; Yoon, W. Y. Quasi-Solid-State Rechargeable Li-O2 Batteries with High Safety and Long Cycle Life at Room Temperature. *ACS Appl. Mater. Interfaces* **2018**, *10* (18), 15634–15641. https://doi.org/10.1021/acsami.8b00529.

(121) Ha, H. J.; Kil, E. H.; Kwon, Y. H.; Kim, J. Y.; Lee, C. K.; Lee, S. Y. UV-Curable Semi-Interpenetrating Polymer Network-Integrated, Highly Bendable Plastic Crystal Composite Electrolytes for Shape-Conformable All-Solid-State Lithium Ion Batteries. *Energy Environ. Sci.* **2012**, *5* (4), 6491–6499. https://doi.org/10.1039/c2ee03025j.

(122) Timmermans, J. Plastic Crystals: A Historical Overview. *J. Phys. Chem. Solids* **1961**, *18* (1), 1–8.

(123) Fan, L.-Z.; Hu, Y.-S.; Bhattacharyya, A. J.; Maier, J. Succinonitrile as a Versatile Additive for Polymer Electrolytes. *Adv. Funct. Mater.* **2007**, *17* (15), 2800–2807. https://doi.org/10.1002/adfm.200601070.

(124) Pringle, J. M. Recent Progress in the Development and Use of Organic Ionic Plastic Crystal Electrolytes. *Phys. Chem. Chem. Phys.* **2013**, *15* (5), 1339–1351. https://doi.org/10.1039/C2CP43267F.

(125) Zhou, D.; Shanmukaraj, D.; Tkacheva, A.; Armand, M.; Wang, G. Polymer Electrolytes for Lithium-Based Batteries: Advances and Prospects. *Chem* **2019**, *5* (9), 2326–2352. https://doi.org/10.1016/j.chempr.2019.05.009.

(126) Macfarlane, D. R.; Huang, J.; Forsyth, M. Lithium-Doped Plastic Crystal Electrolytes Exhibiting Fast Ion Conduction for Secondary Batteries. *Nature* **1999**, *402* (6763), 792–794. https://doi.org/10.1038/45514.

(127) Abu-Lebdeh, Y.; Alarco, P. J.; Armand, M. Conductive Organic Plastic Crystals Based on Pyrazolium Imides. *Angew. Chemie - Int. Ed.* **2003**, *42* (37), 4499–4501. https://doi.org/10.1002/anie.200250706.

(128) Alarco, P. J.; Abu-Lebdeh, Y.; Abouimrane, A.; Armand, M. The Plastic-Crystalline Phase of Succinonitrile as a Universal Matrix for Solid-State Ionic Conductors. *Nat. Mater.* **2004**, *3* (7), 476–481. https://doi.org/10.1038/nmat1158.

(129) Das, S.; Prathapa, S. J.; Menezes, P. V.; Row, T. N. G.; Bhattacharyya, A. J. Study of Ion Transport in Lithium Perchlorate-Succinonitrile Plastic Crystalline Electrolyte via Ionic Conductivity and in Situ Cryo-Crystallography. *J. Phys. Chem. B* **2009**, *113* (15), 5025–5031. https://doi.org/10.1021/jp809465u.

(130) Zhou, D.; He, Y. B.; Liu, R.; Liu, M.; Du, H.; Li, B.; Cai, Q.; Yang, Q. H.; Kang, F. In Situ Synthesis of a Hierarchical All-Solid-State Electrolyte Based on Nitrile Materials for High-Performance Lithium-Ion Batteries. *Adv. Energy Mater.* **2015**, *5* (15). https://doi.org/10.1002/aenm.201500353.

(131) Yoshino, A. The Birth of the Lithium-Ion Battery. *Angew. Chemie - Int. Ed.* **2012**, *51* (24), 5798–5800. https://doi.org/10.1002/anie.201105006.

(132) Deng, D. Salt Concentration Effect on Electrical and Dielectric Properties of Solid Polymer Electrolytes Based Carboxymethyl Cellulose for Lithium-Ion Batteries. *Biointerface Res. Appl. Chem.* **2021**, *12* (5), 6114–6123. https://doi.org/10.33263/BRIAC125.61146123.

(133) Park, M.; Zhang, X.; Chung, M.; Less, G. B.; Sastry, A. M. A Review of Conduction Phenomena in Li-Ion Batteries. *J. Power Sources* **2010**, *195* (24), 7904–7929. https://doi.org/10.1016/j.jpowsour.2010.06.060.

(134) Deng, D.; Kim, M. G.; Lee, J. Y.; Cho, J. Green Energy Storage Materials: Nanostructured TiO2 and Sn-Based Anodes for Lithium-Ion Batteries. *Energy Environ. Sci.* **2009**, *2* (8), 818. https://doi.org/10.1039/b823474d.

(135) Goodenough, J. B.; Park, K. S. The Li-Ion Rechargeable Battery: A Perspective. *J. Am. Chem. Soc.* **2013**, *135* (4), 1167–1176. https://doi.org/10.1021/ja3091438.

(136) Inaguma, Y.; Itoh, M. Influences of Carrier Concentration and Site Percolation on Lithium Ion Conductivity in Perovskite-Type Oxides. *Solid State Ionics* **1996**, *86–88* (PART 1), 257–260. https://doi.org/10.1016/0167-2738(96)00100-2.

(137) Uddin, M.-J.; Cho, S.-J. Reassessing the Bulk Ionic Conductivity of Solid-State Electrolytes. *Sustain. Energy Fuels* **2018**, *2* (7), 1458–1462. https://doi.org/10.1039/C8SE00139A.

(138) Quartarone, E.; Mustarelli, P. Electrolytes for Solid-State Lithium Rechargeable Batteries: Recent Advances and Perspectives. *Chem. Soc. Rev.* **2011**, *40* (5), 2525–2540. https://doi.org/10.1039/c0cs00081g.

(139) Arya, A.; Sharma, A. L. Polymer Electrolytes for Lithium Ion Batteries: A Critical Study. *Ionics (Kiel).* **2017**, *23* (3), 497–540. https://doi.org/10.1007/s11581-016-1908-6.

(140) Xu, K. Electrolytes and Interphases in Li-Ion Batteries and Beyond. *Chem. Rev.* **2014**, *114* (23), 11503–11618. https://doi.org/10.1021/cr500003w.

(141) Deepa, M.; Agnihotry, S. .; Gupta, D.; Chandra, R. Ion-Pairing Effects and Ion–Solvent–Polymer Interactions in LiN(CF3SO2)2–PC–PMMA Electrolytes: A FTIR Study. *Electrochim. Acta* **2004**, *49* (3), 373–383. https://doi.org/10.1016/j.electacta.2003.08.020.

(142) Reddy, V. P.; Smart, M. C.; Chin, K. B.; Ratnakumar, B. V.; Surampudi, S.; Hu, J.; Yan, P.; Surya Prakash, G. K. [13]C NMR Spectroscopic, CV, and Conductivity Studies of Propylene Carbonate-Based Electrolytes Containing Various Lithium Salts. *Electrochem. Solid-State Lett.* **2005**, *8* (6), A294. https://doi.org/10.1149/1.1904466.

(143) Bogle, X.; Vazquez, R.; Greenbaum, S.; Cresce, A. V. W.; Xu, K. Understanding Li+–Solvent Interaction in Nonaqueous Carbonate Electrolytes with 17 O NMR. *J. Phys. Chem. Lett.* **2013**, *4* (10), 1664–1668. https://doi.org/10.1021/jz400661k.

(144) Teo, L. P.; Buraidah, M. H.; Arof, A. K. Development on Solid Polymer Electrolytes for Electrochemical Devices. *Molecules* **2021**, *26* (21), 6499. https://doi.org/10.3390/molecules26216499.

(145) Aziz, S. B.; Woo, T. J.; Kadir, M. F. Z.; Ahmed, H. M. A Conceptual Review on Polymer Electrolytes and Ion Transport Models. *J. Sci. Adv. Mater. Devices* **2018**, *3* (1), 1–17. https://doi.org/10.1016/j.jsamd.2018.01.002.

(146) Yang, H.; Wu, N. Ionic Conductivity and Ion Transport Mechanisms of Solid-state Lithium-ion Battery Electrolytes: A Review. *Energy Sci. Eng.* **2022**, *10* (5), 1643–1671. https://doi.org/10.1002/ese3.1163.

(147) Yahya, M. Z. A.; Arof, A. K. Effect of Oleic Acid Plasticizer on Chitosan–Lithium Acetate Solid Polymer Electrolytes. *Eur. Polym. J.* **2003**, *39* (5), 897–902. https://doi.org/10.1016/S0014-3057(02)00355-5.

(148) Saroj, A. L.; Singh, R. K.; Chandra, S. Studies on Polymer Electrolyte Poly(Vinyl) Pyrrolidone (PVP) Complexed with Ionic Liquid: Effect of Complexation on Thermal Stability, Conductivity and Relaxation Behaviour. *Mater. Sci. Eng. B* **2013**, *178* (4), 231–238. https://doi.org/10.1016/j.mseb.2012.11.007.

(149) Ravi, M.; Pavani, Y.; Bhavani, S.; Sharma, A. K.; Narasimha Rao, V. V. R. Investigations on Structural and Electrical Properties of KClO4 Complexed PVP Polymer Electrolyte Films. *Int. J. Polym. Mater.* **2012**, *61* (5), 309–322. https://doi.org/10.1080/00914037.2011.584225.

(150) Xu, W.; Pei, X.; Diercks, C. S.; Lyu, H.; Ji, Z.; Yaghi, O. M. A Metal-Organic Framework of Organic Vertices and Polyoxometalate Linkers as a Solid-State Electrolyte. *J. Am. Chem. Soc.* **2019**, *141* (44), 17522–17526. https://doi.org/10.1021/jacs.9b10418.

(151) Hou, T.; Xu, W.; Pei, X.; Jiang, L.; Yaghi, O. M.; Persson, K. A. Ionic Conduction Mechanism and Design of Metal–Organic Framework Based Quasi-Solid-State Electrolytes. *J. Am. Chem. Soc.* **2022**, *144* (30), 13446–13450. https://doi.org/10.1021/jacs.2c03710.

(152) Chen, T.; Chen, S.; Chen, Y.; Zhao, M.; Losic, D.; Zhang, S. Metal-Organic Frameworks Containing Solid-State Electrolytes for Lithium Metal Batteries and Beyond. *Mater. Chem. Front.* **2021**, *5* (4), 1771–1794. https://doi.org/10.1039/D0QM00856G.

(153) Kharod, R. A.; Andrews, J. L.; Dincă, M. Teaching Metal-Organic Frameworks to Conduct: Ion and Electron Transport in Metal-Organic Frameworks. *Annu. Rev. Mater. Res.* **2022**, *52* (1), 103–128. https://doi.org/10.1146/annurev-matsci-080619-012811.

(154) Shen, L.; Wu, H. Bin; Liu, F.; Brosmer, J. L.; Shen, G.; Wang, X.; Zink, J. I.; Xiao, Q.; Cai, M.; Wang, G.; Lu, Y.; Dunn, B. Creating Lithium-Ion Electrolytes with Biomimetic Ionic Channels in Metal–Organic Frameworks. *Adv. Mater.* **2018**, *30* (23). https://doi.org/10.1002/adma.201707476.

(155) Chen, N.; Li, Y.; Dai, Y.; Qu, W.; Xing, Y.; Ye, Y.; Wen, Z.; Guo, C.; Wu, F.; Chen, R. A Li + Conductive Metal Organic Framework Electrolyte Boosts the High-Temperature Performance of Dendrite-Free Lithium Batteries. *J. Mater. Chem. A* **2019**, *7* (16), 9530–9536. https://doi.org/10.1039/C8TA12539B.

(156) Farina, M.; Duff, B. B.; Tealdi, C.; Pugliese, A.; Blanc, F.; Quartarone, E. Li + Dynamics of Liquid Electrolytes Nanoconfined in Metal–Organic Frameworks. *ACS Appl. Mater. Interfaces* **2021**, *13* (45), 53986–53995. https://doi.org/10.1021/acsami.1c16214.

(157) Xue, W.; Sewell, C. D.; Zhou, Q.; Lin, Z. Metal–Organic Frameworks for Ion Conduction. *Angew. Chemie Int. Ed.* **2022**, *61* (34). https://doi.org/10.1002/anie.202206512.

(158) Abdul Halim, S. I.; Chan, C. H.; Apotheker, J. Basics of Teaching Electrochemical Impedance Spectroscopy of Electrolytes for Ion-Rechargeable Batteries - Part 2: Dielectric Response of (Non-) Polymer Electrolytes. *Chem. Teach. Int.* **2021**, *3* (2), 117–129. https://doi.org/10.1515/cti-2020-0018.

(159) Laschuk, N. O.; Easton, E. B.; Zenkina, O. V. Reducing the Resistance for the Use of Electrochemical Impedance Spectroscopy Analysis in Materials Chemistry. *RSC Adv.* **2021**, *11* (45), 27925–27936. https://doi.org/10.1039/D1RA03785D.

(160) Abdul Halim, S. I.; Chan, C. H.; Apotheker, J. Basics of Teaching Electrochemical Impedance Spectroscopy of Electrolytes for Ion-Rechargeable Batteries - Part 1: A Good Practice on Estimation of Bulk Resistance of Solid Polymer Electrolytes. *Chem. Teach. Int.* **2021**, *3* (2), 105–115. https://doi.org/10.1515/cti-2020-0011.

(161) Arof, A. K.; Amirudin, S.; Yusof, S. Z.; Noor, I. M. A Method Based on Impedance Spectroscopy to Determine Transport Properties of Polymer Electrolytes. *Phys. Chem. Chem. Phys.* **2014**, *16* (5), 1856–1867. https://doi.org/10.1039/c3cp53830c.

(162) Vadhva, P.; Hu, J.; Johnson, M. J.; Stocker, R.; Braglia, M.; Brett, D. J. L.; Rettie, A. J. E. Electrochemical Impedance Spectroscopy for All-Solid-State Batteries: Theory, Methods and Future Outlook. *ChemElectroChem* **2021**, *8* (11), 1930–1947. https://doi.org/10.1002/celc.202100108.

(163) Talaie, E.; Bonnick, P.; Sun, X.; Pang, Q.; Liang, X.; Nazar, L. F. Methods and Protocols for Electrochemical Energy Storage Materials Research. *Chem. Mater.* **2017**, *29* (1), 90–105. https://doi.org/10.1021/acs.chemmater.6b02726.

(164) Yang, X.; Rogach, A. L. Electrochemical Techniques in Battery Research: A Tutorial for Nonelectrochemists. *Adv. Energy Mater.* **2019**, *9* (25), 1900747. https://doi.org/10.1002/aenm.201900747.

(165) Nath, K.; Bin Rahaman, A.; Moi, R.; Maity, K.; Biradha, K. Porous Li-MOF as a Solid-State Electrolyte: Exploration of Lithium Ion Conductivity through Bio-Inspired Ionic Channels. *Chem. Commun.* **2020**, *56* (94), 14873–14876. https://doi.org/10.1039/D0CC05728B.

(166) Yang, H.; Liu, B.; Bright, J.; Kasani, S.; Yang, J.; Zhang, X.; Wu, N. A Single-Ion Conducting UiO-66 Metal-Organic Framework Electrolyte for All-Solid-State Lithium Batteries. *ACS Appl. Energy Mater.* **2020**, *3* (4), 4007–4013. https://doi.org/10.1021/acsaem.0c00410.

(167) Park, S. S.; Tulchinsky, Y.; Dinca, M. Single-Ion Li + , Na + , and Mg 2+ Solid Electrolytes Supported by a Mesoporous Anionic Cu − Azolate Metal − Organic Framework. **2017**, 2–5. https://doi.org/10.1021/jacs.7b06197.

(168) Wiers, B. M.; Foo, M.-L.; Balsara, N. P.; Long, J. R. A Solid Lithium Electrolyte via Addition of Lithium Isopropoxide to a Metal–Organic Framework with Open Metal Sites. *J. Am. Chem. Soc.* **2011**, *133* (37), 14522–14525. https://doi.org/10.1021/ja205827z.

(169) Shen, L.; Wu, H. Bin; Liu, F.; Brosmer, J. L.; Shen, G.; Wang, X.; Zink, J. I.; Xiao, Q.; Cai, M.; Wang, G.; Lu, Y.; Dunn, B. Creating Lithium-Ion Electrolytes with Biomimetic Ionic Channels in Metal–Organic Frameworks. *Adv. Mater.* **2018**, *30* (23), 1–8. https://doi.org/10.1002/adma.201707476.

(170) Li, M.; Chen, T.; Song, S.; Li, Y.; Bae, J. HKUST-1@IL-Li Solid-State Electrolyte with 3D Ionic Channels and Enhanced Fast Li+ Transport for Lithium Metal Batteries at High Temperature. *Nanomaterials* **2021**, *11* (3), 736. https://doi.org/10.3390/nano11030736.

(171) Yang, H.; Liu, B.; Bright, J.; Kasani, S.; Yang, J.; Zhang, X.; Wu, N. A Single-Ion Conducting UiO-66 Metal–Organic Framework Electrolyte for All-Solid-State Lithium Batteries. *ACS Appl. Energy Mater.* **2020**, *3* (4), 4007–4013. https://doi.org/10.1021/acsaem.0c00410.

(172) Mulfort, K. L.; Hupp, J. T. Chemical Reduction of Metal−Organic Framework Materials as a Method to Enhance Gas Uptake and Binding. *J. Am. Chem. Soc.* **2007**, *129* (31), 9604–9605. https://doi.org/10.1021/ja0740364.

(173) Stock, N.; Biswas, S. Synthesis of Metal-Organic Frameworks (MOFs): Routes to Various MOF Topologies, Morphologies, and Composites. *Chem. Rev.* **2012**, *112* (2), 933–969. https://doi.org/10.1021/cr200304e.

(174) Yuan, S.; Feng, L.; Wang, K.; Pang, J.; Bosch, M.; Lollar, C.; Sun, Y.; Qin, J.; Yang, X.; Zhang, P.; Wang, Q.; Zou, L.; Zhang, Y.; Zhang, L.; Fang, Y.; Li, J.; Zhou, H. C. Stable Metal–Organic Frameworks: Design, Synthesis, and Applications. *Adv. Mater.* **2018**, *30* (37), 1–35. https://doi.org/10.1002/adma.201704303.

(175) Dawood, S.; Yarbrough, R.; Davis, K.; Rathnayake, H. Self-Assembly and Optoelectronic Properties of Isoreticular MOF Nanocrystals. *Synth. Met.* **2019**, *252* (February), 107–112. https://doi.org/10.1016/j.synthmet.2019.04.018.

(176) Mai, Z.; Liu, D. Synthesis and Applications of Isoreticular Metal–Organic Frameworks IRMOFs- n (n = 1, 3, 6, 8). *Cryst. Growth Des.* **2019**, *19* (12), 7439–7462. https://doi.org/10.1021/acs.cgd.9b00879.

(177) Furukawa, H.; Go, Y. B.; Ko, N.; Park, Y. K.; Uribe-Romo, F. J.; Kim, J.; O'Keeffe, M.; Yaghi, O. M. Isoreticular Expansion of Metal–Organic Frameworks with Triangular and Square Building Units and the Lowest Calculated Density for Porous Crystals. *Inorg. Chem.* **2011**, *50* (18), 9147–9152. https://doi.org/10.1021/ic201376t.

(178) Eddaoudi, M.; Kim, J.; Rosi, N.; Vodak, D.; Wachter, J.; O'Keeffe, M.; Yaghi, O. M. Systematic Design of Pore Size and Functionality in Isoreticular MOFs and Their Application in Methane Storage. *Science.* **2002**, *295* (5554), 469–472. https://doi.org/10.1126/science.1067208.

(179) Eddaoudi, M.; Kim, J.; Rosi, N.; Vodak, D.; Wachter, J.; O'Keeffe, M.; Yaghi, O. M. Systematic Design of Pore Size and Functionality in Isoreticular MOFs and Their Application in Methane Storage. *Science.* **2002**, *295* (5554), 469–472. https://doi.org/10.1126/science.1067208.

(180) Yuan, L.; Tian, M.; Lan, J.; Cao, X.; Wang, X.; Chai, Z.; Gibson, J. K.; Shi, W. Defect Engineering in Metal–Organic Frameworks: A New Strategy to Develop Applicable Actinide Sorbents. *Chem. Commun.* **2018**, *54* (4), 370–373. https://doi.org/10.1039/C7CC07527H.

(181) Howarth, A. J.; Peters, A. W.; Vermeulen, N. A.; Wang, T. C.; Hupp, J. T.; Farha, O. K. Best Practices for the Synthesis, Activation, and Characterization of Metal−organic Frameworks. *Chem. Mater.* **2017**, *29* (1), 26–39. https://doi.org/10.1021/acs.chemmater.6b02626.

(182) Kökçam-Demir, Ü.; Goldman, A.; Esrafili, L.; Gharib, M.; Morsali, A.; Weingart, O.; Janiak, C. Coordinatively Unsaturated Metal Sites (Open Metal Sites) in Metal-Organic Frameworks: Design and Applications. *Chem. Soc. Rev.* **2020**, *49* (9), 2751–2798. https://doi.org/10.1039/c9cs00609e.

(183) Mondloch, J. E.; Karagiaridi, O.; Farha, O. K.; Hupp, J. T. Activation of Metal-Organic Framework Materials. *CrystEngComm* **2013**, *15* (45), 9258–9264. https://doi.org/10.1039/c3ce41232f.

(184) Liu, Y. Y.; Zhang, J.; Sun, L. X.; Xu, F.; You, W. S.; Zhao, Y. Solvothermal Synthesis and Characterization of a Lithium Coordination Polymer Possessing a Highly Stable 3D Network Structure. *Inorg. Chem. Commun.* **2008**, *11* (4), 396–399. https://doi.org/10.1016/j.inoche.2007.12.030.

(185) Banerjee, D.; Kim, S. J.; Parise, J. B. Lithium Based Metal−Organic Framework with Exceptional Stability. *Cryst. Growth Des.* **2009**, *9* (5), 2500–2503. https://doi.org/10.1021/cg8014157.

(186) Banerjee, D.; Borkowski, L. A.; Kim, S. J.; Parise, J. B. Synthesis and Structural Characterization of Lithium-Based Metal−Organic Frameworks. *Cryst. Growth Des.* **2009**, *9* (11), 4922–4926. https://doi.org/10.1021/cg900705c.

(187) Han, Y.; Yang, H.; Guo, X. Synthesis Methods and Crystallization of MOFs. In *Synthesis Methods and Crystallization*; IntechOpen, 2020; pp 1–22. https://doi.org/10.5772/intechopen.90435.

(188) Butova, V. V; Soldatov, M. A.; Guda, A. A.; Lomachenko, K. A.; Lamberti, C. Metal-Organic Frameworks: Structure, Properties, Methods of Synthesis and Characterization. *Russ. Chem. Rev.* **2016**, *85* (3), 280–307. https://doi.org/10.1070/RCR4554.

(189) Karthikeyan, N.; Joseph Prince, J.; Ramalingam, S.; Periandy, S. Electronic [UV–Visible] and Vibrational [FT-IR, FT-Raman] Investigation and NMR–Mass Spectroscopic Analysis of Terephthalic Acid Using Quantum Gaussian Calculations. *Spectrochim. Acta Part A Mol. Biomol. Spectrosc.* **2015**, *139*, 229–242. https://doi.org/10.1016/j.saa.2014.11.112.

(190) Kazarian, S. G.; Martirosyan, G. G. ATR-IR Spectroscopy of Superheated Water and in Situ Study of the Hydrothermal Decomposition of Poly(Ethylene Terephthalate). *Phys. Chem. Chem. Phys.* **2002**, *4* (15), 3759–3763. https://doi.org/10.1039/b202119f.

(191) Arias, S.; Eon, J. G.; San Gil, R. A. S.; Licea, Y. E.; Palacio, L. A.; Faro, A. C. Synthesis and Characterization of Terephthalate-Intercalated NiAl Layered Double Hydroxides with High Al Content. *Dalt. Trans.* **2013**, *42* (6), 2084–2093. https://doi.org/10.1039/C2DT31502E.

(192) Desai, A. V.; Rainer, D. N.; Pramanik, A.; Cabañero, J. M.; Morris, R. E.; Armstrong, A. R. Rapid Microwave-Assisted Synthesis and Electrode Optimization of Organic Anode Materials in Sodium-Ion Batteries. *Small Methods* **2021**, *5* (12), 2101016. https://doi.org/10.1002/smtd.202101016.

(193) Zhang, W.; Yin, H.; Yu, Z.; Jia, X.; Liang, J.; Li, G.; Li, Y.; Wang, K. Facile Synthesis of 4,4′-Biphenyl Dicarboxylic Acid-Based Nickel Metal Organic Frameworks with a Tunable Pore Size towards High-Performance Supercapacitors. *Nanomaterials* **2022**, *12* (12), 2062. https://doi.org/10.3390/nano12122062.

(194) Butreddy, P.; Holden, H.; Rathnayake, H. Metal Ion-Directed Coordination Programming of Biomolecules to Bioinspired Nanoflowers. *Macromol. Chem. Phys.* **2022**, *223* (21), 2200237. https://doi.org/10.1002/macp.202200237.

(195) Saha, S.; Dawood, S.; Butreddy, P.; Pathiraja, G.; Rathnayake, H. Novel Biodegradable Low- κ Dielectric Nanomaterials from Natural Polyphenols. *RSC Adv.* **2021**, *11* (27), 16698–16705. https://doi.org/10.1039/D1RA01513C.

(196) Dupin, J.-C.; Gonbeau, D.; Vinatier, P.; Levasseur, A. Systematic XPS Studies of Metal Oxides, Hydroxides and Peroxides. *Phys. Chem. Chem. Phys.* **2000**, *2* (6), 1319–1324. https://doi.org/10.1039/a908800h.

(197) Morais, A.; Alves, J. P. C.; Lima, F. A. S.; Lira-Cantu, M.; Nogueira, A. F. Enhanced Photovoltaic Performance of Inverted Hybrid Bulk-Heterojunction Solar Cells Using TiO 2 /Reduced Graphene Oxide Films as Electron Transport Layers. *J. Photonics Energy* **2015**, *5* (1), 057408. https://doi.org/10.1117/1.JPE.5.057408.

(198) SAHA, D.; MADRAS, G.; BHATTACHARYYA, A. J.; GURU ROW, T. N. Synthesis, Structure and Ionic Conductivity in Scheelite Type Li0·5Ce0·5−x Ln x MoO4 (x = 0 and 0·25, Ln = Pr, Sm). *J. Chem. Sci.* **2011**, *123* (1), 5–13. https://doi.org/10.1007/s12039-011-0068-5.

(199) Elmas Kimyonok, A. B.; Ulutürk, M. Determination of the Thermal Decomposition Products of Terephthalic Acid by Using Curie-Point Pyrolyzer. *J. Energ. Mater.* **2016**, *34* (2), 113–122. https://doi.org/10.1080/07370652.2015.1005773.

(200) Li, H.; Eddaoudi, M.; Groy, T. L.; Yaghi, O. M. Establishing Microporosity in Open Metal−Organic Frameworks: Gas Sorption Isotherms for Zn(BDC) (BDC = 1,4-Benzenedicarboxylate). *J. Am. Chem. Soc.* **1998**, *120* (33), 8571–8572. https://doi.org/10.1021/ja981669x.

(201) Loiseau, T.; Serre, C.; Huguenard, C.; Fink, G.; Taulelle, F.; Henry, M.; Bataille, T.; Férey, G. A Rationale for the Large Breathing of the Porous Aluminum Terephthalate (MIL-53) Upon Hydration. *Chem. - A Eur. J.* **2004**, *10* (6), 1373–1382. https://doi.org/10.1002/chem.200305413.

(202) Liu, Y.-Y.; Zhang, J.; Sun, L.-X.; Xu, F.; You, W.-S.; Zhao, Y. Solvothermal Synthesis and Characterization of a Lithium Coordination Polymer Possessing a Highly Stable 3D Network Structure. *Inorg. Chem. Commun.* **2008**, *11* (4), 396–399. https://doi.org/10.1016/j.inoche.2007.12.030.

(203) Nasruddin; Zulys, A.; Yulia, F.; Buhori, A.; Muhadzib, N.; Ghiyats, M.; Saha, B. B. Synthesis and Characterization of a Novel Microporous Lanthanide Based Metal-Organic Framework (MOF) Using Napthalenedicarboxylate Acid. *J. Mater. Res. Technol.* **2020**, *9* (4), 7409–7417. https://doi.org/10.1016/j.jmrt.2020.05.015.

(204) Banerjee, D.; Borkowski, L. A.; Kim, S. J.; Parise, J. B. Synthesis and Structural Characterization of Lithium-Based Metal-Organic Frameworks. *Cryst. Growth Des.* **2009**, *9* (11), 4922–4926. https://doi.org/10.1021/cg900705c.

(205) Liu, X.; Guo; Liu, B.; Chen, W.-T.; Huang, J.-S. A Novel 2-D Honeycomb-like Lithium Coordination Polymer Containing 42-Membered Rings. *Cryst. Growth Des.* **2005**, *5* (3), 841–843. https://doi.org/10.1021/cg049570r.

(206) Liu, X.; Guo, G.-C.; Wu, A.-Q.; Huang, J.-S. A Novel Stair-like Lithium Coordination Polymer Constructed from 4,4′-Bipyridine. *Inorg. Chem. Commun.* **2004**, *7* (12), 1261–1263. https://doi.org/10.1016/j.inoche.2004.09.023.

(207) Langford, J. I.; Wilson, A. J. C. Scherrer after Sixty Years: A Survey and Some New Results in the Determination of Crystallite Size. *J. Appl. Crystallogr.* **1978**, *11* (2), 102–113. https://doi.org/10.1107/S0021889878012844.

(208) Ambroz, F.; Macdonald, T. J.; Martis, V.; Parkin, I. P. Evaluation of the BET Theory for the Characterization of Meso and Microporous MOFs. *Small Methods* **2018**, *2* (11), 1–17. https://doi.org/10.1002/smtd.201800173.

(209) Thommes, M.; Smarsly, B.; Groenewolt, M.; Ravikovitch, P. I.; Neimark, A. V. Adsorption Hysteresis of Nitrogen and Argon in Pore Networks and Characterization of Novel Micro- and Mesoporous Silicas. *Langmuir* **2006**, *22* (2), 756–764. https://doi.org/10.1021/la051686h.

(210) Galarneau, A.; Cambon, H.; Di Renzo, F.; Fajula, F. True Microporosity and Surface Area of Mesoporous SBA-15 Silicas as a Function of Synthesis Temperature. *Langmuir* **2001**, *17* (26), 8328–8335. https://doi.org/10.1021/la0105477.

(211) Li, H.; Eddaoudi, M.; O'Keeffe, M.; Yaghi, O. M. Design and Synthesis of an Exceptionally Stable and Highly Porous Metal-Organic Framework. *Nature* **1999**, *402* (6759), 276–279. https://doi.org/10.1038/46248.

(212) Brus, J.; Czernek, J.; Urbanova, M.; Rohlíček, J.; Plecháček, T. Transferring Lithium Ions in the Nanochannels of Flexible Metal–Organic Frameworks Featuring Superchaotropic Metallacarborane Guests: Mechanism of Ionic Conductivity at Atomic Resolution. *ACS Appl. Mater. Interfaces* **2020**, *12* (42), 47447–47456. https://doi.org/10.1021/acsami.0c12293.

(213) Li, Z.; Yuan, L.; Yi, Z.; Sun, Y.; Liu, Y.; Jiang, Y.; Shen, Y.; Xin, Y.; Zhang, Z.; Huang, Y. Insight into the Electrode Mechanism in Lithium-Sulfur Batteries with Ordered Microporous Carbon Confined Sulfur as the Cathode. *Adv. Energy Mater.* **2014**, *4* (7), 1301473. https://doi.org/10.1002/aenm.201301473.

(214) Farina, M.; Duff, B. B.; Tealdi, C.; Pugliese, A.; Blanc, F.; Quartarone, E. Li + Dynamics of Liquid Electrolytes Nanoconfined in Metal–Organic Frameworks. *ACS Appl. Mater. Interfaces* **2021**, *13* (45), 53986–53995. https://doi.org/10.1021/acsami.1c16214.

(215) Petrowsky, M.; Frech, R. Temperature Dependence of Ion Transport: The Compensated Arrhenius Equation. *J. Phys. Chem. B* **2009**, *113* (17), 5996–6000. https://doi.org/10.1021/jp810095g.

(216) Aziz, S. B.; Woo, T. J.; Kadir, M. F. Z.; Ahmed, H. M. A Conceptual Review on Polymer Electrolytes and Ion Transport Models. *J. Sci. Adv. Mater. Devices* **2018**, *3* (1), 1–17. https://doi.org/10.1016/j.jsamd.2018.01.002.

(217) Sharma, M.; Yashonath, S. Correlation between Conductivity or Diffusivity and Activation Energy in Amorphous Solids. *J. Chem. Phys.* **2008**, *129* (14), 144103. https://doi.org/10.1063/1.2990744.

(218) Zeier, W. G.; Zhou, S.; Lopez-Bermudez, B.; Page, K.; Melot, B. C. Dependence of the Li-Ion Conductivity and Activation Energies on the Crystal Structure and Ionic Radii in Li 6 MLa 2 Ta 2 O 12. *ACS Appl. Mater. Interfaces* **2014**, *6* (14), 10900–10907. https://doi.org/10.1021/am4060194.

(219) Nath, K.; Rahaman, A. Bin; Moi, R.; Maity, K.; Biradha, K. Porous Li-MOF as Solid-State Electrolyte : Exploration of Lithium Ion Conductivity through Bio-Inspired Ionic Channels Table of Contents : **2020**.

(220) Miner, E. M.; Park, S. S.; Dincă, M. High Li + and Mg 2+ Conductivity in a Cu-Azolate Metal–Organic Framework. *J. Am. Chem. Soc.* **2019**, *141* (10), 4422–4427. https://doi.org/10.1021/jacs.8b13418.

(221) Osman, Z.; Arof, A. K. FTIR Studies of Chitosan Acetate Based Polymer Electrolytes. *Electrochim. Acta* **2003**, *48* (8), 993–999. https://doi.org/10.1016/S0013-4686(02)00812-5.

(222) Ikezawa, Y.; Nishi, H. In Situ FTIR Study of the Cu Electrode/Ethylene Carbonate+dimethyl Carbonate Solution Interface. *Electrochim. Acta* **2008**, *53* (10), 3663–3669. https://doi.org/10.1016/j.electacta.2007.12.038.

(223) Huang, B. Lithium Ion Conduction in Polymer Electrolytes Based on PAN. *Solid State Ionics* **1996**, *85* (1–4), 79–84. https://doi.org/10.1016/0167-2738(96)00044-6.

(224) Wang, Z.; Huang, B.; Huang, H.; Chen, L.; Xue, R.; Wang, F. Infrared Spectroscopic Study of the Interaction between Lithium Salt LiC1O4 and the Plasticizer Ethylene Carbonate in the Polyacrylonitrile-Based Electrolyte. *Solid State Ionics* **1996**, *85* (1–4), 143–148. https://doi.org/10.1016/0167-2738(96)00051-3.

(225) Jiang, B.; Ponnuchamy, V.; Shen, Y.; Yang, X.; Yuan, K.; Vetere, V.; Mossa, S.; Skarmoutsos, I.; Zhang, Y.; Zheng, J. The Anion Effect on Li + Ion Coordination Structure in Ethylene Carbonate Solutions. *J. Phys. Chem. Lett.* **2016**, *7* (18), 3554–3559. https://doi.org/10.1021/acs.jpclett.6b01664.

(226) Angell, C. L. The Infra-Red Spectra and Structure of Ethylene Carbonate. *Trans. Faraday Soc.* **1956**, *52*, 1178. https://doi.org/10.1039/tf9565201178.

(227) Masia, M.; Probst, M.; Rey, R. Ethylene Carbonate - Li+ : A Theoretical Study of Structural and Vibrational Properties in Gas and Liquid Phases. *J. Phys. Chem. B* **2004**, *108*, 2016–2027.

(228) Weber, I.; Schnaidt, J.; Wang, B.; Diemant, T.; Behm, R. J. Model Studies on the Solid Electrolyte Interphase Formation on Graphite Electrodes in Ethylene Carbonate and Dimethyl Carbonate: Highly Oriented Pyrolytic Graphite. *ChemElectroChem* **2019**, *6* (19), 4985–4997. https://doi.org/10.1002/celc.201900909.

(229) Fu, X.; Deng, X.; Deng, Y.; Xiong, X.; Zheng, Y.; Zhang, Z.; Dang, D.; Wang, G. Lithium Perchlorate Additive for Dendritic-Free and Long-Life Li Metal Batteries. *Energy & Fuels* **2022**, *36* (18), 11219–11226. https://doi.org/10.1021/acs.energyfuels.2c02242.

(230) Shutthanandan, V.; Nandasiri, M.; Zheng, J.; Engelhard, M. H.; Xu, W.; Thevuthasan, S.; Murugesan, V. Applications of XPS in the Characterization of Battery Materials. *J. Electron Spectros. Relat. Phenomena* **2019**, *231* (November 2017), 2–10. https://doi.org/10.1016/j.elspec.2018.05.005.

(231) Fingerle, M.; Späth, T.; Schulz, N.; Hausbrand, R. Adsorption of Ethylene Carbonate on Lithium Cobalt Oxide Thin Films: A Synchrotron-Based Spectroscopic Study of the Surface Chemistry. *Chem. Phys.* **2017**, *498–499*, 19–24. https://doi.org/10.1016/j.chemphys.2017.09.004.

(232) Wood, K. N.; Teeter, G. XPS on Li-Battery-Related Compounds: Analysis of Inorganic SEI Phases and a Methodology for Charge Correction. *ACS Appl. Energy Mater.* **2018**, *1* (9), 4493–4504. https://doi.org/10.1021/acsaem.8b00406.

(233) Westhead, O.; Spry, M.; Bagger, A.; Shen, Z.; Yadegari, H.; Favero, S.; Tort, R.; Titirici, M.; Ryan, M. P.; Jervis, R.; Katayama, Y.; Aguadero, A.; Regoutz, A.; Grimaud, A.; Stephens, I. E. L. The Role of Ion Solvation in Lithium Mediated Nitrogen Reduction. *J. Mater. Chem. A* **2023**. https://doi.org/10.1039/D2TA07686A.

(234) Gurumendi, M.; López, F.; Borrero-González, L. J.; Terencio, T.; Caetano, M.; Reinoso, C.; González, G. Enhanced Chitosan Photoluminescence by Incorporation of Lithium Perchlorate. *ACS Omega* **2023**, *8* (15), 13763–13774. https://doi.org/10.1021/acsomega.2c08072.

(235) Metzger, M.; Walke, P.; Solchenbach, S.; Salitra, G.; Aurbach, D.; Gasteiger, H. A. Evaluating the High-Voltage Stability of Conductive Carbon and Ethylene Carbonate with Various Lithium Salts. *J. Electrochem. Soc.* **2020**, *167* (16), 160522. https://doi.org/10.1149/1945-7111/abcabd.

(236) McOwen, D. W.; Seo, D. M.; Borodin, O.; Vatamanu, J.; Boyle, P. D.; Henderson, W. A. Concentrated Electrolytes: Decrypting Electrolyte Properties and Reassessing Al Corrosion Mechanisms. *Energy Environ. Sci.* **2014**, *7* (1), 416–426. https://doi.org/10.1039/C3EE42351D.

(237) Manap, S. M.; Ahmad, A.; Sarjadi, M. S.; Anuar, F. H. Effect of Plasticizers and Lithium Perchlorate on Poly(L-Lactic Acid)-Poly(Propylene Glycol) Solid Polymer Electrolyte. *Malaysian J. Anal. Sci.* **2019**, *23* (4), 703–714. https://doi.org/10.17576/mjas-2019-2304-17.

(238) Zettl, R.; Lunghammer, S.; Gadermaier, B.; Boulaoued, A.; Johansson, P.; Wilkening, H. M. R.; Hanzu, I. High Li+ and Na+ Conductivity in New Hybrid Solid Electrolytes Based on the Porous MIL-121 Metal Organic Framework. *Adv. Energy Mater.* **2021**, *11* (16), 2003542. https://doi.org/10.1002/aenm.202003542.

(239) Zheng, Y.; Guo, J.; Ning, D.; Huang, Y.; Lei, W.; Li, J.; Li, J.; Schuck, G.; Shen, J.; Guo, Y.; Zhang, Q.; Tian, H.; Ian, H.; Shao, H. Design of Metal-Organic Frameworks for Improving Pseudo-Solid-State Magnesium-Ion Electrolytes: Open Metal Sites, Isoreticular Expansion, and Framework Topology. *J. Mater. Sci. Technol.* **2023**, *144*, 15–27. https://doi.org/10.1016/j.jmst.2022.09.058.

(240) Brus, J.; Czernek, J.; Urbanova, M.; Rohlíček, J.; Plecháček, T. Transferring Lithium Ions in the Nanochannels of Flexible Metal-Organic Frameworks Featuring Superchaotropic Metallacarborane Guests: Mechanism of Ionic Conductivity at Atomic Resolution. *ACS Appl. Mater. Interfaces* **2020**, *12* (42), 47447–47456. https://doi.org/10.1021/acsami.0c12293.

(241) Thomas, E. M.; Nguyen, P. H.; Jones, S. D.; Chabinyc, M. L.; Segalman, R. A.; Sivaraj, P.; Abhilash, K. P.; Nalini, B.; Perumal, P.; Selvin, P. C.; Li, S.; Zhang, S. Q.; Shen, L.; Liu, Q.; Ma, J. Bin; Lv, W.; He, Y. B.; Yang, Q. H.; Zha, W.; Xu, Y.; Chen, F.; Shen, Q.; Zhang, L.; Li, M. X.; Wang, X. W.; Yang, Y. Q.; Chang, Z.; Wu, Y. P.; Holze, R.; Osman, Z.; Arof, A. K.; Sulaeman, A. S.; Maddu, A.; Wahyudi, S. T.; Rifai, A.; Rosenwinkel, M. P.; Andersson, R.; Mindemark, J.; Scho, M.; Deepa, M.; Agnihotry, S. .; Gupta, D.; Chandra, R.; Young, J.; Kulick, P. M.; Juran, T. R.; Smeu, M.; Ramesh, S.; Ling, O. P.; State, S.; Genier, F. S.; Hosein, I. D.; Xu, K.; Deng, D.; Yang, H.; Wu, N.; Jennings, P.; Somerville, L.; Bareño, J.; Jennings, P.; Mcgordon, A.; Lyness, C.; Bloom, I.; Remko, M.; Rode, B. M.; Liu, Z.; Zhang, K.; Huang, G.; Bian, S.; Huang, Y.; Jiang, X.; Pan, Y.; Wang, Y.; Xia, X.; Xu, B.; Zhang, G.; Meyer, W. H.; Glikol, L. P.; Bogle, X.; Vazquez, R.; Greenbaum, S.; Cresce, A. V. W.; Xu, K.; Watanabe, M.; Kanba, M. O. T.; Nagaoka, K.; Li, G.; Huang, H.; Wang, F.; Bocharova, V.; Sokolov, A. P.; Aziz, S. B.; Dannoun, E. M. A.; Murad, A. R.; Mahmoud, K. H.; Brza, M. A.; Nofal, M. M.; Elsayed, K. A.; Abdullah, S. N.; Hadi, J. M.; Kadir, M. F. Z.; Baskoro, F.; Wong, H. Q.; Yen, H.; Thomas, S.; Ponnamma, D.; Zachariah, A. K.; Zahreddine, C.; Pak, Y. S.; Xu, G.; Reddy, V. P.; Lett, E. S.; Sahore, R.; Du, Z.; Chen, X. C.; Hawley, W. B.; Westover, A. S.; Dudney, N. J.; Selvalakshmi, S.; Mathavan, T.; Selvasekarapandian, S.; Premalatha, M.; Devices, E.; Teo, L. P.; Buraidah, M. H.; Ninham, B. W.; Nostro, P. Lo; Baglioni, P.; Series, P.--phenolate A.--phenoxy R.; Kotorlenko, L. A.; Aleksandrova, V. S.; Barbosa, J. C.; Gonçalves, R.; Costa, C. M.; Lanceros-Méndez, S.; Roeswitawati, D. Perspectives for Polymer Electrolytes: A View from Fundamentals of Ionic Conductivity. *Electrochim. Acta* **2022**, *10* (5), 14457–14464. https://doi.org/10.1021/cr500003w.

(242) Shen, L.; Wu, H. Bin; Liu, F.; Brosmer, J. L.; Shen, G.; Wang, X.; Zink, J. I.; Xiao, Q.; Cai, M.; Wang, G.; Lu, Y.; Dunn, B. Creating Lithium-Ion Electrolytes with Biomimetic Ionic Channels in Metal–Organic Frameworks. *Adv. Mater.* **2018**, *30* (23), 0–8. https://doi.org/10.1002/adma.201707476.

(243) Zhang, Z.; Shao, Y.; Lotsch, B.; Hu, Y.-S.; Li, H.; Janek, J.; Nazar, L. F.; Nan, C.-W.; Maier, J.; Armand, M.; Chen, L. New Horizons for Inorganic Solid State Ion Conductors. *Energy Environ. Sci.* **2018**, *11* (8), 1945–1976. https://doi.org/10.1039/C8EE01053F.

(244) Yang, H.; Wu, N. Ionic Conductivity and Ion Transport Mechanisms of Solid-State Lithium-Ion Battery Electrolytes: A Review. *Energy Sci. Eng.* **2022**, *10* (5), 1643–1671. https://doi.org/10.1002/ese3.1163.

(245) Perumal, P.; Selvasekarapandian, S.; Abhilash, K. P.; Sivaraj, P.; Hemalatha, R.; Selvin, P. C. Impact of Lithium Chlorate Salts on Structural and Electrical Properties of Natural Polymer Electrolytes for All Solid State Lithium Polymer Batteries. *Vacuum* **2019**, *159*, 277–281. https://doi.org/10.1016/j.vacuum.2018.10.043.

(246) Courtel, F. M.; Niketic, S.; Duguay, D.; Abu-Lebdeh, Y.; Davidson, I. J. Water-Soluble Binders for MCMB Carbon Anodes for Lithium-Ion Batteries. *J. Power Sources* **2011**, *196* (4), 2128–2134. https://doi.org/10.1016/j.jpowsour.2010.10.025.

(247) Yue, Z.; McEwen, I. J.; Cowie, J. M. G. Ion Conducting Behaviour and Morphology of Solid Polymer Electrolytes Based on a Regioselectively Substituted Cellulose Ether with PEO Side Chains. *J. Mater. Chem.* **2002**, *12* (8), 2281–2285. https://doi.org/10.1039/b201804g.

(248) Liu, B.; Huang, Y.; Cao, H.; Song, A.; Lin, Y.; Wang, M.; Li, X. A High-Performance and Environment-Friendly Gel Polymer Electrolyte for Lithium Ion Battery Based on Composited Lignin Membrane. *J. Solid State Electrochem.* **2018**, *22* (3), 807–816. https://doi.org/10.1007/s10008-017-3814-x.

(249) Asghar, A.; Abdul Samad, Y.; Singh Lalia, B.; Hashaikeh, R. PEG Based Quasi-Solid Polymer Electrolyte: Mechanically Supported by Networked Cellulose. *J. Memb. Sci.* **2012**, *421–422*, 85–90. https://doi.org/10.1016/j.memsci.2012.06.037.

(250) Gong, S. D.; Huang, Y.; Cao, H. J.; Lin, Y. H.; Li, Y.; Tang, S. H.; Wang, M. S.; Li, X. A Green and Environment-Friendly Gel Polymer Electrolyte with Higher Performances Based on the Natural Matrix of Lignin. *J. Power Sources* **2016**, *307*, 624–633. https://doi.org/10.1016/j.jpowsour.2016.01.030.

(251) Chupp, J.; Shellikeri, A.; Palui, G.; Chatterjee, J. Chitosan-Based Gel Film Electrolytes Containing Ionic Liquid and Lithium Salt for Energy Storage Applications. *J. Appl. Polym. Sci.* **2015**, *132* (26), 1–8. https://doi.org/10.1002/app.42143.

(252) Chitra, R.; Sathya, P.; Selvasekarapandian, S.; Meyvel, S. Synthesis and Characterization of Iota-Carrageenan Biopolymer Electrolyte with Lithium Perchlorate and Succinonitrile (Plasticizer). *Polym. Bull.* **2020**, *77* (3), 1555–1579. https://doi.org/10.1007/s00289-019-02822-y.

(253) Vieira, D. F.; Avellaneda, C. O.; Pawlicka, A. Conductivity Study of a Gelatin-Based Polymer Electrolyte. *Electrochim. Acta* **2007**, *53* (4), 1404–1408. https://doi.org/10.1016/j.electacta.2007.04.034.

(254) Quideau, S.; Deffieux, D.; Douat-Casassus, C.; Pouységu, L. Plant Polyphenols: Chemical Properties, Biological Activities, and Synthesis. *Angew. Chemie - Int. Ed.* **2011**, *50* (3), 586–621. https://doi.org/10.1002/anie.201000044.

(255) Tian, M.; Wu, P. Nature Plant Polyphenol Coating Silicon Submicroparticle Conjugated with Polyacrylic Acid for Achieving a High-Performance Anode of Lithium-Ion Battery. *ACS Appl. Energy Mater.* **2019**, *2* (7), 5066–5073. https://doi.org/10.1021/acsaem.9b00734.

(256) Slabbert, N. Complexation of Condensed Tannins with Metal Ions. In *Plant Polyphenols*; Springer US: Boston, MA, 1992; pp 421–436. https://doi.org/10.1007/978-1-4615-3476-1_23.

(257) Ejima, H.; Richardson, J. J.; Liang, K.; Best, J. P.; Van Koeverden, M. P.; Such, G. K.; Cui, J.; Caruso, F. One-Step Assembly of Coordination Complexes. *Science.* **2013**, *341* (6142), 154–157. https://doi.org/10.1126/science.1237265.

(258) Sahiner, N.; Sagbas, S.; Aktas, N. Single Step Natural Poly(Tannic Acid) Particle Preparation as Multitalented Biomaterial. *Mater. Sci. Eng. C* **2015**, *49*, 824–834. https://doi.org/10.1016/j.msec.2015.01.076.

(259) Kim, S.; Gim, T.; Kang, S. M. Versatile, Tannic Acid-Mediated Surface PEGylation for Marine Antifouling Applications. *ACS Appl. Mater. Interfaces* **2015**, *7* (12), 6412–6416. https://doi.org/10.1021/acsami.5b01304.

(260) Fei, X.; Wei, W.; Zhao, F.; Zhu, Y.; Luo, J.; Chen, M.; Liu, X. Efficient Toughening of Epoxy-Anhydride Thermosets with a Biobased Tannic Acid Derivative. *ACS Sustain. Chem. Eng.* **2017**, *5* (1), 596–603. https://doi.org/10.1021/acssuschemeng.6b01967.

(261) Rathnayake, H.; Dawood, S.; Pathiraja, G.; Adrah, K.; Ayodele, O. Green Synthesis of De Novo Bioinspired Porous Iron-Tannate Microstructures with Amphoteric Surface Properties. *Sustain. Chem.* **2022**, *3* (2), 192–204. https://doi.org/10.3390/suschem3020013.

(262) Pan, L.; Wang, H.; Wu, C.; Liao, C.; Li, L. Tannic-Acid-Coated Polypropylene Membrane as a Separator for Lithium-Ion Batteries. *ACS Appl. Mater. Interfaces* **2015**, *7* (29), 16003–16010. https://doi.org/10.1021/acsami.5b04245.

(263) Cook, T. R.; Zheng, Y.-R.; Stang, P. J. Metal–Organic Frameworks and Self-Assembled Supramolecular Coordination Complexes: Comparing and Contrasting the Design, Synthesis, and Functionality of Metal–Organic Materials. *Chem. Rev.* **2013**, *113* (1), 734–777. https://doi.org/10.1021/cr3002824.

(264) Hao, Y.; Zhang, N.; Luo, J.; Liu, X. Green Synthesis of Silver Nanoparticles by Tannic Acid with Improved Catalytic Performance Towards the Reduction of Methylene Blue. *Nano* **2018**, *13* (1), 1–13. https://doi.org/10.1142/S1793292018500030.

(265) Pantoja-Castroa, Mayra a. González-rodríGuez, H. Study by Infrared Spectroscopy and Thermogravimetric Analysis of Tannins and Tannic Acid. *Rev. Latinoam. química* **2011**, *39* (3), 107–112.

(266) Abulateefeh, S. R.; Taha, M. O. Enhanced Drug Encapsulation and Extended Release Profiles of Calcium–Alginate Nanoparticles by Using Tannic Acid as a Bridging Cross-Linking Agent. *J. Microencapsul.* **2015**, *32* (1), 96–105. https://doi.org/10.3109/02652048.2014.985343.

(267) Topal, F.; Nar, M.; Gocer, H.; Kalin, P.; Kocyigit, U. M.; Gülçin, İ.; Alwasel, S. H. Antioxidant Activity of Taxifolin: An Activity–Structure Relationship. *J. Enzyme Inhib. Med. Chem.* **2016**, *31* (4), 674–683. https://doi.org/10.3109/14756366.2015.1057723.

(268) Koch, E.-C. Acid-Base Interactions in Energetic Materials: I. The Hard and Soft Acids and Bases (HSAB) Principle-Insights to Reactivity and Sensitivity of Energetic Materials. *Propellants, Explos. Pyrotech.* **2005**, *30* (1), 5–16. https://doi.org/10.1002/prep.200400080.

(269) Nam, S.; Easson, M. W.; Condon, B. D.; Hillyer, M. B.; Sun, L.; Xia, Z.; Nagarajan, R. A Reinforced Thermal Barrier Coat of a Na-Tannic Acid Complex from the View of Thermal Kinetics. *RSC Adv.* **2019**, *9* (19), 10914–10926. https://doi.org/10.1039/c9ra00763f.

(270) Xia, T.; Wang, Y.; Wang, B.; Yang, Z.; Pan, G.; Zhang, L.; Zhang, J. Natural Compounds Gallic Acid Derivatives for Long-Life Li/Na Organic Batteries. *ChemElectroChem* **2019**, *6* (18), 4765–4772. https://doi.org/10.1002/celc.201901064.

(271) Thommes, M.; Kaneko, K.; Neimark, A. V.; Olivier, J. P.; Rodriguez-Reinoso, F.; Rouquerol, J.; Sing, K. S. W. Physisorption of Gases, with Special Reference to the Evaluation of Surface Area and Pore Size Distribution (IUPAC Technical Report). *Pure Appl. Chem.* **2015**, *87* (9–10), 1051–1069. https://doi.org/10.1515/pac-2014-1117.

(272) Nakamura, T.; Homma, K.; Tachibana, K. Impedance Spectroscopy of Manganite Films Prepared by Metalorganic Chemical Vapor Deposition. *J. Nanosci. Nanotechnol.* **2011**, *11* (9), 8408–8411. https://doi.org/10.1166/jnn.2011.5092.

(273) Aziz, S. B. Li+ Ion Conduction Mechanism in Poly (ε-Caprolactone)-Based Polymer Electrolyte. *Iran. Polym. J.* **2013**, *22* (12), 877–883. https://doi.org/10.1007/s13726-013-0186-7.

(274) Aziz, S. B.; Dannoun, E. M. A.; Murad, A. R.; Mahmoud, K. H.; Brza, M. A.; Nofal, M. M.; Elsayed, K. A.; Abdullah, S. N.; Hadi, J. M.; Kadir, M. F. Z. Influence of Scan Rate on CV Pattern: Electrical and Electrochemical Properties of Plasticized Methylcellulose: Dextran (MC:Dex) Proton Conducting Polymer Electrolytes. *Alexandria Eng. J.* **2022**, *61* (8), 5919–5937. https://doi.org/10.1016/j.aej.2021.11.020.

(275) Sivakumar, M.; Subadevi, R.; Rajendran, S.; Wu, H.-C.; Wu, N.-L. Compositional Effect of PVdF–PEMA Blend Gel Polymer Electrolytes for Lithium Polymer Batteries. *Eur. Polym. J.* **2007**, *43* (10), 4466–4473. https://doi.org/10.1016/j.eurpolymj.2007.08.001.

(276) MacHado, G. O.; Ferreira, H. C. A.; Pawlicka, A. Influence of Plasticizer Contents on the Properties of HEC-Based Solid Polymeric Electrolytes. *Electrochim. Acta* **2005**, *50* (19), 3827–3831. https://doi.org/10.1016/j.electacta.2005.02.041.

(277) Sulaeman, A. S.; Maddu, A.; Wahyudi, S. T.; Rifai, A. Salt Concentration Effect on Electrical and Dielectric Properties of Solid Polymer Electrolytes Based Carboxymethyl Cellulose for Lithium-Ion Batteries. *Biointerface Res. Appl. Chem.* **2022**, *12* (5), 6114–6123. https://doi.org/10.33263/BRIAC125.61146123.

(278) Morni, N. M.; Arof, A. K. Chitosan–Lithium Triflate Electrolyte in Secondary Lithium Cells. *J. Power Sources* **1999**, *77* (1), 42–48. https://doi.org/10.1016/S0378-7753(98)00170-0.

(279) Fuentes, S.; Retuert, P. J.; González, G. Transparent Conducting Polymer Electrolyte by Addition of Lithium to the Molecular Complex Chitosane-Poly(Aminopropyl Siloxane). *Electrochim. Acta* **2003**, *48* (14-16 SPEC.), 2015–2019. https://doi.org/10.1016/S0013-4686(03)00180-4.

(280) Selvalakshmi, S.; Mathavan, T.; Selvasekarapandian, S.; Premalatha, M. Effect of Ethylene Carbonate Plasticizer on Agar-Agar: NH4Br-Based Solid Polymer Electrolytes. *Ionics (Kiel).* **2018**, *24* (8), 2209–2217. https://doi.org/10.1007/s11581-017-2417-y.

(281) Asnawi, A. S. F. M.; Aziz, S. B.; Saeed, S. R.; Yusof, Y. M.; Abdulwahid, R. T.; Al-Zangana, S.; Karim, W. O.; Kadir, M. F. Z. Solid-State EDLC Device Based on Magnesium Ion-Conducting Biopolymer Composite Membrane Electrolytes: Impedance, Circuit Modeling, Dielectric Properties and Electrochemical Characteristics. *Membranes (Basel).* **2020**, *10* (12), 389. https://doi.org/10.3390/membranes10120389.

(282) Judeinstein, P.; Sanchez, C. Hybrid Organic-Inorganic Materials : A Land of Multidisciplinarity Chemistry. *J. Mater. Chem.* **1996**, *6* (4), 511–525. https://doi.org/10.1039/JM9960600511.

(283) Wang, C.; Wei, Y.; Ferment, G. R.; Li, W.; Li, T. Poly(Ethylene Oxide)- Silica Hybrid Materials for Lithium Battery Application. *Mater. Lett.* **1999**, *39* (4), 206–210. https://doi.org/https://doi.org/10.1016/S0167-577X(99)00007-5.

(284) Popall, M.; Durand, H. Inorganic-Organic Copolymers as Solid State Li+ Electrolytes. *Electrochim. Acta* **1992**, *37* (9), 1593–1597. https://doi.org/10.1016/0013-4686(92)80118-6.

(285) Lev, O.; Wu, Z.; Bharathi, S.; Glezer, V.; Modestov, A.; Gun, J.; Rabinovich, L.; Sampath, S. Sol-Gel Materials in Electrochemistry. *Chem. Mater.* **1997**, *9* (11), 2354–2375. https://doi.org/10.1021/cm970367b.

(286) Walcarius, A.; Mandler, D.; Cox, J. A.; Collinson, M.; Lev, O. Exciting New Directions in the Intersection of Functionalized Sol-Gel Materials with Electrochemistry. *J. Mater. Chem.* **2005**, *15* (35–36), 3663–3689. https://doi.org/10.1039/b504839g.

(287) Judeinstein, P.; Titman, J.; Stamm, M.; Schmidt, H. Investigation of Ion-Conducting Ormolytes : Structure-Property Relationships. *Chem. Mater.* **1994**, *6* (2), 127–134. https://doi.org/https://doi.org/10.1021/cm00038a007.

(288) Shin, S. C.; Kim, J.; Modigunta, J. K. R.; Murali, G.; Park, S.; Lee, S.; Lee, H.; Park, S. Y.; In, I. Bio-Mimicking Organic-Inorganic Hybrid Ladder-like Polysilsesquioxanes as a Surface Modifier for Polyethylene Separator in Lithium-Ion Batteries. *J. Memb. Sci.* **2021**, *620*, 118886. https://doi.org/10.1016/j.memsci.2020.118886.

(289) Soo Lee, A. S.; Lee, J. H.; Lee, J. C.; Hong, S. M.; Hwang, S. S.; Koo, C. M. Novel Polysilsesquioxane Hybrid Polymer Electrolytes for Lithium Ion Batteries. *J. Mater. Chem. A* **2014**, *2* (5), 1277–1283. https://doi.org/10.1039/c3ta14290f.

(290) Popall, M.; Andrei, M.; Kappel, J.; Kron, J.; Olma, K.; Olsowski, B. ORMOCERs as Inorganic-Organic Electrolytes for New Solid State Lithium Batteries and Supercapacitors. *Electrochim. Acta* **1998**, *43* (10–11), 1155–1161. https://doi.org/10.1016/S0013-4686(97)10014-7.

(291) Wang, Q.; Zhang, H.; Cui, Z.; Zhou, Q.; Shangguan, X.; Tian, S.; Zhou, X.; Cui, G. Siloxane-Based Polymer Electrolytes for Solid-State Lithium Batteries. *Energy Storage Mater.* **2019**, *23*, 466–490. https://doi.org/https://doi.org/10.1016/j.ensm.2019.04.016.

(292) Rathnayake, H.; White, J.; Dawood, S. Polysilsesquioxane-Based Organic-Inorganic Hybrid Nanomaterials and Their Applications towards Organic Photovoltaics. *Synth. Met.* **2021**, *273*, 116705. https://doi.org/10.1016/j.synthmet.2021.116705.

(293) Stober, W. E. R. N. E. R. Controlled Growth of Monodisperse Silica Spheres in the Micron Size Range. *J. Colloid Interface Sci.* **1968**, *26*, 62–69.

(294) Tescione, F.; Tammaro, O.; Bifulco, A.; Del Monaco, G.; Esposito, S.; Pansini, M.; Silvestri, B.; Costantini, A. Silica Meets Tannic Acid: Designing Green Nanoplatforms for Environment Preservation. *Molecules* **2022**, *27* (6), 1944. https://doi.org/10.3390/molecules27061944.

(295) Postnova, I.; Shchipunov, Y. Tannic Acid as a Versatile Template for Silica Monoliths Engineering with Catalytic Gold and Silver Nanoparticles. *Nanomaterials* **2022**, *12* (23), 1–13. https://doi.org/10.3390/nano12234320.

(296) Saha, S.; Dawood, S.; Butreddy, P.; Pathiraja, G.; Rathnayake, H. Novel Biodegradable Low- κ Dielectric Nanomaterials from Natural Polyphenols. *RSC Adv.* **2021**, *11* (27), 16698–16705. https://doi.org/10.1039/D1RA01513C.

(297) Saha, S.; Dawood, S.; Butreddy, P.; Pathiraja, G.; Rathnayake, H. Novel Biodegradable Low- κ Dielectric Nanomaterials from Natural Polyphenols. *RSC Adv.* **2021**, *11* (27), 16698–16705. https://doi.org/10.1039/D1RA01513C.

(298) Hawkins, M.; Saha, S.; Ravindran, E.; Rathnayake, H. A Sol-Gel Polymerization Method for Creating Nanoporous Polyimide Silsesquioxane Nanostructures as Soft Dielectric Materials. *J. Polym. Sci. Part A Polym. Chem.* **2019**, *57* (4), 562–571. https://doi.org/10.1002/pola.29295.

(299) Azizi Samir, M. A. S.; Alloin, F.; Sanchez, J. Y.; Dufresne, A. Cellulose Nanocrystals Reinforced Poly(Oxyethylene). *Polymer (Guildf).* **2004**, *45* (12), 4149–4157. https://doi.org/10.1016/j.polymer.2004.03.094.

(300) Wang, S.; Zhang, L.; Wang, A.; Liu, X.; Chen, J.; Wang, Z.; Zeng, Q.; Zhou, H. H.; Jiang, X.; Zhang, L. Polymer-Laden Composite Lignin-Based Electrolyte Membrane for High-Performance Lithium Batteries. *ACS Sustain. Chem. Eng.* **2018**, *6* (11), 14460–14469. https://doi.org/10.1021/acssuschemeng.8b03117.

(301) Hawkins, M.; Saha, S.; Ravindran, E.; Rathnayake, H. A Sol – Gel Polymerization Method for Creating Nanoporous Polyimide Silsesquioxane Nanostructures as Soft Dielectric Materials. **2018**, 1–10. https://doi.org/10.1002/pola.29295.

(302) Maaz, M.; Elzein, T.; Dragoe, D.; Bejjani, A.; Jarroux, N.; Poulard, C.; Aubry-Barroca, N.; Nsouli, B.; Roger, P. Poly(4-Vinylpyridine)-Modified Silica for Efficient Oil/Water Separation. *J. Mater. Sci.* **2019**, *54* (2), 1184–1196. https://doi.org/10.1007/s10853-018-2888-x.

(303) Boruah, A.; Rasheed, A.; Mendhe, V. A.; Ganapathi, S. Specific Surface Area and Pore Size Distribution in Gas Shales of Raniganj Basin, India. *J. Pet. Explor. Prod. Technol.* **2019**, *9* (2), 1041–1050. https://doi.org/10.1007/s13202-018-0583-8.

(304) Sing, K. S. W.; Williams, R. T. Physisorption Hysteresis Loops and the Characterization of Nanoporous Materials. *Adsorpt. Sci. Technol.* **2004**, *22* (10), 773–782. https://doi.org/10.1260/0263617053499032.

(305) SING, K. S. W.; EVERETT, D. H.; HAUL, R. A. W.; MOSCOU, L.; PIEROTTI, R. A.; ROUQUEROL, J. SIEMIENIEWSKA, T. REPORTING PHYSISORPTION DATA FOR GAS/SOLID SYSTEMS with Special Reference to the Determination of Surface Area and Porosity. *Pure Appl. Chem.* **1985**, *57* (4), 603–619.

(306) Barrett, E. P.; Joyner, L. G.; Halenda, P. P. The Determination of Pore Volume and Area Distributions in Porous Substances. I. Computations from Nitrogen Isotherms. *J. Am. Chem. Soc.* **1951**, *73* (1), 373–380. https://doi.org/10.1021/ja01145a126.

(307) Ibrahim, S.; Yassin, M. M.; Ahmad, R.; Johan, M. R. Effects of Various LiPF6 Salt Concentrations on PEO-Based Solid Polymer Electrolytes. *Ionics (Kiel).* **2011**, *17* (5), 399–405. https://doi.org/10.1007/s11581-011-0524-8.

(308) Watanabe, M.; Nagano, S.; Sanui, K.; Ogata, N. Ionic Conductivity of Network Polymers from Poly(Ethylene Oxide) Containing Lithium Perchlorate. *Polymer Journal*. 1986, pp 809–817. https://doi.org/10.1295/polymj.18.809.

(309) Watanabe, M.; Kanba, M.; Nagaoka, K.; Shinohara, I. Ionic Conductivity of Hybrid Films Composed of Polyacrylonitrile, Ethylene Carbonate, and LiClO4. *J. Polym. Sci. Part A-2, Polym. Phys.* **1983**, *21* (6), 939–948. https://doi.org/10.1002/pol.1983.180210610.

(310) Watanabe, M.; Kanba, M.; Matsuda, H.; Tsunemi, K.; Mizoguchi, K.; Tsuchida, E.; Shinohara, I. High Lithium Ionic Conductivity of Polymeric Solid Electrolytes. *Die Makromol. Chemie, Rapid Commun.* **1981**, *2* (12), 741–744. https://doi.org/10.1002/marc.1981.030021208.

(311) Osman, Z.; Mohd Ghazali, M. I.; Othman, L.; Md Isa, K. B. AC Ionic Conductivity and DC Polarization Method of Lithium Ion Transport in PMMA-LiBF 4 Gel Polymer Electrolytes. *Results Phys.* **2012**, *2*, 1–4. https://doi.org/10.1016/j.rinp.2011.12.001.

(312) Perumal, P.; Christopher Selvin, P.; Selvasekarapandian, S. Characterization of Biopolymer Pectin with Lithium Chloride and Its Applications to Electrochemical Devices. *Ionics (Kiel).* **2018**, *24* (10), 3259–3270. https://doi.org/10.1007/s11581-018-2507-5.

(313) Agrawal, R. C.; Gupta, R. K. Review Superionic Solid: Composite Electrolyte Phase – an Overview. *J. Mater. Sci.* **1999**, *34*, 1131–1162.

Figure A1. (a) XPS survey spectrum and binding energy spectra of TALi-Si-B2 microstructures for: (b) C1s, (c) O 1s, (d) Si 2p, (e) N 1s and (f) Li 1s.

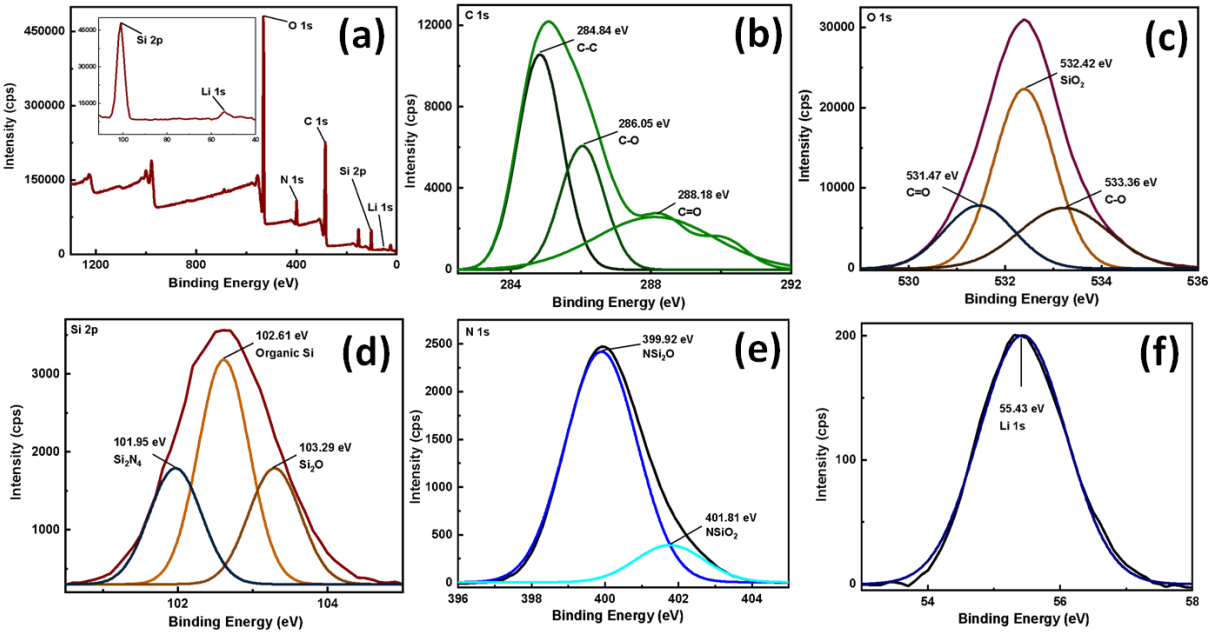

Figure A2. (a) XPS survey spectrum and binding energy spectra of TALi-Si-B3 microstructures for: (b) C1s, (c) O 1s, (d) Si 2p, (e) N 1s and (f) Li 1s.

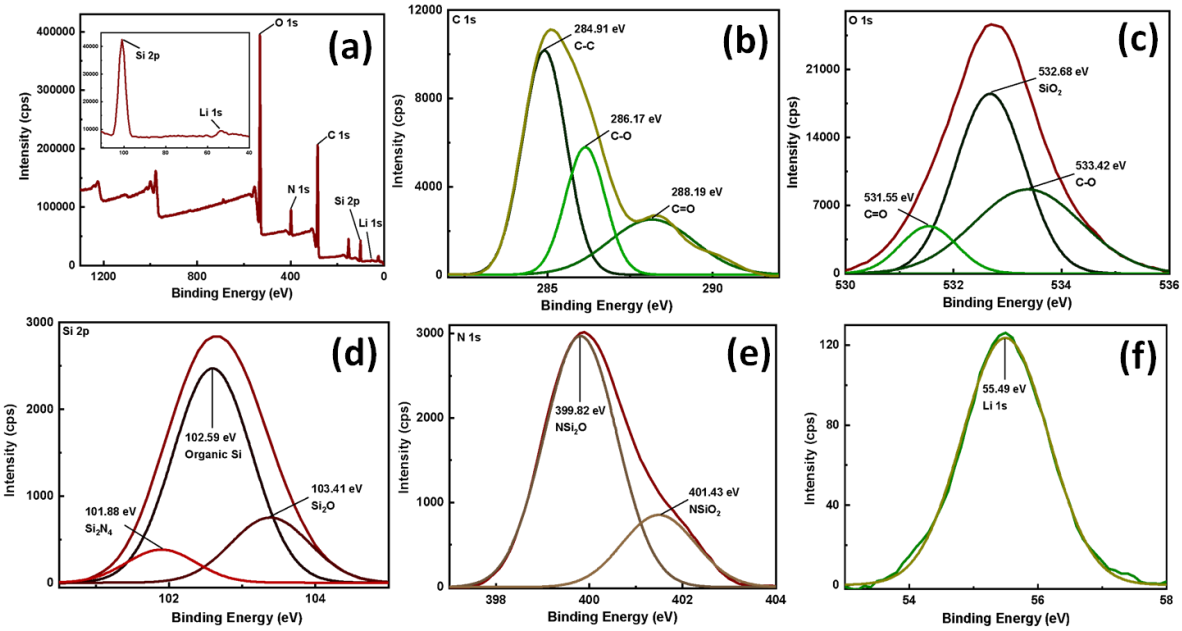

Figure A3. (a) XPS survey spectrum and binding energy spectra of TALi-Si-B4 microstructures for: (b) C1s, (c) O 1s, (d) Si 2p, (e) N 1s and (f) Li 1s.

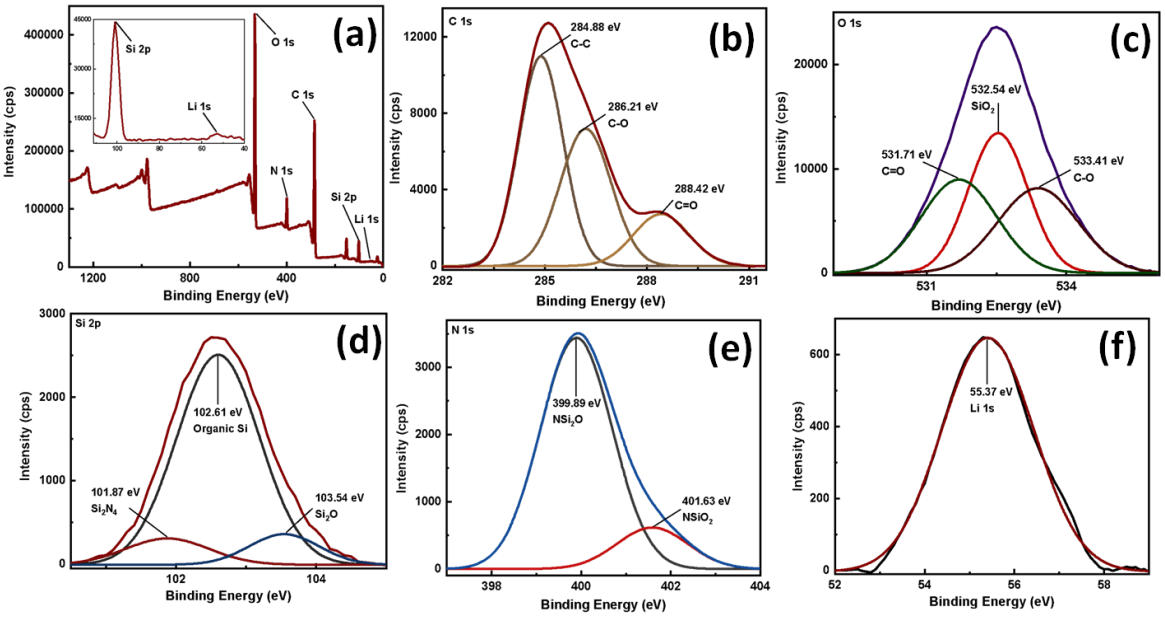

Figure A4. (a) XPS survey spectrum and binding energy spectra of TALi-Si-B5 microstructures for: (b) C1s, (c) O 1s, (d) Si 2p, (e) N 1s and (f) Li 1s.

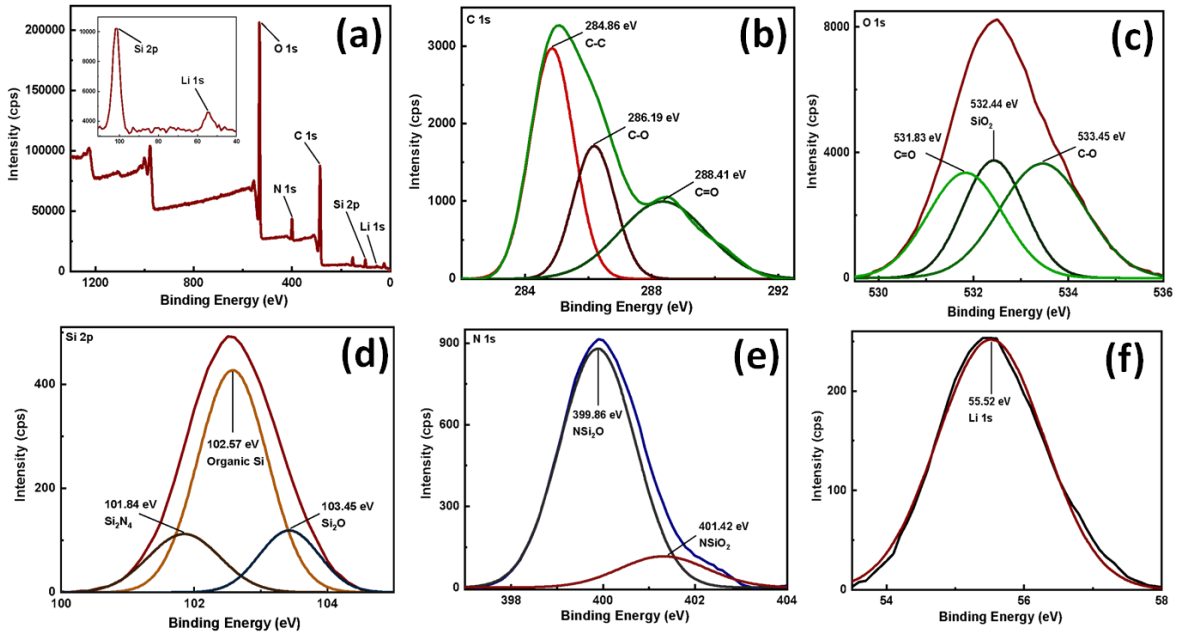

Figure A5. (a) XPS survey spectrum and binding energy spectra of TALi-Si-B6 microstructures for: (b) C1s, (c) O 1s, (d) Si 2p, (e) N 1s and (f) Li 1s.

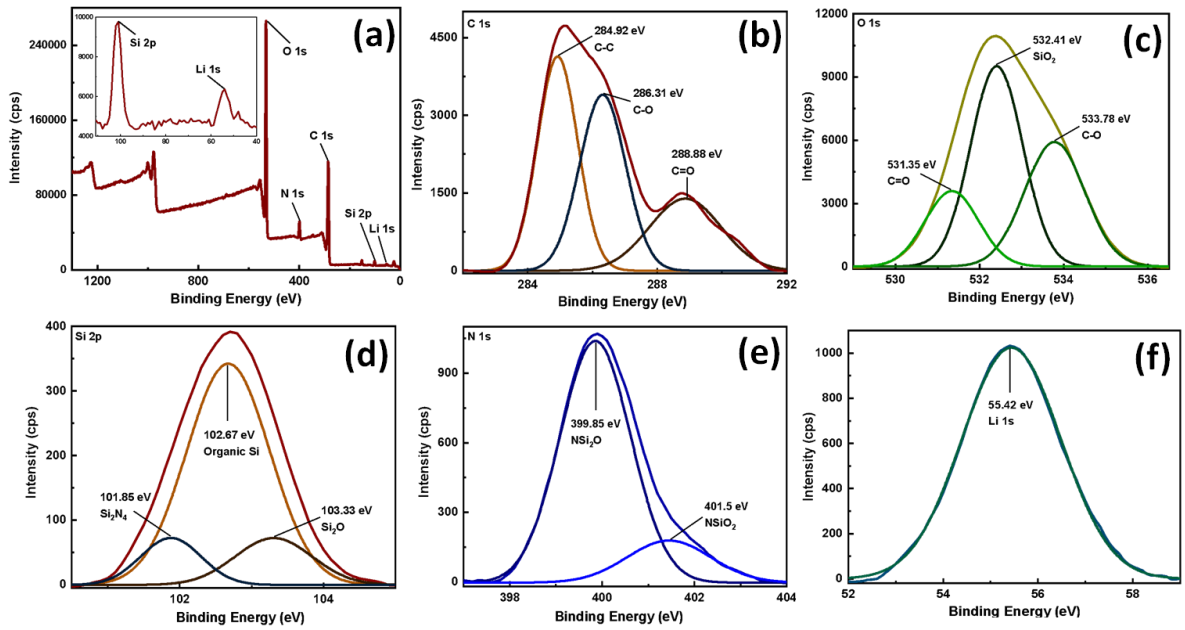

APPENDIX B: TEMPERATURE DEPENDENT IONIC CONDUCTIVITY DATA OF LI-MOF BASED SOLID-STATE ELECTROLYTES

Table B1. Temperature dependent ionic conductivity data for LEC@Li-BDC electrolyte.

Sample Name *(Thickness of pellet = 1.4mm)*	**Temperature (°C)**	**Temperature (K)**	**Ionic Conductivity (σ) (S/cm)**	**1000/T (K^{-1})**	**ln (σ)**	**Standard deviation of ln (σ)**
Li-BDC-EC-5wt% $LiClO_4$	25	298	$(1.72\pm 0.104) \times 10^{-5}$	3.36	-10.97	0.0596
Li-BDC-EC-5wt% $LiClO_4$	35	308	$(4.8\pm 1.604) \times 10^{-5}$	3.24	-9.94	0.3413
Li-BDC-EC-5wt% $LiClO_4$	45	318	$(1.18\pm 0.006) \times 10^{-4}$	3.14	-9.04	0.0049
Li-BDC-EC-5wt% $LiClO_4$	55	328	$(2.17\pm 0.041) \times 10^{-4}$	3.05	-8.43	0.01908

Table B2. Temperature dependent ionic conductivity data for LEC@Li-NDC electrolyte.

Sample Name *(Thickness of pellet = 1.2mm)*	**Temperature (°C)**	**Temperature (K)**	**Ionic Conductivity (σ) (S/cm)**	**1000/T (K^{-1})**	**ln (σ)**	**Standard deviation of ln (σ)**
Li-NDC-EC-5wt% $LiClO_4$	25	298	$(3.66\pm 0.624) \times 10^{-5}$	3.36	-10.21	0.1618
Li-NDC-EC-5wt% $LiClO_4$	35	308	$(7.49 \pm 0.871) \times 10^{-5}$	3.24	-9.49	0.1162
Li-NDC-EC-5wt% $LiClO_4$	45	318	$(1.63\pm 0.305) \times 10^{-4}$	3.14	-8.72	0.1796
Li-NDC-EC-5wt% $LiClO_4$	55	328	$(4.91\pm 0.293) \times 10^{-4}$	3.05	-7.61	0.0288

Table B3. Temperature dependent ionic conductivity data for LEC@Li-BPDC electrolyte.

Sample Name *(Thickness of pellet = 2mm)*	**Temperature (°C)**	**Temperature (K)**	**Ionic Conductivity (σ) (S/cm)**	**1000/T (K^{-1})**	**ln(σ)**	**Standard deviation of ln (σ)**
Li-BPDC-EC-5wt% $LiClO_4$	25	298	$(6.66\pm 0.24) \times 10^{-5}$	3.36	-9.61	0.0357
Li-BPDC-EC-5wt% $LiClO_4$	35	308	$(1.44 \pm 0.2) \times 10^{-4}$	3.24	-8.84	0.14013
Li-BPDC-EC-5wt% $LiClO_4$	45	318	$(3.36\pm 0.375) \times 10^{-4}$	3.14	-7.99	0.11377
Li-BPDC-EC-5wt% $LiClO_4$	55	328	$(6.19\pm 0.265) \times 10^{-4}$	3.05	-7.38	0.04307

Figure B1. Open-circuit graphs of Li-BDC, Li-NDC and Li-BPDC MOFs.

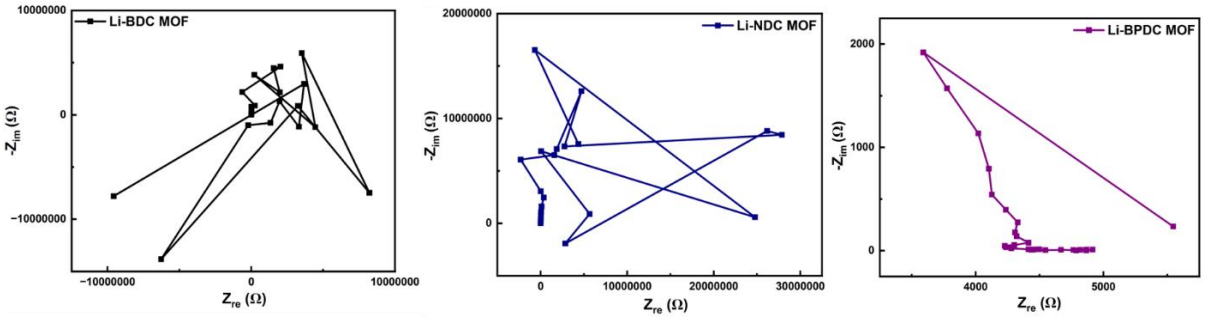

APPENDIX C: TEMPERATURE DEPENDENT IONIC CONDUCTIVITY DATA OF TALI BASED SOLID-STATE ELECTROLYTES

Table C1. Temperature dependent ionic conductivity data for TALi@LEC electrolyte.

Sample Name *(Thickness of pellet = 1mm)*	**Temperature (℃)**	**Temperature (K)**	**Ionic Conductivity (σ) (S/cm)**	**1000/ T (K^{-1})**	**ln (σ)**	**Standard deviation of ln (σ)**
TALi-EC-5wt% $LiClO_4$	25	298	(5.1± 0.411) x 10^{-5}	3.36	-9.89	0.082
TALi-EC-5wt% $LiClO_4$	35	308	(1.4± 0.5) x 10^{-4}	3.24	-8.87	0.339
TALi-EC-5wt% $LiClO_4$	45	318	(4.2± 0.421) x 10^{-4}	3.14	-7.77	0.101
TALi-EC-5wt% $LiClO_4$	55	318	(1.1± 0.075) x 10^{-3}	3.14	-6.81	0.065

Table C2. Temperature dependent ionic conductivity data for TALi-Si-B1@LEC electrolyte.

Sample Name *(Thickness of pellet = 1.92mm)*	**Temperature (℃)**	**Temperature (K)**	**Ionic Conductivity (σ) (S/cm)**	**1000/ T (K^{-1})**	**ln(σ)**	**Standard deviation of ln (σ)**
TALi-Si-B1-EC-5wt% $LiClO_4$	25	298	(1.87±0.085) x 10^{-4}	3.36	-8.58	0.045
TALi-Si-B1-EC-5wt% $LiClO_4$	40	313	(2.79±0.095) x 10^{-4}	3.19	-8.18	0.034
TALi-Si-B1-EC-5wt% $LiClO_4$	60	333	(4.05±0.041) x 10^{-4}	3	-7.81	0.01

Table C3. Temperature dependent ionic conductivity data for TALi-Si-B2@LEC electrolyte.

Sample Name *(Thickness of pellet = 2.72mm)*	**Temperature (℃)**	**Temperature (K)**	**Ionic Conductivity (σ) (S/cm)**	**1000/T (K^{-1})**	**ln(σ)**	**Standard deviation of ln (σ)**
TALi-Si-B2-EC-5wt% $LiClO_4$	35	308	(2.73±0.051) x 10^{-3}	3.24	-5.9	0.017
TALi-Si-B2-EC-5wt% $LiClO_4$	45	318	(3.43±0.136) x 10^{-3}	3.14	-5.67	0.039
TALi-Si-B2-EC-5wt% $LiClO_4$	55	328	(4.15±0.109) x 10^{-3}	3.05	-5.48	0.026
TALi-Si-B2-EC-5wt% $LiClO_4$	65	338	(4.77±0.035) x 10^{-3}	2.96	-5.35	0.007

Table C4. Temperature dependent ionic conductivity data for TALi-Si-B3@LEC electrolyte.

Sample Name *(Thickness of pellet = 2.03mm)*	**Temperature (℃)**	**Temperature (K)**	**Ionic Conductivity (σ) (S/cm)**	**1000/T (K^{-1})**	**ln(σ)**	**Standard deviation of ln (σ)**
TALi-Si-B3-EC-5wt% $LiClO_4$	25	298	(5.78±0.217) x 10^{-4}	3.36	-7.45	0.042
TALi-Si-B3-EC-5wt% $LiClO_4$	35	308	(1.11±0.043) x 10^{-3}	3.24	-6.8	0.039
TALi-Si-B3-EC-5wt% $LiClO_4$	45	318	(1.71±0.035) x 10^{-3}	3.14	-6.37	0.02
TALi-Si-B3-EC-5wt% $LiClO_4$	55	328	(2.17±0.076) x 10^{-3}	3.05	-6.13	0.035
TALi-Si-B3-EC-5wt% $LiClO_4$	65	338	(3.52±0.01) x 10^{-3}	2.96	-5.65	0.003

Table C5. Temperature dependent ionic conductivity data for TALi-Si-B4@LEC electrolyte.

Sample Name *(Thickness of pellet = 2.03mm)*	**Temperature (℃)**	**Temperature (K)**	**Ionic Conductivity (σ) (S/cm)**	**1000/T (K^{-1})**	**ln(σ)**	**Standard deviation of ln (σ)**
TALi-Si-B4-EC-5wt% $LiClO_4$	25	298	(4.35±0.151) x 10^{-4}	3.36	-7.74	0.034
TALi-Si-B4-EC-5wt% $LiClO_4$	35	308	(1.04±0.036) x 10^{-3}	3.24	-6.86	0.034
TALi-Si-B4-EC-5wt% $LiClO_4$	45	318	(1.42±0.015) x 10^{-3}	3.14	-6.55	0.011
TALi-Si-B4-EC-5wt% $LiClO_4$	55	328	(2.21±0.091) x 10^{-3}	3.05	-6.11	0.04
TALi-Si-B4-EC-5wt% $LiClO_4$	65	338	(2.92±0.087) x 10^{-3}	2.96	-5.83	0.03

Table C6. Temperature dependent ionic conductivity data for TALi-Si-B5@LEC electrolyte.

Sample Name *(Thickness of pellet = 1.79mm)*	**Temperature (℃)**	**Temperature (K)**	**Ionic Conductivity (σ) (S/cm)**	**1000/ T (K^{-1})**	**ln(σ)**	**Standard deviation of ln (σ)**
TALi-Si-B5-EC-5wt% $LiClO_4$	25	298	(8.85±0.437) x 10^{-5}	3.36	-9.33	0.05
TALi-Si-B5-EC-5wt% $LiClO_4$	35	308	(1.07±0.005) x 10^{-4}	3.24	-9.14	0.005
TALi-Si-B5-EC-5wt% $LiClO_4$	45	318	(1.31±0.017) x 10^{-4}	3.14	-8.94	0.013
TALi-Si-B5-EC-5wt% $LiClO_4$	55	328	(1.6±0.035) x 10^{-4}	3.05	-8.74	0.022
TALi-Si-B5-EC-5wt% $LiClO_4$	65	338	(2.15±0.119) x 10^{-4}	2.96	-8.44	0.056

Table C7. Temperature dependent ionic conductivity data for TALi-Si-B6@LEC electrolyte.

Sample Name *(Thickness of pellet = 1.37mm)*	**Temperature (℃)**	**Temperature (K)**	**Ionic Conductivity (σ) (S/cm)**	**1000/ T (K^{-1})**	**ln(σ)**	**Standard deviation of ln (σ)**
TALi-Si-B6-EC-5wt% $LiClO_4$	25	298	(5.43±0.492) x 10^{-5}	3.36	-9.82	0.081
TALi-Si-B6-EC-5wt% $LiClO_4$	35	308	(1.2±0.035) x 10^{-4}	3.24	-9.02	0.029
TALi-Si-B6-EC-5wt% $LiClO_4$	45	318	(2.12±0.153) x 10^{-4}	3.14	-8.45	0.071
TALi-Si-B6-EC-5wt% $LiClO_4$	55	328	(4.29±0.366) x 10^{-4}	3.05	-7.75	0.086
TALi-Si-B6-EC-5wt% $LiClO_4$	65	338	(1.05±0.047) x 10^{-3}	2.96	-6.86	0.045

Figure D1. (a) N_2 BET Isotherms, (b) BJH Adsorption dV/dw pore volume distribution plot, and (c) NLDFT Cumulative pore volume distribution plot for TALi-Si-B2 microstructures.

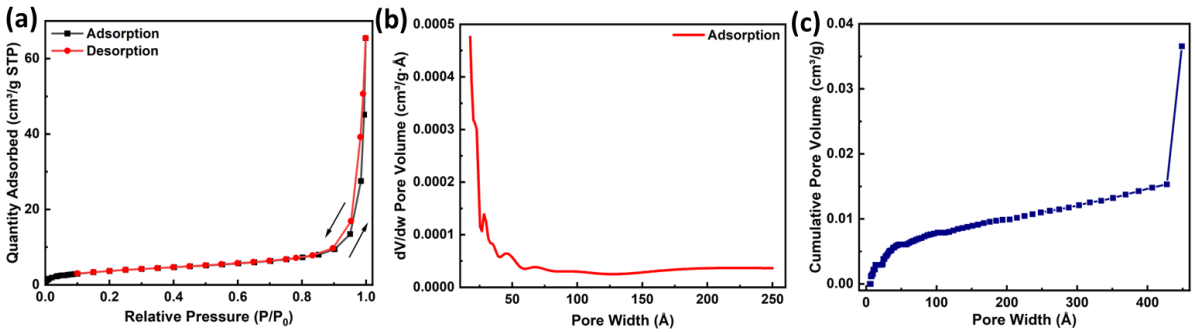

Figure D2. (a) N_2 BET Isotherms, (b) BJH Adsorption dV/dw pore volume distribution plot, and (c) NLDFT Cumulative pore volume distribution plot for TALi-Si-B3 microstructures.

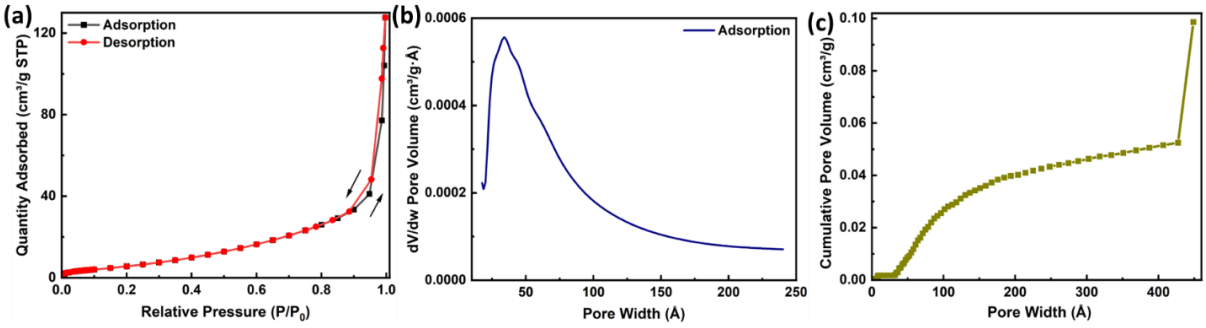

Figure D3. (a) N_2 BET Isotherms, (b) BJH Adsorption dV/dw pore volume distribution plot, and (c) NLDFT Cumulative pore volume distribution plot for TALi-Si-B4 microstructures.

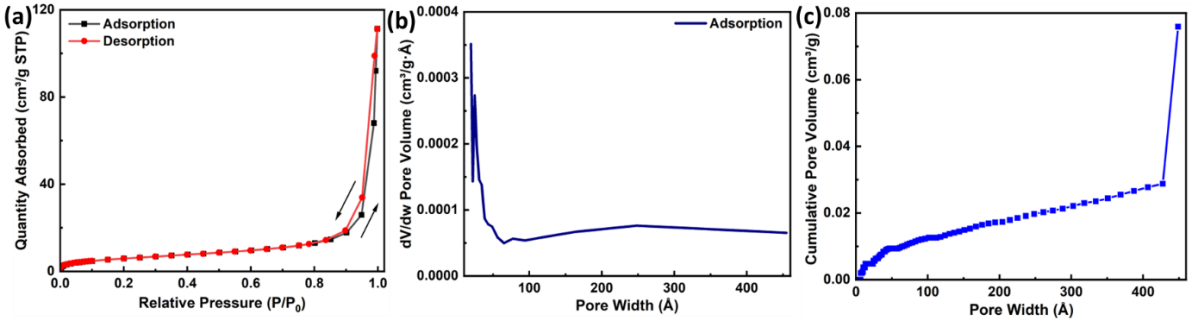

Figure D4. (a) N_2 BET Isotherms, (b) BJH Adsorption dV/dw pore volume distribution plot, and (c) NLDFT Cumulative pore volume distribution plot for TALi-Si-B5 microstructures.

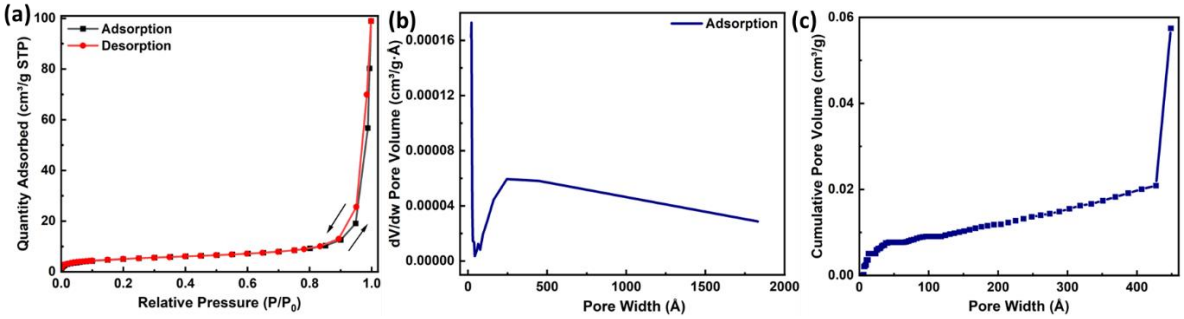

Figure D5. (a) N_2 BET Isotherms, (b) BJH Adsorption dV/dw pore volume distribution plot, and (c) NLDFT Cumulative pore volume distribution plot for TALi-Si-B6 microstructures.